

Nonequilibrium Dynamics of Strongly Correlated Systems

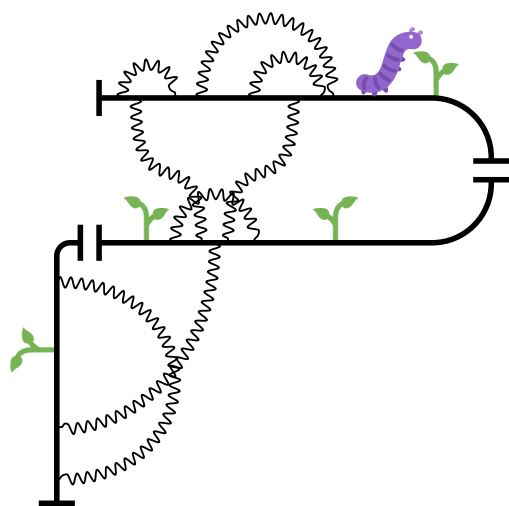
by

Joseph Kleinhenz

A dissertation submitted in partial fulfillment
of the requirements for the degree of
Doctor of Philosophy
(Physics and Scientific Computing)
in The University of Michigan
2021

Doctoral Committee:

Associate Professor Emanuel Gull, Chair
Professor Eitan Geva
Professor Lu Li
Associate Professor Kai Sun
Assistant Professor Liuyan Zhao



Joseph Kleinhenz

jkleinh@umich.edu

ORCID iD: 0000-0003-3670-0431

© Joseph Kleinhenz 2021

To Alissa, who supported me from beginning to end

Acknowledgements

This thesis would not have been possible without all the people who helped and supported me along the way. I would first like to thank my advisor Dr. Emanuel Gull for guiding me through my PhD. His expertise, advice and patience were invaluable.

I am also very grateful to all my colleagues in the Gull group who all contributed so much to making this time intellectually stimulating and enjoyable. At the beginning of my PhD, Dr. Andrey Antipov welcomed me to the group and taught me more `c++` than I ever knew existed. I am thankful for the help and example of Dr. Qiaoyuan Dong who blazed the trail in front of me. I could never have completed this journey without the help of Dr. Igor Krivenko who taught me so many things and patiently reviewed countless pull requests. Over the course of my time in graduate school, I have benefited immensely from discussions with Dr. Sergei Isakov and Dr. Markus Wallerberger who taught me so much about science. Jia Li was an excellent colleague, conference roommate and friend and I am thankful for our many discussions from the first year of graduate school until now. I am grateful to all my fellow graduate students in the Gull group, for their support and many helpful discussions.

I would also like to thank my wife, Alissa Kleinhenz, for her love and support throughout this period of our lives. Finally, I would like to thank my parents for instilling and nurturing my love of science from the very beginning.

Table of Contents

Table of Contents	iv
List of Figures	vi
List of Tables	xiv
List of Algorithms	xv
List of Abbreviations	xvi
Abstract	xvii
Chapter 1: Introduction	1
1.1 Publications	3
Chapter 2: Keldysh Formalism	4
2.1 The Contour Idea	4
2.2 Green's Functions	10
Chapter 3: The Hybridization Expansion	16
3.1 Historical Development	16
3.2 The Bare Expansion	18
3.3 Semi-analytic Approximations	33
3.4 The Inchworm Expansion	38
3.5 Green's Functions	44
3.6 The Hybridization Function	47
Chapter 4: Inchworm Quantum Monte Carlo	52
4.1 Quantum Monte Carlo	52
4.2 The Inchworm Algorithm	60
4.3 Results	65
4.4 Conclusion	72
Chapter 5: Kondo Voltage Splitting	75
5.1 Introduction	75

5.2	Model	76
5.3	Methods	77
5.4	Results	78
5.5	Conclusions	84
5.6	Appendix	85
Chapter 6: Kondo Cloud		89
6.1	Introduction	89
6.2	Model	90
6.3	Methods	94
6.4	Results	95
6.5	Conclusions	104
6.6	Appendix	106
Chapter 7: Inchworm DMFT		112
7.1	Introduction	112
7.2	Methods	113
7.3	Results	119
7.4	Conclusions	123
7.5	Appendix	127
Chapter 8: Nonequilibrium Metal–Insulator Transitions		133
8.1	Introduction	133
8.2	Model	133
8.3	Methods	134
8.4	Results	136
8.5	Conclusions	143
8.6	Appendix	144
Chapter 9: Conclusions and Outlook		145
Appendices		147
Appendix A: NCA		148
Bibliography		159

List of Figures

2.1	Left: Schematic illustration of Keldysh contour. Right: Graphical representation of an expectation value showing placement of operators along the contour.	6
2.2	Left: Schematic illustration of full three branch contour. Right: Graphical representation of an expectation value showing placement of operators along the contour.	8
2.3	Left: Schematic illustration of full three branch contour as a circle. Right: Graphical representation of an expectation value showing the use of the cyclic property of the trace to reorder the evolution operators along the twisted contour beginning at t_-	9
2.4	Graphical representation of $G(t_+, t'_-)$	10
2.5	Illustration of Green's function $G(t, t')$ on the twisted contour. Each color shows a Keldysh component of the Green's function. The colored region shows physical time domain.	13
2.6	Causal (left) and contour causal (right) slices of the time domain of two time contour object. Each color corresponds to a single slice. The circled number indicates the order of each slice.	14
3.1	Left: Diagrammatic representation of the bare propagators $P_\alpha^{(0)}$. Right: Diagrammatic representation of the hybridization vertices $\hat{V}_\sigma, \hat{V}_\sigma^\dagger$	24
3.2	Diagrammatic representation of a hybridization expansion term with topology $T = \{\uparrow\uparrow\}$ for tip state $ 0\rangle$ (left) and $ \uparrow\downarrow\rangle$ (right).	24
3.3	Diagrammatic representation of the second order hybridization expansion term with topology $T = \{\uparrow\downarrow\uparrow\downarrow\}$ for tip state $ 0\rangle$	25
3.4	Diagrammatic representation of a hybridization expansion term with topology $T = \{\uparrow\uparrow\}$ for tip state $ 0\rangle$ (left) and $ \uparrow\downarrow\rangle$ (right).	29
3.5	Diagrammatic representation of a hybridization expansion term with topology $T = \{\uparrow\uparrow\uparrow\uparrow\}$ for tip state $ 0\rangle$	30
3.6	Diagrammatic representation of a hybridization expansion term with topology $T = \{\uparrow\downarrow\uparrow\downarrow\}$ for tip state $ 0\rangle$	31
3.7	Diagrammatic representation of a hybridization expansion term with topology $T = \{\uparrow\uparrow\uparrow\uparrow\uparrow\uparrow\}$ for tip state $ 0\rangle$. Label in parenthesis shows the permutation corresponding to each diagram.	32

3.8	Illustration of the bare expansion for the propagator expressed using the compressed diagrammatic language. Thick (thin) lines represent bold (bare) propagators. The state sequence and spins of the hybridization lines are left implicit.	33
3.9	Diagrammatic representation of a reducible diagram which can be separated by a single cut (left) and a 1PI diagram (right).	34
3.10	Diagrammatic representation of the Dyson equation. The thick (thin) line represents a bold (bare) propagator.	34
3.11	NCA self-energy diagrams. The propagators are bold.	35
3.12	OCA self-energy diagrams. The propagators are bold.	36
3.13	High order contribution to the bold propagator included within NCA.	37
3.14	Illustration of the inchworm expansion for the bold propagator. The diagrams in the bottom row are not inchworm proper because they contain disconnected hybridization lines (marked in red) which are already included in the bold part of the split propagator.	39
3.15	Illustration of the hybridization graph $\mathcal{G}(\mathcal{C}, \mathcal{D})$ for six diagrams. Green nodes represent hybridization lines ending in the connected region (t, t_s) and are said to be “connected”. Blue nodes represent hybridization lines which are part of a connected component of \mathcal{G} containing a connected node. Red nodes represent hybridization lines which are not part of a connected component containing a connected node. The inchworm proper diagrams are diagrams in which every connected component of \mathcal{G} contains at least one connected node.	40
3.16	Inchworm proper diagrams for a configuration with topology $T = \{\uparrow\uparrow\uparrow\uparrow\uparrow\}$ and one vertex in the connected region. Disconnected hybridization lines are marked in red. Only one out of the six bare diagrams is inchworm proper. The propagator lines represent the split propagator P^s	41
3.17	Order 1 and order 2 inchworm proper diagrams contributing to $P_{ 0\rangle}(t, t')$ in the limit where $\Delta t = t - t_s \rightarrow 0$. The propagator lines represent the split propagator P^s	42
3.18	Illustration of the bare expansion for the Green’s function propagator. The virtual hybridization line is represented by a dashed arc, and fixed in all diagrams.	46
3.19	Illustration of the bold expansion for the Green’s function propagator. The crossed out diagrams are not G proper because they contain disconnected hybridization lines (marked in red) which are already included in the bold propagator.	46
3.20	Order 0 diagrams for the Green’s function propagators contributing to the spin up Green’s function $G_{\uparrow}(t, t_-)$	47
3.21	Impurity spectral function for the resonant level model in the wide band limit.	50

4.1	Illustration of the contour causal structure of the bold propagators. A propagator $P(t, t')$ (magenta) depends on all propagators with start point on or after t' and end point up to t_s (blue).	61
4.2	Illustration of the diagonal by diagonal calculation of the propagators. The circled numbers label the diagonals which correspond to sets of inchworm steps which can be taken in parallel. The propagator is computed only on the physical time domain.	62
4.3	Illustration of the causal structure of the Green's function propagators. A Green's function propagator $P^G(t'_+, t'_-; t_1, t_-)$ (red) depends on all bold propagators P with start points or end points up to the maximum physical time t' (we only show the bold propagators that are not obtained by symmetry). This Green's function propagator contributes to the right mixing Green's function $G(t_1, t_-) = G^\Gamma(\tau, t')$	63
4.4	Illustration of the DAG representing the dependency structure of calculation for a Green's function element $G(t, t_-)$ in the physical time domain. Arrows indicate dependencies. The Green's function depends causally on all propagators with start or end times less than or equal to the maximum physical time t' . The propagators depend contour causally on all propagators with a start or end time between t_1 and $t_s = t_2 - \Delta t$	64
4.5	Top panel: Time evolution of the impurity occupation N after a voltage quench using the non-crossing and one-crossing approximations (NCA and OCA, respectively). Black lines: semi-analytically computed NCA and OCA solutions. Blue line: NCA solution generated from an inchworm expansion truncated to order one. Red line: OCA solution from an inchworm expansion truncated to order 2. Bottom panel: Statistical error estimate of the quantities shown in the upper panel.	66
4.6	Top panel: Time evolution of the density on the impurity after a voltage quench with $\Gamma = 1$, $U = 10$, $\epsilon_d = 0$, $D = 5$, $T = 1$ and $V = 6$. Results obtained from a bare QMC calculation are shown for $t \leq 0.6$. The inchworm results with different orders agree with the bare result for $t \leq 0.6$ and coincide with each other for longer times. Bottom panel: Error estimates. Data obtained using the bare method shows an exponential increase of the errors as a function of time, whereas inchworm errors grow slower as a function of time.	67
4.7	Top panel: The current dynamics after a voltage quench with $\Gamma = 1$, $U = 4$, $\epsilon_d = -2$, $D = 5$, $T = 1$ and $V = 4$. The inchworm results with different orders converge as max-order increases. Bottom panel: Error estimates of inchworm data obtained by averaging eight independent calculations. Errors increase as a function of time but avoid the exponential amplification seen in bare calculations.	68

4.8	Top panel: The imaginary time Green's function in equilibrium (half-filling) with $\Gamma = 1$, $U = 4$, $\epsilon_d = -2$, $D = 5$, $T = 1$ and $V = 0$. Inchworm results with different orders all coincide and agree with the bare calculation. Bottom panel: The error estimate for the inchworm data is approximately constant in imaginary time.	69
4.9	Top panel: A contour plot of the dynamics of auxiliary current spectrum $A_{\text{aux}}(\omega, t)$ after a voltage quench with $\Gamma = 1$, $U = 4$, $\epsilon_d = -2$, $D = 5$, $T = 1$ and $V = 4$. The maximum order cut-off for the inchworm calculation is 6. A formation and a splitting of the Kondo peak are observed as a function of time. Middle panel: Slices of auxiliary current spectrum at different times from the top contour plot. A clear splitting of the spectrum is shown. Bottom panel: Error estimate on the spectral function obtained from eight independent simulations.	70
4.10	Top panel: The (half-filling) spectrum at $t = 2.0$ after a voltage quench with $\Gamma = 1$, $U = 4$, $\epsilon_d = -2$, $D = 5$, $T = 1$ and $V = 4$. The spectral function shows the establishment of a split Kondo peak as the diagram order is increased. The data for order 6 is identical to the data shown in Fig. 4.9. Bottom panel: Error estimate for data shown in main panel. The error remains constant as a function of frequency and increases as the maximum order is increased.	72
4.11	Top panel: The (half-filling) spectrum at $t = 2.0$ with no applied voltage with $\Gamma = 1$, $U = 4$, $\epsilon_d = -2$, $D = 5$, $T = 1$ and $V = 0$. Bottom panel: error estimate for data shown in the main panel.	73
4.12	Top panel: Spectral function away from half filling at $t = 2.0$ after a voltage quench with $\Gamma = 1$, $U = 10$, $\epsilon_d = -2$, $D = 5$, $T = 1$ and $V = 4$. Bottom panel: error estimate for data shown in the main panel.	73
5.1	Time evolution of the QD spectral function after a coupling quench and in the presence of a bias voltage V , at interaction strength $U = 8.0\Gamma$ and temperature $T = 0.02\Gamma \ll T_K$. The voltages are $V = 0.5\Gamma$ (upper left), $V = 1.2\Gamma$ (upper right), $V = 1.8\Gamma$ (lower left), and $V = 3.5\Gamma$ (lower right).	79
5.2	Splitting time t_{split} where a single peak splits into two peaks as a function of V at $T = 0.02\Gamma$. Upper panel: inchworm and OCA results at $U = 8.0\Gamma$. Lower panel: OCA results for several U . Insets show the same data on a log-log scale demonstrating power-law behavior.	80
5.3	QD spectral function from the inchworm method at $t = t_{\text{max}} = 8.0\Gamma^{-1}$, corresponding to the steady-state spectrum $A(\omega)$ for $V \geq 1.0\Gamma$. $T = 0.02\Gamma$ (upper panel) and $T = 0.5\Gamma$ (lower panel) for the voltages indicated. . . .	82

5.4	Peak-to-peak distance $\Delta\omega$ between the split Kondo peaks as a function of bias voltage V , at $T = 0.02\Gamma < T_K$. Error bars originate from averaging over finite-time oscillations expected to eventually dissipate. Upper panel: inchworm and OCA results at $U = 8.0\Gamma$ with $t_{\max} = 8.0\Gamma^{-1}$ compared with the linear behavior $\Delta\omega = V$ predicted by various approximate methods. Lower panel: Deviation of splitting from V within OCA at $T = 0.02\Gamma$ for several values U , with $t_{\max} = 15.0\Gamma^{-1}$	83
5.5	Time evolution of the QD spectra $A(\omega, t)$ of the quantum dot for $U = 8\Gamma, T = 0.5\Gamma$. $V = 0.5\Gamma$ (upper left), $V = 1.5\Gamma$ (upper right), $V = 2.5\Gamma$ (lower left), $V = 3.0\Gamma$ (lower right).	86
5.6	Comparison of inchworm (solid) with OCA (dashed) QD spectral functions at $U = 8.0\Gamma, T = 0.02\Gamma$ for voltages indicated.	87
5.7	Transient spectral functions at two values of the bias voltage $V = 1.2\Gamma$ and $V = 1.8\Gamma$ corresponding to two panels in Fig. 5.1. The bold lines show spectra at two times when the “unsplit” transient phase is observed. The dashed line is the steady state solution computed with OCA at the effective temperature $T_{\text{eff}}^{\text{tr}}$ that delivers a good fit to the transient spectra.	87
5.8	Bold lines: Steady state spectral functions at two values of the bias voltage $V = 1.2\Gamma$ and $V = 1.8\Gamma$ corresponding to two panels in Fig. 5.1. Dashed line: fitting curve computed as $[A(\omega + V/2, T_{\text{eff}}^{\text{st}}) + A(\omega - V/2, T_{\text{eff}}^{\text{st}})]/2$, where $A(\omega, T_{\text{eff}}^{\text{st}})$ is OCA equilibrium spectrum at effective temperature $T_{\text{eff}}^{\text{st}}$	88
6.1	Schematic illustration of the model. A quantum dot (QD) is coupled to two non-interacting leads, where each lead is a semi-infinite, one-dimensional tight-binding chain with nearest neighbor hopping t . On the right lead, the hopping between sites L and $L + 1$ is optionally modified to take the value t' . The leads are connected to the QD by a hopping λ . The QD has an on-site local Coulomb interaction U	90
6.2	Coupling density $\Gamma(\omega)$ for $\alpha = 0$ (black) and $\alpha \neq 0$ for two different cavity lengths L (blue/orange). For $\alpha \neq 0$ the resonance width is given by $\Delta_L = \pi v_f/L$. Inset shows zoom around the Fermi energy illustrating Δ_L	92
6.3	Impurity DOS at interaction strength $U = 9\Gamma$ as the temperature is lowered below the Kondo temperature T_K . Inset shows zoom of the peak at the Fermi energy in the $\beta = 50\Gamma^{-1}$ results. Dashed black line shows Lorentzian fit used to estimate the width $\gamma_{\text{imp}} \approx 0.062\Gamma$ which gives an estimate of the Kondo temperature T_K	96
6.4	Top: Kondo peak width γ_{imp} as a function of the size of the Fabry-Pérot cavity length L for $\alpha = 0.1$ and $U = \{7\Gamma, 8\Gamma, 9\Gamma\}$. Solid (dashed) lines show data for L odd (even). Horizontal lines show data in the absence of the cavity ($\alpha = 0$). Bottom: Logarithm of peak width γ_{imp} normalized by peak width in the absence of the cavity γ_0	98
6.5	Lead LDOS at interaction strength $U = 9\Gamma$ at sites 3 (top) and 4 (bottom) as the temperature is lowered below the Kondo temperature. Dashed black line shows LDOS for non-interacting lead decoupled from impurity.	100

6.6	Difference between lead LDOS above and below T_K on four different sites. Dashed black line shows Lorentzian fit of central peak used to estimate $\gamma(x)$.	101
6.7	Top: Width of lead LDOS normalized by impurity width for $U = \{7\Gamma, 8\Gamma, 9\Gamma\}$. Bottom: Logarithm of LDOS width as function of rescaled distance. Inset: Extracted length scale ξ varies inversely with $\gamma_{\text{imp}} \approx T_K$.	103
6.8	Top: Impurity DOS for applied voltages $V = \{0.0\Gamma, 0.2\Gamma, 0.5\Gamma, 1.0\Gamma\}$. Bottom: Difference between lead LDOS at $\beta\Gamma = 1$ and $\beta\Gamma = 50$ for each applied voltage on four different sites.	105
6.9	Comparison of the time-dependent retarded QD Green's function (top) and QD DOS (bottom) obtained from OCA (blue) and inchworm QMC (orange/green) at $\beta = 20\Gamma^{-1}$, $U = 7\Gamma$, $\alpha = 0$. The inchworm QMC results are parameterized by the maximum allowed expansion order (see legend).	110
7.1	Real and imaginary parts of the greater dynamical mean field Green's function $G^>(t)$ as a function of real time t up to a maximum time of $tv = 2$. $U/v = 4$, $T/v = 0.05$, equilibrium. Shown is the convergence with DMFT iteration.	118
7.2	Real and imaginary parts of the greater DMFT Green's function $G^>(t)$, for times up to $tv = 2$, with $T/v = 0.5$, half filling, equilibrium, at on-site interaction strengths $U/v \in \{2.0, 4.0, 6.0, 8.0\}$.	120
7.3	Real and imaginary parts of the greater DMFT Green's function $G^>(t)$, for times up to $tv = 2$, half filling, equilibrium, for $U/v = 4$, at temperatures $T/v \in \{0.5, 0.1, 0.05\}$.	121
7.4	Retarded components of the DMFT Green's function, bare Green's function and self-energy computed for $U/v = 8.0$ at half-filling and temperature $T/v = 0.5$. $G_{\text{rec}}^{\text{ret}}(t)$ (dashed orange curve lying on top of the black one) is a Green's function reconstructed by iterative substitution of $\Sigma^{\text{ret}}(t)$ into the Dyson equation. Data obtained using 2001 interpolation slices.	122
7.5	Retarded component of the imaginary part of the DMFT self-energy for interaction strengths $U/v \in \{2.0, 4.0, 6.0, 8.0\}$ at half-filling and temperature $T/v = 0.5$.	123
7.6	The converged DMFT spectral function $A(\omega)$ obtained by directly performing the Fourier transform on the real time Green's function with a cutoff at $t_{\text{max}}v = 2$ with $T/v = 0.5$ and at on-site interaction strengths $U/v \in \{2.0; 4.0; 6.0; 8.0\}$.	124
7.7	Comparison of raw Green's function data up to $tv = 2$ (black) and $tv = 4$ (red) with results from linear prediction of the $tv = 2$ data (blue) and $tv = 4$ data (green) for $U/v = 8$, $T/v = 0.5$. For the linear prediction we use $p = 9$, $t_{\text{fit}}v = 1.0$.	125
7.8	Comparison of spectral function obtained from raw Green's function data up to $tv = 2$ (black) and $tv = 4$ (red) with results from linear prediction of the $tv = 2$ data (blue) and $tv = 4$ data (green) for $U/v = 8$, $T/v = 0.5$. For the linear prediction we use $p = 9$, $t_{\text{fit}}v = 1.0$.	125

7.9	The converged DMFT spectral function $A(\omega)$ obtained by extrapolating the real-time Green's function from $tv = 2.0$ to $tv = 10.0$ using linear prediction with $p = 9$, $t_{\text{fit}}v = 1.0$ for temperature $T/v = 0.5$ at on-site interaction strengths $U/v \in \{2.0, 4.0, 6.0, 8.0\}$	126
7.10	The converged DMFT spectral function $A(\omega)$ obtained by extrapolating the real-time Green's function from $tv = 2.0$ to $tv = 10.0$ using linear prediction with $p = 9$, $t_{\text{fit}}v = 1.0$ for $U/v = 4$ at temperatures $T/v \in \{0.5, 0.1, 0.05\}$	126
7.11	Matsubara Green's function $G(\tau)$ computed for the impurity model in equilibrium with $U/v = 4.6$ at two temperatures and with different inchworm order truncations. Results from an equilibrium hybridization expansion solver (TRIQS/CTHYB[71, 204]) are given as a reference.	128
7.12	The converged DMFT spectral function $A(\omega)$ obtained by extrapolating the real-time Green's function from $t = 2.0$ to $t = 10.0$ using linear prediction with $p = \{5, 10\}$, $t_{\text{fit}} = \{1.0, 2.0\}$ for $U = 4$ at temperatures $T = 0.05$	129
7.13	The converged DMFT spectral function $A(\omega)$ obtained by extrapolating the real-time Green's function from $tv = 2.0$ to $tv = 10.0$ using linear prediction with $p = \{5, 10\}$, $t_{\text{fit}}v = \{1.0, 2.0\}$ for $U/v = 6$ at temperature $T/v = 0.5$	130
7.14	Retarded components of the DMFT Green's function, bare Green's function and self-energy computed in equilibrium with $U/v = 8.0$ at $T/v = 0.5$. The self-energy curves are obtained by a direct solution of the Dyson equation in its discretized matrix form. $G^{\text{ret}}(t)$ has been measured on 41 time slices, while a larger number of slices and cubic interpolation have been used to perform matrix inversions. The four subplots correspond to different numbers of interpolation points. $G_{\text{rec}}^{\text{ret}}(t)$ (orange curve) is a Green's function reconstructed by iterative substitution of $\Sigma^{\text{ret}}(t)$ into the Dyson equation. Top left: 41 slices. Top right: 101 slices. Bottom left: 1001 slices. Bottom right: 2001 slices.	131
8.1	A: Spectral weight at $\omega = 0$ as a function of λ for metallic (dashed orange) and insulating (solid blue) initialization of the DMFT loop. The dashed black lines show the boundaries of the coexistence region ($\lambda_{c_1} = 0.115$, $\lambda_{c_2} = 0.145$). B: Spectral function for several different λ . C: Spectral functions of metallic and insulating solutions in the coexistence region.	136
8.2	A: Evolution of $A(\omega = 0, t)$ for equilibrium metallic and insulating solutions (dashed green/red) and for switched solutions (solid orange/blue). B: Switching protocol for $\lambda(t)$. Dashed black lines show the coexistence region. C: $A(\omega, tv = 100)$ for equilibrium metal (dashed green) and "switched" metal (solid blue). D: $A(\omega, tv = 100)$ for equilibrium insulator (dashed red) and "switched" insulator (solid orange).	137

8.3	<p>A: Evolution of $A(\omega = 0, t)$ for equilibrium metallic and insulating solutions (dashed green/red) and for switched solutions (solid orange/blue). B: Switching protocol for $\lambda(t)$. Dashed black lines show the coexistence region. C: $A(\omega, tv = 100)$ for equilibrium metal (dashed green) and “switched” metal (solid blue). D: $A(\omega, tv = 100)$ for equilibrium insulator (dashed red) and “switched” insulator (solid orange).</p>	139
8.4	<p>Illustration of proposed device for realizing dynamic control of $\lambda(t)$. The voltage between the outer metallic plates can be controlled in two ways depending on the mode of operation of the device. Without the red connections, the voltage between the plates is modulated by an external signal (blue circle) and the device is operated as a transistor. Adding the red connections couples the voltage between the plates to the source-drain voltage and turns the device into a two terminal memristor.</p>	141
8.5	<p>Simulation of the system configured as a two terminal memristive device. A: Current voltage characteristic of device under sinusoidal driving. The inset shows the shape and minima of the potential $\Phi(x, \lambda)$ at $\lambda = \lambda_c, \lambda_c \pm 1$. B: Use of device as a resistive memory element.</p>	142
8.6	<p>Comparison of the retarded Green’s function (A) and spectral function (B) obtained from OCA (green) and inchworm (blue/orange) at $\beta = 20v^{-1}$, $U = 4.0v$, $\lambda = 0.25$.</p>	144

List of Tables

2.1	Keldysh components of the Green's function.	11
3.1	Examples of operator and state sequences for different topologies and tip states.	23

List of Algorithms

3.1	Inchworm proper diagram selector.	43
4.1	Metropolis-Hastings Algorithm	58
4.2	Wang-Landau Algorithm	60

List of Abbreviations

DMFT Dynamical Mean Field Theory

DOS Density of States

STM Scanning Tunneling Microscopy

ARPES Angle Resolved Photoemission Spectroscopy

NCA Non-Crossing Approximation

OCA One-Crossing Approximation

2CA Two-Crossing Approximation

SIAM Single-Impurity Anderson Model

QMC Quantum Monte Carlo

MCMC Markov Chain Monte Carlo

CT-QMC Continuous Time Quantum Monte Carlo

CT-HYB Continuous Time Hybridization Expansion

HPX High Performance ParallelX

DAG Directed Acyclic Graph

DFT Density Functional Theory

Abstract

In this thesis, we describe methods for solving quantum impurity models out of equilibrium, and consider several applications of these methods. Quantum impurity models describe systems in which a small subsystem (the impurity) is coupled to a large external environment (the bath). These models are useful in describing a wide variety of physical systems, including quantum dots, adsorbed adatoms, and molecular junctions. They are also important for the study of lattice models, such as the Hubbard model, where they appear as auxiliary problems within the framework of dynamical mean field theory (DMFT).

Many interesting phenomena in these systems, such as transport through a quantum dot, or optical pumping of a Mott insulator, occur away from equilibrium. Theoretical description of these phenomena requires methods that are capable of handling both real time evolution and strong correlation effects presenting a formidable challenge. In this thesis, we describe several methods for the solution of non-equilibrium quantum impurity models which meet this challenge. These methods are based on an expansion in the coupling between the impurity and the bath known as the hybridization expansion.

Chapter 1 gives an introduction to the problems addressed in this thesis. Chapter 2 provides a brief overview of Keldysh formalism for nonequilibrium problems. Chapter 3 describes the bare hybridization expansion for the Anderson impurity model as well as its bold extensions. In particular we derive the non-crossing approximation (NCA), the one-crossing approximation (OCA), the inchworm expansion, and a bold expansion for the impurity Green's function. Chapter 4 describes the implementation of a quantum Monte Carlo algorithm based on the inchworm expansion. The rest of the thesis describes applications of these algorithms to problems of physical interest.

Chapters 5 and 6 apply the methods previously described to understanding the Kondo effect in quantum dot systems. The first chapter examines the behavior of the Kondo effect under an applied voltage bias, a classic non-equilibrium strongly-correlated problem. The second chapter examines different ways of measuring the cloud of electrons which screen the impurity spin in the Kondo regime.

Chapters 7 and 8 apply the same methods to the Hubbard model using the Dynamical mean-field theory (DMFT) mapping. The first chapter studies the Hubbard model in equilibrium using the numerically exact inchworm quantum Monte Carlo method. The second chapter studies the possibility of dynamic switching between the metal and Mott-insulator states of the Hubbard model using the one-crossing approximation (OCA).

Finally chapter 9 gives some overall conclusions and suggests future directions for the development of hybridization expansion methods.

CHAPTER I

Introduction

Condensed matter physics seeks to describe the collective behavior of systems consisting of large numbers of interacting particles. These include the metals, glasses, insulators, and fluids which make up the objects of everyday experience, as well as more exotic systems such as superconductors and Bose-Einstein condensates. Quantum condensed matter physics applies the principles of quantum mechanics to this challenge. Like so many developments in physics, quantum condensed matter can be traced back to Einstein, whose 1907 calculation of the low temperature behavior of the specific heat of solids demonstrated the necessity of quantum mechanics in describing the microscopic underpinnings of regular materials [1, 2]. In his paper, Einstein postulated that the vibrational modes of atoms in solids had to be quantized in order to explain their specific heat, just as radiation had had to be quantized in order to explain the observed black body spectrum. Einstein’s proposal proved controversial at the time, but his approach was vindicated and the quantized vibrational modes he postulated—now known as phonons—are a fundamental piece of modern condensed matter physics.

In the decades after 1907, our understanding of quantum mechanics and its applications to condensed matter physics rapidly grew and by 1929, Dirac could famously declare

The underlying physical laws necessary for the mathematical theory of a large part of physics and the whole of chemistry are thus completely known, and the difficulty is only that the exact application of these laws leads to equations much too complicated to be soluble. It therefore becomes desirable that approximate practical methods of applying quantum mechanics should be developed, which can lead to an explanation of the main features of complex atomic systems without too much computation.

in his work on the quantum mechanics of many-electron systems [3]. Since then, Dirac’s desire has been fulfilled by a plethora of “approximate practical methods”. In this thesis, we will describe several such methods for solving what are known as quantum impurity

models, although we will drop the qualifier “without too much computation”.

Quantum impurity models describe systems in which a small subsystem (the impurity) is coupled to a large external environment (the bath). The Hamiltonian for a generic quantum impurity model can be written as

$$\hat{H} = \hat{H}_{\text{loc}} + \hat{H}_{\text{bath}} + \hat{H}_T \quad (1.1)$$

where \hat{H}_{loc} is the local Hamiltonian of the impurity, \hat{H}_{bath} is the bath Hamiltonian, and \hat{H}_T is the tunneling Hamiltonian which describes hopping between the impurity and the bath. The single impurity Anderson model (SIAM)—one of the simplest impurity models—was originally introduced in 1961 to describe the physics of dilute alloys containing magnetic impurities embedded in a non-magnetic host [4]. In 1964, Kondo showed that the scattering rate of the bath electrons on an impurity with an anti-ferromagnetic coupling would diverge at low temperatures explaining the decades old puzzle of the resistance minimum observed in these dilute magnetic alloys [5, 6]. This phenomena, in which the impurity becomes strongly coupled to the bath at low temperatures, is now known as the Kondo effect and is a paradigmatic example of strongly correlated physics in which the interactions between electrons play a key role and an independent particle description is not possible.

Further research into quantum impurity models has been enormously fruitful, yielding many new theoretical techniques including Wilson’s numerical renormalization group (NRG) approach [7, 8], as well hybridization expansion techniques [9–11] based on perturbation theory in \hat{H}_T which are the precursors of the methods described in this thesis. Additionally, although initially introduced in the context of dilute magnetic alloys, quantum impurity models have been used to describe an huge variety of physical systems such as quantum dots [12–15], adsorbed adatoms [16–19], and molecular junctions [20–22]. They are also important for the study of lattice models, such as the Hubbard model [23], where they appear as auxiliary problems within the framework of dynamical mean field theory (DMFT) [24, 25]. DMFT is able to capture a variety of strongly correlated phenomena such as Mott metal-insulator transitions [26–28] which are beyond the reach of methods based on an independent particle approximation such as Kohn-Sham density functional theory (DFT) [29].

Description of phenomena such as transport through a quantum dot or optical pumping of a Mott insulator require the solution of quantum impurity models out of equilibrium [22, 30]. This requires methods that are capable of handling both real time evolution and strong correlation effects presenting a formidable challenge. In this thesis, we describe several methods for the solution of non-equilibrium quantum impurity models which meet

this challenge. Chapter 2 describes the Keldysh formalism for nonequilibrium problems that we will use throughout this thesis. Chapter 3 describes hybridization expansion techniques for the Anderson impurity model. Chapter 4 describes implementation of the inchworm quantum Monte Carlo method. The rest of the thesis describes applications of these algorithms to problems of physical interest.

Chapters 5 and 6 apply the methods previously described to understanding the Kondo effect in quantum dot systems. The first chapter examines the behavior of the Kondo effect under an applied voltage bias, a classic non-equilibrium strongly-correlated problem. The second chapter examines different ways of measuring the cloud of electrons which screen the impurity spin in the Kondo regime.

Chapters 7 and 8 apply the same methods to the Hubbard model using the Dynamical mean-field theory (DMFT) mapping. The first chapter studies the Hubbard model in equilibrium using a numerically exact QMC method. The second chapter studies the possibility of dynamic switching between the metal and Mott-insulator states of the Hubbard model using the one-crossing approximation (OCA).

1.1 Publications

This thesis is based on work from the following publications:

1. A. E. Antipov, Q. Dong, J. Kleinhenz, G. Cohen, and E. Gull, “Currents and Green’s functions of impurities out of equilibrium: Results from inchworm quantum Monte Carlo”, [Physical Review B **95**, 085144 \(2017\)](#)
2. Q. Dong, I. Krivenko, J. Kleinhenz, A. E. Antipov, G. Cohen, and E. Gull, “Quantum Monte Carlo solution of the dynamical mean field equations in real time”, [Physical Review B **96**, 155126 \(2017\)](#)
3. I. Krivenko, J. Kleinhenz, G. Cohen, and E. Gull, “Dynamics of Kondo voltage splitting after a quantum quench”, [Physical Review B **100**, 201104 \(2019\)](#)
4. J. Kleinhenz, I. Krivenko, G. Cohen, and E. Gull, “Dynamic control of nonequilibrium metal-insulator transitions”, [Physical Review B **102**, 205138 \(2020\)](#)
5. J. Kleinhenz, I. Krivenko, G. Cohen, and E. Gull, “The Kondo Cloud in a 1D Nanowire”, (In Preparation)

CHAPTER II

Keldysh Formalism

In this chapter, we present a brief introduction to the Keldysh formalism that we will use throughout this thesis. This formalism provides an elegant language for expressing time dependent expectation values for nonequilibrium problems. Our discussion of this topic follows the excellent treatment given in [36]. See also [37] which gives a more computationally oriented description of various aspects of nonequilibrium formalism.

2.1 The Contour Idea

The time-dependent expectation value of an operator $\hat{O}(t)$ for a quantum system is given by

$$O(t) = \langle \hat{O}_H(t) \rangle \tag{2.1}$$

$$= \text{Tr} \left[\hat{\rho} \hat{O}_H(t) \right] \tag{2.2}$$

$$= \text{Tr} \left[\hat{\rho} \hat{U}(0, t) \hat{O}(t) \hat{U}(t, 0) \right] \tag{2.3}$$

where $\hat{\rho} = \sum_i w_i |\phi_i\rangle \langle \phi_i|$ is the initial density matrix, $\hat{O}_H(t)$ is the Heisenberg picture operator, and $\hat{U}(t, t')$ is the time evolution operator. We retain the time argument for the Schrödinger picture operator $\hat{O}(t)$ in order to keep track of the evolution operators associated with it, and to allow for the possibility of an explicit time dependence. The time-evolution operator satisfies the Schrödinger equation

$$i\hbar \partial_t \hat{U}(t, t') = \hat{H}(t) \hat{U}(t, t') \tag{2.4}$$

with boundary condition $U(t, t) = 1$ where $\hat{H}(t)$ is the Hamiltonian of the system. Throughout the rest of this thesis we will set $\hbar \equiv 1$. Integrating the Schrödinger equation and

taking into account the boundary condition, we obtain

$$\hat{U}(t, 0) = 1 - i \int_0^t dt_1 \hat{H}(t_1) \hat{U}(t_1, 0). \quad (2.5)$$

Note that \hat{U} appears on both the left-hand side and right-hand side of the equation. We can repeatedly substitute this definition of U into the right-hand side to obtain a series

$$\hat{U}(t, 0) = 1 - i \int_0^t dt_1 \hat{H}(t_1) \hat{U}(t_1, 0) \quad (2.6)$$

$$= 1 - i \int_0^t dt_1 \hat{H}(t_1) + (-i)^2 \int_0^t dt_1 \int_0^{t_1} dt_2 \hat{H}(t_1) \hat{H}(t_2) \hat{U}(t_2, 0) \quad (2.7)$$

$$= \sum_{n=0}^{\infty} (-i)^n \int_0^t dt_1 \int_0^{t_1} \dots \int_0^{t_{n-1}} dt_n \hat{H}(t_1) \dots \hat{H}(t_n). \quad (2.8)$$

Note that the operators here are time ordered, i.e. $t \geq t_1 \geq t_2 \geq \dots \geq t_n$. In order to conveniently express this, we introduce the time-ordering operator \mathcal{T} which takes a string of operators and orders them so that operators at later times occur to the left of operators at earlier times. \mathcal{T} is formally defined by

$$\mathcal{T} \left\{ \hat{O}_1(t_1) \dots \hat{O}_n(t_n) \right\} = (\pm 1)^{N(x)} \hat{O}_{x_1}(t_{x_1}) \dots \hat{O}_{x_n}(t_{x_n}) \quad (2.9)$$

where x is the permutation which orders the times such that $t_{x_1} \geq t_{x_2} \geq \dots \geq t_{x_n}$, $N(x)$ is the number of transpositions in x , and we take the plus (minus) sign if the operators $\{\hat{O}_i\}$ are bosonic (fermionic). In the case of two operators, \mathcal{T} can be written explicitly as

$$\mathcal{T} \left\{ \hat{A}(t) \hat{B}(t') \right\} = \Theta(t - t') \hat{A}(t) \hat{B}(t') \pm \Theta(t' - t) \hat{B}(t') \hat{A}(t) \quad (2.10)$$

where Θ is the Heaviside function. We can now rewrite our previous expression as

$$\hat{U}(t, 0) = \sum_{n=0}^{\infty} (-i)^n \int_0^t dt_1 \int_0^{t_1} \dots \int_0^{t_{n-1}} dt_n \hat{H}(t_1) \dots \hat{H}(t_n) \quad (2.11)$$

$$= \mathcal{T} \left\{ \sum_{n=0}^{\infty} (-i)^n \int_0^t dt_1 \int_0^{t_1} \dots \int_0^{t_{n-1}} dt_n \hat{H}(t_1) \dots \hat{H}(t_n) \right\} \quad (2.12)$$

$$= \mathcal{T} \left\{ \sum_{n=0}^{\infty} \frac{(-i)^n}{n!} \int_0^t dt_1 \int_0^t \dots \int_0^t dt_n \hat{H}(t_1) \dots \hat{H}(t_n) \right\} \quad (2.13)$$

$$= \mathcal{T} \left\{ e^{-i \int_0^t dt \hat{H}(t)} \right\} \quad (2.14)$$

where in the second to last line we have used \mathcal{T} to expand the integration bounds and divided by $n!$ to account for the $n!$ permutations of the time points.

Because \hat{H} is Hermitian, $\hat{U}(t, t')$ is unitary and satisfies $\hat{U}(t, t')^\dagger = \hat{U}(t', t)$. Therefore the conjugate equation is given by

$$\hat{U}(0, t) = \hat{U}(t, 0)^\dagger \quad (2.15)$$

$$= \left(\mathcal{T} \left\{ e^{-i \int_0^t d\bar{t} \hat{H}(\bar{t})} \right\} \right)^\dagger \quad (2.16)$$

$$= \bar{\mathcal{T}} \left\{ e^{-i \int_t^0 d\bar{t} \hat{H}(\bar{t})} \right\} \quad (2.17)$$

where we have introduced the anti-time-ordering operator $\bar{\mathcal{T}}$ which takes a string of operators and orders them so that operators at earlier times occur to the left of operators at later times. This takes into account the reversal of the operator order induced by the Hermitian conjugate. Using these results, the time-dependent expectation value of an operator can be written

$$O(t) = \text{Tr} \left[\hat{\rho} \hat{U}(0, t) \hat{O}(t) \hat{U}(t, 0) \right] \quad (2.18)$$

$$= \text{Tr} \left[\hat{\rho} \bar{\mathcal{T}} \left\{ e^{-i \int_t^0 dt' \hat{H}(t')} \right\} \hat{O}(t) \mathcal{T} \left\{ e^{-i \int_0^t dt' \hat{H}(t')} \right\} \right]. \quad (2.19)$$

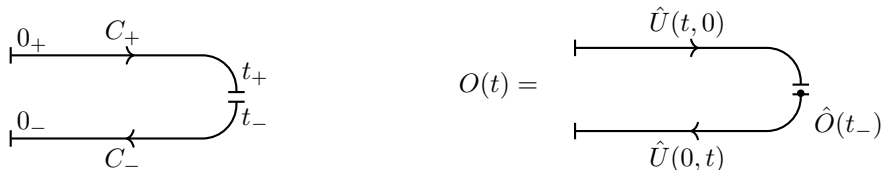


Figure 2.1: Left: Schematic illustration of Keldysh contour. Right: Graphical representation of an expectation value showing placement of operators along the contour.

We can simplify this expression by introducing a contour $C = C_+ \cup C_-$ which is the union of a “plus” branch $C_+ = (0_+, t_+)$ associated with the forward propagation $U(t, 0)$, and a “minus” branch $C_- = (t_-, 0_-)$ associated with the backward propagation $U(0, t)$. We refer to this two branch contour as the Keldysh contour, although the idea has been introduced independently several times [38, 39]. Figure 2.1 shows an illustration of this two branch Keldysh contour. Points on the contour are described by a time t and a Keldysh index \pm which specifies which branch they belong to. The contour runs $0_+ \rightarrow t_+ \rightarrow t_- \rightarrow 0_-$ and points are ordered along this path. We write $t_2 \succ t_1$ to indicate that t_2 comes after t_1 on the contour. By convention we place the operator $\hat{O}(t)$ at t_- .

We could equally well place it at t_+ but the placement on the “minus” branch will later prove useful.

A function of a contour time z is defined by

$$F(z) = \begin{cases} F_+(z) & z \in C_+ \\ F_-(z) & z \in C_- \end{cases} \quad (2.20)$$

where F_+ is the value taken on C_+ and F_- is the value taken on C_- . It is occasionally useful to consider functions which take different values on each branch (see for example [40]). However, in all cases considered here we will use $F_+ = F_-$ so that functions and operators do not explicitly depend on the Keldysh branch index. The purpose of the Keldysh index in an expression such as $\hat{O}(t_-)$ is to specify the placement of the operator on the contour. We define integration on the contour as the sum of integrals along each branch

$$\int_C dz = \int_{C_+} dz + \int_{C_-} dz = \int_{0_+}^{t_+} dz_+ + \int_{t_-}^{0_-} dz_-. \quad (2.21)$$

Note, the branches included in the contour integral depend on the integration bounds.

We now introduce the contour ordering operator \mathcal{T}_C which takes a string of operators and orders them so that operators occurring later on the contour C occur to the left of operators occurring earlier. In the case of two operators, \mathcal{T}_C can be written explicitly as

$$\mathcal{T}_C \{ \hat{A}(z) \hat{B}(z') \} = \begin{cases} \mathcal{T} \{ \hat{A}(z) \hat{B}(z') \} & z \in C_+, z' \in C_+ \\ \hat{A}(z) \hat{B}(z') & z \in C_-, z' \in C_+ \\ \pm \hat{B}(z') \hat{A}(z) & z \in C_+, z' \in C_- \\ \bar{\mathcal{T}} \{ \hat{A}(z) \hat{B}(z') \} & z \in C_-, z' \in C_- \end{cases} \quad (2.22)$$

so that operators on C_+ are time-ordered, operators on C_- are anti-time-ordered, and all operators on C_+ precede operators on C_- . We can now write the time-dependent

expectation value of an operator as

$$O(t) = \text{Tr} \left[\hat{\rho} \hat{U}(0, t) \hat{O}(t) \hat{U}(t, 0) \right] \quad (2.23)$$

$$= \text{Tr} \left[\hat{\rho} \bar{\mathcal{T}} \left\{ e^{-i \int_t^0 dt' \hat{H}(t')} \right\} \hat{O}(t) \mathcal{T} \left\{ e^{-i \int_0^t dt' \hat{H}(t')} \right\} \right] \quad (2.24)$$

$$= \text{Tr} \left[\hat{\rho} \bar{\mathcal{T}} \left\{ e^{-i \int_{C_-} dz' \hat{H}(z')} \right\} \hat{O}(t) \mathcal{T} \left\{ e^{-i \int_{C_+} dz' \hat{H}(z')} \right\} \right] \quad (2.25)$$

$$= \text{Tr} \left[\hat{\rho} \mathcal{T}_C \left\{ e^{-i \int_C dz' \hat{H}(z')} \hat{O}(t) \right\} \right] \quad (2.26)$$

where in the last line we have used the contour ordering operator \mathcal{T}_C to combine the forward and backward propagation into a single exponential.

So far we have considered a general density matrix $\hat{\rho} = \sum_i w_i |\phi_i\rangle \langle \phi_i|$. However, frequently we will be interested in starting our time evolution from the equilibrium density matrix of $\hat{H}(t=0) \equiv \hat{H}_0$ given by $\hat{\rho} = \frac{1}{Z} e^{-\beta \hat{H}_0}$ where $Z = \text{Tr} \left[e^{-\beta \hat{H}_0} \right]$ is the partition function. This density matrix can be written as an evolution in imaginary time from 0 to $-i\beta$.

$$\hat{\rho} = \frac{1}{Z} \exp \left(-\beta \hat{H}_0 \right) = \frac{1}{Z} \exp \left(-i \int_0^{-i\beta} dz \hat{H}_0 \right) = \frac{1}{Z} \hat{U}(-i\beta, 0) \quad (2.27)$$

Motivated by this, we introduce a third branch $C_1 = (0, -i\beta)$ and define a contour $C = C_+ \cup C_- \cup C_1$. This three branch contour has various names including the L-shaped, the Kadanoff-Baym-Keldysh, and the Konstantinov–Perel’ contour [41, 42]. In this thesis we will refer to it as the full or three branch contour.

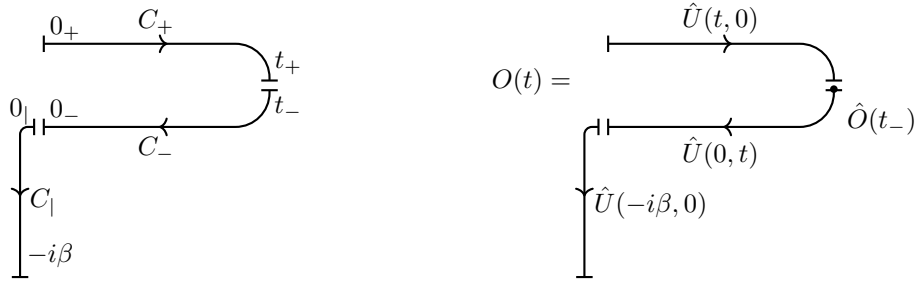


Figure 2.2: Left: Schematic illustration of full three branch contour. Right: Graphical representation of an expectation value showing placement of operators along the contour.

Figure 2.2 shows an illustration of the full contour. Points on this contour are described by a time t , which can now be imaginary, and a Keldysh index $\{+, -, |\}$ which specifies which branch they belong to. The contour runs $0_+ \rightarrow t_+ \rightarrow t_- \rightarrow 0_- \rightarrow 0_1 \rightarrow -i\beta$ and points are ordered along this path. The definitions of functions, integrals and ordering

defined on the full contour are straightforward generalizations of the two branch case.

Let $C' = C_+ \cup C_-$ denote the two branch contour, and $C = C' \cup C_1$ denote the full three branch contour. We can then write the time-dependent expectation value of an observable with an equilibrium initial state as

$$O(t) = \text{Tr} \left[\hat{\rho} \mathcal{T}_{C'} \left\{ e^{-i \int_{C'} dz' \hat{H}(z')} \hat{O}(t) \right\} \right] \quad (2.28)$$

$$= \frac{1}{Z} \text{Tr} \left[e^{-\beta \hat{H}_0} \mathcal{T}_{C'} \left\{ e^{-i \int_{C'} dz' \hat{H}(z')} \hat{O}(t) \right\} \right] \quad (2.29)$$

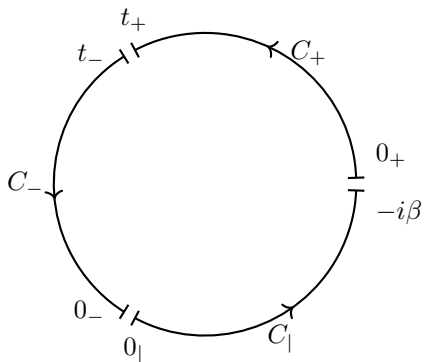
$$= \frac{1}{Z} \text{Tr} \left[e^{-i \int_0^{-i\beta} dz' \hat{H}_0} \mathcal{T}_{C'} \left\{ e^{-i \int_{C'} dz' \hat{H}(z')} \hat{O}(t) \right\} \right] \quad (2.30)$$

$$= \frac{1}{Z} \text{Tr} \left[e^{-i \int_{C_1} dz' \hat{H}_0} \mathcal{T}_{C'} \left\{ e^{-i \int_{C'} dz' \hat{H}(z')} \hat{O}(t) \right\} \right] \quad (2.31)$$

$$= \frac{1}{Z} \text{Tr} \left[\mathcal{T}_C \left\{ e^{-i \int_C dz' \hat{H}(z')} \hat{O}(t) \right\} \right] \quad (2.32)$$

where in the last line we have used the contour ordering operator \mathcal{T}_C to combine the imaginary time evolution with the forward/backward propagation into a single exponential. This expression for the time-dependent expectation value of an operator in terms of a contour ordered exponential will be the starting point for our perturbation theory.

Before moving on, it is worth noting that the cyclic property of the trace allows us to cyclically permute the operators in our expression for the expectation value freely. In particular, we can cyclically permute the order of the evolution operators associated with each branch, or equivalently permute the order of the branches. Because of this freedom it



$$\begin{aligned} O(t) &= \text{Tr} \left[\hat{U}(-i\beta, 0) \hat{U}(0, t) \hat{O}(t) \hat{U}(t, 0) \right] \\ &= \text{Tr} \left[\hat{U}(t, 0) \hat{U}(-i\beta, 0) \hat{U}(0, t) \hat{O}(t) \right] \\ &= \begin{array}{c} \hat{U}(t, 0) \quad \hat{U}(-i\beta, 0) \quad \hat{U}(0, t) \\ \leftarrow C_+ \quad \leftarrow C_1 \quad \leftarrow C_- \end{array} \hat{O}(t_-) \end{aligned}$$

Figure 2.3: Left: Schematic illustration of full three branch contour as a circle. Right: Graphical representation of an expectation value showing the use of the cyclic property of the trace to reorder the evolution operators along the twisted contour beginning at t_- .

is useful to think of the contour as a circle as shown in figure 2.3 (left). In this thesis we will make extensive use of the twisted contour \tilde{C} which begins at t_- . The twisted contour

is useful because it makes t_- the first point on the contour so that the twisted contour ordering operator $\mathcal{T}_{\hat{C}}$ will always place $\hat{O}(t_-)$ to the far right where it acts on the external state first. This allows us to avoid having to keep track of the location of $\hat{O}(t)$ on the contour.

Although these representations of the contour as a circle, or L shape are conceptually helpful, they are inconvenient when drawing diagrams. Therefore, when representing the contour we will frequently unfold it and draw it as a single straight line with contour time increasing to the left so that the order of operators on the contour matches the order in which they appear in contour ordered expressions as in figure 2.3 (right).

2.2 Green's Functions

The contour formalism generalizes straightforwardly to correlators of multiple operators. A particularly important case is the single-particle Green's function which encodes many key physical properties, and will be a core object of study in this thesis. The single-particle Green's function is defined as the contour ordered expectation value

$$G(t, t') = -i \langle \mathcal{T}_C \hat{c}(t) \hat{c}^\dagger(t') \rangle = -\frac{i}{Z} \text{Tr} \left[\mathcal{T}_C \left\{ e^{-i \int_C dz \hat{H}(z)} \hat{c}(t) \hat{c}^\dagger(t') \right\} \right] \quad (2.33)$$

where \hat{c} (\hat{c}^\dagger) are annihilation (creation) operators, and t and t' take values on the contour C . The operators \hat{c} and \hat{c}^\dagger may also carry some orbital indices, but for now we only consider the structure of the time domain. Figure 2.4 shows a graphical representation of

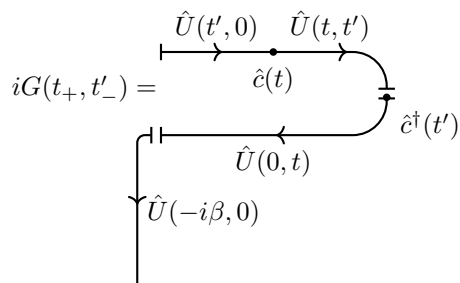


Figure 2.4: Graphical representation of $G(t_+, t_-)$.

the Green's function element $G(t_+, t_-)$.

On the twisted three branch contour, the Green's function takes the form of a 3×3

block matrix

$$G(t, t') = \begin{pmatrix} G_{--} & G_{-|} & G_{-+} \\ G_{|-} & G_{||} & G_{|+} \\ G_{+-} & G_{+|} & G_{++} \end{pmatrix} \quad (2.34)$$

where the blocks are indexed by the Keldysh indices of t and t' . Each of these blocks is

Block	Component	Name
G_{--}	$G^{\bar{T}}$	anti-time-ordered
$G_{ -}$	G^{\lceil}	right-mixing
G_{+-}	$G^{<}$	lesser
$G_{- }$	G^{\lfloor}	left-mixing
$G_{ }$	iG^M	matsubara
$G_{+ }$	G^{\lfloor}	left-mixing
G_{-+}	$G^{>}$	greater
$G_{ +}$	G^{\rceil}	right-mixing
G_{++}	G^T	time-ordered

Table 2.1: Keldysh components of the Green's function.

related to one of the Keldysh components shown in table 2.1 [37]. These components are related by a number of symmetries. Note $G_{-|} = G_{+|} = G^{\lfloor}$ and $G_{|-} = G_{|+} = G^{\rceil}$ because we can freely move the operator at the maximum physical time between C_- and C_+ since all evolution past the maximum physical time cancels. The time-ordered and anti-time-ordered components are defined in terms of the greater and lesser components by

$$G^T(t, t') = \Theta(t, t')G^{>}(t, t') + \Theta(t', t)G^{<}(t, t') \quad (2.35)$$

$$G^{\bar{T}}(t, t') = \Theta(t', t)G^{>}(t, t') + \Theta(t, t')G^{<}(t, t'). \quad (2.36)$$

The greater and lesser components are anti-hermitian and satisfy

$$G^{>}(t, t')^* = -G^{>}(t', t) \quad (2.37)$$

$$G^{<}(t, t')^* = -G^{<}(t', t). \quad (2.38)$$

The right-mixing and left-mixing components are related by

$$G^{\lceil}(t, \tau)^* = -\xi G^{\lceil}(\beta - \tau, t) \quad (2.39)$$

where ξ is +1 (-1) for bosons (fermions) and $\tau = it$ is the imaginary time. Finally, the Matsubara component satisfies

$$G^M(\tau)^* = G^M(\tau) \quad (2.40)$$

$$G^M(\tau, \tau') = G^M(\tau - \tau') \quad (2.41)$$

$$G^M(\tau) = \xi G^M(\tau + \beta) \quad (2.42)$$

where we define $G^M = -iG_{\parallel}$ in order to match the usual imaginary time conventions. Using these symmetries we can specify the full Green's function by the reduced set of components $\{G^>, G^<, G^{\lceil}, G^M\}$. These components can be defined by the values of the Green's function over the physical time domain

$$D(\tilde{C}) = \{(t, t') \mid 0_{\parallel} \succ t' \succ t_{-}^{\max}, t'_{+} \succ t \succ t'_{-}, \} \quad (2.43)$$

where t_{-}^{\max} is the first point on C_{-} and corresponds to the maximum physical time.

In order to numerically represent two-time objects such as the Green's function, we introduce a uniform discretization of real and imaginary time: $t_n = n\Delta t$, $n = 0, \dots, N_t$ and $\tau_n = n\Delta\tau$, $n = 0, \dots, N_{\tau}$, where $\Delta t = t_{-}^{\max}/N_t$, and $\Delta\tau = \beta/N_{\tau}$. Note, the number real (imaginary) discretization points is $N_t + 1$ ($N_{\tau} + 1$). This can be thought of as a discretization of each branch of the contour, so that the total contour in the three branch case has $2N_t + N_{\tau} + 3$ points. Figure 2.5 displays a representation of a discretized Green's function on the three branch twisted contour with $N_t = N_{\tau} = 2$. The colored region shows the physical time domain and the Keldysh components necessary to fully specify the Green's function. Note we only need half of the $++$ and $--$ blocks because of the anti-hermitian symmetry of the greater and lesser components.

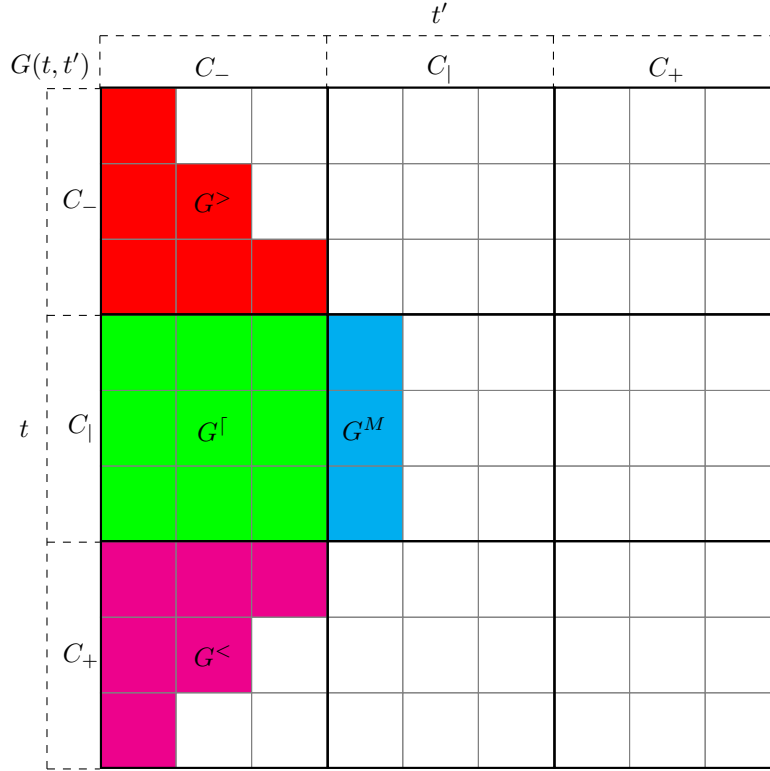


Figure 2.5: Illustration of Green's function $G(t, t')$ on the twisted contour. Each color shows a Keldysh component of the Green's function. The colored region shows physical time domain.

The Spectral Function

In addition to the components described above, we also define the retarded Green's function

$$G^R(t, t') = \Theta(t, t') [G^>(t, t') - G^<(t, t')]. \quad (2.44)$$

In equilibrium the retarded Green's function is time shift invariant [$G^R(t, t') = G^R(t - t')$] and can be used to define the spectral function

$$A(\omega) = -\frac{1}{\pi} \text{Im} G^R(\omega) = -\frac{1}{\pi} \text{Im} \int dt e^{i\omega t} G^R(t). \quad (2.45)$$

Causality of the retarded Green's function implies that the spectral function is non-negative, and using the Lehmann representation one can show that the spectral function obeys the sum rule $\int d\omega A(\omega) = 1$ [43]. In equilibrium, the entire Green's function is defined by the

spectral function via

$$G(t, t') = -i \int d\omega e^{-i\omega(t-t')} A(\omega) [\Theta_C(t, t') - f(\omega, \beta)] \quad (2.46)$$

where $f(\omega, \beta) = 1/(e^{\beta\omega} + 1)$ is the Fermi function and $\beta = 1/T$ is the inverse temperature [30]. Physically, the spectral function $A(\omega)$ describes the density of single-particle excitations with energy ω , and is often referred to as the density of states (DOS). The spectral function is an important physical observable and can be experimentally measured using a variety of techniques such as scanning tunneling microscopy (STM) [22] and angle-resolved photoemission spectroscopy (ARPES) [44].

Out of equilibrium the definition and meaning of the spectral function become more complicated (positivity may be violated for example) [45]. In this thesis we make use of the auxiliary lead formalism [46–48] to define a time-dependent spectral function which agrees with the equilibrium spectral function in steady state.

Causal and Contour Causal Slices

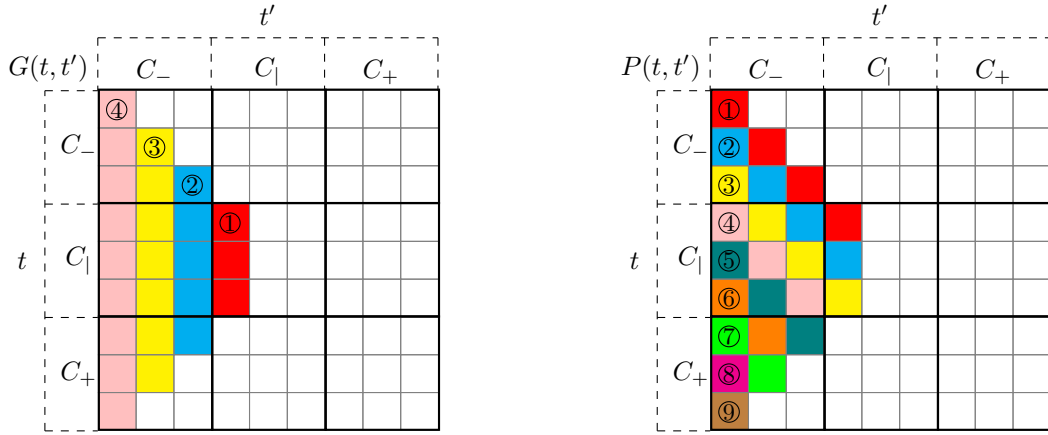


Figure 2.6: Causal (left) and contour causal (right) slices of the time domain of two time contour object. Each color corresponds to a single slice. The circled number indicates the order of each slice.

In addition to the symmetries discussed above, the Green’s function G is also causal. This means that a Green’s function element $G(t, t')$ only depends on the time evolution operator $U(t_2, t_1)$ for $t_1, t_2 < \max(t, t')$. One can see this by looking at figure 2.4 and noticing that all evolution past the maximum physical time of the Green’s function operators will cancel. When computing the Green’s function and other causal objects it is advantageous to use this structure. We can do this by computing the Green’s function

in a series of slices where each slice extends the maximum physical time of the Green's function by one step Δt . This corresponds to iterating over the time domain D column by column moving from right to left. The left panel of figure 2.6 shows the causal slices of a Green's function.

Another class of objects that we will deal with in this thesis are propagators which are matrix elements of the time evolution operator $U(t, t')$. We describe these objects as “contour causal” because they depend on the time evolution operator $U(t_2, t_1)$ for $t \succ t_2 \succ t_1 \succ t'$ on the contour. Note that this is more restrictive than simply being causal. Contour causal objects $P(t, t')$ depend only on the time evolution between t' and t on the contour, whereas causal objects $G(t, t')$ depend on the time evolution over the whole contour up to the physical time $\max(t, t')$. When computing contour causal objects it is also advantageous to use this special structure. We can do this by computing the propagator in a series of slices where each slice extends the length of the segment (t, t') by one step Δt . This corresponds to iterating over the time domain D diagonal by diagonal. The right panel of figure 2.6 shows the contour causal slices of a propagator.

CHAPTER III

The Hybridization Expansion

In this chapter, we review hybridization expansion techniques for the single-impurity Anderson model (SIAM) out of equilibrium. The hybridization expansion is a perturbation theory in the tunneling Hamiltonian \hat{H}_T around the disconnected limit $\hat{H}_0 \equiv \hat{H}_{\text{loc}} + \hat{H}_{\text{bath}}$ where the impurity is decoupled from the bath. We begin by briefly reviewing the historical development of the hybridization expansion. We then derive the bare expansion on a general contour [49–52]. Following this, we derive nonequilibrium versions [53] of the non-crossing approximation (NCA) [9, 10] and one-crossing approximation (OCA) [54] methods. Finally, we introduce the Inchworm method [31, 55].

3.1 Historical Development

The Anderson model was introduced in 1961 to describe the physics of dilute alloys containing magnetic impurities embedded in a non-magnetic host [4]. Solution of the Anderson model was—and continues to be—a major motivation for the development of hybridization expansion techniques. One of the first applications of the hybridization expansion was a calculation of the magnetic susceptibility of the Anderson model to fourth order in H_T [56]. This approach was enhanced by the introduction of the non-crossing approximation (NCA) which was used to resum an infinite class of terms in the hybridization expansion [9]. The NCA approach was further developed throughout the 1970s and 1980s by a number of authors [9, 10, 57–62]. A particularly notable development was the introduction of the pseudo-particle representation by Coleman in 1984 [61] which is often used in the modern literature (see for example [53]). For a detailed review of the early development of the hybridization expansion see [10].

NCA is a useful technique which has been widely applied, but suffers from some significant deficiencies, notably a failure to reproduce the Fermi liquid properties of the Anderson model at low temperatures [63, 64]. Additionally, NCA was typically defined only

in the strong interaction ($U \rightarrow \infty$) limit of the Anderson model. In order to address these deficiencies in NCA, the one-crossing approximation (OCA) [54] and symmetrized finite- U NCA (SUNCA) [65] were introduced, which resum a larger set of diagrams and more accurately describes the Anderson model at finite interaction strength U . OCA corrects the most severe problems of NCA and provides reasonable results for many problems, particularly at large U [66, 67]. However, OCA is still an approximate method and error estimation is not straightforward.

The next step in the development of the hybridization expansion came with the introduction of a continuous-time quantum Monte Carlo (CT-QMC) method based stochastically summing the hybridization expansion to all orders [11, 68, 69]. This technique, known as the continuous-time hybridization expansion (CT-HYB), has been very successful in equilibrium, and several mature implementations are available [70–72]. Because CT-HYB sums all hybridization diagrams, it is numerically exact asymptotically as the number of Monte Carlo measurements goes to infinity. We call CT-HYB a “bare” algorithm because it directly expands around the disconnected limit $H_T = 0$. Later, “bold” methods were introduced which take the NCA/OCA solutions as a starting point instead [73].

So far, all the techniques we have reviewed have been for equilibrium problems. One of the first applications of the hybridization expansion to nonequilibrium problems was in [74], in which the authors introduce a nonequilibrium version of NCA in order to investigate the timescale associated with building up the Kondo effect. Later, nonequilibrium versions of NCA, OCA, and the next order extension, the two-crossing approximation (2CA), were introduced and benchmarked [53]. The authors found that these methods were quite successful in describing the Mott insulating phase of the Hubbard model on the Bethe lattice within DMFT, with 2CA achieving almost quantitative agreement with numerically exact QMC methods.

Around the same time, the CT-HYB method was applied to nonequilibrium problems on the two branch [49–51] and three branch [52] contour. Unfortunately the nonequilibrium CT-HYB method was only able to reach very short times due to a severe dynamical sign problem stemming from the complex exponential terms associated with propagation in real time. This problem was partially addressed by applying bold methods based on an expansion around the NCA/OCA solution to the nonequilibrium case [75, 76]. Initially, these methods were only applicable to single time quantities, e.g. the density, but were later extended in order to allow calculation of Green’s functions and spectral functions [47, 77].

Although they offered improvements over the bare CT-HYB method, these bold

methods based on expansion around NCA/OCA did not fully overcome the dynamical sign problem encountered in nonequilibrium simulations. This spurred the development of the inchworm method based on a new bold resummation which successfully overcame the dynamical sign problem [55]. The initial inchworm method was able to compute single time observables for the Anderson model on the two branch contour. This was later generalized to computing Green's functions for the Anderson model on the three branch contour [31]. The inchworm method has also been successfully applied to the spin-boson model [78, 79], and multi-orbital impurity problems in equilibrium [80].

Several algorithmic improvements to the original inchworm method have been introduced. As we will see, a major cost of the inchworm method is summing over hybridization configurations, since the number of valid configurations grows factorially with expansion order. A fast algorithm based on the inclusion-exclusion principle has been developed which reduces asymptotic scaling of this summation from factorial to exponential [81]. Additionally, an improved time stepping scheme has recently been implemented [82]. Currently, the inchworm method is the most successful numerically exact approach to the hybridization expansion for nonequilibrium problems. There are also complementary approaches based on expansion in the interaction U [83–85].

3.2 The Bare Expansion

The local Hamiltonian for the single impurity Anderson model (SIAM) is given by

$$\hat{H}_{\text{loc}} = \sum_{\sigma} \epsilon_d \hat{d}_{\sigma}^{\dagger} \hat{d}_{\sigma} + U \hat{n}_{\uparrow} \hat{n}_{\downarrow} \quad (3.1)$$

where $\hat{d}_{\sigma}^{\dagger}$ (\hat{d}_{σ}) creates (annihilates) electrons localized on the impurity with spin σ , $\hat{n}_{\sigma} = \hat{d}_{\sigma}^{\dagger} \hat{d}_{\sigma}$ is the impurity number operator, ϵ_d is the single-particle energy, and U is the Coulomb interaction between electrons on the impurity. The impurity Hilbert space is spanned by the four states

$$|0\rangle \quad (3.2)$$

$$\hat{d}_{\uparrow}^{\dagger} |0\rangle = |\uparrow\rangle \quad (3.3)$$

$$\hat{d}_{\downarrow}^{\dagger} |0\rangle = |\downarrow\rangle \quad (3.4)$$

$$\hat{d}_{\uparrow}^{\dagger} \hat{d}_{\downarrow}^{\dagger} |0\rangle = |\uparrow\downarrow\rangle \quad (3.5)$$

which we refer to as to empty, spin up, spin down, and doubly occupied. Throughout this thesis we will always work within this occupation number basis unless otherwise noted. The bath Hamiltonian is given by

$$\hat{H}_{\text{bath}} = \sum_{k\sigma} \epsilon_{k\sigma} \hat{c}_{k\sigma}^\dagger \hat{c}_{k\sigma} \quad (3.6)$$

where $\hat{c}_{k\sigma}^\dagger$ ($\hat{c}_{k\sigma}$) creates (annihilates) bath electrons with quasimomentum k and spin σ , and $\epsilon_{k\sigma}$ describes the bath dispersion. The tunneling Hamiltonian is given by

$$\hat{H}_T = \sum_{k\sigma} \left(\mathcal{V}_k \hat{c}_{k\sigma}^\dagger \hat{d}_\sigma + \mathcal{V}_k^* \hat{d}_\sigma^\dagger \hat{c}_{k\sigma} \right) \quad (3.7)$$

where \mathcal{V}_k is the tunneling matrix element describing the coupling between the impurity and the bath.

Traditionally, the hybridization expansion is developed for the partition function $Z = \text{Tr} [\mathcal{T}_C \{ e^{-i \int_C dz H(z)} \}]$ and observables are calculated from partition function configurations [11, 68]. Instead, we will develop an expansion for the bold propagators

$$P_\alpha(t, t') = -i \xi_\alpha^{\theta_C(t', t)} \text{Tr}_c \left[\langle \alpha | \mathcal{T}_{\tilde{C}} \left\{ \exp \left(-i \int_{t'}^t dz \hat{H}(z) \right) \right\} | \alpha \rangle \right] \quad (3.8)$$

which represent the time evolution between t' and t on the twisted contour projected onto a single impurity state $|\alpha\rangle \in \{|0\rangle, |\uparrow\rangle, |\downarrow\rangle, |\uparrow\downarrow\rangle\}$. The integral should be understood as an integral along the twisted contour \tilde{C} . The ξ factors are given by $\xi_\alpha = \langle \alpha | \hat{\xi} | \alpha \rangle$ where $\hat{\xi} = (-1)^{\hat{N}} = (-1)^{\hat{n}_\uparrow + \hat{n}_\downarrow}$. These factors at first appear somewhat obscure, but we will see that they account for a sign factor that comes from working on the twisted contour. They can also be understood from the pseudo-particle perspective where they come from the fermionic/bosonic statistics of the particles associated with each state $|\alpha\rangle$ [53, 61]. Note the Heaviside function $\theta_C(t', t)$, is defined with respect to ordering on C *not* the twisted contour \tilde{C} , and indicates that we pick up the sign factor ξ_α when the propagator winds around 0_+ on the twisted contour, e.g. in $P_\alpha(t_+, t_-)$. We can think of this as coming from an insertion of the operator $\hat{\xi}$ at 0_+ whenever $t \succ 0_+ \succ t'$ on the twisted contour. Note $\hat{\xi}$ anti-commutes with \hat{d} and \hat{d}^\dagger and commutes with \hat{H}_{loc} .

The impurity populations, i.e., the diagonal elements of the impurity density matrix $\rho_\alpha(t)$, which describe the probability of finding the impurity in state $|\alpha\rangle$ can be expressed

in terms of the propagators

$$\rho_\alpha(t) = \frac{1}{Z} i \xi_\alpha P_\alpha(t_+, t_-) \quad (3.9)$$

where the partition function is given by

$$Z = i \sum_\alpha \xi_\alpha P_\alpha(t_+, t_-) \quad (3.10)$$

which is fixed by the condition that the populations sum to unity. The partition function is time-independent due to the unitarity of the evolution operator and therefore can be calculated as $Z = i \sum_\alpha \xi_\alpha P_\alpha(0_+, 0_-)$. In practical calculations, the deviation of $\sum_\alpha \rho_\alpha(t)$ from unity provides a useful check on the numerical error.

To begin, we write the Hamiltonian for the system as $\hat{H} = \hat{H}_0 + \hat{H}_T$ where $\hat{H}_0 = \hat{H}_{\text{loc}} + \hat{H}_{\text{bath}}$ is the Hamiltonian in the limit where the impurity is disconnected from the bath. We write the tunneling Hamiltonian as $\hat{H}_T = \sum_\sigma \hat{V}_\sigma + \hat{V}_\sigma^\dagger$, and refer to $\hat{V}_\sigma = \sum_k \mathcal{V}_k \hat{c}_{k\sigma}^\dagger \hat{d}_\sigma$ and its conjugate \hat{V}_σ^\dagger as the annihilation and creation hybridization vertices. Using the contour formalism, the propagators can be expressed

$$P_\alpha(t, t') = -i \xi_\alpha^{\theta_C(t', t)} \text{Tr}_c \left[\langle \alpha | \mathcal{T}_{\tilde{C}} \left\{ e^{-i \int_{t'}^t dz \hat{H}(z)} \right\} | \alpha \rangle \right] \quad (3.11)$$

$$= -i \xi_\alpha^{\theta_C(t', t)} \text{Tr}_c \left[\langle \alpha | \mathcal{T}_{\tilde{C}} \left\{ e^{-i \int_{t'}^t dz \hat{H}_0(z)} e^{-i \int_{t'}^t dz \hat{H}_T(z)} \right\} | \alpha \rangle \right] \quad (3.12)$$

$$= -i \xi_\alpha^{\theta_C(t', t)} \sum_n \sum_{T_n} (-i)^{2n} \int_{t'}^t dz_{2n} \int_{t'}^{z_{2n}} dz_{2n-1} \dots \int_{t'}^{z_2} dz_1 \quad (3.13)$$

$$\text{Tr}_c \left[\langle \alpha | \mathcal{T}_{\tilde{C}} \left\{ e^{-i \int_{t'}^t dz \hat{H}_0(z)} \hat{v}(2n) \dots \hat{v}(1) \right\} | \alpha \rangle \right]$$

where $\hat{v}(i)$ are insertions of the vertices, and we sum over all topologies T_n which specify the identity of each vertex insertion, i.e. its spin σ_i and whether it is an annihilation vertex $\hat{V}_{\sigma_i}(z_i)$ or a creation vertex $\hat{V}_{\sigma_i}^\dagger(z_i)$. We define the topologies T_n specifically as the set of vertex insertion orders which return the bath to its original state so that the trace is non-zero. Because of this, at order n we include $2n$ vertex insertions, since every creation vertex must be paired with an annihilation vertex in order to return the bath to its initial state. The contour times $t \succ z_{2n} \succ z_{2n-1} \succ \dots \succ z_1 \succ t'$ are ordered on the twisted contour \tilde{C} . We refer to $|\alpha\rangle$ as the ‘‘tip’’ state since we project onto $|\alpha\rangle$ at the tip of the contour (t_-). Because the bath and impurity are completely decoupled in \hat{H}_0 , the

operators can be separated to obtain

$$\begin{aligned}
P_\alpha(t, t') = & \\
& - i \xi_\alpha^{\theta_C(t', t)} \sum_n \sum_{T_n} (-i)^{2n} \int_{\mathcal{S}_{2n}(t, t')} dz \quad \langle \alpha | \mathcal{T}_{\tilde{C}} \left\{ e^{-i \int_{t'}^t dz \hat{H}_{\text{loc}}(z)} \hat{v}_d(2n) \dots \hat{v}_d(1) \right\} | \alpha \rangle \quad (3.14) \\
& \times \text{Tr}_c \left[\mathcal{T}_{\tilde{C}} \left\{ e^{-i \int_{t'}^t dz \hat{H}_{\text{bath}}(z)} \hat{v}_c(2n) \dots \hat{v}_c(1) \right\} \right]
\end{aligned}$$

where $\mathcal{S}_{2n}(t, t')$ is the $2n$ dimensional simplex of time ordered points on the twisted contour $t \succ z_{2n} \succ z_{2n-1} \succ \dots \succ z_1 \succ t'$, and \hat{v}_d (\hat{v}_c) is the impurity (bath) part of the vertex.

We first turn our attention to evaluation of the local factor $\langle \alpha | \dots | \alpha \rangle$. Note, because the impurity Hamiltonian \hat{H}_{loc} is interacting, Wick's theorem does not apply and we must perform the evaluation directly. To do this, we introduce the local time evolution operator

$$\hat{U}_{\text{loc}}(z_{i+1}, z_i) = \mathcal{T}_{\tilde{C}} \left\{ \exp \left(-i \int_{z_i}^{z_{i+1}} dz \hat{H}_{\text{loc}}(z) \right) \right\} \quad (3.15)$$

which represents the evolution of the disconnected impurity. Using this, the local factor may be written

$$\langle \alpha | \mathcal{T}_{\tilde{C}} \left\{ e^{-i \int_{t'}^t dz \hat{H}_{\text{loc}}(z)} \hat{v}_d(2n) \dots \hat{v}_d(1) \right\} | \alpha \rangle \quad (3.16)$$

$$= \langle \alpha | \hat{U}_{\text{loc}}(2n+1, 2n) \hat{v}_d(2n) \dots \hat{U}_{\text{loc}}(2, 1) \hat{v}_d(1) \hat{U}_{\text{loc}}(1, 0) | \alpha \rangle \quad (3.17)$$

$$\begin{aligned}
= & \sum_{\phi_1, \dots, \phi_{2n+1}} \langle \alpha | \hat{U}_{\text{loc}}(2n+1, 2n) | \phi_{2n+1} \rangle \langle \phi_{2n+1} | \hat{v}_d(2n) | \phi_{2n} \rangle \dots \quad (3.18) \\
& \dots \hat{U}_{\text{loc}}(2, 1) | \phi_2 \rangle \langle \phi_2 | \hat{v}_d(1) | \phi_1 \rangle \langle \phi_1 | \hat{U}_{\text{loc}}(1, 0) | \alpha \rangle
\end{aligned}$$

where $\hat{v}_d(i)$ can be either an impurity creation or annihilation operator depending on the topology, $\hat{U}_{\text{loc}}(n+1, n) = \hat{U}_{\text{loc}}(z_{n+1}, z_n)$, and we have defined $z_{2n+1} \equiv t$, $z_0 \equiv t'$. In the last line, we insert a complete set of states around each vertex.

In order to evaluate this expression, we must evaluate matrix elements of the local time evolution operator $\langle \alpha | \hat{U}_{\text{loc}}(z_{i+1}, z_i) | \beta \rangle$. For the Anderson model, this is simplified because \hat{H}_{loc} is diagonal in the occupation number basis so we only need to deal with the diagonal elements. We express the local evolution in terms of the bare atomic propagators

which are defined analogously to the bold propagators

$$P_\alpha^{(0)}(t, t') = -i \xi_\alpha^{\theta_C(t', t)} \langle \alpha | \hat{U}_{\text{loc}}(t, t') | \alpha \rangle \quad (3.19)$$

$$= -i \xi_\alpha^{\theta_C(t', t)} \exp \left(-i \int_t^{t'} dz E_\alpha(z) \right) \quad (3.20)$$

where $E_\alpha(z)$ are the eigenvalues of $\hat{H}_{\text{loc}}(z)$ which we refer to as the impurity levels. Note, on the three branch contour, the propagator picks up a factor proportional to the density matrix from the integration over the imaginary time branch when it winds around 0_+ . However, on the two branch contour this factor must be inserted by hand, so we use the modified definition

$$P_\alpha^{(0)}(t, t') = -i (\xi_\alpha \rho_\alpha(0))^{\theta_C(t', t)} \exp \left(-i \int_t^{t'} dz E_\alpha(z) \right) \quad (3.21)$$

where $\rho_\alpha(0)$ is the initial impurity density matrix which we may choose freely. Using the atomic propagators, the local factor may be written

$$\langle \alpha | \dots | \alpha \rangle = \sum_{\phi_1, \dots, \phi_{2n+1}} \langle \alpha | \hat{U}_{\text{loc}}(2n+1, 2n) | \phi_{2n+1} \rangle \langle \phi_{2n+1} | \hat{v}_d(2n) | \phi_{2n} \rangle \dots \quad (3.22)$$

$$\begin{aligned} & \dots \hat{U}_{\text{loc}}(2, 1) | \phi_2 \rangle \langle \phi_2 | \hat{v}_d(1) | \phi_1 \rangle \langle \phi_1 | \hat{U}_{\text{loc}}(1, 0) | \alpha \rangle \\ &= \underbrace{\left(\prod_{i=1}^{2n} \langle \alpha_i | \hat{v}_d(i) | \alpha_{i-1} \rangle \right)}_{=s_1} \prod_{i=0}^{2n} \langle \alpha_i | \hat{U}_{\text{loc}}(i+1, i) | \alpha_i \rangle \end{aligned} \quad (3.23)$$

$$= s_1 (i)^{2n+1} (-1)^{k_+} \xi_\alpha^{\theta_C(t', t)} \prod_{i=0}^{2n} P_{\alpha_i}^{(0)}(z_{i+1}, z_i) \quad (3.24)$$

where $\{\alpha_0, \dots, \alpha_{2n}\}$ is the state sequence implied by the order of vertex insertions defined by the topology T_n , s_1 is the sign factor from acting with the local operators, and k_+ counts the number of local operators on the plus branch. The sign factor $(-1)^{k_+} \xi_\alpha^{\theta_C(t', t)}$ can be understood by anti-commuting the $\hat{\xi}$ operator at 0_+ to the left through all impurity operators on C_+ to act on the outer state $\langle \alpha |$.

Because the local evolution is diagonal in the occupation number basis, in order for a topology to have a non-zero contribution, the creation and annihilation operators for each spin must come in alternating order with the identity of the first operator fixed by the tip state. Because of this structure, a topology can be specified uniquely by

a sequence of $2n$ spins $T_n = \{\sigma_{2n}, \dots, \sigma_1\}$ together with the tip state $|\alpha\rangle$. Using this language, the requirement that the operator sequence return the bath to its original state becomes simply that the number of occurrences of each spin is even. At order $n = 1$ the valid topologies are $\{\uparrow\uparrow, \downarrow\downarrow\}$. The topology $\{\uparrow\uparrow\}$ and tip state $|0\rangle$ imply an operator sequence $d_\uparrow d_\uparrow^\dagger$, and state sequence $|0\rangle \succ |\uparrow\rangle \succ |0\rangle$. The same topology with the tip state $|\uparrow\rangle$ imply the opposite operator sequence $d_\uparrow^\dagger d_\uparrow$ since the tip state holds a spin up electron which must be annihilated first. At order $n = 2$ the valid topologies are $\{\uparrow\uparrow\uparrow\uparrow, \downarrow\downarrow\uparrow\uparrow, \downarrow\uparrow\downarrow\uparrow, \uparrow\downarrow\uparrow\downarrow, \downarrow\uparrow\uparrow\downarrow, \uparrow\downarrow\downarrow\uparrow, \uparrow\uparrow\downarrow\downarrow, \downarrow\downarrow\downarrow\downarrow\}$. Table 3.1 shows the operator and

T	$ \alpha\rangle$	operator sequence	state sequence must be
$\uparrow\uparrow$	$ 0\rangle$	$d_\uparrow d_\uparrow^\dagger$	$ 0\rangle \succ \uparrow\rangle \succ 0\rangle$
$\uparrow\uparrow$	$ \uparrow\rangle$	$d_\uparrow^\dagger d_\uparrow$	$ \uparrow\rangle \succ 0\rangle \succ \downarrow\rangle$
$\uparrow\uparrow$	$ \downarrow\rangle$	$d_\uparrow d_\uparrow^\dagger$	$ \downarrow\rangle \succ \uparrow\downarrow\rangle \succ \downarrow\rangle$
$\uparrow\uparrow$	$ \uparrow\downarrow\rangle$	$d_\uparrow^\dagger d_\uparrow$	$ \uparrow\downarrow\rangle \succ \downarrow\rangle \succ \uparrow\downarrow\rangle$
$\uparrow\uparrow\uparrow\uparrow$	$ 0\rangle$	$d_\uparrow d_\uparrow^\dagger d_\uparrow d_\uparrow^\dagger$	$ 0\rangle \succ \uparrow\rangle \succ 0\rangle \succ \uparrow\rangle \succ 0\rangle$
$\uparrow\uparrow\uparrow\uparrow$	$ \uparrow\rangle$	$d_\uparrow^\dagger d_\uparrow d_\uparrow^\dagger d_\uparrow$	$ \uparrow\rangle \succ 0\rangle \succ \uparrow\rangle \succ 0\rangle \succ \uparrow\rangle$
$\uparrow\uparrow\uparrow\uparrow$	$ \downarrow\rangle$	$d_\uparrow d_\uparrow^\dagger d_\uparrow d_\uparrow^\dagger$	$ \downarrow\rangle \succ \uparrow\downarrow\rangle \succ \downarrow\rangle \succ \uparrow\downarrow\rangle \succ \downarrow\rangle$
$\uparrow\uparrow\uparrow\uparrow$	$ \uparrow\downarrow\rangle$	$d_\uparrow^\dagger d_\uparrow d_\uparrow^\dagger d_\uparrow$	$ \uparrow\downarrow\rangle \succ \downarrow\rangle \succ \uparrow\downarrow\rangle \succ \downarrow\rangle \succ \uparrow\downarrow\rangle$
$\uparrow\downarrow\uparrow\downarrow$	$ 0\rangle$	$d_\uparrow d_\downarrow d_\uparrow^\dagger d_\downarrow^\dagger$	$ 0\rangle \succ \uparrow\rangle \succ \uparrow\downarrow\rangle \succ \downarrow\rangle \succ 0\rangle$
$\uparrow\downarrow\uparrow\downarrow$	$ \uparrow\rangle$	$d_\uparrow^\dagger d_\downarrow d_\uparrow^\dagger d_\downarrow^\dagger$	$ \uparrow\rangle \succ 0\rangle \succ \downarrow\rangle \succ \uparrow\downarrow\rangle \succ \uparrow\rangle$
$\uparrow\downarrow\uparrow\downarrow$	$ \downarrow\rangle$	$d_\uparrow d_\downarrow^\dagger d_\uparrow^\dagger d_\downarrow$	$ \downarrow\rangle \succ \uparrow\downarrow\rangle \succ \uparrow\rangle \succ 0\rangle \succ \downarrow\rangle$
$\uparrow\downarrow\uparrow\downarrow$	$ \uparrow\downarrow\rangle$	$d_\uparrow^\dagger d_\downarrow^\dagger d_\uparrow d_\downarrow$	$ \uparrow\downarrow\rangle \succ \downarrow\rangle \succ 0\rangle \succ \uparrow\rangle \succ \uparrow\downarrow\rangle$

Table 3.1: Examples of operator and state sequences for different topologies and tip states.

state sequences implied for each tip state for several topologies.

Calculation of the sign factor s_1 requires some care. For topology $\{\uparrow\uparrow\}$ and tip state $|0\rangle$ we have

$$s_1 = \langle 0 | \hat{d}_\uparrow | \uparrow \rangle \langle \uparrow | \hat{d}_\uparrow^\dagger | 0 \rangle = \left| \langle 0 | \hat{d}_\uparrow | \uparrow \rangle \right|^2 = 1 \quad (3.25)$$

Generalizing from this, we see that for topologies $\{\uparrow \dots \uparrow\downarrow \dots \downarrow\}$ there will be no sign since every creation term comes with a corresponding annihilation term. To see how we can get a sign factor consider the topology $\{\uparrow\downarrow\uparrow\downarrow\}$. For this topology and tip state $|0\rangle$ we

have

$$s_1 = \underbrace{\langle 0 | \hat{d}_\uparrow | \uparrow \rangle}_{=+1} \underbrace{\langle \uparrow | \hat{d}_\downarrow | \uparrow \downarrow \rangle}_{=-1} \underbrace{\langle \uparrow \downarrow | \hat{d}_\uparrow^\dagger | \downarrow \rangle}_{=+1} \underbrace{\langle \downarrow | \hat{d}_\downarrow^\dagger | 0 \rangle}_{=+1} = -1 \quad (3.26)$$

where the overall sign arises because the up and down operators cross. Generalizing from this, we see that s_1 is given by the sign of the permutation which permutes the operator sequence so that all spin up operators are on the left, i.e. by the number of crossings between operators of different spins.

To keep track of the topologies, it is useful to introduce a diagrammatic language. We will represent a bare propagator $P_\alpha^{(0)}(t, t')$ by two horizontal lines running from right to left with the upper (lower) line showing the occupation of the spin up (down) level. A solid (dashed) line indicates an occupied (empty) level. We refer to solid lines as segments and dashed lines as anti-segments. A vertex insertion is represented by an open (closed) dot for an annihilation (creation) vertex. The vertex flips the occupation of the level on which it occurs. Figure 3.1 shows the diagrammatic representation of the bare atomic propagators and hybridization vertices.

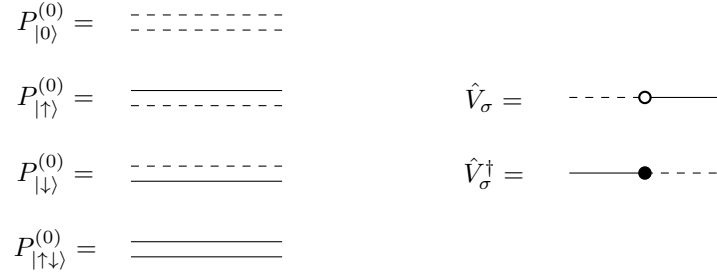


Figure 3.1: Left: Diagrammatic representation of the bare propagators $P_\alpha^{(0)}$. Right: Diagrammatic representation of the hybridization vertices $\hat{V}_\sigma, \hat{V}_\sigma^\dagger$.

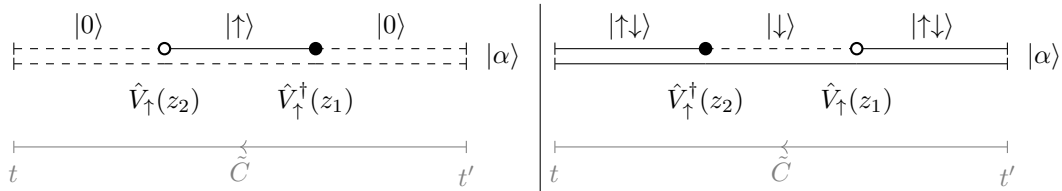


Figure 3.2: Diagrammatic representation of a hybridization expansion term with topology $T = \{\uparrow\uparrow\}$ for tip state $|0\rangle$ (left) and $|\uparrow\downarrow\rangle$ (right).

Using this language we can graphically represent terms in the hybridization expansion. Figure 3.2 shows the diagrammatic representation of a term with topology $T = \{\uparrow\uparrow\}$

for tip states $|0\rangle$ and $|\uparrow\downarrow\rangle$. Twisted contour time runs from right to left. For the empty tip state, the creation vertex precedes the annihilation vertex, while this is reversed for the doubly occupied state. Figure 3.3 shows the diagrammatic representation of a more complicated second order term with topology $T = \{\uparrow\downarrow\uparrow\downarrow\}$ for tip state $|0\rangle$. Using this

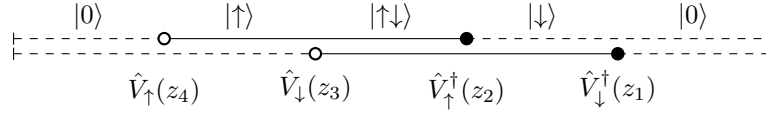


Figure 3.3: Diagrammatic representation of the second order hybridization expansion term with topology $T = \{\uparrow\downarrow\uparrow\downarrow\}$ for tip state $|0\rangle$.

diagrammatic language, we can enumerate all terms in the hybridization expansion for $P_\alpha(t, t')$, by drawing all diagrams made up of insertions of the hybridization vertices such that the diagram begins and ends in state $|\alpha\rangle$. For now we don't associate a concrete value with each diagram since we still have to evaluate the bath contribution.

We now turn our attention to the evaluation of the bath factor which can be written as

$$\text{Tr}_c \left[\mathcal{T}_{\tilde{C}} \left\{ e^{-i \int_{t'}^t dz \hat{H}_{\text{bath}}(z)} \hat{v}_c(2n) \dots \hat{v}_c(1) \right\} \right] \quad (3.27)$$

$$= s_2 \sum_{\{k_i\}} \sum_{\{k'_i\}} \mathcal{V}_{k_1} \dots \mathcal{V}_{k_n} \mathcal{V}_{k'_1}^* \dots \mathcal{V}_{k'_n}^* \quad (3.28)$$

$$\text{Tr}_c \left[\mathcal{T}_{\tilde{C}} \left\{ e^{-i \int_{t'}^t dz \hat{H}_{\text{bath}}(z)} \hat{c}(n) \hat{c}^\dagger(n') \dots \hat{c}(1) \hat{c}^\dagger(1') \right\} \right]$$

$$= s_1 s_2 \prod_{\sigma} \sum_{\{k_i\}} \sum_{\{k'_i\}} \mathcal{V}_{k_1} \dots \mathcal{V}_{k_{m_\sigma}} \mathcal{V}_{k'_1}^* \dots \mathcal{V}_{k'_{m_\sigma}}^* \quad (3.29)$$

$$\text{Tr}_c \left[\mathcal{T}_{\tilde{C}} \left\{ e^{-i \int_{t'}^t dz \hat{H}_{\text{bath}}(z)} \hat{c}_\sigma(m_\sigma) \hat{c}_\sigma^\dagger(m'_\sigma) \dots \hat{c}_\sigma(1) \hat{c}_\sigma^\dagger(1') \right\} \right]$$

where $2m_\sigma$ is the number of vertices with spin σ , $\hat{c}_\sigma(i)$ ($\hat{c}_\sigma^\dagger(i')$) refers to the i th annihilation (creation) operator with spin σ , and s_1 and s_2 are sign factors. Note, we have used that \hat{H}_{bath} is diagonal in σ to factorize the expression by spin.

The sign factor s_2 is the sign of the permutation which takes the operators from their time ordered sequence to the alternating sequence $\hat{c}\hat{c}^\dagger \dots \hat{c}\hat{c}^\dagger$. Note each bath operator is tied to an impurity operator, so like the impurity operators they must come in an alternating sequence of creation/annihilation operators. If σ is occupied in the tip state $|\alpha\rangle$, i.e. if the line corresponding to spin σ begins with a segment, then the operator sequence is already given by $\hat{c}\hat{c}^\dagger \dots \hat{c}\hat{c}^\dagger$ and there is no additional sign. However if σ is not occupied in the tip state, i.e. the line corresponding to spin σ begins with an anti-segment, then the operator sequence is $\hat{c}^\dagger\hat{c} \dots \hat{c}^\dagger\hat{c}$ and we pick up a sign $(-1)^{m_\sigma}$ from permuting it.

We can express this as

$$s_2 = \prod_{\sigma} (-1)^{m_{\sigma}(1-\langle \alpha | \hat{n}_{\sigma} | \alpha \rangle)} = \prod_{\sigma} s_{\sigma} \quad (3.30)$$

where \hat{n}_{σ} is the impurity number operator. This gives a convenient expression for s_2 in terms of just the tip state and the order of expansion for each spin.

The sign factor s_1 is the sign of the permutation which permutes the operators so that all the spin up operators occur to the left of the spin down operators so that the expression can be factorized by spin. Note that this sign factor is exactly the same as the sign factor s_1 which appeared in the local part and these two terms will cancel. This can be understood by noticing that the vertices \hat{v} contain two fermion operators and therefore commute rather than anti-commute under the time ordering. Because of this, the overall sign of the diagram should not be affected by permuting two vertices. However, because we separate the bath and impurity operators, we get these sign factors which must cancel each other out in the final expression. The conclusion of this analysis is that we can ignore the signs generated by acting with the local operators provided we also ignore the sign from factorizing the bath operators by spin. However, in a more general setting containing for example off diagonal hybridizations, these signs cannot be neglected.

The bath is non-interacting so Wick's theorem can be applied to evaluate the bath correlators. To facilitate this, we introduce the bath hybridization function

$$\Delta_{\sigma}(z, z') = -i \sum_k |\mathcal{V}_k|^2 \langle \mathcal{T}_C \hat{c}_{k\sigma}(z) \hat{c}_{k\sigma}^{\dagger}(z') \rangle \quad (3.31)$$

which parameterizes the tunneling matrix elements as well as the bath dispersion. Note that in this definition we use the contour ordering on C , rather than the twisted contour ordering on \tilde{C} . We do this so that $\Delta_{\sigma}(z, z')$ follows the usual convention. As we will see, this choice results in some sign factors that need to be kept track of. By integrating out the \hat{c} operators exactly using Wick's theorem, the bath factor (equation 3.29) may be

written as

$$s_1 s_2 \prod_{\sigma} \sum_{\{k_i\}} \sum_{\{k'_i\}} \mathcal{V}_{k_1} \cdots \mathcal{V}_{k_{m_\sigma}} \mathcal{V}_{k'_1}^* \cdots \mathcal{V}_{k'_{m_\sigma}}^* \quad (3.32)$$

$$\begin{aligned} & \text{Tr}_c \left[\mathcal{T}_{\tilde{C}} \left\{ e^{-i \int_{t'}^t dz \hat{H}_{\text{bath}}(z)} \hat{c}_\sigma(m_\sigma) \hat{c}_\sigma^\dagger(m'_\sigma) \cdots \hat{c}_\sigma(1) \hat{c}_\sigma^\dagger(1') \right\} \right] \\ &= s_1 s_2 s_3 \prod_{\sigma} \sum_{x \in S_{m_\sigma}} \left(\text{sgn}(x) \prod_{i=1}^{m_\sigma} \sum_{k_i, k'_{x_i}} \mathcal{V}_{k_i} \mathcal{V}_{k'_{x_i}}^* \langle \mathcal{T}_C \hat{c}_\sigma(i) \hat{c}_\sigma^\dagger(x(i)') \rangle \right) \quad (3.33) \end{aligned}$$

$$= s_1 s_2 s_3 (i)^n \prod_{\sigma} \sum_{x \in S_{m_\sigma}} \left(\text{sgn}(x) \prod_{i=1}^{m_\sigma} \Delta_\sigma(z_i^\sigma, z'_{x(i)}{}^\sigma) \right) \quad (3.34)$$

$$= s_1 s_2 s_3 (i)^n \prod_{\sigma} \det \Delta_\sigma \quad (3.35)$$

where $z_i^\sigma, z'_j{}^\sigma$ are the times corresponding to the i th annihilation and j th creation operator on spin σ , Δ_σ is an $m_\sigma \times m_\sigma$ matrix with elements $\Delta_{ij} = \Delta_\sigma(z_i^\sigma, z'_j{}^\sigma)$, and s_3 is a new sign factor to take into account the fact that we use the regular contour ordering on C in the definition of the hybridization function but the original correlator was ordered on \tilde{C} . The sign factor s_3 can be computed by counting the number of pairs (z_i, z'_i) which are out of order on C relative to \tilde{C} . Note the difference between the regular and twisted contours is that the plus branch comes at the beginning of the regular contour but at the end of the twisted contour. For example $z_+ \succ z_-$ on \tilde{C} but $z_+ \prec z_-$ on C . From this we can see that all pairs (z_i, z'_i) with one time on the plus branch will give a sign. Therefore the total factor is given by $s_3 = (-1)^{k_+}$ where k_+ is the number of bath operators on the plus branch. Note that this sign also emerged in our evaluation of the impurity trace due to the $\hat{\xi}$ factors in the bare atomic propagators. In this way, the ξ factors cancel the sign we get from evaluating on the twisted contour.

Putting these results (equation 3.24 and equation 3.35) together we can express the

propagator as

$$P_\alpha(t, t') = -i \xi_\alpha^{\theta_C(t', t)} \text{Tr}_c \left[\langle \alpha | \mathcal{T}_{\tilde{C}} \left\{ \exp \left(-i \int_{t'}^t dz \hat{H}(z) \right) \right\} | \alpha \rangle \right] \quad (3.36)$$

$$= -i \xi_\alpha^{\theta_C(t', t)} \sum_n \sum_{T_n} (-i)^{2n} \int_{S_{2n}(t, t')} dz \quad (3.37)$$

$$\left(s_1 (i)^{2n+1} (-1)^{k_+} \xi_\alpha^{\theta_C(t', t)} \prod_{i=0}^{2n} P_{\alpha_i}^{(0)}(z_{i+1}, z_i) \right) \left(s_1 s_2 (-1)^{k_+} (i)^n \prod_\sigma \det \Delta_\sigma \right) \quad (3.38)$$

$$= \sum_n \sum_{T_n} \int_{S_{2n}(t, t')} dz \underbrace{\left(s_\uparrow s_\downarrow i^n \prod_{i=0}^{2n} P_{\alpha_i}^{(0)}(z_{i+1}, z_i) \right)}_{w_{\text{loc}}} \underbrace{\left(\prod_\sigma \det \Delta_\sigma \right)}_{w_{\text{hyb}}} \quad (3.39)$$

$$= \sum_{\mathcal{C}_\alpha} w_{\text{loc}}(\mathcal{C}_\alpha) w_{\text{hyb}}(\mathcal{C}_\alpha) \quad (3.40)$$

where we call $\mathcal{C}_\alpha = \{(t \succ z_{2n} \succ \dots \succ z_1 \succ t'), \{\sigma_{2n} \dots \sigma_1\}, |\alpha\rangle\}$ the configuration, and $s_\sigma = (-1)^{m_\sigma(1 - \langle \alpha | \hat{n}_\sigma | \alpha \rangle)}$ is the only sign factor that we end up retaining. We interpret the sum over configurations as a sum over all discrete topologies, and an integral over the continuous variables \mathbf{z} . The hybridization determinant can be written

$$w_{\text{hyb}}(\mathcal{C}_\alpha) = \prod_\sigma \det \Delta_\sigma = \prod_\sigma \sum_{x \in S_{m_\sigma}} \text{sgn}(x) \prod_{i=1}^{m_\sigma} \Delta_\sigma(z_i^\sigma, z_{x(i)}^{\prime\sigma}) \quad (3.41)$$

$$= \sum_{x_\uparrow \in S_{m_\uparrow}} \sum_{x_\downarrow \in S_{m_\downarrow}} \prod_\sigma \underbrace{\left(\text{sgn}(x_\sigma) \prod_{i=1}^{m_\sigma} \Delta_\sigma(z_i^\sigma, z_{x_\sigma(i)}^{\prime\sigma}) \right)}_{w'_{\text{hyb}}} \quad (3.42)$$

$$= \sum_{\mathcal{D}(\mathcal{C}_\alpha)} w'_{\text{hyb}}(\mathcal{D}) \quad (3.43)$$

where we call $\mathcal{D} = \{x_\uparrow, x_\downarrow\}$ the diagram, and sum over the $m_\uparrow! \times m_\downarrow!$ diagrams specifying all possible matchings between creation and annihilation vertices for each spin. We write

our final result as

$$\begin{aligned}
P_\alpha(t, t') &= \sum_{\mathcal{C}_\alpha} w_{\text{loc}}(\mathcal{C}_\alpha, P^{(0)}) w_{\text{hyb}}(\mathcal{C}_\alpha, \Delta) \\
w_{\text{loc}}(\mathcal{C}_\alpha, P^{(0)}) &= s_\uparrow s_\downarrow i^n \prod_{i=0}^{2n} P_{\alpha_i}^{(0)}(z_{i+1}, z_i), \quad s_\sigma = (-1)^{m_\sigma(1-\langle \alpha | \hat{n}_\sigma | \alpha \rangle)} \\
w_{\text{hyb}}(\mathcal{C}_\alpha, \Delta) &= \sum_{\mathcal{D}(\mathcal{C}_\alpha)} w'_{\text{hyb}}(\mathcal{D}, \Delta) \\
w'_{\text{hyb}}(\mathcal{D}, \Delta) &= \prod_{\sigma} \left(\text{sgn}(x_\sigma) \prod_{i=1}^{m_\sigma} \Delta_\sigma(z_i^\sigma, z'_{x_\sigma(i)}) \right)
\end{aligned} \tag{3.44}$$

where $2m_\sigma$ is the number of vertices with spin σ , $z_{2n+1} \equiv t$, $z_0 \equiv t'$, and $z_i^\sigma, z'_j{}^\sigma$ refer to the i th creation j th annihilation vertex on spin σ (note the annihilation vertex \hat{V}_σ is associated with a bath *creation* operator \hat{c}^\dagger).

With these results we can complete our diagrammatic language. A diagram has two parts. The first is the local part, consisting of horizontal lines representing the occupation of each spin, which has been introduced previously. The local factor w_{loc} is given by the product of the $2n+1$ propagators for each intermediate state α_i and the sign factor $s_\uparrow s_\downarrow (i)^n$. The second is the hybridization part, consisting of arcs running from each annihilation vertex to the creation vertex specified by the permutations x_σ . For each arc we associate a factor of the hybridization function $\Delta_\sigma(z_i^\sigma, z'_{x_\sigma(i)})$. The hybridization factor is given by the product of these hybridization functions and the sign of each permutation x_\uparrow, x_\downarrow .

To get a feel for these diagram rules it is helpful to consider several examples. Figure

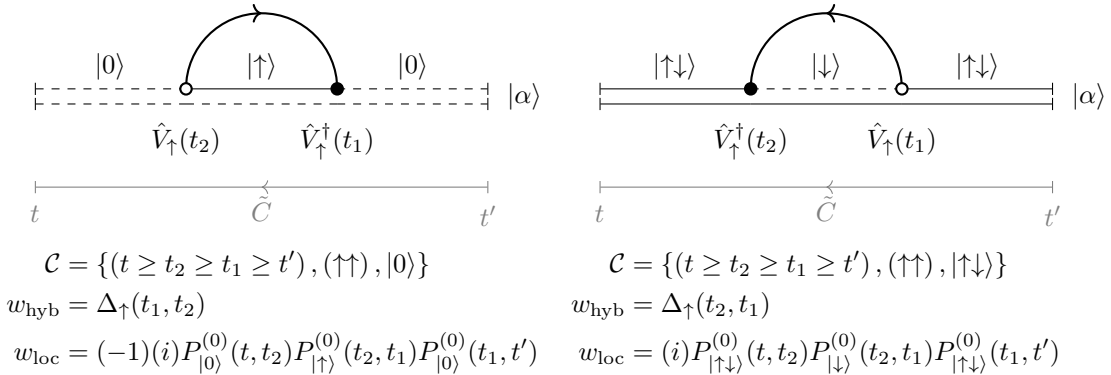


Figure 3.4: Diagrammatic representation of a hybridization expansion term with topology $T = \{\uparrow\uparrow\}$ for tip state $|0\rangle$ (left) and $|\uparrow\downarrow\rangle$ (right).

3.4 shows two first order hybridization diagrams along with the associated values. Note for

each configuration there is only one diagram, because at order 1 there is only one possible matching between vertices. Figure 3.5 shows the diagrams and associated values for a more

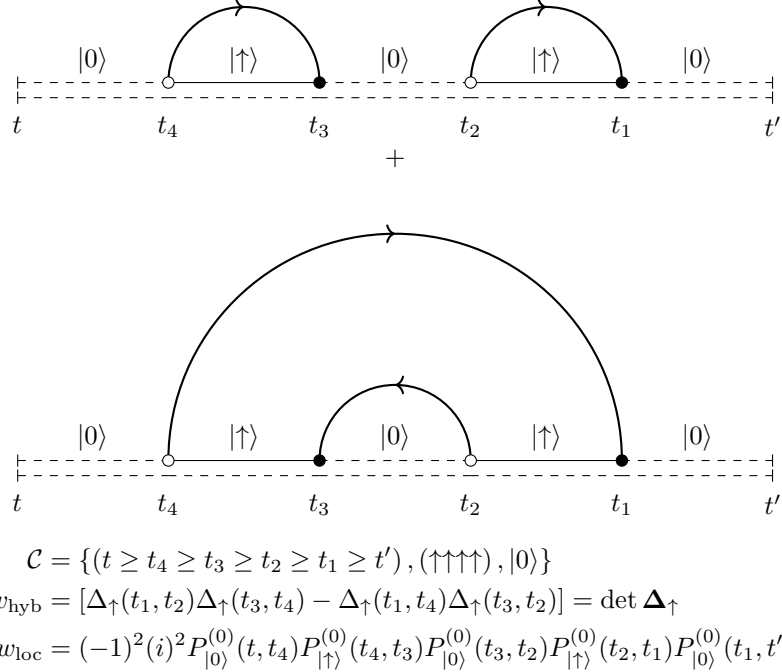
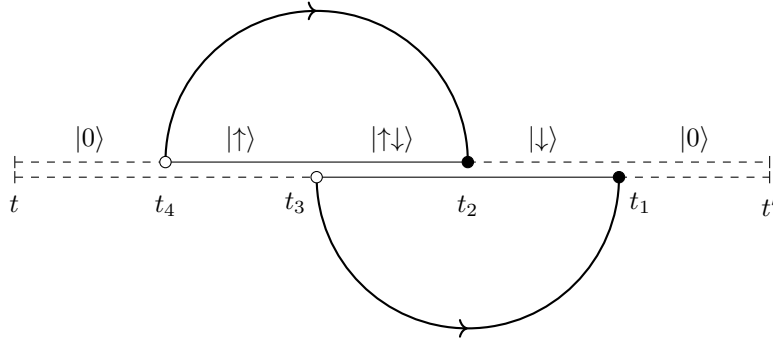


Figure 3.5: Diagrammatic representation of a hybridization expansion term with topology $T = \{\uparrow\uparrow\uparrow\uparrow\}$ for tip state $|0\rangle$.

complicated second order configuration. Note here we have two diagrams corresponding to the two possible matchings of vertices. The $(-1)^2$ factor in w_{loc} comes because the spin up line begins with an anti-segment and holds two vertex pairs, or equivalently, because in the diagram corresponding to the identity permutation both hybridization lines points from left to right against the time ordering. Figure 3.6 shows the diagram and associated values for another second order configuration. For this configuration there is again only one diagram even though we are at second order because there is only one vertex pair for each spin. We again pick up a $(-1)^2$ prefactor in w_{loc} because both lines begin with an anti-segment and hold one vertex pair. Note, there is no sign from the action of the local operators (recall $\langle \uparrow | \hat{d}_{\downarrow} | \uparrow \downarrow \rangle = -1$), and also no sign from factorizing the hybridization term by spin, because these signs exactly cancel each other. Figure 3.7 shows the diagrams and associated values for a third order configuration. In this case, since all vertices have the same spin there are $3! = 6$ diagrams which contribute.



$$\begin{aligned}
 \mathcal{C} &= \{(t \geq t_4 \geq t_3 \geq t_2 \geq t_1 \geq t'), (\uparrow\downarrow\uparrow\downarrow), |0\rangle\} \\
 w_{\text{hyb}} &= \Delta_{\uparrow}(t_2, t_4) \Delta_{\downarrow}(t_1, t_3) \\
 w_{\text{loc}} &= (-1)^2 (i)^2 P_{|0\rangle}^{(0)}(t, t_4) P_{|\uparrow\rangle}^{(0)}(t_4, t_3) P_{|\uparrow\downarrow\rangle}^{(0)}(t_3, t_2) P_{|\downarrow\rangle}^{(0)}(t_2, t_1) P_{|0\rangle}^{(0)}(t_1, t')
 \end{aligned}$$

Figure 3.6: Diagrammatic representation of a hybridization expansion term with topology $T = \{\uparrow\downarrow\uparrow\downarrow\}$ for tip state $|0\rangle$.

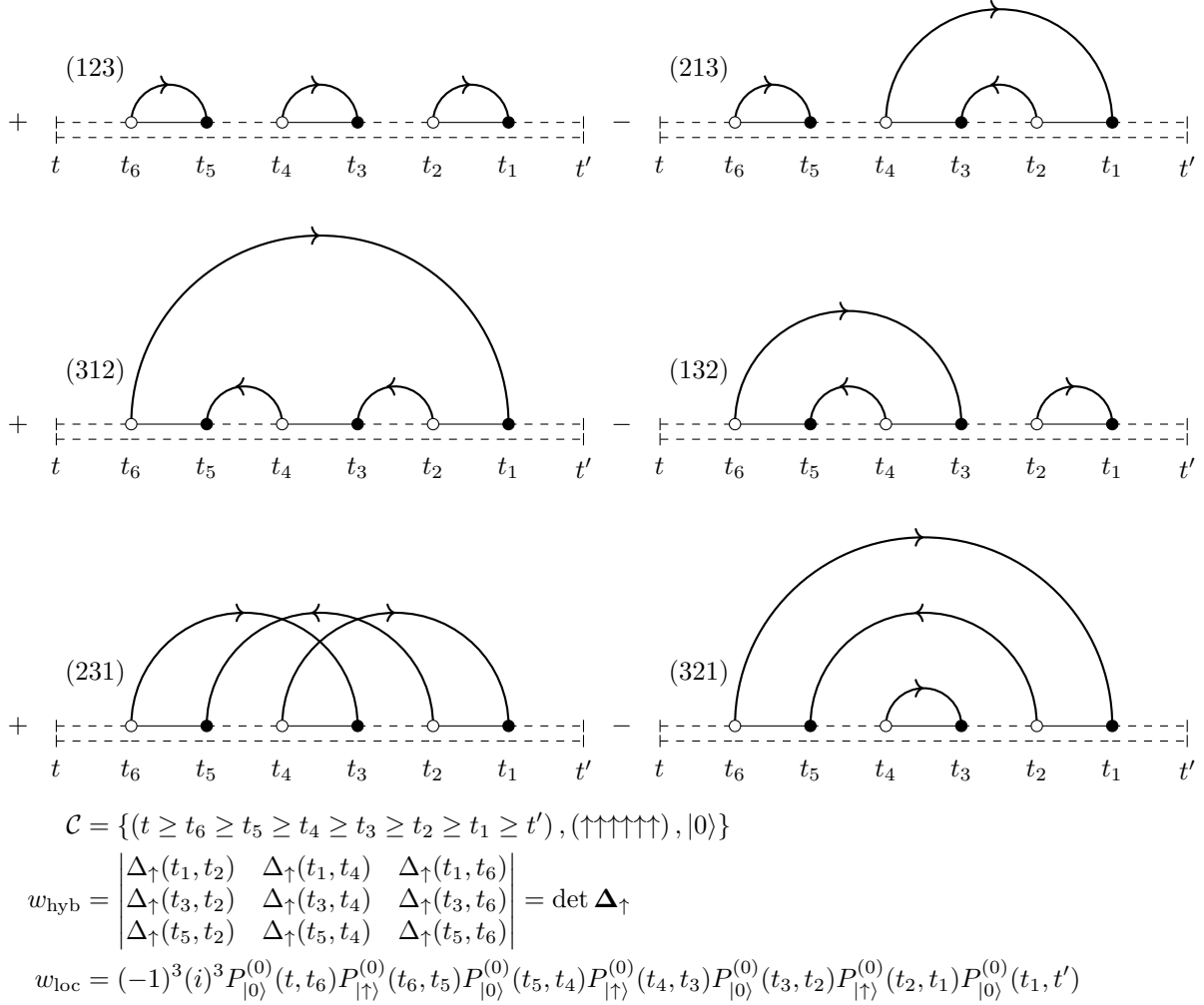


Figure 3.7: Diagrammatic representation of a hybridization expansion term with topology $T = \{\uparrow\uparrow\uparrow\uparrow\uparrow\}$ for tip state $|0\rangle$. Label in parenthesis shows the permutation corresponding to each diagram.

So far the diagrams we have presented have been in one-to-one correspondence with single terms in equation 3.44. It is useful to also introduce a compressed diagrammatic language in which we leave the state sequence and spins of the hybridization lines implicit. Figure 3.8 shows the bare expansion for the propagator expressed using this compressed

$$\begin{aligned}
 P^{(0)} &= \text{—————} \\
 P &= \text{—————} \\
 &= \text{—————} + \text{—————} \\
 &+ \text{—————} + \text{—————} + \text{—————} \\
 &+ \text{—————} + \text{—————} + \text{—————} + \text{—————} \\
 &+ \text{—————} + \text{—————} + \text{—————} + \text{—————} \\
 &+ \text{—————} + \text{—————} + \text{—————} + \text{—————} \\
 &+ \text{—————} + \dots
 \end{aligned}$$

Figure 3.8: Illustration of the bare expansion for the propagator expressed using the compressed diagrammatic language. Thick (thin) lines represent bold (bare) propagators. The state sequence and spins of the hybridization lines are left implicit.

language. In order to translate a compressed diagram to a set of full diagrams we must specify a tip state $|\alpha\rangle$ and sum over all possible spin assignments to the hybridization lines. Although less explicit than the full diagrams, these compressed diagrams show the crossings between hybridization lines which as we will see are extremely important.

We refer to the expansion shown in figure 3.8 as the “bare” expansion because all local propagators on the right hand side are bare atomic propagators $P_\alpha^{(0)}$, i.e. all lines in the diagrams are thin. We now turn our attention to “bold” methods in which we use bold propagators on the right hand side in order to efficiently reach much higher orders.

3.3 Semi-analytic Approximations

Similarly to regular Feynman diagrams in the interaction expansion, diagrams in the hybridization expansion can also be classified by their degree of reducibility. A one-particle irreducible (1PI) diagram cannot be separated into two disconnected pieces by cutting a single propagator line. Figure 3.9 shows a reducible and a 1PI diagram. Note, 1PI diagrams cannot have external legs, i.e. propagators that extend beyond the times of the

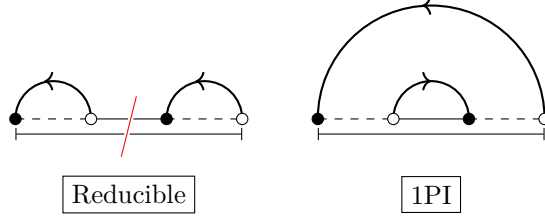


Figure 3.9: Diagrammatic representation of a reducible diagram which can be separated by a single cut (left) and a 1PI diagram (right).

hybridization vertices. We define the self-energy for the impurity propagators as the sum over all 1PI diagrams

$$\Sigma_\alpha = \sum_{\mathcal{C}_\alpha} w_{\text{loc}}(\mathcal{C}_\alpha, P^{(0)}) \sum_{\mathcal{D}(\mathcal{C}_\alpha) \in \text{1PI}} w'_{\text{hyb}}(\mathcal{D}, \Delta). \quad (3.45)$$

A bold propagator is then given by all possible insertions of the self-energy linked by bare propagators. Figure 3.10 shows diagrammatically how this leads to the Dyson

$$\begin{aligned} P &= \text{thick line} \\ &= \text{thin line} + \text{thin line} \circlearrowleft \Sigma \text{thin line} + \text{thin line} \circlearrowleft \Sigma \circlearrowleft \Sigma \text{thin line} + \dots \\ &= \text{thin line} + \text{thin line} \circlearrowleft \Sigma \text{thick line} \\ &= P^{(0)} + P^{(0)} \circlearrowleft \Sigma \circlearrowleft P \end{aligned}$$

Figure 3.10: Diagrammatic representation of the Dyson equation. The thick (thin) line represents a bold (bare) propagator.

equation

$$P_\alpha(t, t') = P_\alpha^{(0)}(t, t') + \int_{t'}^t dt_2 \int_{t'}^{t_2} dt_1 P_\alpha^{(0)}(t, t_2) \Sigma_\alpha(t_2, t_1) P_\alpha(t_1, t') \quad (3.46)$$

$$= P_\alpha^{(0)}(t, t') + [P_\alpha^{(0)} \circlearrowleft \Sigma_\alpha \circlearrowleft P_\alpha](t, t') \quad (3.47)$$

where \circlearrowleft denotes the contour causal convolution

$$[A \circlearrowleft B](t, t') = \int_{t'}^t d\bar{t} A(t, \bar{t}) B(\bar{t}, t'). \quad (3.48)$$

We call this “contour causal” because the integration runs between t' and t rather than over the whole contour. This reflects the structure of the propagators which depend only on the evolution between t' and t on the contour and stands in contrast to the “causal”

structure of objects such as the Green's function $G(t, t')$ which depend on the evolution on the whole contour up to the maximum physical time of their arguments. The causal structure of the propagators can be seen from the bounds of integration in their definition (see equation 3.8) and is key to designing efficient algorithms as we will see in chapter 4.

The Dyson equation for the propagators leads us to seek useful approximations to the self-energy. An important class of such schemes is given by the M -crossing approximations [53]. These are based on truncation of the skeleton series for the self-energy, in which the bare propagators are replaced by bold propagators and we only include skeleton diagrams which contain no internal self-energy insertions. The skeleton diagrams of order M are the diagrams containing M hybridization line crossings, since hybridization lines with no crossings are already included in the bold propagators.

The lowest order truncation of the skeleton series for the self-energy gives the non-crossing approximation (NCA). Figure 3.11 shows the NCA self-energy diagrams. Their

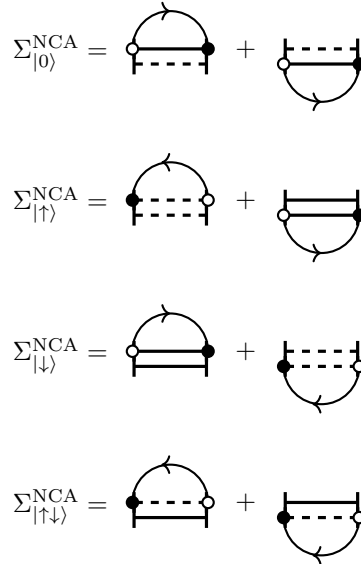


Figure 3.11: NCA self-energy diagrams. The propagators are bold.

values are given by

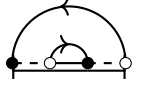
$$\Sigma_{|0\rangle}^{\text{NCA}}(t, t') = i (-P_{|\uparrow\rangle}(t, t')\Delta_{\uparrow}(t', t) - P_{|\downarrow\rangle}(t, t')\Delta_{\downarrow}(t', t)) \quad (3.49)$$

$$\Sigma_{|\uparrow\rangle}^{\text{NCA}}(t, t') = i (+P_{|0\rangle}(t, t')\Delta_{\uparrow}(t, t') - P_{|\uparrow\downarrow\rangle}(t, t')\Delta_{\downarrow}(t', t)) \quad (3.50)$$

$$\Sigma_{|\downarrow\rangle}^{\text{NCA}}(t, t') = i (-P_{|\uparrow\downarrow\rangle}(t, t')\Delta_{\uparrow}(t', t) + P_{|0\rangle}(t, t')\Delta_{\downarrow}(t, t')) \quad (3.51)$$

$$\Sigma_{|\uparrow\downarrow\rangle}^{\text{NCA}}(t, t') = i (+P_{|\downarrow\rangle}(t, t')\Delta_{\uparrow}(t, t) + P_{|\uparrow\rangle}(t, t')\Delta_{\downarrow}(t, t')) \quad (3.52)$$

which follow from the same rules given in equation 3.44, with the bare propagator replaced by the bold propagator. The next order truncation gives the one-crossing approximation

(OCA). Figure 3.12 shows the OCA self-energy diagrams. Note we do not include 

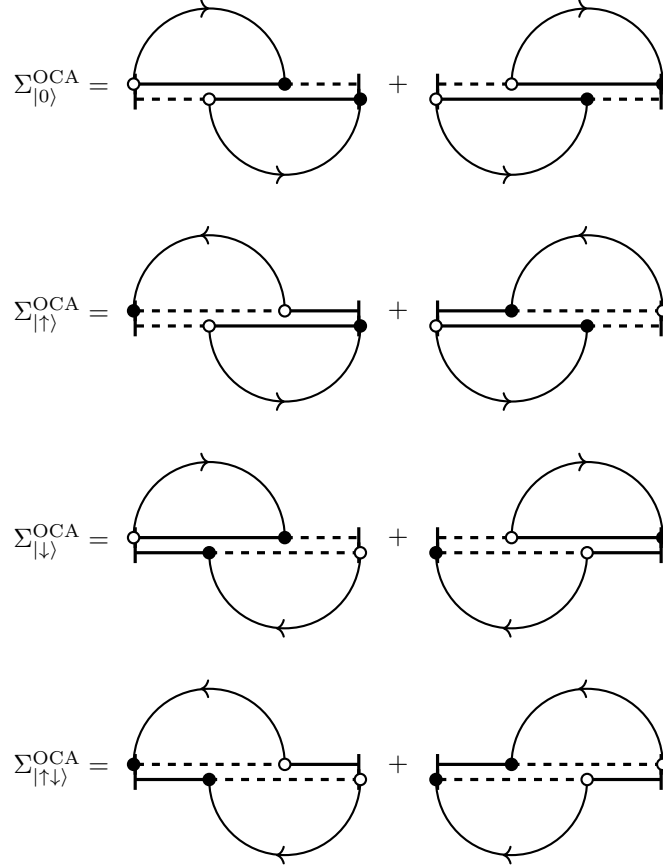


Figure 3.12: OCA self-energy diagrams. The propagators are bold.

because although it is 1PI, it is not a skeleton diagram because it contains a self-energy insertion which is already included in the bold propagator. The values of these diagrams are given by

$$\begin{aligned}
 \Sigma_{|0\rangle}^{OCA}(t, t') &= (i)^2(-1)^2 \int_{t'}^t dt_2 \int_{t'}^{t_2} dt_1 P_{|\uparrow\rangle}(t, t_2) P_{|\uparrow\downarrow\rangle}(t_2, t_1) P_{|\downarrow\rangle}(t_1, t') \Delta_{\uparrow}(t_1, t) \Delta_{\downarrow}(t', t_2) \\
 &+ (i)^2(-1)^2 \int_{t'}^t dt_2 \int_{t'}^{t_2} dt_1 P_{|\downarrow\rangle}(t, t_2) P_{|\uparrow\downarrow\rangle}(t_2, t_1) P_{|\uparrow\rangle}(t_1, t') \Delta_{\uparrow}(t', t_2) \Delta_{\downarrow}(t_1, t)
 \end{aligned}
 \tag{3.53}$$

$$\begin{aligned}
\Sigma_{|\uparrow\rangle}^{\text{OCA}}(t, t') &= (i)^2(-1) \int_{t'}^t dt_2 \int_{t'}^{t_2} dt_1 P_{|0\rangle}(t, t_2) P_{|\downarrow\rangle}(t_2, t_1) P_{|\uparrow\downarrow\rangle}(t_1, t') \Delta_{\uparrow}(t, t_1) \Delta_{\downarrow}(t', t_2) \\
&\quad + (i)^2(-1) \int_{t'}^t dt_2 \int_{t'}^{t_2} dt_1 P_{|\uparrow\downarrow\rangle}(t, t_2) P_{|\downarrow\rangle}(t_2, t_1) P_{|0\rangle}(t_1, t') \Delta_{\uparrow}(t_2, t') \Delta_{\downarrow}(t_1, t)
\end{aligned} \tag{3.54}$$

$$\begin{aligned}
\Sigma_{|\downarrow\rangle}^{\text{OCA}}(t, t') &= (i)^2(-1) \int_{t'}^t dt_2 \int_{t'}^{t_2} dt_1 P_{|\uparrow\downarrow\rangle}(t, t_2) P_{|\uparrow\rangle}(t_2, t_1) P_{|0\rangle}(t_1, t') \Delta_{\uparrow}(t_1, t) \Delta_{\downarrow}(t_2, t') \\
&\quad + (i)^2(-1) \int_{t'}^t dt_2 \int_{t'}^{t_2} dt_1 P_{|0\rangle}(t, t_2) P_{|\uparrow\rangle}(t_2, t_1) P_{|\uparrow\downarrow\rangle}(t_1, t') \Delta_{\uparrow}(t', t_2) \Delta_{\downarrow}(t, t_1)
\end{aligned} \tag{3.55}$$

$$\begin{aligned}
\Sigma_{|\uparrow\downarrow\rangle}^{\text{OCA}}(t, t') &= (i)^2 \int_{t'}^t dt_2 \int_{t'}^{t_2} dt_1 P_{|\downarrow\rangle}(t, t_2) P_{|0\rangle}(t_2, t_1) P_{|\uparrow\rangle}(t_1, t') \Delta_{\uparrow}(t, t_1) \Delta_{\downarrow}(t_2, t') \\
&\quad + (i)^2 \int_{t'}^t dt_2 \int_{t'}^{t_2} dt_1 P_{|\uparrow\rangle}(t, t_2) P_{|0\rangle}(t_2, t_1) P_{|\downarrow\rangle}(t_1, t') \Delta_{\uparrow}(t_2, t') \Delta_{\downarrow}(t, t_1)
\end{aligned} \tag{3.56}$$

where we integrate over the internal vertices, and use the bold propagator P . The total self-energy within OCA also includes the NCA contribution: $\Sigma = \Sigma^{\text{NCA}} + \Sigma^{\text{OCA}}$.

These truncations of the skeleton series for the self-energy give us an equation for the self-energy $\Sigma[P]$ in terms of the bold propagator P . This must be solved simultaneously with the Dyson equation $P = P_0 + P_0 \circ \Sigma \circ P$ which relates the bold propagator with the self-energy. By solving these equations simultaneously we sum an infinite class of diagrams consisting of all diagrams with M or fewer crossings where M is the order of truncation of the skeleton series. Figure 3.13 shows an example of a high order diagram

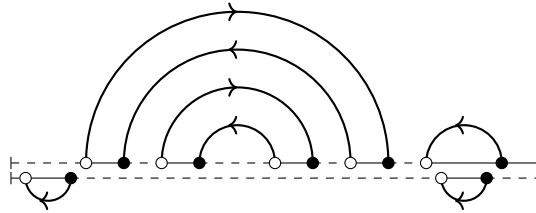


Figure 3.13: High order contribution to the bold propagator included within NCA.

which is included within NCA.

A solution of these equations can be obtained iteratively. We start with an initial guess for the bold propagator \tilde{P} , typically the bare propagator $P^{(0)}$. Using this guess we compute our M -crossing approximation to the self-energy $\Sigma[\tilde{P}]$. We then plug this into

the Dyson equation to obtain a new bold propagator $\tilde{P}' = P^{(0)} + P^{(0)} \circlearrowleft \Sigma[\tilde{P}] \circlearrowright \tilde{P}$. We repeat this iteration until $\tilde{P}' = \tilde{P}$ indicating that we have reached a self-consistent solution of the Dyson equation with our chosen self-energy approximation.

These M -crossing approximations, particularly the two lowest order truncations, NCA and OCA, are extremely useful approximate methods which are not too difficult to implement and not too computationally expensive. In appendix A we show an example implementation of the NCA. However, the requirement that we solve a self-consistency is somewhat inconvenient. In the next section, we will introduce the inchworm expansion which provides an alternative scheme for summing the same set of diagrams without solving a self-consistency.

3.4 The Inchworm Expansion

In the bare expansion (figure 3.8), we express the bold propagator $P(t, t')$ in terms of a sum over bare diagrams containing the bare propagators $\{P^{(0)}(t_2, t_1) \mid t \succ t_2 \succ t_1 \succ t'\}$. The core idea of the inchworm expansion, is to reduce the number of diagrams we have to sum over by replacing a subset of these bare propagators by bold propagators. Specifically, we choose a time $t \succ t_s \succ t'$ which we call the splitting time, and replace all bare propagators which begin and end before the splitting time with bold propagators. The local time evolution is then given by the split propagator

$$P_\alpha^s(t, t'; t_s) = \begin{cases} P_\alpha(t, t') & t_s \succ t \succ t' \\ P_\alpha^{(0)}(t, t_s)P_\alpha(t_s, t') & t \succ t_s \succ t' \\ P_\alpha^{(0)}(t, t') & t \succ t' \succ t_s \end{cases} \quad (3.57)$$

$$= \begin{array}{c} \text{---} \\ | \\ t \quad t_s \quad t' \end{array} \quad (3.58)$$

which describes evolution with the bold propagator up to time t_s followed by evolution with the bare propagator, and has the simple diagrammatic representation shown above. By rewriting the diagrammatic sum for the bold propagator in terms of the split propagator, we greatly reduce the number of diagrams which contribute. We call this the inchworm expansion, and call diagrams which contribute ‘‘inchworm proper’’ diagrams [55]. We typically choose $t_s = t - \Delta t$ where Δt is small, and call the process of extending the bold propagator by computing $P(t_s + \Delta t, t')$ ‘‘inching’’ or taking an inchworm step. A useful way to think about inching is as a process of gluing a short bare propagator onto the end

of a bold propagator in order to extend it.

The inchworm proper diagrams are most easily defined negatively as diagrams which do not contain disconnected clusters of hybridization lines in the bold region (t_s, t') , since these are already counted as part of the split propagator. Figure 3.14 shows the inchworm

$$\begin{aligned}
 P(t, t') = & \text{—————} \\
 = & \text{—} \text{—————} + \text{—} \text{—} \text{—————} + \text{—} \text{—} \text{—} \text{—————} + \text{—} \text{—} \text{—} \text{—} \text{—————} \\
 + & \text{—} \text{—} \text{—} \text{—} \text{—} \text{—————} + \text{—} \text{—} \text{—} \text{—} \text{—} \text{—} \text{—————} + \text{—} \text{—} \text{—} \text{—} \text{—} \text{—} \text{—————} + \text{—} \text{—} \text{—} \text{—} \text{—} \text{—} \text{—} \text{—————} \\
 + & \text{—} \text{—} \text{—} \text{—} \text{—} \text{—} \text{—} \text{—} \text{—————} + \text{—} \text{—} \text{—} \text{—} \text{—} \text{—} \text{—} \text{—} \text{—} \text{—————} + \text{—} \text{—} \text{—} \text{—} \text{—} \text{—} \text{—} \text{—} \text{—} \text{—————} + \text{—} \text{—} \text{—} \text{—} \text{—} \text{—} \text{—} \text{—} \text{—} \text{—} \text{—————} \\
 + & \dots
 \end{aligned}$$

Figure 3.14: Illustration of the inchworm expansion for the bold propagator. The diagrams in the bottom row are not inchworm proper because they contain disconnected hybridization lines (marked in red) which are already included in the bold part of the split propagator.

expansion for the bold propagator. Diagrams which are not inchworm proper are crossed out and the disconnected hybridization lines are marked in red.

The inchworm proper diagrams can be defined formally in terms of the hybridization graph $\mathcal{G}(\mathcal{C}, \mathcal{D})$ in which each node is a hybridization line, and two nodes are joined by an edge if their hybridization lines cross. We say a node is “connected” if it represents a hybridization line which begins or ends in the connected region (t, t_s) . A diagram is inchworm proper if all connected components of \mathcal{G} contain at least one connected node. This can be tested by traversing the graph starting from each connected node and checking that all nodes are visited. Algorithm 3.1 shows a procedure for computing if a diagram is inchworm proper using depth first traversal of \mathcal{G} . Figure 3.15 shows several inchworm proper and improper diagrams along with their hybridization graphs.

Within the inchworm expansion, the bold propagator is given by the sum over all inchworm proper diagrams

$$P_\alpha(t, t') = \sum_{\mathcal{C}_\alpha} w_{\text{loc}}(\mathcal{C}_\alpha, P^s) \sum_{\mathcal{D}(\mathcal{C}_\alpha) \in \text{inch proper}} w'_{\text{hyb}}(\mathcal{D}, \Delta) \quad (3.59)$$

where $w_{\text{loc}}(\mathcal{C}_\alpha, P^s)$ and $w'_{\text{hyb}}(\mathcal{D}, \Delta)$ are defined by the same rules given in equation 3.44 with the local part evaluated using the split propagator P^s . Note unlike the bare expansion, the inchworm expansion requires prior knowledge of the bold propagators between t' and

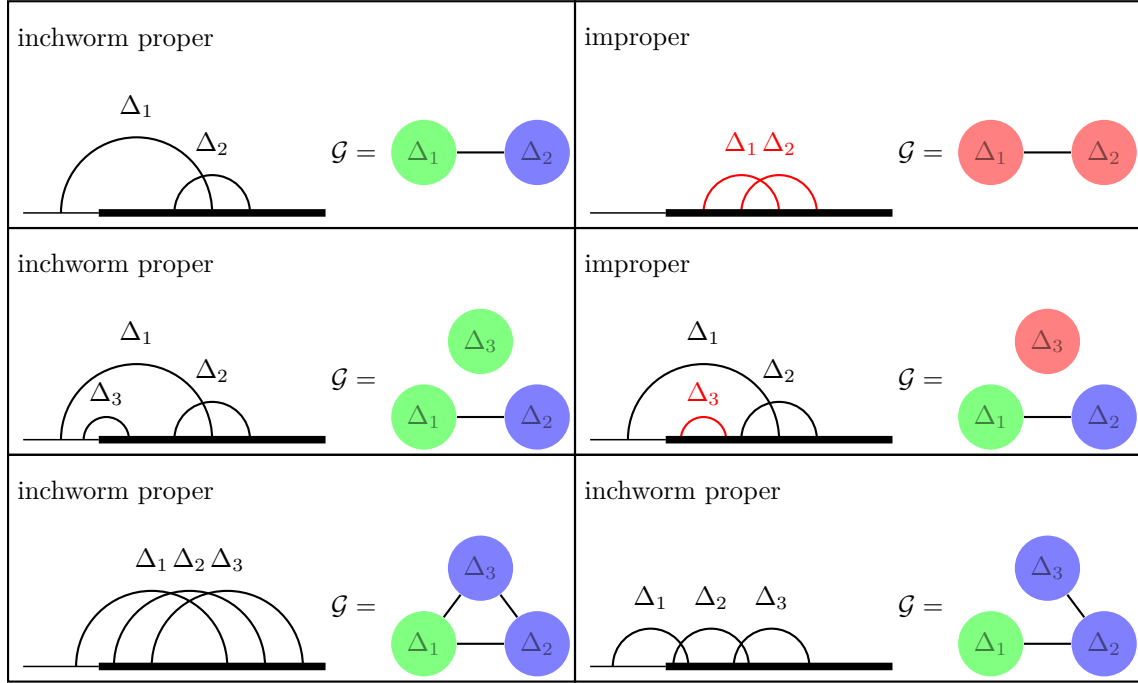
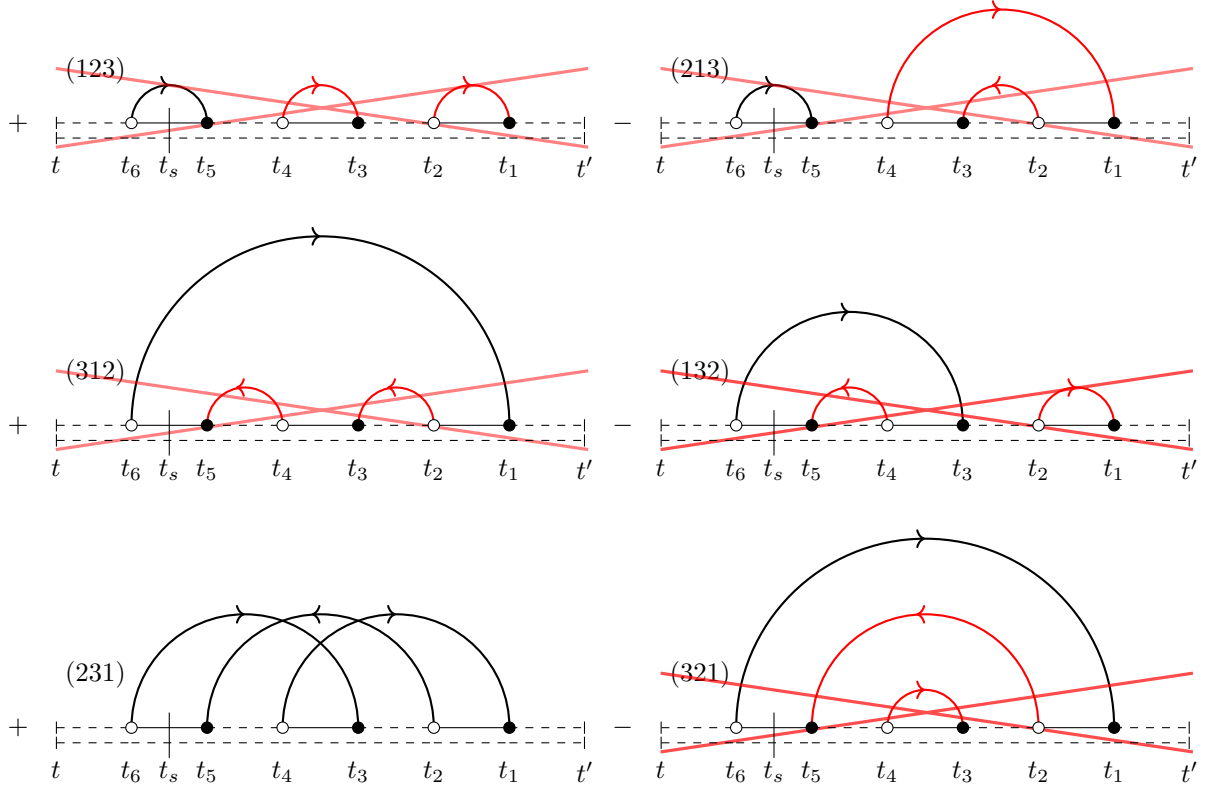


Figure 3.15: Illustration of the hybridization graph $\mathcal{G}(\mathcal{C}, \mathcal{D})$ for six diagrams. Green nodes represent hybridization lines ending in the connected region (t, t_s) and are said to be “connected”. Blue nodes represent hybridization lines which are part of a connected component of \mathcal{G} containing a connected node. Red nodes represent hybridization lines which are not part of a connected component containing a connected node. The inchworm proper diagrams are diagrams in which every connected component of \mathcal{G} contains at least one connected node.

t_s in order to evaluate the split propagator. This generates a contour causal dependency structure between the bold propagators which we will discuss in chapter 4.

In return for this additional complexity, the inchworm expansion dramatically reduces the number of diagrams which need to be summed. This can be seen in figure 3.16 which shows the inchworm proper diagrams for a configuration with topology $T = \{\uparrow\uparrow\uparrow\uparrow\uparrow\}$ and one vertex in the connected region. Note, only one of the six bare diagrams is inchworm proper. However, this reduction in the number of diagrams also comes with a cost. Because we now are summing over only a subset of diagrams, the hybridization factor can no longer be evaluated in terms of a single determinant. Instead we must explicitly sum over each permutation, or else employ a more complicated fast summation scheme [81].

Although it is not immediately obvious, the inchworm expansion is related to the M -crossing methods discussed in the previous section. Specifically, if we truncate the inchworm expansion to order M , and consider the limit where $\Delta t = t - t_s \rightarrow 0$, then this scheme will reproduce the M -crossing approximation hierarchy (NCA, OCA, 2CA, etc.)



$$\begin{aligned}
\mathcal{C} &= \{(t \geq t_6 \geq t_5 \geq t_4 \geq t_3 \geq t_2 \geq t_1 \geq t'), (\uparrow\uparrow\uparrow\uparrow\uparrow), |0\rangle\}, t_6 \succ t_s \succ t_5 \\
w_{\text{hyb}} &= \Delta_{\uparrow}(t_1, t_4) \Delta_{\uparrow}(t_5, t_2) \Delta_{\uparrow}(t_3, t_6) \\
w_{\text{loc}} &= (-1)^3 (i)^3 P_{|0\rangle}^s(t, t_6) P_{|\uparrow\rangle}^s(t_6, t_5) P_{|0\rangle}^s(t_5, t_4) P_{|\uparrow\rangle}^s(t_4, t_3) P_{|0\rangle}^s(t_3, t_2) P_{|\uparrow\rangle}^s(t_2, t_1) P_{|0\rangle}^s(t_1, t')
\end{aligned}$$

Figure 3.16: Inchworm proper diagrams for a configuration with topology $T = \{\uparrow\uparrow\uparrow\uparrow\uparrow\}$ and one vertex in the connected region. Disconnected hybridization lines are marked in red. Only one out of the six bare diagrams is inchworm proper. The propagator lines represent the split propagator P^s .

[55]. To see this note that in the $\Delta t \rightarrow 0$ limit there can only be one hybridization vertex in the connected region. In this limit, the sum over inchworm proper diagrams of order M is exactly a sum over M -crossing diagrams, because all hybridization lines must cross, either directly or indirectly, with the one line touching the connected region. Figure 3.17 shows the order 1 and order 2 inchworm proper diagrams that contribute in the $\Delta t \rightarrow 0$ limit. Note the correspondence with the self-energy diagrams discussed earlier (see figure 3.11, and 3.12). Assuming that the bold propagator up to t_s is given by the M -crossing approximation, taking an inchworm step with expansion order M to extend the propagator will maintain this property.

$$\begin{aligned}
P_{|0\rangle}(t, t') &= \overbrace{t \quad t_s}^{\Delta t \rightarrow 0} \quad \quad \quad t \\
& \left. \begin{array}{l} \text{---} \\ \text{---} \\ \text{---} \end{array} \right\} \text{order 0} \\
& + \left. \begin{array}{l} \text{---} \\ \text{---} \\ \text{---} \end{array} \right\} \text{order 1} \\
& + \left. \begin{array}{l} \text{---} \\ \text{---} \\ \text{---} \end{array} \right\} \text{order 2}
\end{aligned}$$

Figure 3.17: Order 1 and order 2 inchworm proper diagrams contributing to $P_{|0\rangle}(t, t')$ in the limit where $\Delta t = t - t_s \rightarrow 0$. The propagator lines represent the split propagator P^s .

Algorithm 3.1: Inchworm proper diagram selector.

Input: A list L of pairs of starting and ending times for all hybridization lines
The splitting time t_s

Output: A Boolean describing if the diagram is inchworm proper

Function `is_inchworm_proper(L, t_s)`

 initialize an empty stack S ;

foreach $l_i \in L$ **do**

if `is_connected(l_i, t_s)` **then**

 push l_i to S ;

 erase l_i from L ;

end

end

while S is not empty **do**

 pop l from top of S ;

foreach $l_i \in L$ **do**

if `is_crossing(l, l_i)` **then**

 push l_i to S ;

 erase l_i from L ;

end

end

end

 return `is_empty(L)`;

end

Function `is_connected(l, t_s)`

 /* l is connected if it ends in (t, t_s) */

$t_f, t_i \leftarrow l$;

 return $t_f \succ t_s$;

end

Function `is_crossing(l_i, l_j)`

$a, b \leftarrow l_i$;

$c, d \leftarrow l_j$;

 return $a \succ c \succ b \succ d$ or $c \succ a \succ d \succ b$;

end

3.5 Green's Functions

So far we have been concerned with calculation of the bold propagators $P_\alpha(t, t')$ which give direct access to single-time impurity observables such as the density, magnetization, and double occupancy. However, it is also desirable to be able to compute two-time correlators such as the impurity Green's function

$$G_\sigma(t, t') = -i \langle \mathcal{T}_C \hat{d}_\sigma(t) \hat{d}_\sigma^\dagger(t') \rangle \quad (3.60)$$

which contains additional information about the system. Recall the Green's function only needs to be computed over the physical time domain (see figure 2.5) which is defined by $t'_+ \succeq_{\bar{C}} t \succeq_{\bar{C}} t'_-$. On this time domain, the Green's function can be expressed

$$G_\sigma(t, t') = -i \langle \mathcal{T}_C \hat{d}_\sigma(t) \hat{d}_\sigma^\dagger(t') \rangle \quad (3.61)$$

$$= -i (-1)^{\theta_C(t', t)} \frac{1}{Z} \text{Tr} \left[\mathcal{T}_{\bar{C}} \left\{ e^{-i \int_{\bar{C}} dz \hat{H}(z)} \hat{d}_\sigma(t) \hat{d}_\sigma^\dagger(t') \right\} \right] \quad (3.62)$$

$$= \frac{1}{Z} \sum_\alpha \xi_\alpha \underbrace{\left(-i \xi_\alpha (-1)^{\theta_C(t', t)} \text{Tr}_c \left[\langle \alpha | \mathcal{T}_{\bar{C}} \left\{ e^{-i \int_{\bar{C}} dz \hat{H}(z)} \hat{d}_\sigma(t) \hat{d}_\sigma^\dagger(t') \right\} | \alpha \rangle \right] \right)}_{P_\alpha^G(t'_+, t'_-; t, t')} \quad (3.63)$$

$$= \frac{1}{Z} \sum_{\alpha \in \{|0\rangle, |\bar{\sigma}\rangle\}} \xi_\alpha P_\alpha^G(t'_+, t'_-; t, t') \quad (3.64)$$

where we refer to P_α^G as the Green's function propagator. Unlike the regular propagators, these Green's function propagators run over the full contour from t'_- to t'_+ , and contain an insertion of the impurity creation operator \hat{d}_σ^\dagger at the tip (t'_-), and the impurity annihilation operator \hat{d}_σ at t . The $(-1)^{\theta_C(t', t)}$ factor comes from the action of the time ordering operator \mathcal{T}_C in the definition of the Green's function. The states $|0\rangle$ and $|\bar{\sigma}\rangle$ are the states that survive the creation operator \hat{d}_σ^\dagger acting at the tip. We introduce the ξ factors for convenience to match the definition of the regular propagators as closely as possible.

Using the contour formalism the Green's function propagators can be expressed

$$P_\alpha^G(t'_+, t'_-; t, t') \quad (3.65)$$

$$= -i\xi_\alpha(-1)^{\theta_C(t', t)} \text{Tr}_c \left[\langle \alpha | \mathcal{T}_{\hat{C}} \left\{ e^{-i \int_{t'_-}^{t'_+} dz \hat{H}(z)} \hat{d}_\sigma(t) \hat{d}_\sigma^\dagger(t') \right\} | \alpha \rangle \right] \quad (3.66)$$

$$= -i\xi_\alpha(-1)^{\theta_C(t', t)} \sum_n \sum_{T_n} (-i)^{2n} \int_{t'_-}^{t'_+} dz_{2n} \int_{t'_-}^{z_{2n}} dz_{2n-1} \dots \int_{t'_-}^{z_2} dz_1 \quad (3.67)$$

$$\text{Tr}_c \left[\langle \alpha | \mathcal{T}_{\hat{C}} \left\{ e^{-i \int_{t'_-}^{t'_+} dz \hat{H}_0(z)} \hat{v}(2n+2) \dots \hat{v}(1) \right\} | \alpha \rangle \right]$$

where we associate the Green's function operators with two special fixed vertices $\hat{v}(i) = \hat{d}_\sigma$ and $\hat{v}(1) = \hat{d}_\sigma^\dagger$, which unlike the other vertices do not contain a bath part. We mark these vertices with an asterisk when specifying the topology, e.g. $T = \{\uparrow^* \uparrow^*\}$ for the order 0 configuration.

Evaluation of the local factor w_{loc} goes through in the same way as before, except that the state sequence now begins with $\alpha_0 = \hat{d}_\sigma^\dagger | \alpha \rangle$ and contains $2n + 2$ states because of the action of the annihilation operator \hat{d}_σ at t . Note, there is an extra sign factor from pulling the local operators apart from the bath operators since they no longer always come together, but this cancels with the sign factor from acting with the Green's function operators so there is no extra sign in the final expression.

Evaluation of the hybridization factor w_{hyb} also goes through in the same way as before, except that we associate the contraction of the two special vertices with a "virtual" hybridization line with value i . Diagrams which do not match the two special vertices are equal to zero. This virtual hybridization line does not come with a factor of the hybridization function because the special vertices do not contain the bath operators. The purpose of the i factor is to cancel the extra factor of $-i$ which comes from the extra propagator. We diagrammatically represent the virtual hybridization line with a dashed arc. Note the $(-1)^{\theta(t', t)}$ factor is taken care of by the $\hat{\xi}$ operator at 0_+ which gives us an extra factor of (-1) if the $\hat{d}(t)$ operator occurs on the plus branch (this factor is not cancelled since the virtual hybridization line does not come with a hybridization function). Figure 3.18 shows the bare expansion for the Green's function propagator. Note that the virtual hybridization line is fixed in all diagrams.

In order to reduce the number of diagrams that need to be summed, we will develop a bold expansion for the Green's function propagator by replacing all bare propagators with bold propagators. We call diagrams which contribute to this bold expansion "G proper"

$$\begin{aligned}
P^G &= \text{---} \\
&= \text{---} \text{---} + \text{---} \text{---} \\
&+ \text{---} \text{---} + \text{---} \text{---} + \text{---} \text{---} \\
&+ \text{---} \text{---} + \text{---} \text{---} + \text{---} \text{---} + \text{---} \text{---} \\
&+ \text{---} \text{---} + \text{---} \text{---} + \text{---} \text{---} + \text{---} \text{---} \\
&+ \text{---} \text{---} + \text{---} \text{---} + \text{---} \text{---} + \text{---} \text{---} \\
&+ \text{---} \text{---} + \dots
\end{aligned}$$

Figure 3.18: Illustration of the bare expansion for the Green’s function propagator. The virtual hybridization line is represented by a dashed arc, and fixed in all diagrams.

diagrams [31]. The G proper diagrams are those diagrams in which every hybridization line crosses, directly or indirectly, with the virtual hybridization line. Because of this, the G proper diagrams are sometimes also referred to as “all crossing” diagrams. Diagrams which are not G proper contain disconnected clusters of hybridization lines which are already included in the bold propagators.

More formally, we say a diagram is G proper if the hybridization graph \mathcal{G} is fully connected, where the virtual hybridization line is included in \mathcal{G} . Figure 3.19 shows the

$$\begin{aligned}
P^G &= \text{---} \\
&= \text{---} \text{---} + \text{---} \text{---} \\
&+ \text{---} \text{---} + \text{---} \text{---} + \text{---} \text{---} \\
&+ \text{---} \text{---} + \text{---} \text{---} + \text{---} \text{---} + \text{---} \text{---} \\
&+ \text{---} \text{---} + \text{---} \text{---} + \text{---} \text{---} + \text{---} \text{---} \\
&+ \text{---} \text{---} + \text{---} \text{---} + \text{---} \text{---} + \text{---} \text{---} \\
&+ \text{---} \text{---} + \dots
\end{aligned}$$

Figure 3.19: Illustration of the bold expansion for the Green’s function propagator. The crossed out diagrams are not G proper because they contain disconnected hybridization lines (marked in red) which are already included in the bold propagator.

bold expansion for the Green's function propagator. Diagrams which are not G proper are crossed out and the disconnected hybridization lines are marked in red. The Green's function propagators are given by the sum over G proper diagrams

$$P_{\alpha}^G(t'_+, t'_-; t, t'_+) = \sum_{\mathcal{C}_{\alpha}} w_{\text{loc}}(\mathcal{C}_{\alpha}, P) \sum_{\mathcal{D}(\mathcal{C}_{\alpha}) \in G \text{ proper}} w'_{\text{hyb}}(\mathcal{D}, \Delta) \quad (3.68)$$

where $w_{\text{loc}}(\mathcal{C}_{\alpha}, P)$ and $w'_{\text{hyb}}(\mathcal{D}, \Delta)$ are defined by the same rules given in equation 3.44 except that the local part is evaluated using the bold propagator, and we use the extra rules defined above for dealing with the virtual vertices.

$$\begin{array}{cc}
 P_{|0\rangle}^G(t'_+, t'_-; t, t'_-) & = & \text{Diagram 1} & P_{|\downarrow\rangle}^G(t'_+, t'_-; t, t'_-) & = & \text{Diagram 2} \\
 \mathcal{C} = \{(t, t'_-), (\uparrow^* \uparrow^*), |0\rangle\} & & & \mathcal{C} = \{(t, t'_-), (\uparrow^* \uparrow^*), |\downarrow\rangle\} & & \\
 w_{\text{hyb}} = i & & & w_{\text{hyb}} = i & & \\
 w_{\text{loc}} = P_{|0\rangle}(t'_+, t) P_{|\uparrow\rangle}(t, t'_-) & & & w_{\text{loc}} = P_{|\downarrow\rangle}(t'_+, t) P_{|\uparrow\downarrow\rangle}(t, t'_-) & &
 \end{array}$$

Figure 3.20: Order 0 diagrams for the Green's function propagators contributing to the spin up Green's function $G_{\uparrow}(t, t'_-)$.

Figure 3.20 shows the order 0 diagrams for the Green's function propagators contributing to the spin up Green's function $G_{\uparrow}(t, t'_-)$. Note the propagators extend from t'_- all the way around to the corresponding point on the plus branch t'_+ . We call this an order 0 diagram because we do not count the special fixed vertices in the expansion order. From the diagram, we see that calculation of the Green's function propagators can be thought of as gluing together two bold propagators.

The bold expansion gives us a method for efficiently computing the Green's function by taking advantage of the work we have done computing the bold propagators. Note, the bold expansion requires prior knowledge of the bold propagators over the whole contour up to the physical time t' . This generates a causal dependency structure between the Green's function propagators and the bold propagators which will discuss in chapter 4.

3.6 The Hybridization Function

In order to proceed in applying the hybridization expansion methods we have introduced, we need a way to specify and compute the hybridization function Δ . Recall that we defined

the hybridization function by

$$\Delta_\sigma(t, t') = -i \sum_k |\mathcal{V}_k|^2 \langle \mathcal{T}_C \hat{c}_{k\sigma}(t) \hat{c}_{k\sigma}^\dagger(t') \rangle = \sum_k |\mathcal{V}_k|^2 G_{k\sigma}(t, t') \quad (3.69)$$

where $G_{k\sigma}$ is the bath Green's function. Typically we will consider situations where the bath is in equilibrium, so it is convenient to work in terms of retarded frequency space Green's functions. Fourier transforming, we can write

$$\Delta_\sigma^R(\omega) = \sum_k |\mathcal{V}_k|^2 G_{k\sigma}(\omega + i\delta) = \sum_k |\mathcal{V}_k|^2 \frac{1}{\omega - \epsilon_k + i\delta} \quad (3.70)$$

where δ is an infinitesimal which shifts the poles below the real axis so that the expression is analytic in the upper complex plane, i.e. causal/retarded. Using the identity

$$\frac{1}{x - y \pm i\epsilon} = P \left(\frac{1}{x - y} \right) \mp i\pi\delta(x - y) \quad (3.71)$$

where P denotes the principal value, we define the coupling density

$$\Gamma_\sigma(\omega) = -\text{Im} \Delta_\sigma^R(\omega) = \pi \sum_k |\mathcal{V}_k|^2 \delta(\omega - \epsilon_k) \quad (3.72)$$

which parameterizes the hopping matrix elements \mathcal{V}_k and the bath dispersion ϵ_k . Note that this is almost identical to the definition of the spectral function (see equation 2.45) up to a factor of $1/\pi$. We will use this coupling density to specify the hybridization function.

In frequency space, the hybridization function can be obtained from the coupling density by

$$\Delta^R(\omega) = \sum_k |\mathcal{V}_k|^2 \frac{1}{\omega - \epsilon_k + i\delta} \quad (3.73)$$

$$= \sum_k \int d\omega' \delta(\omega' - \epsilon_k) |\mathcal{V}_k|^2 \frac{1}{\omega - \omega' + i\delta} \quad (3.74)$$

$$= \int d\omega' \frac{\Gamma(\omega')}{\pi} \left[\frac{1}{\omega - \omega' + i\delta} \right] \quad (3.75)$$

$$= \int d\omega' \frac{\Gamma(\omega')}{\pi} \left[P \left(\frac{1}{\omega - \omega'} \right) - i\pi\delta(\omega - \omega') \right] \quad (3.76)$$

$$= -i\Gamma(\omega) + P \int \frac{d\omega'}{\pi} \frac{\Gamma(\omega')}{\omega - \omega'} \quad (3.77)$$

where we have dropped the spin index for convenience. Note the negative imaginary part

is given exactly by $\Gamma(\omega)$ as expected. The real-time hybridization function can be written in terms of the coupling density as

$$\Delta(t, t') = -\frac{i}{\pi} \int d\omega e^{-i\omega(t-t')} \Gamma(\omega) [\Theta_C(t, t') - f(\omega, \beta)] \quad (3.78)$$

where $f(\omega, \beta) = 1/(e^{\beta\omega} + 1)$ is the Fermi function, and $\beta = 1/T$ is the inverse temperature. Note that this is almost identical to equation 2.46 up to a factor of $1/\pi$. This factor comes from the missing factor of $1/\pi$ in the definition of the coupling density relative to the spectral function. In practice, we implement equation 2.46 and use $\Gamma(\omega)/\pi$ as input when computing the hybridization function.

To understand the meaning of the coupling density, it is helpful to consider the non-interacting limit ($U = 0$), where the Anderson model reduces to the resonant level model which can be solved exactly [22]. In equilibrium, the impurity Green's function for the resonant level model is given by $G = G^{(0)} + G^{(0)}\Delta G$ where $G^{(0)} = 1/(\omega - \epsilon_d)$ is the Green's function for the disconnected impurity. This can be solved to obtain

$$G_\sigma^R(\omega) = \frac{1}{\omega - \epsilon_d - \Delta_\sigma^R(\omega)} \quad (3.79)$$

which shows that the hybridization function acts as a self-energy for the impurity Green's function.

Consider a flat coupling density $\Gamma_\sigma(\omega) = \Gamma\Theta(D - |\omega|)$ where D is the half-bandwidth and Γ is the coupling strength. For this coupling density, the hybridization function can be computed analytically as

$$\Delta^R(\omega) = -i\Gamma\Theta(D - |\omega|) + P \int_{-D}^D \frac{d\omega'}{\pi} \frac{\Gamma}{\omega - \omega'}. \quad (3.80)$$

For $|\omega| < D$ the integral goes through a pole so the principal value is given by

$$P \int_{-D}^D d\omega' \frac{1}{\omega - \omega'} = \lim_{\epsilon \rightarrow 0} \left[\int_{-D}^{\omega - \epsilon} d\omega' \frac{1}{\omega - \omega'} + \int_{\omega + \epsilon}^D d\omega' \frac{1}{\omega - \omega'} \right] \quad (3.81)$$

$$= \lim_{\epsilon \rightarrow 0} \left[\log\left(\frac{\omega + D}{\epsilon}\right) + \log\left(\frac{-\epsilon}{\omega - D}\right) \right] \quad (3.82)$$

$$= \lim_{\epsilon \rightarrow 0} \log\left(\frac{D + \omega}{D - \omega}\right) \quad (3.83)$$

$$= \log\left(\frac{D + \omega}{D - \omega}\right). \quad (3.84)$$

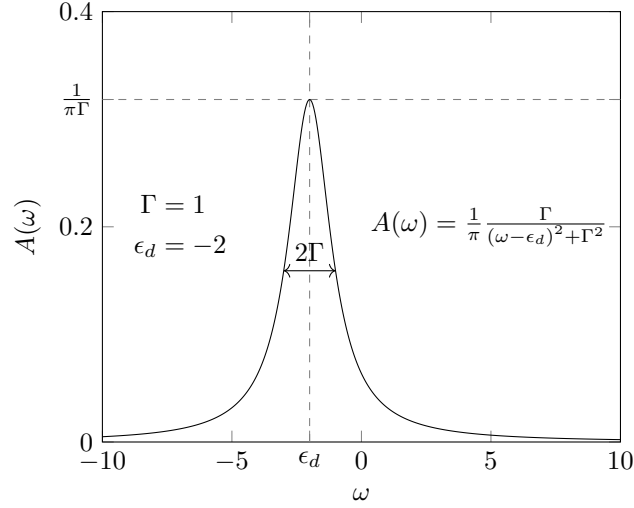


Figure 3.21: Impurity spectral function for the resonant level model in the wide band limit.

Using this, the hybridization function can be expressed

$$\Delta^R(\omega) = \frac{\Gamma}{\pi} \log \left(\frac{D + \omega}{D - \omega} \right) - i\Gamma \quad |\omega| < D. \quad (3.85)$$

Taking the wide band limit $D \gg \omega$, this reduces to $\Delta^R(\omega) = -i\Gamma$. The impurity spectral function for $|\omega| < D$ is then given by

$$A(\omega) = -\frac{1}{\pi} \text{Im} G^R(\omega) \quad (3.86)$$

$$= -\frac{1}{\pi} \text{Im} \left\{ \frac{1}{\omega - \epsilon_d + i\Gamma} \right\} \quad (3.87)$$

$$= \frac{\Gamma/\pi}{(\omega - \epsilon_d)^2 + \Gamma^2}. \quad (3.88)$$

which is simply a Lorentzian with width Γ centered at $\omega = \epsilon_d$ (see figure 3.21). Because of this the parameter Γ is often referred to as the “level broadening”. This is the motivation for defining the coupling density without a factor of $1/\pi$.

Multiple baths

In the case of multiple baths, the bath and tunneling Hamiltonians are given by

$$\hat{H}_{\text{bath}} = \sum_{\alpha} \sum_{k\sigma} \epsilon_{\alpha k\sigma} \hat{c}_{\alpha k\sigma}^{\dagger} \hat{c}_{\alpha k\sigma} \quad (3.89)$$

$$\hat{H}_T = \sum_{\alpha} \sum_{k\sigma} \left(\mathcal{V}_{\alpha k} \hat{c}_{\alpha k\sigma}^{\dagger} \hat{d}_{\sigma} + \mathcal{V}_{\alpha k}^* \hat{d}_{\sigma}^{\dagger} \hat{c}_{\alpha k\sigma} \right) \quad (3.90)$$

where α is the bath index and the impurity Hamiltonian is unchanged. We will often encounter this kind of setup in the context of a quantum dot which is attached to multiple leads (see chapter 5). In this case, the hybridization function is simply given by a sum over the hybridization functions for each bath

$$\Delta(t, t') = \sum_{\alpha} \Delta_{\alpha}(t, t') \quad (3.91)$$

where $\Delta_{\alpha}(t, t')$ can be computed from the coupling density for bath α , $\Gamma_{\alpha}(\omega)$. It is often interesting to consider applying a voltage to each bath. This can be modeled as a time-dependent shift in the chemical potential $\mu_{\alpha}(t)$ where we set $\mu_{\alpha}(0) = 0$ so that the equilibrium filling is not changed. The effect of the voltage is to modify the hybridization function $\Delta_{\alpha}(t, t')$ by a phase factor $e^{-i\phi_{\alpha}(t, t')}$ where

$$\phi_{\alpha}(t, t') = \exp \left(\int_{t'}^t d\bar{t} \mu_{\alpha}(\bar{t}) \right). \quad (3.92)$$

CHAPTER IV

Inchworm Quantum Monte Carlo

In the previous chapter, we derived expressions for the bold propagators and Green's functions for the single impurity Anderson model. In this chapter we discuss practical implementation of numerical methods based on these equations. We will focus on the inchworm algorithm which is derived from the inchworm expansion for the bold propagator. We begin by discussing quantum Monte Carlo (QMC) techniques for computing the high dimensional integrals that we encounter. We then discuss the causal structure of the inchworm equations and show how the calculations of the propagators and Green's functions should be organized and efficiently parallelized. Finally we show some benchmark results of the inchworm algorithm which demonstrate its ability to overcome the dynamical sign problem.

4.1 Quantum Monte Carlo

The objects of interest to us, i.e. the propagators and Green's function propagators, are written as configuration space integrals

$$X_\alpha = \sum_{\mathcal{C}_\alpha} w(\mathcal{C}_\alpha) = \sum_{\mathcal{C}_\alpha} w_{\text{loc}}(\mathcal{C}_\alpha, P) \sum_{\mathcal{D}(\mathcal{C}_\alpha) \in S} w'_{\text{hyb}}(\mathcal{D}, \Delta) \quad (4.1)$$

where the configuration \mathcal{C}_α consists of $2n$ time-ordered points $\mathbf{z} = \{z_{2n}, \dots, z_1\}$, a topology $T = \{\sigma_{2n} \dots \sigma_1\}$, and a tip state $|\alpha\rangle$, the diagram \mathcal{D} consists of a pair of permutations x_\uparrow, x_\downarrow , specifying a matching between the creation and annihilation vertices on each spin, and S represents some subset of all diagrams depending on the object we are computing. To compute the object, we must sum over all topologies, and integrate over all time points.

In order to perform these high dimensional configuration space integrals we turn to

Monte Carlo techniques. To begin, note that the integral of a function f can be expressed

$$I = \int_{\Omega} dx f(x) \tag{4.2}$$

$$= \int_{\Omega} dx \frac{f(x)}{w(x)/Z} (w(x)/Z) \tag{4.3}$$

$$= Z \int_{\Omega} dx \frac{f(x)}{w(x)} (w(x)/Z) \tag{4.4}$$

$$= Z \langle f/w \rangle_w \tag{4.5}$$

where $w(x)$ is an unnormalized probability distribution, $Z = \int_{\Omega} dx w(x)$ is the normalization constant, and Ω is a configuration space which may contain both discrete and continuous variables. Using this we can write a Monte Carlo estimate for the normalized integral

$$\frac{I}{Z} = \langle f/w \rangle_w \approx Q_N = \frac{1}{N} \sum_{i=1}^N \frac{f(x_i)}{w(x_i)} \tag{4.6}$$

where the points x_i are drawn from the distribution $w(x)/Z$. The variance of this estimate can be expressed

$$\text{Var}(Q_N) = \frac{1}{N} \text{Var}(f/w) = \frac{1}{N} [\langle (f/w)^2 \rangle_w - \langle f/w \rangle_w^2] \tag{4.7}$$

which shows that asymptotically the error will scale with the number of samples as $\delta I \sim \sqrt{\text{Var}(Q_N)} \sim N^{-1/2}$. Note, the convergence rate is independent of the dimension of the configuration space Ω . Because of this Monte Carlo methods are very useful for high dimensional problems where traditional quadrature methods quickly run into the curse of dimensionality. The error scales with the variance of f/w which implies that we can decrease the error by sampling from a distribution that approximates f , an idea known as importance sampling.

In order for $w(x)$ to be interpreted as a probability distribution, it must be non-negative.

If $w(x)$ is negative we can still use Monte Carlo methods by taking the absolute value

$$\frac{I}{Z} = \frac{\int_{\Omega} dx \frac{f(x)}{w(x)} w(x)}{\int_{\Omega} dx w(x)} \quad (4.8)$$

$$= \frac{\int_{\Omega} dx \frac{f(x)}{|w(x)|} |w(x)|}{\int_{\Omega} dx \frac{w(x)}{|w(x)|} |w(x)|} \quad (4.9)$$

$$= \frac{\langle f/|w| \rangle_{|w|}}{\langle w/|w| \rangle_{|w|}} \quad (4.10)$$

where we call the factor in the denominator $\langle w/|w| \rangle_{|w|}$ the average sign. However, if the average sign is small, then the relative error will be large and our Monte Carlo estimate will not be accurate. This is the “sign problem” which is often a major barrier to the application of Monte Carlo methods. A sign problem can have many different causes. Lattice systems often have a “fermion sign problem” which emerges from the negative sign associated with exchanging two fermions. In our case, the sign problem comes from the oscillatory complex exponential factors associated with propagation in real time. This sign problem is referred to as the “dynamical sign problem”. Because of the dynamical sign problem, applying Monte Carlo to the bare hybridization expansion, results in an algorithm which scales exponentially with the maximum simulation time, making it impracticable. We will show that by using the inchworm expansion for the bold propagator we can overcome this sign problem.

Markov Chain Monte Carlo

In order to apply Monte Carlo integration we must be able to generate samples from a distribution which approximates the integrand. This can be done using Markov chain Monte Carlo (MCMC) which generates samples from a Markov chain with the desired equilibrium distribution.

Consider a probability distribution $p(x)$ over a configuration space Ω . A Markov chain is defined by a transition matrix W_{xy} which describes the probability to transition from state x to state y at each step where $x, y \in \Omega$. The equilibrium distribution of states in the Markov chain will follow $p(x)$ provided that the transition matrix satisfies two conditions. First, that it is ergodic so that every state in Ω is reachable from every other state in a

finite number of steps. Secondly, that is satisfies the balance condition

$$\sum_{x \in \Omega} p(x)W_{xy} = p(y). \quad (4.11)$$

In practice we use the detailed balance condition

$$p(x)W_{xy} = p(y)W_{yx} \quad (4.12)$$

which implies balance.

The Metropolis-Hastings algorithm gives a simple recipe for satisfying detailed balance by factorizing the transition probability into a proposal probability and a acceptance probability $W_{xy} = W_{xy}^{\text{proposal}}W_{xy}^{\text{acceptance}}$ [86, 87]. The proposal probability can be chosen freely provided we satisfy ergodicity. The acceptance probability is

$$W_{xy}^{\text{acceptance}} = \min \left(1, \frac{p(y)W_{yx}^{\text{proposal}}}{p(x)W_{xy}^{\text{proposal}}} \right) \quad (4.13)$$

which gives a total transition probability satisfying the detailed balance condition. Note that this only requires computing the ratio $p(y)/p(x)$ which allows us to sample from unnormalized distributions.

Using this factorization, the Metropolis-Hastings algorithm computes the next state in the Markov chain in three steps. First we propose a move $x \rightarrow y$ sampled from the proposal distribution W^{proposal} . Secondly, we compute the acceptance ratio R_{xy} which is the product of the weight ratio $p(y)/p(x)$ and the proposal ratio $W_{yx}^{\text{proposal}}/W_{xy}^{\text{proposal}}$. Finally, we accept the move with probability $\min(1, R_{xy})$ so moves with $R > 1$ are unconditionally accepted and moves with $R < 1$ are accepted with probability R . If the move is accepted then the Markov chain transitions to state y otherwise it remains in state x . By following this procedure, the equilibrium distribution of states in the Markov chain will follow $p(x)$. However, states in the Markov chain are correlated and we must take a number of Metropolis steps to get an independent sample.

We apply this algorithm to computing the configuration space integrals for the propagators. We define the configuration distribution by

$$p(\mathcal{C}) = w(\mathcal{C})dz_{2n} \dots dz_1 \quad (4.14)$$

$$w(\mathcal{C}) = \sqrt{\sum_{\alpha} w(\mathcal{C}_{\alpha})^2} \quad (4.15)$$

where \mathcal{C} is the configuration $\{(\sigma_{2n} \dots \sigma_1), (z_{2n}, \dots, z_1)\}$ ignoring the tip state, $w(\mathcal{C}_\alpha)$ is the value of the integrand for tip state $|\alpha\rangle$, and we call $w(\mathcal{C})$ the configuration weight. The differential factors in p will all cancel when we compute the acceptance ratios R and we will only have to deal with weight ratios. Note the weight takes into account the magnitude of the integrand for all four tip states which allows us to efficiently measure all four propagators using the same Markov chain.

We define a set of three moves which describe changes to the configuration ($\mathcal{C} \rightarrow \mathcal{C}'$) and allow the Markov chain to travel ergodically through the configuration space. The weight ratios $w(\mathcal{C}')/w(\mathcal{C})$ for these moves are computed directly and do not make use of any fast ratio formulas like those commonly used in optimized CT-HYB implementations [71]. This is because within inchworm we are summing over a subset of diagrams and so do not have a determinant structure for the hybridization weight and therefore cannot straightforwardly make use of fast formulas for determinant ratios. Additionally, because \hat{H}_{loc} is diagonal in the occupation number basis, the local weight is simply a product of scalars and it is not worth caching intermediate results.

In our description of the moves we use the term ‘‘segment’’ to refer to a pair of adjacent vertices with the same spin. This conflicts with our previous definition in which a segment (anti-segment) was a pair of adjacent vertices in which the impurity creation operator came first (last). Here we use ‘‘segment’’ to refer to both segments and anti-segments because from the perspective of the Markov chain there is no need to treat them separately. The total number of segments in a configuration is given by $n^{\text{seg}} = n_{\uparrow}^{\text{seg}} + n_{\downarrow}^{\text{seg}}$ where $n_{\sigma}^{\text{seg}} = \max(0, 2m_{\sigma} - 1)$, and $2m_{\sigma}$ is the number of vertices with spin σ .

The three moves are described below.

- **Add Segment.** This move takes a configuration and adds a single pair of vertices to it, e.g. $\{\uparrow\uparrow\} \rightarrow \{\uparrow\uparrow\downarrow\downarrow\}$. This is done by picking a random spin, picking a random point on the contour, and finally picking a second random point in the segment containing the first point. We then insert two vertices on the chosen spin at the pair of times we have picked. The acceptance ratio for this move is given by

$$R(\mathcal{C} \rightarrow \mathcal{C}') = \frac{w(\mathcal{C}') W^{\text{proposal}}(\mathcal{C}' \rightarrow \mathcal{C})}{w(\mathcal{C}) W^{\text{proposal}}(\mathcal{C} \rightarrow \mathcal{C}')} = \frac{w(\mathcal{C}') l_{\text{contour}} l_{\text{segment}}}{w(\mathcal{C}) n^{\text{seg}}(\mathcal{C}')} \quad (4.16)$$

where l_{contour} is the total length of the contour, l_{segment} is the length of the segment containing the proposed segment, and $n^{\text{seg}}(\mathcal{C}')$ is the number of segments in the proposed configuration.

- **Remove Segment.** This move takes a configuration and removes a single pair of

adjacent vertices on the same spin from it, e.g. $\{\uparrow\uparrow\uparrow\uparrow\} \rightarrow \{\uparrow\uparrow\}$. The segment to remove is picked uniformly at random from the set of n^{seg} total segments. Note this is different from picking a spin and then picking a segment uniformly on that spin. The acceptance ratio for this move is given by

$$R(\mathcal{C} \rightarrow \mathcal{C}') = \frac{w(\mathcal{C}') W^{\text{proposal}}(\mathcal{C}' \rightarrow \mathcal{C})}{w(\mathcal{C}) W^{\text{proposal}}(\mathcal{C} \rightarrow \mathcal{C}')} = \frac{w(\mathcal{C}')}{w(\mathcal{C})} \frac{n^{\text{seg}}(\mathcal{C})}{l_{\text{contour}} l_{\text{segment}}} \quad (4.17)$$

where now l_{segment} is the length of the segment containing the segment which we are proposing to remove and $n^{\text{seg}}(\mathcal{C})$ is the number of segments in the current configuration.

- **Remove-Add Segment.** This move takes a configuration, removes a segment, and then adds a new segment, e.g. $\{\uparrow\uparrow\} \rightarrow \{\downarrow\downarrow\}$. The purpose of this move is to improve the ergodicity of the Markov chain since it may allow us to directly propose a configuration that otherwise would require passing through an intermediate configuration with low weight. The segments that are added and removed are chosen in the same way as in the corresponding “add segment” and “remove segment” moves. The acceptance ratio for this move is given by

$$R(\mathcal{C} \rightarrow \mathcal{C}') = \frac{w(\mathcal{C}') W^{\text{proposal}}(\mathcal{C}' \rightarrow \mathcal{C})}{w(\mathcal{C}) W^{\text{proposal}}(\mathcal{C} \rightarrow \mathcal{C}')} = \frac{w(\mathcal{C}')}{w(\mathcal{C})} \frac{n^{\text{seg}}(\mathcal{C}) l_{\text{add}}}{n^{\text{seg}}(\mathcal{C}') l_{\text{remove}}} \quad (4.18)$$

where l_{add} (l_{remove}) is the length of the segment containing the segment which we are proposing to add (remove).

With these three moves, we can use the Metropolis-Hastings algorithm to sample configurations from the distribution $p(\mathcal{C})$ and accumulate expectation values (see algorithm 4.1).

As we sample configurations we accumulate measurements

$$ZO \approx \frac{1}{N} \sum_{i=1}^N \frac{O(\mathcal{C}_i)}{w(\mathcal{C}_i)} \quad (4.19)$$

where $O(\mathcal{C})$ is some function of the configuration and Z is an unknown normalization constant (not the partition function). The core measurement is the propagator itself

$$ZP_\alpha \approx \frac{1}{N} \sum_{i=1}^N \frac{w(\mathcal{C}_i^\alpha)}{w(\mathcal{C}_i)} s_m(\mathcal{C}_i) \quad (4.20)$$

Algorithm 4.1: Metropolis-Hastings Algorithm

Input: Number of metropolis steps between measurements N
Number of measurements M

Output: Normalized propagator

initialize configuration \mathcal{C} ;

for $m = 1$ **to** M **do**

for $n = 1$ **to** N **do**

$\mathcal{C} \leftarrow \text{metropolis_step}(\mathcal{C});$

end

foreach *measurement* $O \in \{P, V_0\}$ **do**

$\text{accumulate}(O(\mathcal{C}));$

end

end

Compute normalized propagator $P = (ZP) / (ZV_0);$

Function `metropolis_step`(\mathcal{C})

 Choose a move m uniformly at random;

 Use m to generate a proposal configuration \mathcal{C}' ;

 Compute the acceptance ratio $R(\mathcal{C} \rightarrow \mathcal{C}')$;

 Generate a uniform random number $u \in [0, 1]$;

if $R \geq u$ **then**

$\mathcal{C} \leftarrow \mathcal{C}';$ /* accept the proposed move

*/

else

$\mathcal{C} \leftarrow \mathcal{C};$ /* reject the proposed move

*/

end

return \mathcal{C}

end

where the contour factor s_m

$$s_m(\mathcal{C}) = \prod_{i=1}^{2n} s_m(z_i), \quad s_m(z) = \begin{cases} +1 & z \in C_+ \\ -1 & z \in C_- \\ -i & z \in C_\downarrow \end{cases} \quad (4.21)$$

accounts for the integration measure. In order to normalize the propagators we also measure the hypervolume V_n for each order

$$ZV_n \approx \frac{1}{N} \sum_{i=1}^N \frac{[\text{order}(\mathcal{C}_i) = n]}{w(\mathcal{C}_i)} \quad (4.22)$$

which corresponds to the volume of the configuration space at order n . Using this we can

write

$$P_\alpha = \frac{(ZP_\alpha)}{(ZV_n)}V_n \quad (4.23)$$

which gives an expression for the normalized bold propagators in terms of the accumulated values and the hypervolume V_n . At order 0 there is nothing to integrate over, and the hypervolume is given by $V_0 = 1$ which gives us a simple normalization scheme.

We can also analytically compute the higher order hypervolumes V_n . However, note that the accumulated estimate ZV_n comes from Monte Carlo integration of the constant function $f(\mathcal{C}) = 1$ using distribution $w(\mathcal{C})$. At higher order it is not clear that this is a good idea as there may be configurations with very low weight which we do not efficiently sample, but which contribute equally to the hypervolume. Because of this we will normalize our results using the order zero hypervolume.

Wang-Landau

In order to normalize by the order 0 hypervolume, the Markov chain must spend a sufficient number of steps at order 0 to accumulate good enough statistics for the measurement of ZV_0 . For the bold propagators this is usually not a problem. However, for the Green's function propagators this can become an issue especially on the three branch contour. To overcome this problem we employ a reweighting

$$w'(\mathcal{C}) = w_o(\text{order}(\mathcal{C}))w(\mathcal{C}) \quad (4.24)$$

where the weight for each configuration is multiplied by a factor $w_o(n)$ which depends only on the order of the configuration.

We use the Wang-Landau algorithm [88–90] to find factors $w_o(n)$ so that the order histogram

$$h(n) = \sum_{i=1}^N [\text{order}(\mathcal{C}_i) = n] \quad (4.25)$$

is flat, implying an approximately equal number of steps spent at each order. The Wang-Landau algorithm (see algorithm 4.2) works by multiplicatively modifying a density of states $\text{DOS}[n]$ by a factor $f > 1$ every time a configuration of order n is sampled, and reweighting by the inverse of this DOS. Note, the reweighting is done “online” as we generate samples. This procedure is run until the order histogram becomes flat, at which

point the histogram is reset and the procedure is repeated with a smaller modification factor f to more finely tune the reweighting.

Algorithm 4.2: Wang-Landau Algorithm

Input: Initial modification factor f
Histogram flatness tolerance ϵ
Number of iterations
Maximum number of steps per iteration

Output: Reweighting factors w_o

Data: w_o , DOS, hist: Arrays with length equal to the maximum expansion order

initialize DOS to all ones;
initialize w_o to all ones;
foreach *iteration* **do**

clear hist;
while *step* < *maximum steps* and hist is not flat **do**

Take a metropolis step with reweighting w_o ;
 $n \leftarrow$ expansion order of current configuration;
hist[n] \leftarrow hist[n] + 1;
DOS[n] $\leftarrow f \cdot$ DOS[n];
 $w_o[n] \leftarrow 1/\text{DOS}[n]$;

end
 $f \leftarrow \sqrt{f}$;

end

Function is_flat(hist, ϵ)

max \leftarrow maximum value of hist;
avg \leftarrow average value of hist;
return $(1 - \epsilon) \cdot \text{max} < \text{avg}$;

end

By modifying the DOS multiplicatively the Wang-Landau algorithm can handle very large reweighting factors. In practice, to avoid overflow we store the logarithm of the density of states which allows us to write the update as $\log(\text{DOS}) \leftarrow \log(\text{DOS}) + \log(f)$. We run this Wang-Landau calculation as a pre-computation in order to obtain the reweighting factors w_o before running the main Monte Carlo simulation where we accumulate the measurements.

4.2 The Inchworm Algorithm

Using the QMC algorithm defined above, we can numerically compute the configuration space integrals for the bold propagator $P_\alpha(t, t')$ at a single pair of time points. Now

we must efficiently assemble these individual calculations in order to compute the bold propagator over the full physical time domain. For the bare expansion this is trivial since the only inputs are the bare propagators $P^{(0)}$ and the hybridization function Δ which are both known ahead of time (we are not yet considering DMFT). In this case we can simply compute the propagators over the whole time domain in parallel.

However, the situation is more complicated for the inchworm expansion. Recall that in the inchworm expansion we compute the bold propagator $P(t, t')$ by summing the inchworm proper diagrams which glue together a bare propagator $P^{(0)}(t, t_s)$ and a shorter bold propagator $P(t_s, t')$ where we call t_s the splitting time. Because the diagrams can contain vertex insertions anywhere between t' and t , the inchworm expansion requires that we already know the bold propagator $P(t_2, t_1)$ for all times $t_s \succ t_2 \succ t_1 \succ t'$. Figure 4.1

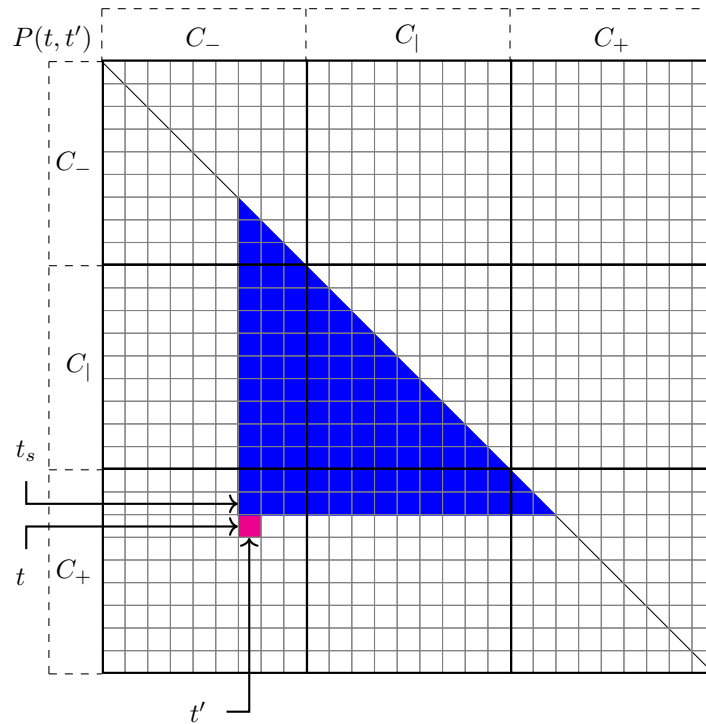


Figure 4.1: Illustration of the contour causal structure of the bold propagators. A propagator $P(t, t')$ (magenta) depends on all propagators with start point on or after t' and end point up to t_s (blue).

shows the set of bold propagators (blue) needed to compute a new bold propagator (magenta), in this case $P(t_+, t'_-)$. This dependency structure is a consequence of the propagators being “contour causal”, i.e. only containing vertex insertions that occur between t' and t on the contour. Note this is more restrictive than simply being “causal” like the Green’s functions which can contain vertex insertions that occur at physical times

less than or equal to the maximum physical time of their arguments.

We choose $t_s = t - \Delta t$ where Δt is our discretization of the contour so that each step extends the propagator by Δt . These steps can be repeated in order to generate longer and longer propagators from sets of shorter ones. The dependency structure of the propagators

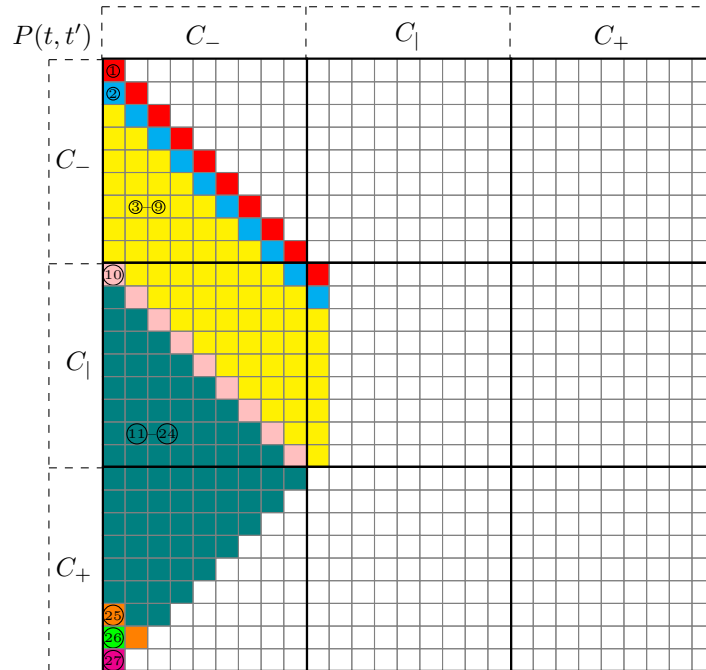


Figure 4.2: Illustration of the diagonal by diagonal calculation of the propagators. The circled numbers label the diagonals which correspond to sets of inchworm steps which can be taken in parallel. The propagator is computed only on the physical time domain.

suggests an iterative algorithm in which the bold propagators are computed diagonal by diagonal as illustrated in Figure 4.2. We call this the inchworm algorithm [31, 55]. Note we only need to compute the propagators on the physical time domain; all other points are obtained by symmetry. Also note, on the first diagonal (red) we have $t_s = t - \Delta t = t'$ so the entire propagator $P(t, t')$ is in the connected region (t, t_s) and the inchworm expansion reduces to the bare expansion.

Each diagonal can be computed in parallel since the dependency structure makes these calculations fully independent. At the beginning of the calculation this leads to a relatively large amount of parallelism. However, as the calculation proceeds the diagonals become shorter and shorter until finally we reach the bottom left corner where $P(t_{\max}^+, t_{\max}^-)$ is the only element left to compute. This loss of parallelism as the calculation progresses has serious consequences for efficiency since at the end of the calculation almost all cpu cores will be idle.

To improve the parallel efficiency of the inchworm algorithm we overlap the computation of the propagators with the computation of the Green's function propagators. Recall that the Green's function propagators $P^G(t'_+, t'_-; t, t_-)$ wind all the way around the contour from t'_- to t'_+ . This makes them causal, i.e. dependent on all bold propagators with physical times less than t' , rather than contour causal. Figure 4.3 shows the set of bold

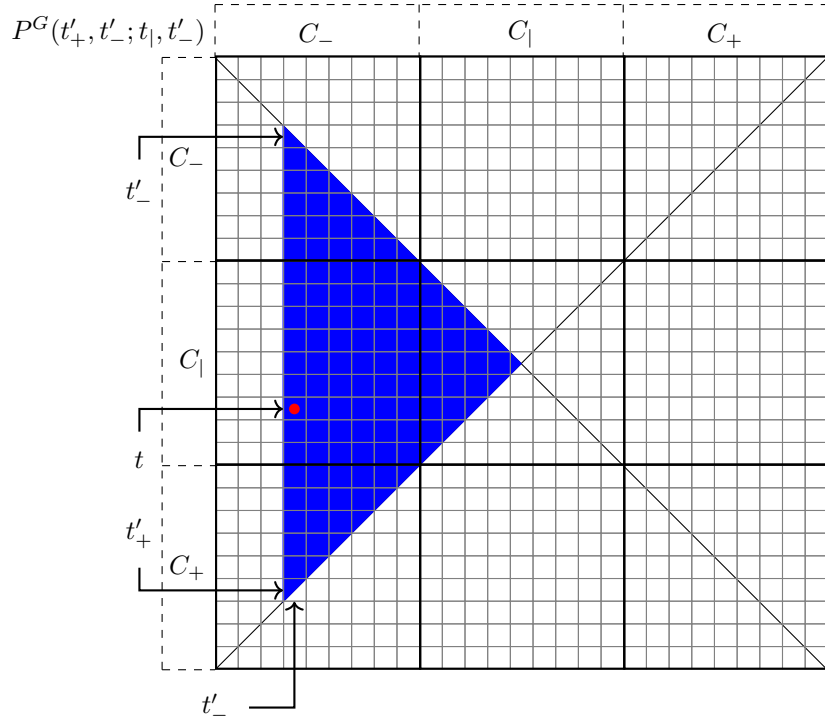


Figure 4.3: Illustration of the causal structure of the Green's function propagators. A Green's function propagator $P^G(t'_+, t'_-; t_1, t'_-)$ (red) depends on all bold propagators P with start points or end points up to the maximum physical time t' (we only show the bold propagators that are not obtained by symmetry). This Green's function propagator contributes to the right mixing Green's function $G(t_1, t'_-) = G^\Gamma(\tau, t')$.

propagators (blue) needed to compute a Green's function propagator (red). We emphasize that the blue area represents the regular bold propagators *not* the Green's function propagators; the Green's function propagators P^G do not have any mutual dependencies. Once we have computed all the propagators up to some maximum physical time t' we can begin computing the Green's function propagators $P^G(t'_+, t'_-; t, t_-)$ where $t'_+ > t > t'_-$ corresponding to a vertical column between the diagonal and anti-diagonal in figure 4.3.

By overlapping these two calculations, we expose significantly more parallelism than is possible with the bold propagators alone. In particular, we prevent the loss of parallelism towards the end of the bold propagator calculation, since the number of Green's function

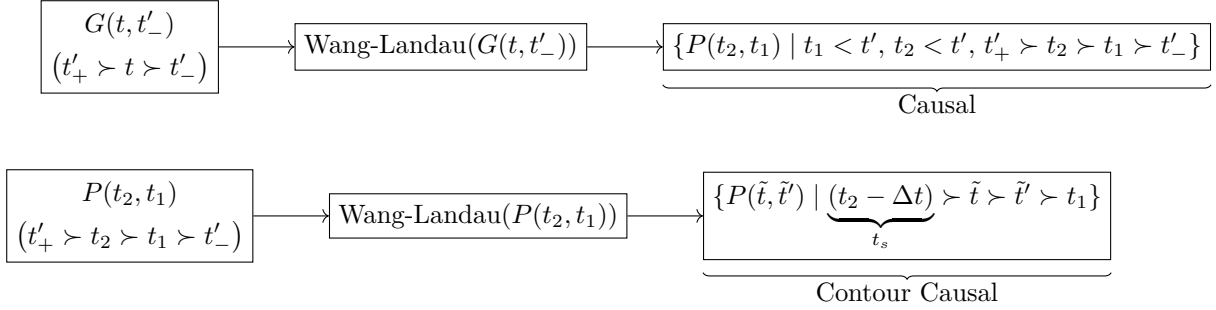


Figure 4.4: Illustration of the DAG representing the dependency structure of calculation for a Green’s function element $G(t, t'_-)$ in the physical time domain. Arrows indicate dependencies. The Green’s function depends causally on all propagators with start or end times less than or equal to the maximum physical time t' . The propagators depend contour causally on all propagators with a start or end time between t_1 and $t_s = t_2 - \Delta t$.

propagators that can be computed increases as more and more bold propagators are computed. However, the combination of the contour causal dependencies of the bold propagators and the causal dependencies of the Green’s function propagators is quite complicated. To efficiently overlap these calculations we make use the High Performance ParallelX (HPX) framework [91] which provides primitives for task based parallelism. Using HPX, the problem of computing all propagators and Green’s function propagators is expressed as a dynamically specified directed acyclic graph (DAG) which describes the dependency structure of the calculations. Figure 4.4 shows the structure of the dependency graph for a single Green’s function element. The HPX framework efficiently manages parallel execution of the DAG distributed over multiple workers.

DMFT

The above analysis was for the case of a simple impurity problem in which the bare propagators and the hybridization function are both known fully in advance. The situation is changed in the case of nonequilibrium DMFT [30, 92] where the hybridization function must be determined self-consistently with the impurity Green’s function. In this case, the DMFT self-consistency can be dealt with in two ways.

The simplest solution is to place the DMFT self-consistency completely externally to the impurity solver so that the impurity problem is solved over the whole time domain before updating the hybridization function. This is how DMFT is done in imaginary time and how we perform the DMFT self-consistency in chapter 7. However, in real time this procedure is inefficient because it does not take into account the causal structure of the DMFT equations. Specifically, the effort to obtain the solution all the way to

the maximum time is almost entirely wasted during early DMFT iterations where the hybridization function is only converged out to a short time.

Instead, it is better to take advantage of the causal structure of the DMFT equations. Concretely, this can be done by solving the DMFT self-consistency causal slice by causal slice (see the left panel of figure 2.6). However, note that if the solution is propagated causally, then the propagator calculation is entirely serial, and only the Green's function calculation retains some parallelism.

4.3 Results

In order to benchmark the inchworm quantum Monte Carlo method we consider a setup in which the impurity is coupled to two leads with a voltage applied across the leads. The leads are described by the Hamiltonian

$$\hat{H}_\alpha = \sum_{k\sigma} \left(\epsilon_k + \frac{\alpha V(t)}{2} \right) \hat{n}_{\alpha k\sigma} \quad (4.26)$$

where $\alpha = \pm 1$ labels the left (+) and right (-) leads, $\hat{n}_{\alpha k\sigma}$ is the lead number operator, ϵ_k is the lead dispersion, and $V(t)$ is a symmetrically applied voltage. We consider two cases: the equilibrium case, where none of the parameters are time-dependent and $V(t) = 0$; and the case of a symmetric voltage quench $V(t) = V\Theta(t)$, with $\Theta(t)$ being a Heaviside step function. In the second case, the system is in equilibrium for $t < 0$, and for $t > 0$ the lead levels ϵ_k are instantaneously moved to $\epsilon_k \pm \frac{V}{2}$, with the sign depending on the lead index α . We are interested in computing equilibrium and nonequilibrium Green's functions, spectral functions, time-dependent and steady state currents and occupations.

The parameters \mathcal{V}_k^α and ϵ_k are chosen such that the coupling density

$$\Gamma^\alpha(\omega) = -\text{Im} \Delta(\omega) = \pi \sum_k |\mathcal{V}_k^\alpha|^2 \delta(\omega - \epsilon_k) \quad (4.27)$$

describes a flat band centered at zero with a Fermi function like cutoff,

$$\Gamma^\alpha(\omega) = \frac{\pi \Gamma^\alpha}{(1 + e^{\nu(\omega-D)})(1 + e^{-\nu(\omega+D)})}. \quad (4.28)$$

Note the extra factor of π in the numerator which makes the level broadening for one lead $\pi\Gamma_\alpha$ rather than Γ_α as in the traditional convention. We use $\Gamma^\alpha = \Gamma = 1$; $D = 5$; $\nu = 3$ (unless specified as $\nu = 10$); $U = 4$ and $U = 10$; and temperature $T = 1$.

Populations

Recall from the previous chapter that the inchworm expansion at order $M + 1$ is equivalent to the M -crossing approximation. Fig. 4.5 illustrates agreement within error bars of

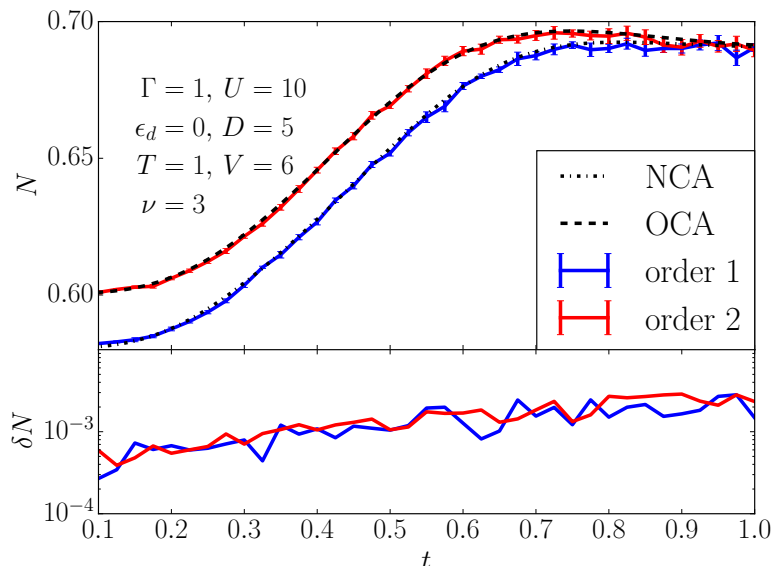


Figure 4.5: Top panel: Time evolution of the impurity occupation N after a voltage quench using the non-crossing and one-crossing approximations (NCA and OCA, respectively). Black lines: semi-analytically computed NCA and OCA solutions. Blue line: NCA solution generated from an inchworm expansion truncated to order one. Red line: OCA solution from an inchworm expansion truncated to order 2. Bottom panel: Statistical error estimate of the quantities shown in the upper panel.

numerical results for the propagators truncated to $n = 1$ and $n = 2$ to the NCA and OCA approximations. Below, it is shown that the size of the inchworm error does not strongly depend on time. This implies that for ‘crossing’ expansions on the order of the OCA and above, inchworm Monte Carlo provides an efficient alternative to the direct integration of the equations of motion.

Continuous-time QMC requires the sampling of diagrams to all orders. In bare expansions very high order diagrams are easily sampled, because (due to Wick’s theorem) the sum over all diagrams for a particular configuration of order $2k$, of which there are $k!$, can be written as the determinant of a $k \times k$ matrix and evaluated at polynomial scaling using linear algebra algorithms.[69] However, in bold and inchworm Monte Carlo a factorial number of diagrams must be explicitly summed over at each order, and the cost of enumerating these diagrams quickly becomes prohibitive (evaluating the sum over

permutations stochastically leads to a sizable increase in the overall sign problem). We therefore truncate the series at a predetermined maximum order and observe convergence as that order is increased. This corresponds to observing convergence in the hierarchy $NCA \rightarrow OCA \rightarrow 2CA \dots$, each of which contains an infinite subseries of all the bare diagrams which extends to infinite order. In this work, we typically truncate this hierarchy at order 5–7.

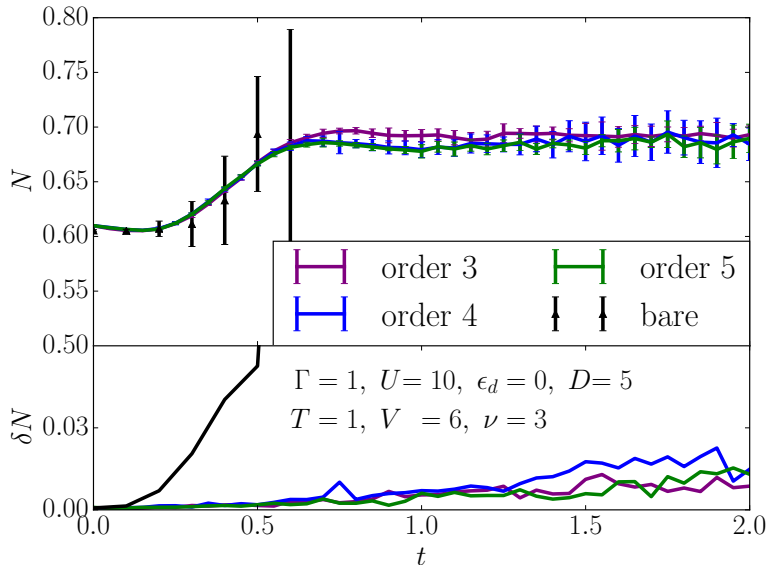


Figure 4.6: Top panel: Time evolution of the density on the impurity after a voltage quench with $\Gamma = 1$, $U = 10$, $\epsilon_d = 0$, $D = 5$, $T = 1$ and $V = 6$. Results obtained from a bare QMC calculation are shown for $t \leq 0.6$. The inchworm results with different orders agree with the bare result for $t \leq 0.6$ and coincide with each other for longer times. Bottom panel: Error estimates. Data obtained using the bare method shows an exponential increase of the errors as a function of time, whereas inchworm errors grow slower as a function of time.

The top panel of Fig. 4.6 shows results for the time-evolution of the density after a voltage quench of an impurity with parameters $\Gamma = 1$, $U = 10$, $\epsilon_d = 0$, $D = 5$, $T = 1$ and $V = 6$. Black triangles denote values obtained in a bare QMC simulation, and colored lines the inchworm results with respective maximum order constraints of order 3, 4, and 5 as labeled in the plot. At short times ($t \leq 0.6$ in these units), the inchworm results agree with the bare calculation within error bars, but for $t \gtrsim 0.3$ the bare QMC error bars are too large to be useful. Inchworm results for orders 4 and 5 coincide within error bars at long times, indicating that a solution obtained within a three-crossing approximation calculation would be accurate. The bottom panel of Fig. 4.6 shows statistical error bars

for the data shown in the top panel. Errors for the bare calculation increase exponentially as a consequence of the dynamical sign problem. In contrast, the statistical inchworm error estimate grows slowly, allowing access to significantly longer times. We note that in order to account for error propagation and non-linear cross-correlations from short-time propagators to long-time propagators within the inchworm algorithm, the error bars have been obtained by running multiple (in this case eight) complete independent calculations, each of which includes a different realization of the statistical noise at all times. The standard deviation between the different runs provides a useful estimate of the confidence interval, whereas the standard deviation within each run—which does not account for error propagation—grossly underestimates the error.

It is remarkable that no exponential growth of the errors is seen, signaling that the dynamical sign problem has been overcome. However, a gradual, approximately linear increase of errors with time is visible.

Current

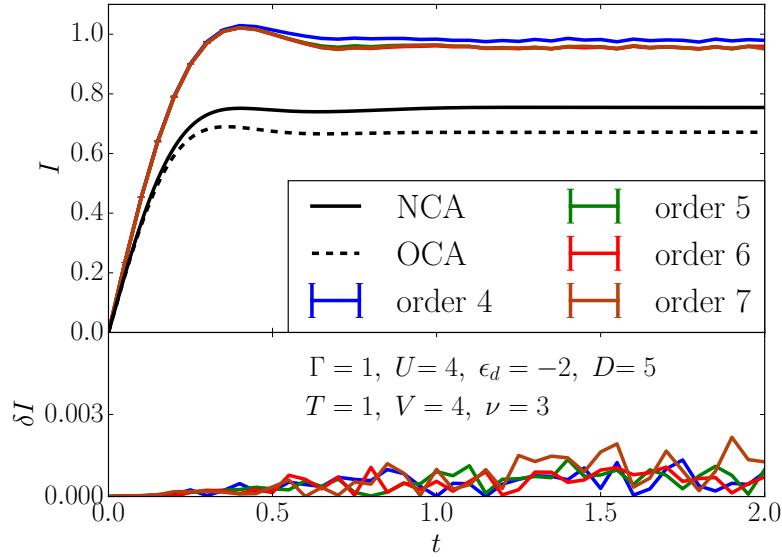


Figure 4.7: Top panel: The current dynamics after a voltage quench with $\Gamma = 1$, $U = 4$, $\epsilon_d = -2$, $D = 5$, $T = 1$ and $V = 4$. The inchworm results with different orders converge as max-order increases. Bottom panel: Error estimates of inchworm data obtained by averaging eight independent calculations. Errors increase as a function of time but avoid the exponential amplification seen in bare calculations.

Fig. 4.7 shows results for the time dependence of a current passing through the impurity

after a voltage quench from a thermalized equilibrium state. Parameters are $\Gamma = 1$, $U = 4$, $\epsilon_d = -2$, $D = 5$, $T = 1$ and $V = 4$. In the top panel, we observe that both NCA and OCA produce qualitatively wrong results for both the transient and long-time response. In contrast, inchworm results at orders 5–7 are in excellent agreement with each other, and order 4 is within about a percent from the converged result. Convergence at order 5 is well within reach of inchworm calculations but far beyond what could be realistically treated with semi-analytical methods. The bottom panel shows a rough estimate of the statistical error of the data shown in the top panel, obtained from the standard deviation of eight independent simulations of this problem. As observed for the densities, the inchworm error grows sub-exponentially in time and order constraint, indicating that the algorithm is able to overcome the dynamical sign problem.

Green's function

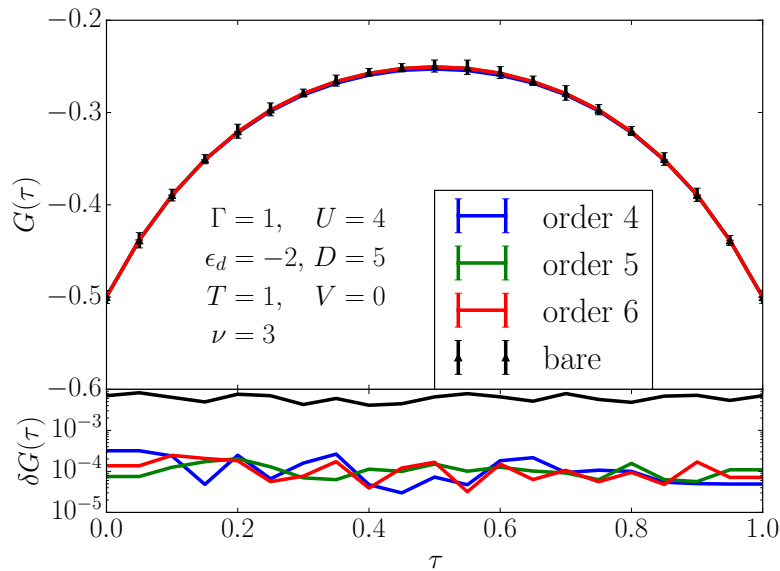


Figure 4.8: Top panel: The imaginary time Green's function in equilibrium (half-filling) with $\Gamma = 1$, $U = 4$, $\epsilon_d = -2$, $D = 5$, $T = 1$ and $V = 0$. Inchworm results with different orders all coincide and agree with the bare calculation. Bottom panel: The error estimate for the inchworm data is approximately constant in imaginary time.

Simulation of diagrams as shown in Fig. 3.19 enable both the simulation of currents and of two-time Green's functions. On the full Keldysh contour, a total of nine different types of Green's functions exist. One of them, the imaginary time Green's function, is

shown in Fig. 4.8. The parameters used are $\Gamma = 1$, $U = 4$ and $\epsilon_d = -2$ (such that the system is at half filling), $D = 5$, $T = 1$, and $V = 0$.

As is visible in the upper panel, orders 4, 5, and 6 agree perfectly within error bars with the result obtained by a bare reference hybridization expansion calculation. Statistical error bars, which do not estimate the systematic errors caused by the order truncation, are shown in the lower panel of Fig. 4.8. These errors are on the order of 10^{-4} . The remaining components of the Green's function are similarly obtained by simulating the diagrams of Fig. 3.19.

Steady state spectral function

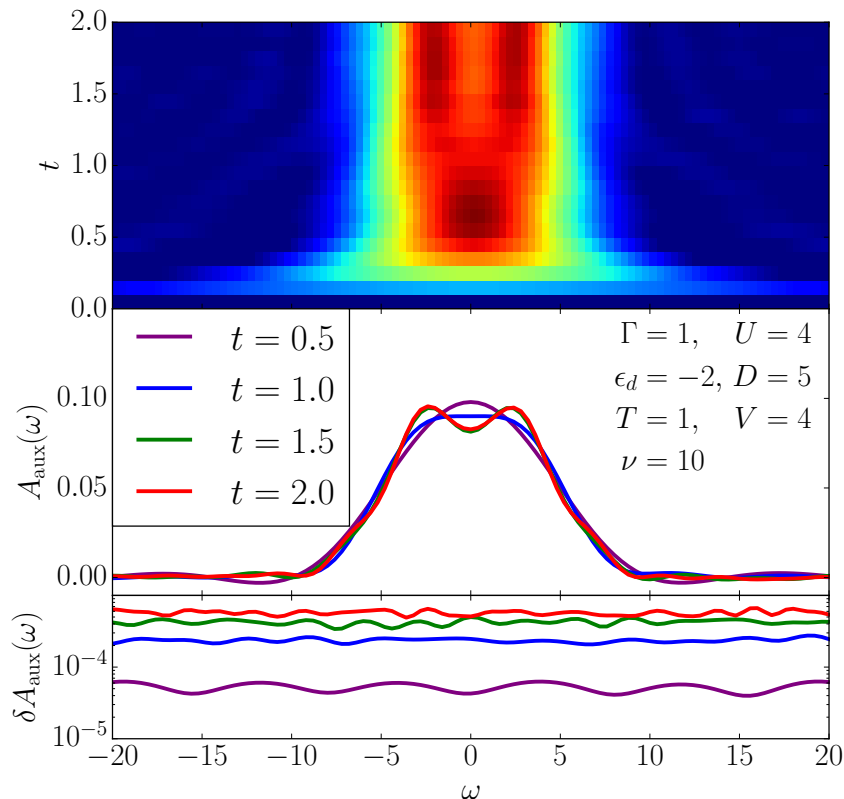


Figure 4.9: Top panel: A contour plot of the dynamics of auxiliary current spectrum $A_{\text{aux}}(\omega, t)$ after a voltage quench with $\Gamma = 1$, $U = 4$, $\epsilon_d = -2$, $D = 5$, $T = 1$ and $V = 4$. The maximum order cut-off for the inchworm calculation is 6. A formation and a splitting of the Kondo peak are observed as a function of time. Middle panel: Slices of auxiliary current spectrum at different times from the top contour plot. A clear splitting of the spectrum is shown. Bottom panel: Error estimate on the spectral function obtained from eight independent simulations.

Knowledge of Green’s functions and currents makes the calculation of interacting single-particle spectral functions possible. Ref. [77] introduced a method for computing steady state spectral functions $A(\omega)$ by obtaining steady state currents in two narrow auxiliary leads coupled at frequency ω . Fig. 4.9 shows the result in the spirit of the auxiliary lead scheme, but generalized to the full Keldysh contour: initially, at $t = 0$, no current is flowing. As the voltage in the main leads, along with the auxiliary lead voltage, is instantaneously switched on, an auxiliary current starts flowing and relaxes on a time scale of about 1.5 to 2.

The upper panel shows the time-evolution of this current as a false-color contour plot. The vertical axis is time, the horizontal axis is frequency and the color represents the value of the auxiliary spectral function $A(\omega)$ obtained from the auxiliary currents. This quantity is equivalent to the physical spectral function at the long time limit. The middle panel shows frequency cuts through these data, illustrating a buildup of a more-or-less featureless spectral function at intermediate times ($t = 0.5, t = 1.0$), which splits into two sub-peaks (associated with the onset of Kondo physics[47, 93]) as time is extended towards time $t = 1.5$ and 2.0. By time $t = 1.5$, all features are converged.

In this parameter regime, both the final steady state spectral function and the time-scale on which results converge are comparable after a quench from an equilibrium thermal state and after a quench from a decoupled initial state[47, 77], illustrating that in this case the presence of equilibrium correlations in the initial state did not substantially accelerate convergence.

The bottom panel shows the statistical errors of these data, obtained by computing the standard deviation of numerical data from several independent calculations. It is clearly visible that as t is increased, errors increase. However, the errors do not increase exponentially, again hinting that the dynamical sign problem has been overcome.

Fig. 4.10 shows the convergence of the data shown at the final time $t = 2.0$ in Fig. 4.9 as a function of the maximum diagram order sampled. It is evident that high orders $\gtrsim 5$ are needed to accurately capture the split peak, hinting that its correct description is related to strong dot–bath entanglement. It is also evident that deviations remain between orders 5 and 6, indicating that even higher orders may be necessary to fully capture the physics.

This is even more pronounced in the equilibrium case, Fig. 4.11, where contributions coming from long-lived correlations cause both an increase of the statistical errors (bottom panel) and a substantial difference order-by-order (main panel).

No additional complications arise away from half filling. Fig. 4.12 shows a sample

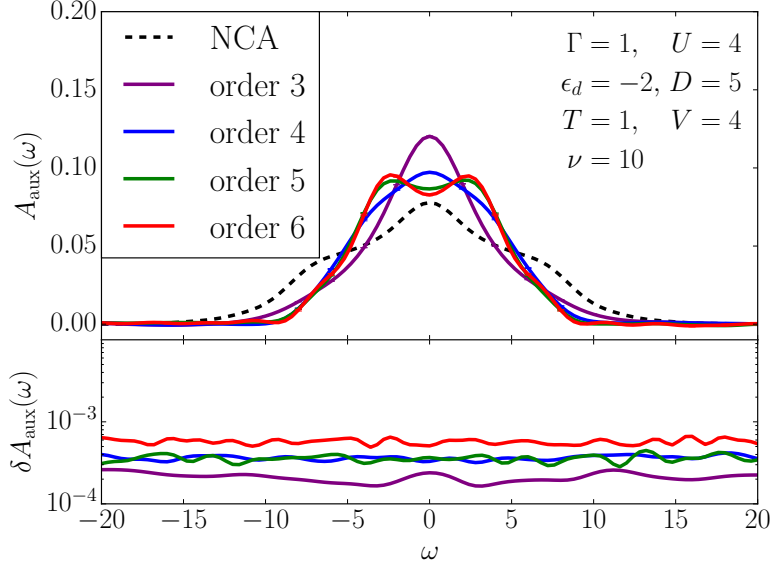


Figure 4.10: Top panel: The (half-filling) spectrum at $t = 2.0$ after a voltage quench with $\Gamma = 1$, $U = 4$, $\epsilon_d = -2$, $D = 5$, $T = 1$ and $V = 4$. The spectral function shows the establishment of a split Kondo peak as the diagram order is increased. The data for order 6 is identical to the data shown in Fig. 4.9. Bottom panel: Error estimate for data shown in main panel. The error remains constant as a function of frequency and increases as the maximum order is increased.

steady state spectral function of a system obtained at time $t = 2.0$, away from particle-hole symmetry, after a voltage quench. The result is once again obtained with the auxiliary current setup, and is converged both in expansion order (orders 5 and 6 were needed) and time. While general features of the system are visible even within a low-order NCA approximation, finer details such as the precise location of the peaks or their height and width clearly require analysis with more precise methods.

4.4 Conclusion

In conclusion, we have demonstrated the inchworm quantum Monte Carlo method for a simple benchmark calculation. The method is numerically exact when all diagrams to all orders are considered. It is controlled if a sequence of results truncated to gradually increasing diagram orders is considered, and in particular generates non-crossing diagrams when truncated to order one, one-crossing diagrams when truncated to order two, and two-crossing diagrams when truncated to order three. We showed that for the applications considered in this chapter, diagrams of order five to seven were sufficient to achieve

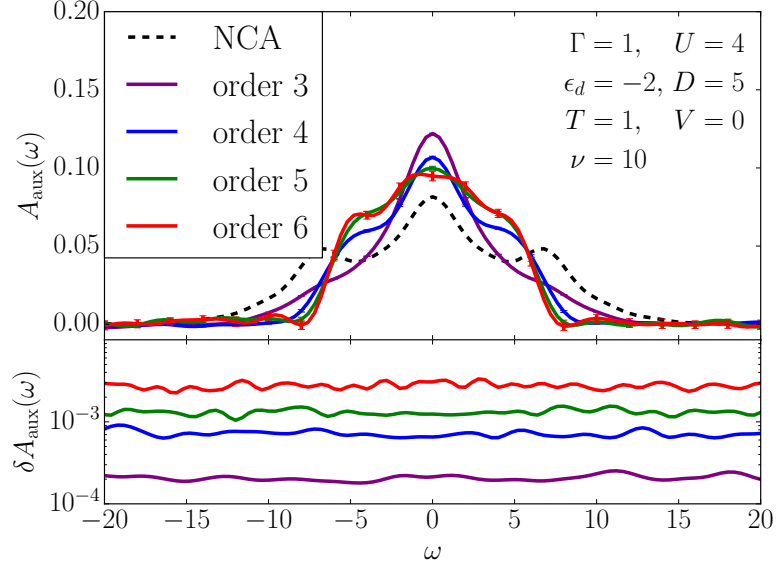


Figure 4.11: Top panel: The (half-filling) spectrum at $t = 2.0$ with no applied voltage with $\Gamma = 1, U = 4, \epsilon_d = -2, D = 5, T = 1$ and $V = 0$. Bottom panel: error estimate for data shown in the main panel.

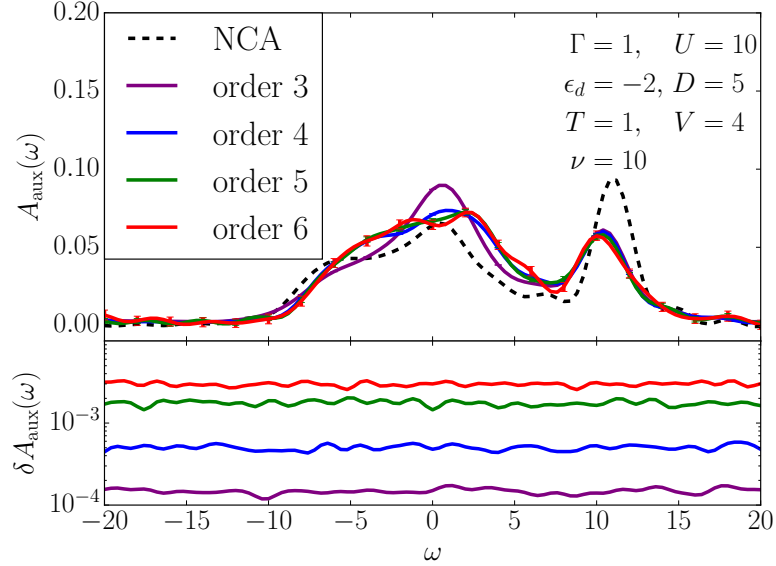


Figure 4.12: Top panel: Spectral function away from half filling at $t = 2.0$ after a voltage quench with $\Gamma = 1, U = 10, \epsilon_d = -2, D = 5, T = 1$ and $V = 4$. Bottom panel: error estimate for data shown in the main panel.

convergence.

The method makes the simulation of a wide range of problem setups possible: voltage and interaction quenches out of initially thermalized states, perturbations with explicit time-dependence, long-time steady-state setups, and equilibrium problems. It can in particular be used for obtaining spectral functions in real time, eliminating the need for the numerically ill-conditioned analytical continuation procedure of imaginary time data.

Inchworm Monte Carlo overcomes the dynamical sign problem in the sense that as t is increased, the effort for reaching longer times increases sub-exponentially. Unlike in the case of the forward–backward contour, we did not always observe a plateau of the error as a function of time, indicating that the scaling is generally worse than quadratic in time. Several exponential barriers remain in the system: as temperature is lowered, higher orders proliferate and the number of diagrams needed to be considered increases quickly. Similarly, a larger impurity size exponentially increases the size of the local Hilbert space and thereby the cost of simulating the system.

The results shown here illustrate that it is now possible to calculate reliable currents, Green’s functions, and spectral functions for equilibrium and nonequilibrium impurity problems with general time dependence, and imply that unbiased impurity solvers, which form a fundamental component for non-equilibrium dynamical mean field theory, are now available.

CHAPTER V

Kondo Voltage Splitting

5.1 Introduction

Interacting quantum many-body systems often exhibit highly entangled states that cannot be described within an independent particle formalism. The Kondo effect in a quantum dot [14, 94] coupled to noninteracting leads is the paradigmatic example for such a state, as the dot electrons hybridize with the leads to form a highly correlated Kondo singlet state [95]. This state manifests itself as a sharp peak in the local density of states [94, 96]. The establishment of Kondo correlations can be examined in a quantum quench scenario, where an initially uncorrelated state slowly develops a coherence peak over time [74, 97].

In the presence of a voltage, the Kondo peak is strongly suppressed and splits into two smaller peaks [77, 93, 98–100]. Previous work has argued that the peak-to-peak distance is given by the voltage [101–106] and that the split state is significantly less correlated than the equilibrium state [101]. It is therefore natural to examine the establishment of splitting after a quench from an initially uncorrelated state, and to expect that this less correlated state forms on a timescale shorter than that of the equilibrium state.

Despite significant analytical progress [107–113], an accurate investigation of this scenario requires numerical methods that are able to simulate the real-time evolution after a quench accurately, for times long enough to reach the steady state. Additionally, a full account of the continuous lead spectrum is crucial for correct treatment of the nonequilibrium steady state. The major families of numerical methods include the noncrossing approximation and its higher-order generalizations [53], wave-function-based methods [114–119], real-time path integral techniques [120–123], the time-dependent numerical renormalization group [124–128], hierarchical equations of motion [129–132], the auxiliary master equation approach [133–137], and a wide variety of quantum Monte Carlo methods [47, 49–51, 75, 76, 83, 84, 138–146]. Most of these approaches fall short in at least one of the aforementioned requirements. This situation has changed with the development

of the numerically exact inchworm quantum Monte Carlo method [31, 55, 78, 79, 81, 82] that in many cases eliminates the dynamical sign problem and is thereby able to reach the relevant timescales.

In this chapter, we examine the voltage splitting of the Kondo peak in detail. We focus on the time-dependent formation of the peak after a quantum quench and on its shape at long times. We find that while the peak-to-peak distance is roughly proportional to the voltage, there is a notable deviation from this simple picture. We also find that the appearance of the split peak is preceded by the formation of a single, unsplit Kondo peak, and that the splitting occurs at a later time whose scaling with the voltage is consistent with a power law. Since the splitting timescale is 1–10 ps in mesoscopic quantum dots, the delayed splitting should be observable in recently developed ultrafast tunneling microscopy [147, 148] and spectroscopy [21, 149] experiments.

5.2 Model

We describe a correlated quantum dot (QD) attached to two extended metallic leads using a single impurity Anderson model [4],

$$\hat{H} = \hat{H}_D + \sum_{\alpha=\pm 1} \hat{H}_\alpha + \hat{H}_T, \quad (5.1a)$$

$$\hat{H}_D = \sum_{\sigma} \varepsilon_d n_{\sigma} + U n_{\uparrow} n_{\downarrow}, \quad (5.1b)$$

$$\hat{H}_\alpha = \sum_{k\sigma} \left(\varepsilon_k + \frac{\alpha V}{2} \right) n_{\alpha k \sigma}, \quad (5.1c)$$

$$\hat{H}_T = \sum_{\alpha k \sigma} \mathcal{V}_k^\alpha(t) (c_{\alpha k \sigma}^\dagger d_{\sigma} + d_{\sigma}^\dagger c_{\alpha k \sigma}). \quad (5.1d)$$

The quantum dot \hat{H}_D is coupled to two noninteracting leads \hat{H}_α by tunneling terms \hat{H}_T . The operators d_{σ}^\dagger (d_{σ}) create (annihilate) electrons localized on the quantum dot, while $c_{\alpha k \sigma}^\dagger$ ($c_{\alpha k \sigma}$) create (annihilate) electrons in lead α [$\alpha = \pm 1$ labels the left (+) and right (−) lead] with quasimomentum k and spin σ (\uparrow or \downarrow). The respective occupation number operators are $n_{\sigma} = d_{\sigma}^\dagger d_{\sigma}$ and $n_{\alpha k \sigma} = c_{\alpha k \sigma}^\dagger c_{\alpha k \sigma}$. The dot Hilbert space is spanned by four “atomic states” $|\phi\rangle = |0\rangle, |\uparrow\rangle, |\downarrow\rangle, |\uparrow\downarrow\rangle$. We consider the symmetric situation $\varepsilon_d = -U/2$ such that every energy level of the dot Hamiltonian \hat{H}_D is doubly degenerate ($E_0 = E_{\uparrow\downarrow} = 0$, $E_{\uparrow} = E_{\downarrow} = -U/2$). \mathcal{V}_k^α denotes the tunneling matrix element describing hopping processes between the dot and the leads. The coupling to the leads is characterized by a coupling density $\Gamma_\alpha(\omega) = \pi \sum_k |\mathcal{V}_k^\alpha|^2 \delta(\omega - \varepsilon_k)$ that parametrizes the lead dispersion ε_k and the

tunneling elements. We consider a wide, flat coupling density with soft edges for both leads, $\Gamma_\alpha(\omega) = (\Gamma/2)/[(1 + e^{\nu(\omega-D)})(1 + e^{-\nu(\omega+D)})]$ (the soft edges eliminate unphysical transient oscillations in the dynamics [141]), choosing the inverse cutoff width $\nu = 10\Gamma^{-1}$ and the half-bandwidth $D = 10\Gamma$ such that the band edge exceeds all other relevant energy scales. Γ is used as the energy unit. Experimental values for Γ in semiconductor QDs are of the order of 1 meV [14, 94]. We consider a setup where the dot is initially empty (in the pure $|0\rangle$ state) and detached from the leads. The leads are suddenly attached at $t = 0$ ($\mathcal{V}_k^\alpha(t) = \mathcal{V}\theta(t)$), and are kept at a constant temperature T with a symmetric bias voltage V between them. This quench protocol is equivalent to suddenly changing a gate voltage from a value substantially larger than half the bias voltage to zero at $t = 0$. At zero bias, the Kondo temperature for this model is $T_K \simeq \sqrt{\Gamma U/2} \exp[-\pi U/(8\Gamma) + \pi\Gamma/(2U)]$ [95, 150].

5.3 Methods

The numerical methods we use in this Rapid Communication are based on a diagrammatic expansion in the tunneling Hamiltonian \hat{H}_T formulated on the two-branch Keldysh contour (the imaginary Matsubara branch is not required due to the factorized initial condition). Our main numerical tool is a massively parallel implementation of the inchworm quantum Monte Carlo solver [78, 79] based on the High Performance ParalleX framework [91] and the ALPS libraries [151, 152]. The inchworm solver performs a stochastic summation of the hybridization contributions to the dressed QD propagators $p_\phi(t, t') = \langle \phi | \text{Tr}_c[\hat{\rho} e^{-i \int_{t'}^t d\bar{t} \hat{H}(\bar{t})}] | \phi \rangle$. The calculations are organized to take advantage of the contour-causal structure of $p_\phi(t, t')$ so that short time propagators are incrementally extended to longer times, significantly alleviating the dynamical sign problem [31, 79]. After all dressed propagators are computed, the stochastic summation procedure proposed in [31] is employed to calculate the QD Green's function. Because the inchworm method recurrently couples together the output of many stochastic simulations, the analysis of the Monte Carlo error is not straightforward. One useful approach is considering deviations from exactly conserved properties like the total probability of all QD states or the normalization of the steady-state spectral function, neither of which varies by more than a few percent in our simulations. Using the inchworm method we obtained numerically exact results for times as long as $8.0\Gamma^{-1}$, but required significant computational resources to do so. In order to investigate longer times, we also make use of the computationally less demanding one crossing approximation (OCA) [53, 54] which we validate against numerically exact inchworm results at our smallest considered

interaction strength $U = 8.0\Gamma$ where OCA is expected to be the least accurate. We find that while details of the spectral function are rather sensitive to this approximation (see section 5.6 for a comparison), it is accurate to within $\lesssim 10\%$ for the other observables considered here.

The main physical quantity of interest to us is the time-dependent QD spectral function. We use the auxiliary current formalism [46, 47] to write this as

$$A(\omega, t) = \lim_{\eta \rightarrow 0} -\frac{2\hbar}{e\pi\eta} [I_A^f(\omega, t) - I_A^e(\omega, t)], \quad (5.2)$$

where $I_A^f(\omega, t)$ and $I_A^e(\omega, t)$ are currents through two additional auxiliary leads weakly coupled to the QD at frequency ω by a coupling density $\Gamma_A(\omega') = \eta\delta(\omega' - \omega)$, and with chemical potentials set such that the leads are full and empty, respectively. $A(\omega, t)$ approaches the conventional spectral function $A(\omega) = -(1/\pi)\text{Im}G^r(\omega)$ at steady state and provides rich spectral information at all times. It is related to a finite-time Fourier transform, but also has a direct operational realization [46–48, 77]. We have direct access to the QD Green's function $G_\sigma(t, t') = -i\langle T_C d_\sigma(t) d_\sigma^\dagger(t') \rangle$ [31], such that auxiliary currents are calculated using the Meir-Wingreen formula [153, 154] $I_A^{f(e)}(\omega, t) = -2\text{Re} \left\{ \int_C dt' G_\sigma(t', t) \Delta_A^{f(e)}(t, t') \right\}$. Here, the hybridization functions $\Delta_A^{f(e)}(t, t')$ are derived from $\Gamma_A(\omega)$ using the procedures established in Ref. [31].

5.4 Results

In Fig. 5.1, we present the time evolution of the (auxiliary) QD spectral function after a coupling quench. The time-dependent spectra are shown at four values of the bias voltage, $V = 0.5\Gamma, 1.2\Gamma, 1.8\Gamma$, and 3.5Γ . The interaction strength U is 8.0Γ , such that $T_K \approx 0.11\Gamma$ [95]. The lead temperature is set to $T = 0.02\Gamma \ll T_K$, placing the system deep in the Kondo regime at zero bias. This temperature was inaccessible in the earlier bold-line hybridization expansion QMC study [77], where only the edge of the Kondo regime $T \gtrsim T_K$ was reached at a weaker interaction strength $U = 6\Gamma$.

For $V \lesssim 2.0\Gamma$, we observe the formation of a single peak at the mean chemical potential. For $V \gtrsim 1.0\Gamma$, this peak first forms, then splits into two secondary peaks near the two lead chemical potentials. At larger $V \gtrsim 2.0\Gamma$, the initial single-peak state is no longer visible. Instead, the split peaks appear immediately after the transient charging dynamics visible at short times.

The overall behavior of the system can be characterized by two quantities: the time

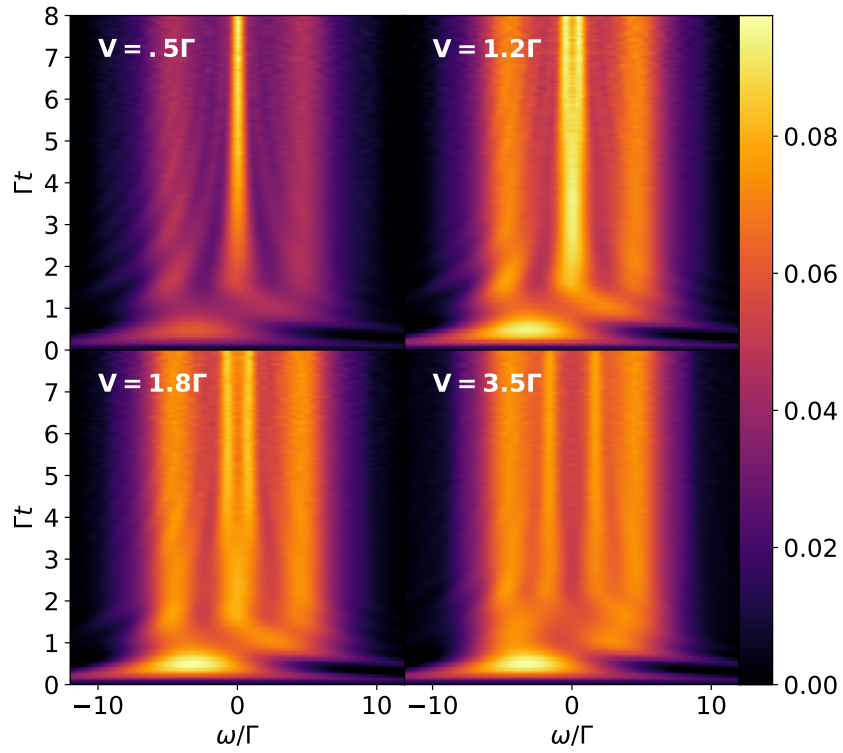


Figure 5.1: Time evolution of the QD spectral function after a coupling quench and in the presence of a bias voltage V , at interaction strength $U = 8.0\Gamma$ and temperature $T = 0.02\Gamma \ll T_K$. The voltages are $V = 0.5\Gamma$ (upper left), $V = 1.2\Gamma$ (upper right), $V = 1.8\Gamma$ (lower left), and $V = 3.5\Gamma$ (lower right).

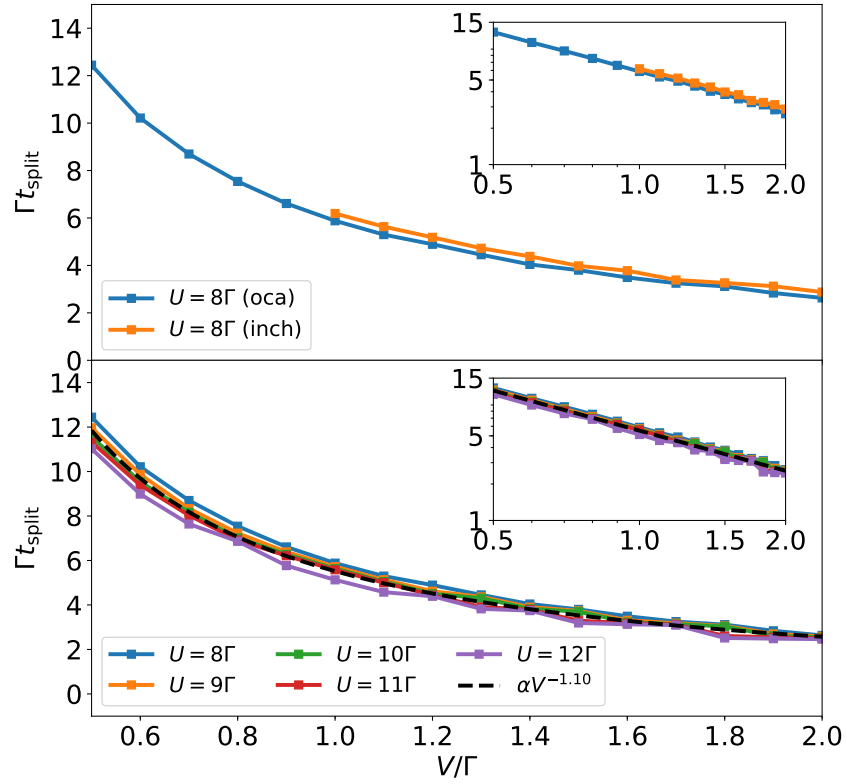


Figure 5.2: Splitting time t_{split} where a single peak splits into two peaks as a function of V at $T = 0.02\Gamma$. Upper panel: inchworm and OCA results at $U = 8.0\Gamma$. Lower panel: OCA results for several U . Insets show the same data on a log-log scale demonstrating power-law behavior.

t_{split} at which the peak splits, and the peak-to-peak separation $\Delta\omega$ of the resulting split peaks in steady state. We first show how t_{split} evolves as a function of the bias voltage V at $T = 0.02\Gamma$. t_{split} is calculated as the first time point where the second derivative $\partial_{\omega}^2 A(\omega, t)|_{\omega=0}$ changes its sign, i.e. where the zero-frequency peak becomes a dip. As seen in the upper panel of Fig. 5.2, the OCA is qualitatively consistent with inchworm regarding the functional form of $t_{\text{split}}(V)$. A log-log plot (inset) reveals that within the voltage range shown both results are consistent with power-law behavior, which from the slope must obey $t_{\text{split}}(V) \propto (V/\Gamma)^{-1.10}$. OCA results for a set of larger interaction strengths (lower panel of Fig. 5.2) provide evidence that this behavior is largely independent of U . It is worth noting that the transient state manifested by the single peak is significantly less correlated than the equilibrium Kondo singlet at $V = 0$. One can indirectly assess the strength of correlations by fitting the transient spectra with the equilibrium ones obtained for an effective temperature $T_{\text{eff}}^{\text{tr}}$. Similarly, the steady-state spectra $A(\omega, V, T)$ can be qualitatively fitted with $[A(\omega + V/2, 0, T_{\text{eff}}^{\text{st}}) + A(\omega - V/2, 0, T_{\text{eff}}^{\text{st}})]/2$ (superposition of contributions from two Kondo states with different chemical potentials and effective temperature $T_{\text{eff}}^{\text{st}}$) (see figures 5.7 and 5.8). It turns out that the effective temperature, serving as a measure of correlations, satisfies $T_{\text{eff}}^{\text{tr}} \gg T_{\text{eff}}^{\text{st}} \gtrsim T_K \gg T$.

An analysis at $T > T_K$ shows that the initial single-peak state is not present for $T > T_K$. Instead, the voltage-split peaks are formed directly after the initial equilibration (see Fig. 5.5).

Our results suggest that the time-dependent formation of the spectrum evolves in two stages. First, on a very fast timescale, a mixed Kondo singlet is formed between the QD and an effective chemical potential set by those of both leads. Later, on a slower timescale $t = t_{\text{split}}$, this singlet state is destroyed by the current and replaced with a new state that couples to each of the two leads at a frequency comparable to its chemical potential.

So far, we have focused on the dynamics leading up to the formation of a steady state. We now shift to a discussion of the frequency-dependent spectral properties of the steady state itself. Figure 5.3 provides a detailed view of $A(\omega, t_{\text{max}})$, which gives an estimate of the steady-state spectra for $V \geq 1.0\Gamma$ both below (upper panel) and above (lower panel) the Kondo temperature at $U = 8.0\Gamma$. At low temperature ($T = 0.02\Gamma < T_K$) and intermediate bias voltage ($1.0\Gamma \leq V \leq 2.0\Gamma$) the split Kondo peaks and the Hubbard bands together form a clearly distinguishable four-peak structure, confirming previous approximate results that suggested its existence [134, 155] (see also very recent results where partial splitting is visible in Ref. [156]). An increase in V enhances peak-to-peak separation $\Delta\omega$ and suppresses peak height [101]. In contrast, the side bands are largely

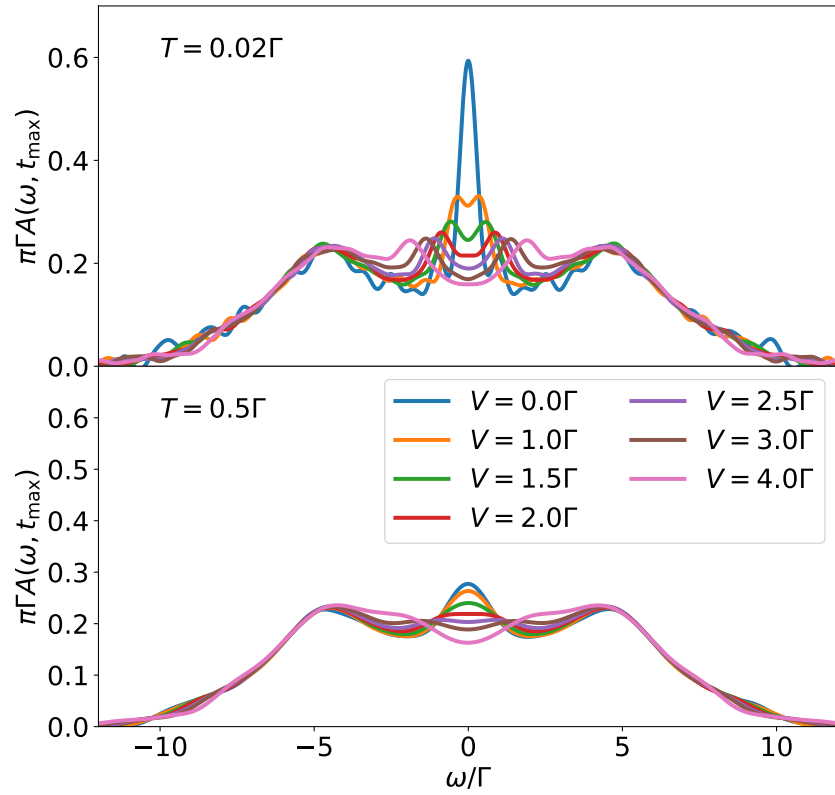


Figure 5.3: QD spectral function from the inchworm method at $t = t_{\max} = 8.0\Gamma^{-1}$, corresponding to the steady-state spectrum $A(\omega)$ for $V \geq 1.0\Gamma$. $T = 0.02\Gamma$ (upper panel) and $T = 0.5\Gamma$ (lower panel) for the voltages indicated.

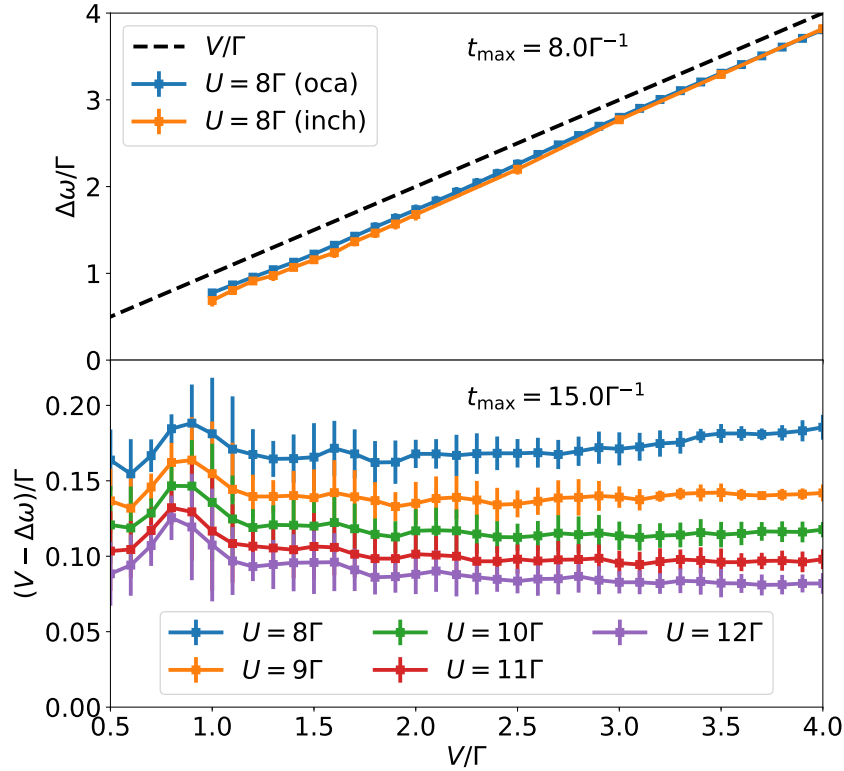


Figure 5.4: Peak-to-peak distance $\Delta\omega$ between the split Kondo peaks as a function of bias voltage V , at $T = 0.02\Gamma < T_K$. Error bars originate from averaging over finite-time oscillations expected to eventually dissipate. Upper panel: inchworm and OCA results at $U = 8.0\Gamma$ with $t_{\max} = 8.0\Gamma^{-1}$ compared with the linear behavior $\Delta\omega = V$ predicted by various approximate methods. Lower panel: Deviation of splitting from V within OCA at $T = 0.02\Gamma$ for several values U , with $t_{\max} = 15.0\Gamma^{-1}$.

insensitive to changes in V in this regime. (The small rapid oscillations seen at $V = 0$ are remnants of the initial condition that have not fully dissipated.) At high temperature ($T = 0.5\Gamma > T_K$), some remnants of the four-peak structure can be seen between $V = 2.5\Gamma$ and $V = 3.0\Gamma$. However, these features are much less pronounced.

In Fig. 5.4, we present the peak-to-peak distance $\Delta\omega$ at steady state as a function of the applied bias voltage V . Parameters match the respective panels in Fig. 5.2. We estimate the steady-state value from propagation to a finite time. Although the large-scale features of the spectrum have reached steady state by our maximal propagation time, there remain small finite-time oscillations that are expected to eventually dissipate. The error bars in this figure therefore come from averaging $\Delta\omega$ over the time window in which splitting is visible. As seen in the upper panel of Fig. 5.4, $\Delta\omega$ is systematically below the linear $\Delta\omega = V$ law predicted by perturbation theory, renormalization group, and flow

equation studies of the Anderson model [102] and the effective s - d (Kondo) model [101, 103]. We reiterate that the inchworm results presented here are numerically exact, whereas the various approximate approaches are, e.g., perturbative in U or assume a $U \rightarrow \infty$ limit where charge fluctuations on the QD are suppressed. We expect our prediction to be experimentally verifiable using steady-state multiprobe schemes [46, 48].

If we acknowledge that the trend evident in Fig. 5.2 may continue to smaller bias voltages $V < 1.0\Gamma$, it is clear that no conclusion about the presence of splitting can be drawn from the inchworm results at lower voltages because t_{split} can exceed t_{max} . We employ OCA in order to reach longer times $t_{\text{max}} = 15.0\Gamma^{-1}$ and explore a wider parameter range. The larger t_{max} in these OCA results extends the accessible voltage range down to $V = 0.5\Gamma$, but at the cost of introducing an approximation. To test the quality of this approximation, the upper panel of Fig. 5.4 shows numerically exact inchworm data together with OCA results at $t_{\text{max}} = 8.0\Gamma^{-1}$. The agreement in $\Delta\omega/\Gamma$ between inchworm and OCA is on the order of 10% and improves at larger V , with OCA somewhat underestimating the deviation from linear behavior at smaller V . This observation suggests that electronic correlations beyond those accounted for by the OCA become less important as the bias voltage grows. Together with the diminishing height of the split peaks, this supports the scenario in which the Kondo state is partially destroyed by the current-induced decoherence [101].

The lower panel of Fig. 5.4 shows OCA results for $V - \Delta\omega$ at several larger values U where OCA is expected to be increasingly accurate. These OCA calculations show that $V - \Delta\omega$ becomes smaller with increasing U . This supports the conclusion that deviations from the linear approximation are due to charge fluctuations at finite U .

5.5 Conclusions

We presented a numerically exact treatment of the transient and steady-state dynamics of a quantum dot spectral function after a coupling quench with a bias voltage V applied to the dot, focusing on the Kondo regime.

Our examination of the quench dynamics revealed transient dynamical states in which the formation of a single Kondo peak at the average chemical potential is followed by a sudden splitting at a timescale t_{split} . t_{split} exhibits a robust power-law dependence on the voltage. In the case of realistic molecular electronic devices $\Gamma \approx 100$ meV. At a voltage of ~ 50 meV our predicted timescale approaches $t_{\text{split}} \sim 10^{-1}$ ps, but if the power law holds at lower voltages, at a voltage of ~ 5 meV we expect $t_{\text{split}} \sim 1$ ps, which is already

experimentally accessible. Furthermore, in semiconductor quantum dot experiments Γ is orders of magnitude smaller, e.g. 0.1 – 1.0 meV according to Refs. [14] and [94]. A typical high-voltage $t_{\text{split}} = 5\Gamma^{-1}$ would then correspond to $\sim 3\text{--}30$ ps. These predictions concern the transient dynamics of the time-dependent spectral density. Although measuring it is still challenging, recent experimental progress [21, 147, 149] may put it within reach. One possible direction is to extract the time dependent current from DC measurements with pulse trains as suggested by Ref. [149] in a three-terminal setup.

For voltages significantly exceeding the Kondo temperature, we presented numerically exact results for steady-state spectral functions exhibiting a well pronounced four-peak structure. The position and shape of the side bands are unaffected by the bias voltage V , while the distance $\Delta\omega$ between the split Kondo peaks is roughly proportional to V but systematically falls below the previously proposed $\Delta\omega = V$ behavior. This effect weakens at large U , and we therefore surmise that it is related to charge fluctuations that are energetically forbidden when U becomes very large. These predictions could be verified using three-terminal steady-state measurements as discussed in Refs. [46] and [48].

Our application of the inchworm method to exploring nonequilibrium Kondo physics after a quench elucidates the dynamical formation of Kondo splitting, and provides experimentally relevant predictions thereof. Looking forward, this work points the way towards answering a variety of long-standing questions, such as whether further splitting should be expected when a magnetic field is present; how correlations form in the leads; and how local symmetries affect the Kondo coupling far from equilibrium. Another interesting direction is application of the inchworm QMC to direct modeling of response to realistic short pump pulses, as used in pump-probe experiments.

5.6 Appendix

Time evolution of QD spectra above T_K

Fig. 5.5 is the above- T_K counterpart of Fig. 5.1. It shows the time evolution of the QD spectra for $U = 8.0\Gamma$, $T = 0.5\Gamma$ and $V = 0.5\Gamma, 1.5\Gamma, 2.5\Gamma$ and 3.0Γ . The $V = 2.5\Gamma$ and $V = 3.0\Gamma$ spectra feature a faint four-peak structure that emerges immediately after the quench. No single Kondo peak is visible. This observation supports the connection between the Kondo singlet state below T_K in equilibrium and the finite t_{split} .

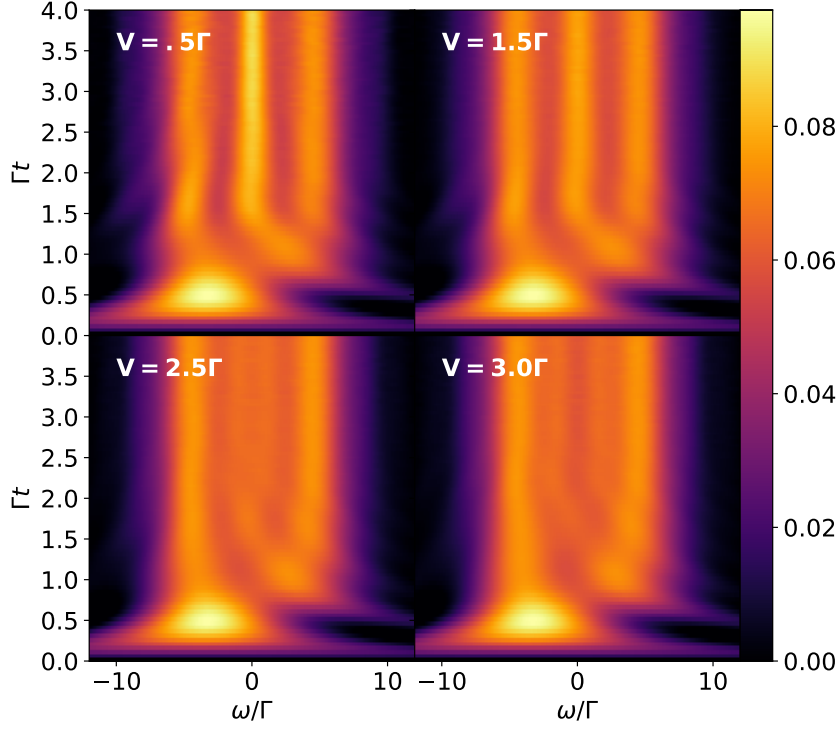


Figure 5.5: Time evolution of the QD spectra $A(\omega, t)$ of the quantum dot for $U = 8\Gamma, T = 0.5\Gamma$. $V = 0.5\Gamma$ (upper left), $V = 1.5\Gamma$ (upper right), $V = 2.5\Gamma$ (lower left), $V = 3.0\Gamma$ (lower right).

Comparison of OCA and inchworm spectral functions at $t = 8\Gamma^{-1}$

Fig. 5.6 shows a comparison between inchworm results and the OCA approximation. Data is obtained for the parameters indicated, at a maximum time of $t = 8.0\Gamma^{-1}$. It is evident, especially at low voltages, that the OCA approximation to the spectrum is severe. However, for the features analyzed in this chapter, *i.e.* the splitting time and the peak-to-peak distance of the steady state split peak, OCA and inchworm data is compatible.

Fits of $A(\omega, t)$ with equilibrium OCA spectra

We performed a series of OCA calculations in absence of bias and with other Hamiltonian parameters set to the values used in the main text. A temperature sweep showed that the spectral function in the initially formed single peak state ($T = 0.02\Gamma$) can be reasonably well approximated with the equilibrium spectrum at an efficient temperature $T_{\text{eff}}^{\text{tr}}$ (Fig. 5.7). For both studied voltages where the transient state is observed, we find $T_{\text{eff}}^{\text{tr}}$ strongly exceeding $T_K = 0.11\Gamma$ ($T_{\text{eff}}^{\text{tr}} \approx 0.34\Gamma$ and 0.53Γ for $V = 1.2$ and 1.8 respectively).

The double peak spectral structure cannot be described by an equilibrium system

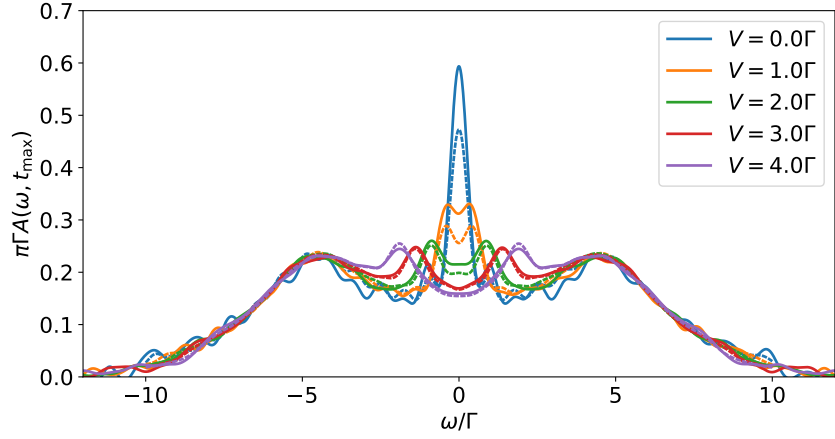


Figure 5.6: Comparison of inchworm (solid) with OCA (dashed) QD spectral functions at $U = 8.0\Gamma$, $T = 0.02\Gamma$ for voltages indicated.

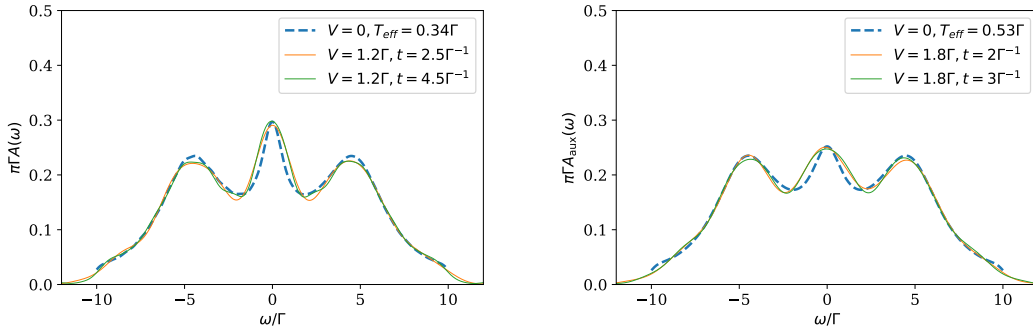


Figure 5.7: Transient spectral functions at two values of the bias voltage $V = 1.2\Gamma$ and $V = 1.8\Gamma$ corresponding to two panels in Fig. 5.1. The bold lines show spectra at two times when the “unsplit” transient phase is observed. The dashed line is the steady state solution computed with OCA at the effective temperature $T_{\text{eff}}^{\text{tr}}$ that delivers a good fit to the transient spectra.

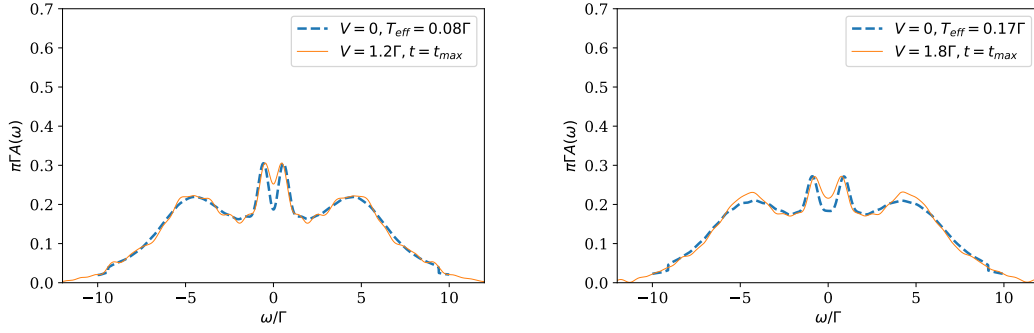


Figure 5.8: Bold lines: Steady state spectral functions at two values of the bias voltage $V = 1.2\Gamma$ and $V = 1.8\Gamma$ corresponding to two panels in Fig. 5.1. Dashed line: fitting curve computed as $[A(\omega + V/2, T_{\text{eff}}^{\text{st}}) + A(\omega - V/2, T_{\text{eff}}^{\text{st}})]/2$, where $A(\omega, T_{\text{eff}}^{\text{st}})$ is OCA equilibrium spectrum at effective temperature $T_{\text{eff}}^{\text{st}}$.

with an effective temperature. However, it can be roughly approximated by a sum of two equilibrium systems with an effective temperature and chemical potentials set to $\pm V/2$: $A(\omega, V, T) \approx [A(\omega + V/2, 0, T_{\text{eff}}^{\text{st}}) + A(\omega - V/2, 0, T_{\text{eff}}^{\text{st}})]/2$ (Fig. 5.8). OCA calculations reveal that the effective temperature necessary to fit the steady state spectra is much lower than that used to fit the transient state. For both considered voltages $T_{\text{eff}}^{\text{st}}$ is comparable to the Kondo temperature.

CHAPTER VI

Kondo Cloud

6.1 Introduction

The Kondo effect is characterized by the screening of an impurity spin by a cloud of conduction electrons to form a singlet state at temperatures below the Kondo temperature T_K [95]. The equilibrium physics of the impurity spin are by now well understood, but the structure of the Kondo cloud has remained elusive [157].

The Kondo cloud can be defined in a number of ways. Theoretically, the most natural definition is in terms of the impurity-spin bath-spin correlation function which can be readily computed using a variety of techniques including NRG [158, 159] and DMRG [160]. Although theoretically convenient, this correlation function is not directly observable. The Kondo cloud is theoretically observable by its effect on the magnetic susceptibility, but attempts to observe this via NMR have so far been unsuccessful [161]. There have been a number of theoretical [162–166] and experimental [18, 19, 167] efforts to characterize the Kondo cloud via its effect on the bath density of states which can be measured experimentally by scanning tunneling spectroscopy (STS). These studies have revealed various signatures of the Kondo cloud, but a complete picture is still missing.

In [168] the authors proposed to study the Kondo cloud by examining the effects of perturbations to the bath on the impurity. Perturbations of bath electrons inside the Kondo cloud should have a large effect on the impurity Kondo resonance whereas perturbations of bath electrons outside the Kondo cloud should have little effect. By varying the distance at which the perturbation is applied it is possible to map out the Kondo cloud. This proposal was recently realized experimentally by measuring the effect of applying electrostatic perturbations to a 1D channel coupled to a quantum dot (QD), and the extent of the Kondo cloud was successfully measured [169].

In this chapter we study a model proposed to describe this experimental setup. We characterize the Kondo cloud in this model in two complementary ways. First, we compute

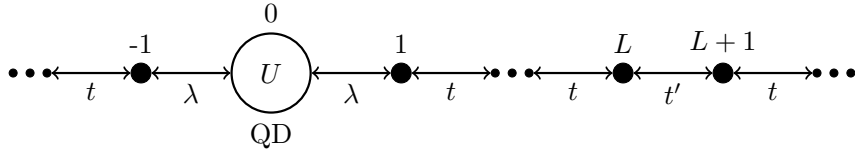


Figure 6.1: Schematic illustration of the model. A quantum dot (QD) is coupled to two non-interacting leads, where each lead is a semi-infinite, one-dimensional tight-binding chain with nearest neighbor hopping t . On the right lead, the hopping between sites L and $L + 1$ is optionally modified to take the value t' . The leads are connected to the QD by a hopping λ . The QD has an on-site local Coulomb interaction U .

the effect of lead perturbations applied a variable distance L away from the impurity on the Kondo resonance width which is related to the Kondo temperature. Our results confirm the general scenario found in [169] in which lead perturbations drive Kondo temperature fluctuations which decay with L . At large interactions, we find a non-monotonic dependence of the Kondo resonance width on L which may be observable in future experiments. Secondly, we compute the lead local density of states (LDOS), observe features associated with the emergence of the Kondo state, and show that these features are suppressed by an applied voltage bias. These results provide a detailed picture of the Kondo cloud in this system which may be observed via future STM experiments.

6.2 Model

We study the model proposed in [169] to describe an experimental setup for observing the Kondo cloud. The model consists of a single orbital quantum dot (QD) coupled to two non-interacting, one-dimensional leads (see Fig. 6.1). The Hamiltonian for the model is

$$H = H_{\text{QD}} + H_l + H_r + H_T, \quad (6.1)$$

where H_{QD} is the quantum dot Hamiltonian, H_l (H_r) is the Hamiltonian of the left (right) lead, and H_T is the tunneling Hamiltonian which describes hopping between the QD and the leads.

The QD Hamiltonian is

$$H_{\text{QD}} = \sum_{\sigma} \epsilon_d n_{\sigma} + U n_{\uparrow} n_{\downarrow}, \quad (6.2)$$

where d_{σ}^{\dagger} (d_{σ}) creates (annihilates) electrons localized on the QD with spin σ , $n_{\sigma} = d_{\sigma}^{\dagger} d_{\sigma}$ is

the QD number operator, ϵ_d is the single-particle energy, and U is the Coulomb interaction between electrons on the QD.

The left lead is modeled as a uniform one-dimensional tight-binding chain with Hamiltonian

$$H_l = - \sum_{\sigma} \sum_{i=1}^{\infty} t c_{l,i,\sigma}^{\dagger} c_{l,(i+1),\sigma} + \text{h.c.}, \quad (6.3)$$

where $c_{l,i,\sigma}^{\dagger}$ ($c_{l,i,\sigma}$) creates (annihilates) electrons on site i of lead l with spin σ , and t is the nearest-neighbor hopping amplitude. The right lead is the same as the left lead except that the hopping between sites L and $L + 1$ is optionally reduced, partially pinching off the lead at site L . The Hamiltonian for the right lead is

$$H_r = - \sum_{\sigma} \left[\sum_{i \neq L} t c_{r,i,\sigma}^{\dagger} c_{r,(i+1),\sigma} + t' c_{r,L,\sigma}^{\dagger} c_{r,(L+1),\sigma} + \text{h.c.} \right], \quad (6.4)$$

where $c_{r,i,\sigma}^{\dagger}$ ($c_{r,i,\sigma}$) creates (annihilates) electrons on site i of lead r with spin σ , and t' is the modified hopping amplitude between sites L and $L + 1$. We specify the strength of the modification in terms of the non-dimensional parameter $\alpha = 1 - (t'/t)^2$ which describes a continuum between no modification ($\alpha = 0$) and completely pinching off the lead at L ($\alpha = 1$). The coupling of the QD to the leads is described by the tunneling Hamiltonian

$$H_T = \sum_{\sigma} \sum_{w=l,r} \lambda_w \left(c_{w,1,\sigma}^{\dagger} d_{\sigma} + \text{h.c.} \right) \quad (6.5)$$

where λ_w is the hopping amplitude between the QD and lead w .

The leads are at half-filling with Fermi wavevector $k_f = \pi/2$ and bulk Fermi velocity $v_f = 2ta/\hbar$ where a is the spacing between the sites which we take as our unit of distance. The dynamics of the leads are described by the non-interacting lead Green's functions which can be formally computed by

$$g_w(\omega) = (\omega I - H_w)^{-1} \quad (6.6)$$

where I is the identity matrix and H_w is the single-particle Hamiltonian for lead w . The calculation of the lead Green's functions is detailed in appendix 6.6.

Because the leads are non-interacting, they can be integrated out exactly to obtain a

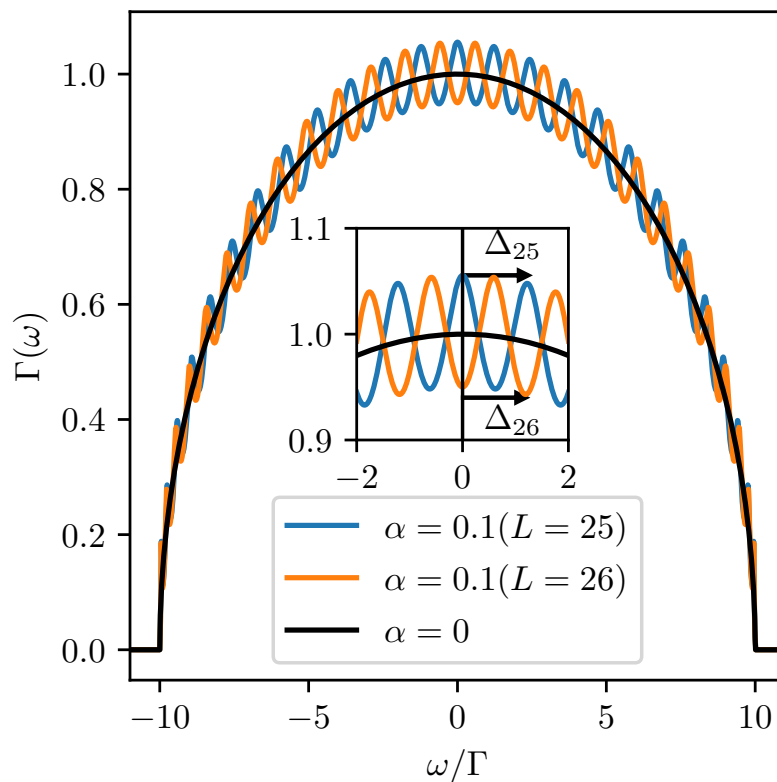


Figure 6.2: Coupling density $\Gamma(\omega)$ for $\alpha = 0$ (black) and $\alpha \neq 0$ for two different cavity lengths L (blue/orange). For $\alpha \neq 0$ the resonance width is given by $\Delta_L = \pi v_f/L$. Inset shows zoom around the Fermi energy illustrating Δ_L .

hybridization function which describes the effect of the leads on the QD by parameterizing both the lead band structure and the tunneling Hamiltonian. The hybridization function is described by the coupling density

$$\Gamma(\omega) = -\text{Im} \sum_{w=l,r} \lambda_w^2 g_{w,11}(\omega), \quad (6.7)$$

where $g_{w,11}$ is the local Green's function of the site on lead w adjacent to the quantum dot [22]. A procedure for computing $g_{w,11}$ is given in appendix 6.6. In the uniform ($\alpha = 0$) case, the coupling density is semi-circular

$$\Gamma(\omega) = \sum_{w=l,r} \frac{\lambda_w^2}{2t^2} \begin{cases} \sqrt{4t^2 - \omega^2} & |\omega| \leq 2t \\ 0 & |\omega| > 2t \end{cases}, \quad (6.8)$$

with half-bandwidth $2t$. In the pinched case ($\alpha > 0$), the reduced hopping between sites L and $L + 1$ creates a Fabry-Pérot cavity in the right lead with resonance width $\Delta = \pi v_f/L$. Changing L switches the cavity between on- and off-resonance ($e^{2ik_f L} = \pm 1$) and flips $\Gamma(0)$ between a minimum and a maximum. Fig. 6.2 shows the coupling density for both the uniform and pinched cases. The overall hybridization strength is parameterized by the $\alpha = 0$ level broadening, $\Gamma = \Gamma(\omega = 0) = \sum_w \lambda_w^2/t$ which we use as our unit of energy.

An important property of this model is its Kondo temperature T_K . At temperatures below T_K , the QD spin is screened by the lead electrons to form a singlet state. The bare cloud length $\xi_0 = v_f/T_K$ is the theoretically expected spatial extent of the cloud of lead electrons which make up this singlet state [157].

In [169], the authors provide detailed experimental parameter estimates for this model which we use as a guide in choosing our parameter values. The level broadening Γ is estimated to be approximately 0.1 meV, which implies a unit of temperature given by $\Gamma/k_B \approx 1.16$ Kelvin. Following [169], we choose $\alpha = 1 - (t'/t)^2 = 0.1$ for all cases with modified hopping. Parameter estimates suggest a coupling asymmetry given by $\lambda_r \approx 4\lambda_l$, although this is experimentally tunable. For simplicity we choose $\lambda_l = \lambda_r = \lambda$ so that the leads are symmetrically coupled to the QD. Note that our choice of energy unit $\Gamma = 1$ implies $\lambda = \sqrt{t/2}$.

Parameter estimates suggest $U \approx 6\Gamma$. In our calculations we consider slightly larger interactions ($U = 7\Gamma, 8\Gamma, 9\Gamma$) in order to be in a regime where our impurity solver is more accurate. Following [169], we consider only the symmetric situation where $\epsilon_d = -U/2$ so that each QD energy level is doubly degenerate. The model is also spin-symmetric

and spin indices on Green's functions and observables will be omitted. We choose the lead half-bandwidth $D = 2t = 10\Gamma$. This follows the experimental parameter estimates in making the lead half-bandwidth the largest scale in the problem, while reducing it from the experimental value ($D \approx 60\Gamma$) for computational convenience. The experimental Fermi velocity is estimated to be $v_f \approx 2.5 \times 10^5$ m/s which implies $a = \hbar v_f / (2t) \approx 150$ nm. Note that a should be thought of as a phenomenological parameter rather than the spacing between physical atoms in the system.

The first quantity of interest is the QD density of states (DOS)

$$\rho_{\text{imp}}(\omega) = -\frac{1}{\pi} \text{Im} G_{\text{imp}}(\omega), \quad (6.9)$$

where $G_{\text{imp}}(\omega)$ is the frequency dependent, retarded, QD Green's function. The second quantity of interest is the site-dependent local density of states (LDOS) of the leads

$$\rho_w(\omega, i) = -\frac{1}{\pi} \text{Im} G_{w,ii}(\omega), \quad (6.10)$$

where $G_{w,ii}(\omega)$ is the frequency dependent, retarded, local Green's function of site i of lead w in the presence of the QD. This Green's function is obtained from the QD Green's function using

$$G_{w,ii}(\omega) = g_{w,ii}(\omega) + \lambda^2 g_{w,i1}(\omega) G_{\text{imp}}(\omega) g_{w,1i}(\omega), \quad (6.11)$$

where g_w is the non-interacting Green's function of lead w . A derivation of this result is given in appendix 6.6.

6.3 Methods

There are a number of methods that can be used to compute the QD Green's function $G_{\text{imp}}(\omega)$ for this model, notably NRG [7, 8, 168, 169]. We focus on methods based on diagrammatic expansion in the tunneling Hamiltonian H_T formulated on the three branch Keldysh contour. Using these methods the time-dependent, steady-state, retarded QD Green's function

$$G_{\text{imp}}(t - t') = -i \langle \{ d_\sigma(t), d_\sigma^\dagger(t') \} \rangle, \quad (6.12)$$

can be computed up to some maximum time t_{\max} . The frequency dependent Green's function is then obtained by a Fourier transform

$$G_{\text{imp}}(\omega) = \int_0^{t_{\max}} dt e^{i\omega t} G_{\text{imp}}(t) \quad (6.13)$$

and all further analysis is performed in the frequency domain.

Inchworm quantum Monte Carlo (QMC) is a numerically exact method based on expansion in H_T [31, 55]. Inchworm QMC is highly computationally demanding, and it is not yet feasible to reach long enough t_{\max} to resolve fine spectral features without broadening. Because of this, we make use of the less computationally demanding one crossing approximation (OCA) which corresponds to a second order truncation of the inchworm diagram series and is therefore approximate [53, 54]. Although OCA is not exact, it becomes more accurate as U is increased. We validate our OCA results against numerically exact inchworm QMC results in the parameter regime where this is feasible (see appendix 6.6).

6.4 Results

Fig. 6.3 shows the impurity DOS at $U = 9\Gamma$ for a sequence of inverse temperatures ($\beta = 1/T$) between $\beta\Gamma = 1$ and $\beta\Gamma = 50$. These results are computed with $\alpha = 0$, in the absence of any cavity. As the temperature is decreased below the Kondo temperature T_K , the impurity spectrum builds up a sharp Kondo peak at the Fermi energy with width γ_{imp} . We obtain the width of the peak by fitting a Lorentzian with offset to the spectrum around the Fermi energy. The fit function is given by

$$f(\omega) = A \frac{1}{\omega^2 + \gamma_{\text{imp}}^2} + B \quad (6.14)$$

where A and B are fit parameters and γ_{imp} is the estimated width of the Kondo peak. The inset of Fig. 6.3 shows the impurity spectrum (blue line) around the Fermi energy together with the fit (dashed black line).

As $T \rightarrow 0$, $\gamma_{\text{imp}}(T)$ converges to the Kondo temperature [170, 171]. At $\beta\Gamma = 50$, γ_{imp} is not fully converged to the zero temperature value and therefore overestimates T_K . Nevertheless it still provides a useful estimate which tracks changes in the Kondo temperature. For $U = \{7\Gamma, 8\Gamma, 9\Gamma\}$ we estimate inverse widths of $1/\gamma_{\text{imp}} = \{13.3\Gamma^{-1}, 14.8\Gamma^{-1}, 16.1\Gamma^{-1}\}$ respectively.

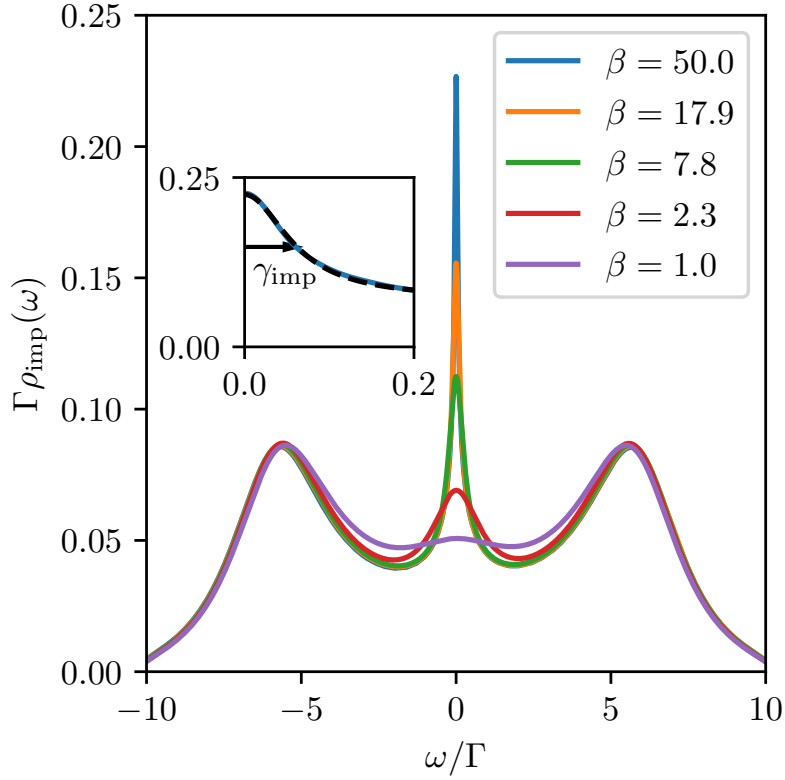


Figure 6.3: Impurity DOS at interaction strength $U = 9\Gamma$ as the temperature is lowered below the Kondo temperature T_K . Inset shows zoom of the peak at the Fermi energy in the $\beta = 50\Gamma^{-1}$ results. Dashed black line shows Lorentzian fit used to estimate the width $\gamma_{\text{imp}} \approx 0.062\Gamma$ which gives an estimate of the Kondo temperature T_K .

Note that this procedure is different from the method for estimating the Kondo temperature used in [169], which defines T_K as the temperature at which the conductance reaches half of its zero temperature value [15]. Since T_K defines a crossover scale rather than a sharp transition, its exact value is ambiguous. In [171], the authors find that within the non-crossing approximation (NCA) the T_K estimated from the impurity spectrum is approximately half the T_K estimated from the conductance.

Following the approach taken in [169], we consider the effect of lead perturbations ($\alpha = 0.1$) a distance L away from the impurity. We study how the perturbations change the width γ_{imp} which we take as a proxy for changes in the Kondo temperature T_K . In the experimental setup L is varied on the order of the Fermi wavelength around three fixed distances. The experimental parameter estimates of the resonance width give $\Delta = \pi v_f/L \approx \{3\Gamma, 1.2\Gamma, 0.75\Gamma\}$ which correspond to $L = \pi v_f/\Delta \approx \{10a, 26a, 42a\}$. This implies a maximum experimental L on the order of twice the bare cloud length estimated from the theoretical formula $\xi_0 = v_f/T_K$.

The top panel of Fig. 6.4 shows our results for the Kondo peak width γ_{imp} as a function of L . For scale, $v_f/\gamma_{\text{imp}} = \{133a, 148a, 161a\}$ for $U = \{7\Gamma, 8\Gamma, 9\Gamma\}$ respectively. Note v_f/γ_{imp} underestimates the bare cloud length $\xi_0 = v_f/T_K$ since at $\beta\Gamma = 50$ γ_{imp} overestimates T_K due to thermal broadening. The width shows a pronounced even-odd effect which comes from changing the cavity between on- and off-resonance ($e^{2ik_f L} = \pm 1$). The bottom panel of Fig. 6.4 shows γ_{imp} for odd sites only, normalized by the peak width in the absence of the cavity. These results agree with the results of [168, 169] in predicting Kondo temperature oscillations which decay with L . The magnitude of the oscillations is somewhat smaller, likely due to thermal broadening of the Kondo peak, and our choice of a symmetric coupling to both leads, instead of having a stronger coupling to the right lead hosting the cavity as in the experiment.

These results provide a detailed picture of the effect of the lead perturbation. Notably, the amplitude of the width oscillations is a non-monotonic function of the distance L . For small L ($\lesssim 50a$) the oscillation amplitude slowly increases with L . For larger L ($\lesssim 100a$) the oscillation amplitude linearly decays. Interestingly, for $L \gtrsim 100a$ what happens depends on the value of U . For $U = 7\Gamma$ (the case closest to the experimental value) the oscillation amplitude simply decays and remains very small as L is increased. However for larger U , the lines for even and odd L cross over and the even-odd effect flips direction. This crossover should be observables in future experiments. The oscillation amplitude then flattens off around $L \simeq 150a$ and begins a slow decay.

A non-monotonic dependence of T_K on L was previously seen in [168] using Anderson's

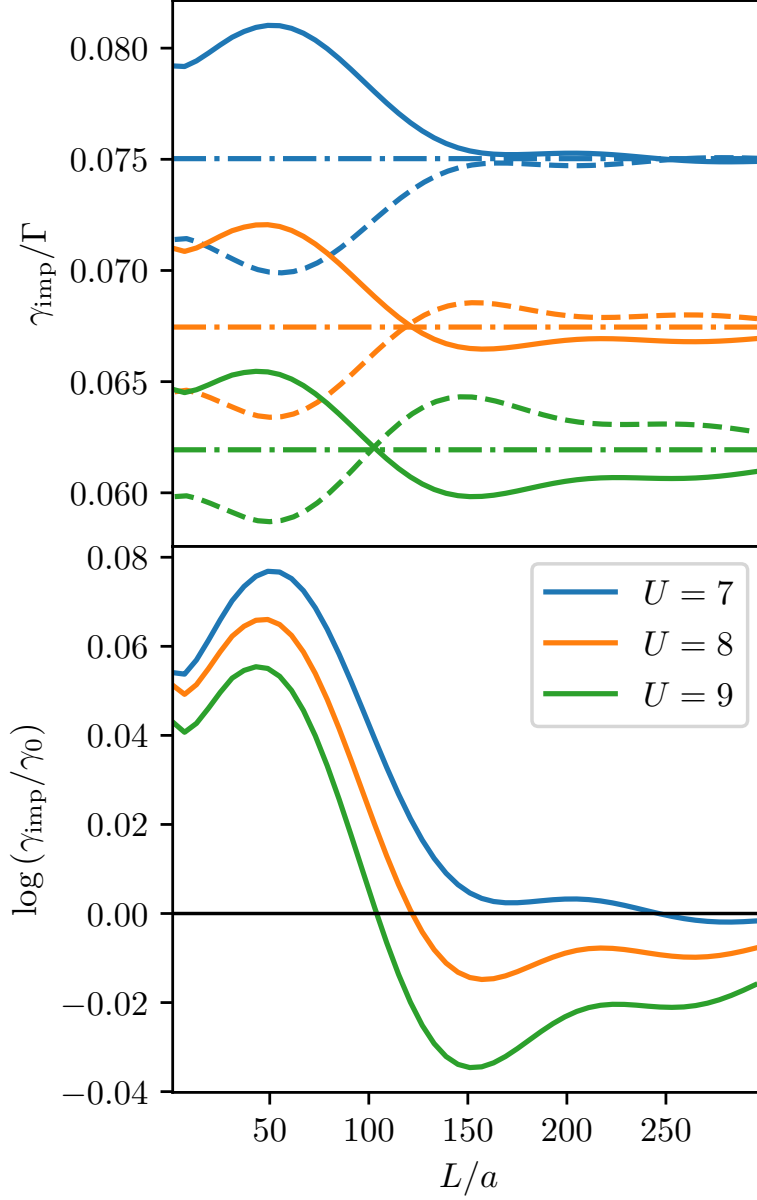


Figure 6.4: Top: Kondo peak width γ_{imp} as a function of the size of the Fabry-Pérot cavity length L for $\alpha = 0.1$ and $U = \{7\Gamma, 8\Gamma, 9\Gamma\}$. Solid (dashed) lines show data for L odd (even). Horizontal lines show data in the absence of the cavity ($\alpha = 0$). Bottom: Logarithm of peak width γ_{imp} normalized by peak width in the absence of the cavity γ_0 .

poor man's scaling technique [172], but not NRG. In that paper, the authors attribute the monotonic dependence seen in their NRG results to a failure of the logarithmic discretization to fully resolve the energy scale Δ introduced by the lead perturbation. Our results provide further evidence that the expected dependence is non-monotonic and may not be well captured by the logarithmic discretization employed in traditional NRG methods. It would be interesting to revisit this problem with newer NRG methods which allow a more flexible band discretization [173].

Due to the complicated, non-monotonic behavior, it is difficult to extract a numerical value for the Kondo cloud length from these data. The results clearly reveal that the lead perturbation has a pronounced effect on the Kondo state which shows an overall decay with L and reveals something about the Kondo cloud. However the exact interpretation of this behavior in order to extract a length scale remains difficult especially at large U . Because of this, it is interesting to consider other experimental modalities that could be applied to the same system in order to obtain a complementary view of the Kondo cloud.

A promising alternative view is provided by the lead local density of states (LDOS) which is accessible via STM to future experiments. Fig. 6.5 shows the lead LDOS at two sites on the right lead as the temperature is lowered below the Kondo temperature T_K . Note, for all following results we have set $\alpha = 0$ and there is no cavity formed in the leads. As the Kondo peak emerges at the Fermi energy in the QD DOS below T_K , a corresponding feature emerges at the Fermi energy in the lead LDOS. For odd sites, this feature is seen as a dip around the Fermi energy relative to the high temperature spectrum, whereas for even sites the feature is seen as a peak.

In order to observe how the Kondo cloud manifests itself in the lead LDOS we compare the non-Kondo LDOS $\rho^{NK}(\omega)$ which we observe at $T = 1\Gamma \gg T_K$ to the Kondo LDOS $\rho^K(\omega)$ which we observe at $T = 0.02\Gamma \ll T_K$. Fig. 6.6 shows the difference $\rho^K(\omega) - \rho^{NK}(\omega)$ for four different sites. The difference is largest at the Fermi energy, decays rapidly with ω and becomes oscillatory with increasing distance from the QD. This approach to characterization of the Kondo cloud has previously been explored in [162, 163].

In [162], the authors propose measuring the extent of the Kondo cloud by examining the function

$$F(n) = \int d\omega [\rho_n^K(\omega) - \rho_n^{NK}(\omega)] L_\gamma(\omega) \quad (6.15)$$

where $L_\gamma(\omega)$ is a Lorentzian with width given by the width of the Kondo peak on the impurity. This proposal successfully gives a function which appears to measure the extent

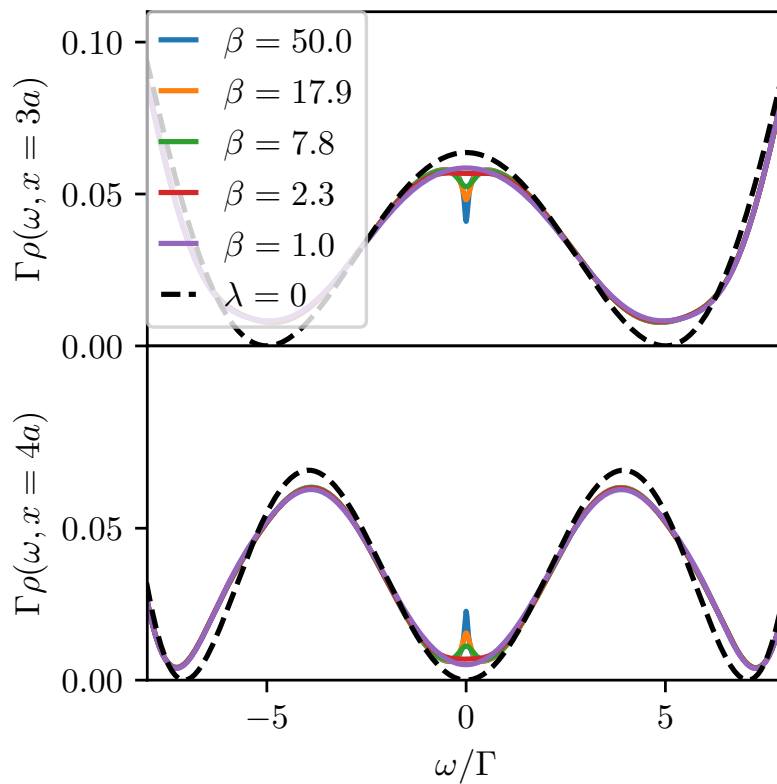


Figure 6.5: Lead LDOS at interaction strength $U = 9\Gamma$ at sites 3 (top) and 4 (bottom) as the temperature is lowered below the Kondo temperature. Dashed black line shows LDOS for non-interacting lead decoupled from impurity.

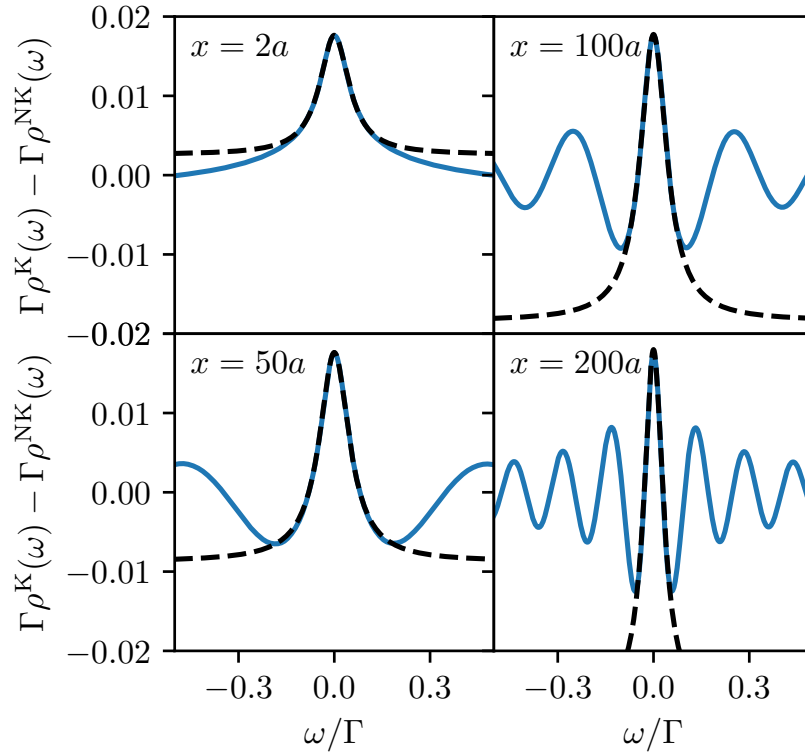


Figure 6.6: Difference between lead LDOS above and below T_K on four different sites. Dashed black line shows Lorentzian fit of central peak used to estimate $\gamma(x)$.

of the Kondo cloud. However, it has the unfortunate feature of directly inserting the Kondo temperature (via the impurity DOS width γ) into the measurement of the Kondo cloud. Ideally, one would like to have a measurement of the Kondo cloud which is as independent as possible from other measurements in order to be able to check its scaling properties.

In [163], the authors propose measuring the extent of the Kondo cloud by examining the function

$$L(n) = \int d\omega |\rho_n^K(\omega) - \rho_n^{NK}(\omega)| \quad (6.16)$$

which integrates the absolute difference between the Kondo and the non-Kondo spectra over the entire bandwidth. This procedure avoids inserting the Kondo temperature into the measurement. However, it also makes the measurement experimentally impracticable because the magnitude of the difference becomes very small and highly oscillatory away from the Fermi energy and so would require extremely high precision measurements over the entire energy window.

As an alternative to these methods, we propose to measure the Kondo cloud in the lead LDOS by looking at the width of the peak/dip at the Fermi energy. This avoids unnecessarily introducing T_K into the measurement and the need for extremely high precision measurements over the whole bandwidth. The black dashed lines in Fig. 6.6 show fits of a Lorentzian to the central peak which we use to extract the width $\gamma(x)$. From the figure we see that a Lorentzian provides a good fit of the central peak and that the peak narrows with distance from the QD.

The top panel of Fig. 6.7 shows the dependence of the LDOS width $\gamma(x)$ on distance from the QD for $U = \{7\Gamma, 8\Gamma, 9\Gamma\}$. Note this data contains both even and odd sites, demonstrating that there is no even-odd effect in the width. For small x the data shows $\gamma(x)$ slightly increasing. As x increases, $\gamma(x)$ begins a smooth monotonic decay. It is worth noting that this behavior appears much simpler than the behavior of T_K as a function of L in the presence of a cavity.

The bottom panel of Fig. 6.7 shows that $\gamma(x)$ appears to demonstrate universal scaling behavior. To extract the length scale ξ we fit a function $f(x) = c \exp\left[-(x/\xi)^{1/5}\right]$ to $\gamma(x)$ over the range $100a \leq x \leq 500a$ for each U . The particular form of this fit function was empirically determined. In particular, the exponent was initially a free parameter but was found to take values $\approx 1/5$ and was then fixed. The plot shows the curve collapse generated by plotting $\log(\gamma(\tilde{x})/c)$ against $\tilde{x} = (x/\xi)^{1/5}$. The robust linear behavior for

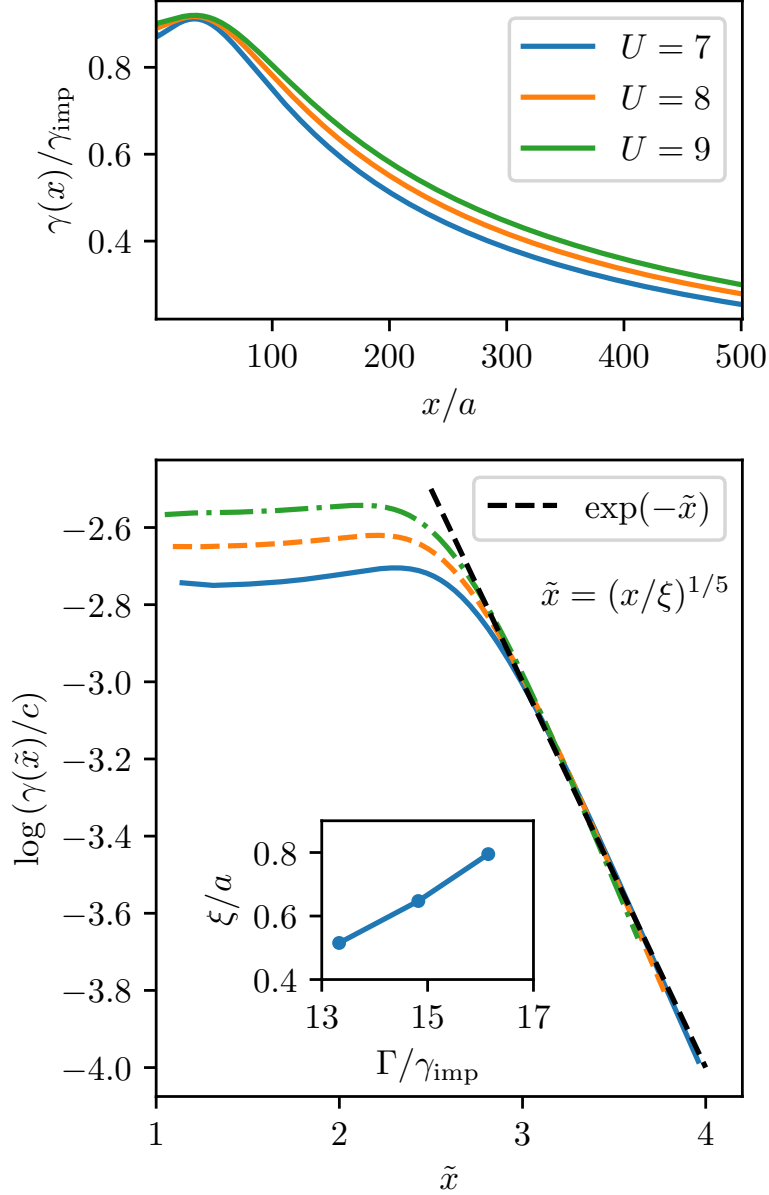


Figure 6.7: Top: Width of lead LDOS normalized by impurity width for $U = \{7\Gamma, 8\Gamma, 9\Gamma\}$. Bottom: Logarithm of LDOS width as function of rescaled distance. Inset: Extracted length scale ξ varies inversely with $\gamma_{\text{imp}} \approx T_K$.

$\tilde{x} \gtrsim 3$ shows that this correctly describes the scaling behavior.

In the inset of Fig. 6.7 we plot the extracted length scale ξ against the inverse Kondo peak width. As expected, this shows linear behavior consistent with the theoretical relationship $\xi_0 = v_f/T_K$. Note that the values of ξ are small relative to the expected length scales of $\sim 100a$. However, this small value should not be taken to imply that there is no Kondo cloud. The small values of the length scale ξ describing the asymptotic decay are due to the small exponent of our fit function. The top panel of Fig. 6.7 shows that the width remains a substantial fraction of the impurity peak width over length scales of $\sim 100a$.

This method offers a view of the Kondo cloud complementary to the view provided by the lead perturbation method. In particular, the expected functional dependence is simpler and the process of extracting a length scale more straightforward. However, this method does require high precision STM measurements. In this model, the peak widths are on the order of $0.05\Gamma \approx 5\mu\text{eV}$.

We now consider the effect of a voltage bias V on the Kondo cloud. Because we are using a real time impurity solver, nonequilibrium scenarios can be simulated in exactly the same way as equilibrium ones. Fig. 6.8 shows the impurity DOS and lead LDOS for several applied voltages. On the impurity, the applied voltage suppresses the Kondo peak and splits it creating two lower peaks at $\omega \approx \pm V/2$ [33]. Near to the impurity at $x = 2a$ this same phenomena can be observed in the difference between the Kondo and non-Kondo LDOS (top left of bottom panel). As we move further away from the impurity the effect of the voltage becomes more complicated as the underlying spectrum becomes more oscillatory. Nevertheless increasing the voltage consistently suppresses the overall difference between the Kondo and non-Kondo LDOS at all distances. This provides a new experimentally accessible window into the mechanism by which an applied voltage destroys the Kondo effect [101, 174]. This correspondence also provides some evidence for the relevance of the lead LDOS for Kondo physics on the impurity.

6.5 Conclusions

We have demonstrated how to calculate the Kondo cloud using two different modalities. Following recent experimental [169] and theoretical [168] work, we first measure the Kondo cloud by observing the effect of lead perturbations a distance L away from the QD on the Kondo temperature. Consistent with previous results, we find oscillations in the Kondo temperature which decay with L . In addition to confirming the general scenario seen in

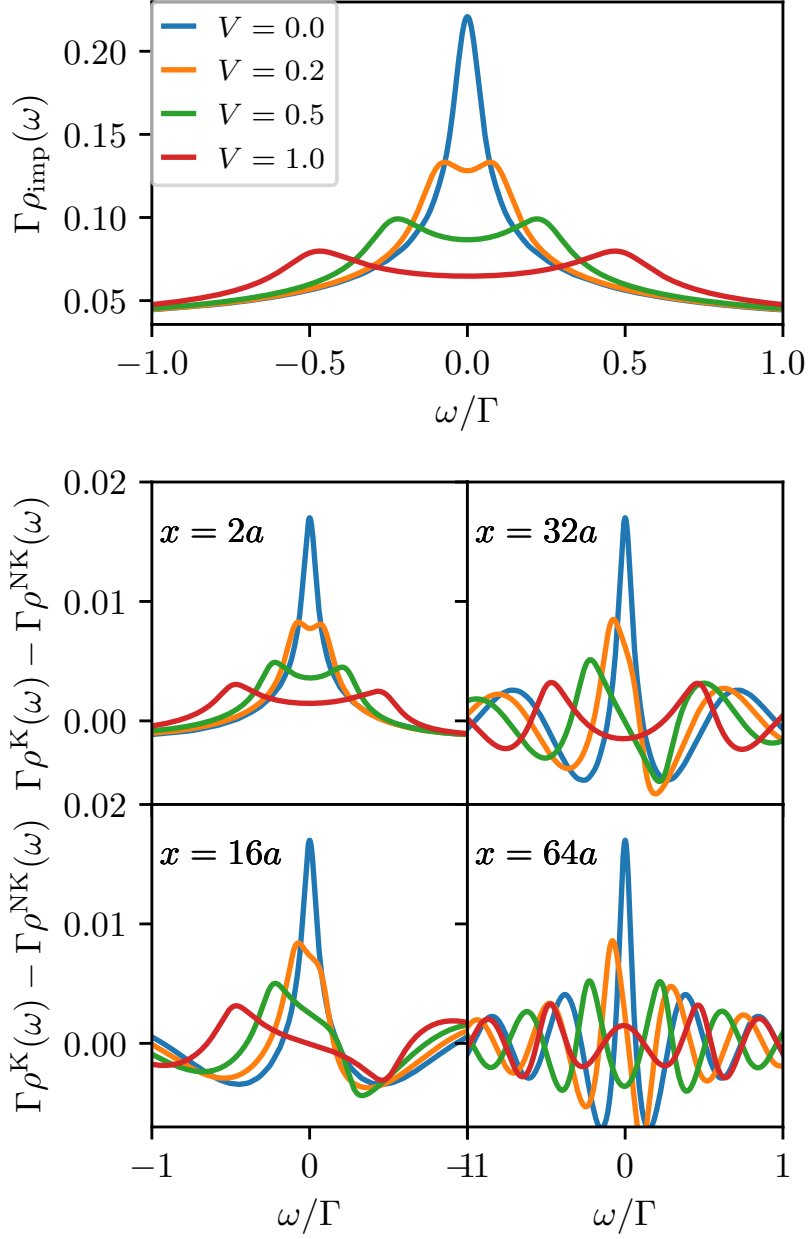


Figure 6.8: Top: Impurity DOS for applied voltages $V = \{0.0\Gamma, 0.2\Gamma, 0.5\Gamma, 1.0\Gamma\}$. Bottom: Difference between lead LDOS at $\beta\Gamma = 1$ and $\beta\Gamma = 50$ for each applied voltage on four different sites.

[169] we also uncover a more detailed picture of the spatial dependence of the Kondo temperature oscillations which may be observed in future experiments with greater spatial resolution. In particular, we show that the even-odd effect which generates the oscillations may flip for large L resulting in a non-monotonic dependence in the oscillation amplitude.

Having established that we reproduce the key existing experimental observations, we show how the Kondo cloud might be observed in a complementary way in the same system via future STM experiments. We identify features in the lead LDOS corresponding to the onset of Kondo physics. In particular, we show that the width of a peak (dip) in the lead LDOS at the Fermi energy decays with distance from the QD and that the length scale of this decay can be used to define a measurement of the Kondo cloud which appears to displays the correct scaling behavior. We also investigate the effects of an applied voltage bias and find that the suppression of the Kondo resonance on the impurity by a voltage is accompanied corresponding changes in the lead LDOS. These effects should be observable with STM. Measuring the width of the central LDOS peak would require $\sim\mu\text{eV}$ resolution which is already experimentally possible in some systems [175].

6.6 Appendix

Calculation of Lead Green's Functions

In this appendix we derive equations for the lead Green's functions. We proceed in three steps. First we derive a general form for the Dyson equation. We then apply this result to derive equations for the non-interacting lead Green's functions which appear in equation 6.7 and 6.11. Finally, we apply the same techniques to derive equation 6.11 for the local lead Green's function in the presence of the QD.

Consider a non-interacting Hamiltonian $H = H_0 + V$ where both H_0 and V are single-particle operators. The Green's function for this system is given by

$$G(\omega) = (\omega I - H)^{-1} = (\omega I - H_0 - V)^{-1} \quad (6.17)$$

where H , H_0 , and V are matrices in the single-particle space. From this we can obtain

$$(\omega I - H_0 - V) G = I \quad (6.18a)$$

$$\implies (I - (\omega I - H_0)^{-1} V) G = (\omega I - H_0)^{-1} \quad (6.18b)$$

$$\implies (I - gV) G = g \quad (6.18c)$$

$$\implies G = g + gVG \quad (6.18d)$$

where $g(\omega) = (\omega I - H_0)^{-1}$ is the Green's function for H_0 . Note that the equation $G = g + GVg$ can be obtained in the same way.

Using these results, we can derive an equation for the non-interacting lead Green's function $g_w(\omega) = (\omega I - H_w)^{-1}$. The main difficulty in computing g_w is that the leads are semi-infinite so the matrices are infinite dimensional. To solve this issue, we let V be the operator describing hopping between site N and $N + 1$ of the lead. Note that $H_0 = H_w - V$ is then partitioned into two disconnected blocks, A and B , consisting of the first N sites, and the rest of the semi-infinite chain respectively. Applying 6.18, and dropping the lead index w , we obtain the equations

$$g_{ij} = \tilde{g}_{ij} + \tilde{g}_{iN} t g_{N+1,j} \quad (6.19)$$

$$g_{N+1,j} = 0 + \tilde{g}_{N+1,N+1} t g_{Nj} \quad (6.20)$$

$$g_{Nj} = \tilde{g}_{Nj} + \tilde{g}_{NN} t g_{N+1,j} \quad (6.21)$$

where $\tilde{g} = (\omega I - H_0)^{-1}$ is the Green's function of the lead without V , t is the hopping amplitude between sites N and $N + 1$ and we assume $i, j \leq N$. Note, in the second equation the first term is zero because there are no terms in H_0 connecting sites on different sides of the partition. Also note that the Green's function $\tilde{g}_{N+1,N+1}$ is simply the surface Green's function for a uniform semi-infinite chain which we denote \mathcal{G} . \mathcal{G} can be computed analytically (see chapter 5 of [22]). Combining the second and third equations we obtain

$$g_{N+1,j} = \mathcal{G} t \tilde{g}_{Nj} + \mathcal{G} t \tilde{g}_{NN} t g_{N+1,j} \quad (6.22)$$

$$\implies g_{N+1,j} = \frac{t \tilde{g}_{Nj}}{\mathcal{G}^{-1} - t^2 \tilde{g}_{NN}}. \quad (6.23)$$

Combining this with the first equation we obtain

$$g_{ij} = \tilde{g}_{ij} + t^2 \frac{\tilde{g}_{iN} \tilde{g}_{Nj}}{\mathcal{G}^{-1} - t^2 \tilde{g}_{NN}}. \quad (6.24)$$

Now note that H_0 is block diagonal and can therefore be written as $H_0 = H_0^A \oplus H_0^B$. We write

$$\tilde{g} = (\omega I - H_0)^{-1} \quad (6.25)$$

$$= (\omega I - H_0^A \oplus H_0^B)^{-1} \quad (6.26)$$

$$= (\omega I - H_0^A)^{-1} \oplus (\omega I - H_0^B)^{-1}. \quad (6.27)$$

Since we assumed that $i, j \leq N$ we have $\tilde{g}_{ij} = (\omega I - H_0^A)^{-1}$ which is given entirely in terms of finite dimensional matrices and can be directly computed. Using this procedure we can compute the non-interacting lead Green's functions $g_w(\omega)$ which appear in equation 6.7 for the coupling density and in equation 6.11 for the lead Green's functions in the presence of the QD.

The derivation of equation 6.11 proceeds in much the same way, but is complicated by the fact that the system now contains interactions. In the presence of interactions, the full Green's function may be written as

$$G(\omega) = (\omega I - H_0 - V - \Sigma)^{-1} \quad (6.28)$$

where $H = H_0 + V$ is the single-particle Hamiltonian and Σ is the self-energy generated by the interaction. Following the same steps as above we again obtain $G = g + gVG$ with the difference that now $g(\omega) = (\omega I - H_0 - \Sigma)^{-1}$ contains the self-energy. This amounts to the observation that one can write the Dyson equation relative to an arbitrary part of the single-particle Hamiltonian rather than the interaction self-energy.

To derive equation 6.11, let V be the operator describing hopping between the impurity (at site 0) and lead w . Without loss of generality we take $w = r$. Note that $H_0 = H - V$ is then partitioned into two disconnected blocks, A and B consisting of the impurity together with lead l , and lead r respectively. We then obtain the equations

$$G_{ii} = \hat{g}_{ii} + \hat{g}_{i1} \lambda G_{0i} \quad (6.29)$$

$$G_{0i} = 0 + G_{00} \lambda \hat{g}_{1i} \quad (6.30)$$

where G is the full Green's function in the presence of the QD, $\hat{g}(\omega) = (\omega I - H_0 - \Sigma)^{-1}$,

and λ is the hopping amplitude between the impurity and lead r . Combining these equations we obtain

$$G_{ii} = \hat{g}_{ii} + \lambda^2 \hat{g}_{i1} G_{00} \hat{g}_{1i} \quad (6.31)$$

which reproduces the form of equation 6.11. However \hat{g} still contains the self-energy Σ and so requires some additional simplification. In this model the self-energy is local to the impurity. Therefore Σ is zero in subspace B , which does not contain the impurity, and can be written $\Sigma = \Sigma^A \oplus \Sigma^B = \Sigma^A \oplus 0$. Additionally because of our choice of V the Hamiltonian H_0 is partitioned into two disconnected blocks and can be written as $H_0 = H_0^A \oplus H_0^B = H_0^A + H_r$. We can write

$$\hat{g}(\omega) = (\omega I - H_0 - \Sigma)^{-1} \quad (6.32)$$

$$= (\omega I - H_0^A \oplus H_r - \Sigma^A \oplus 0)^{-1} \quad (6.33)$$

$$= (\omega I - H_0^A - \Sigma^A)^{-1} \oplus (\omega I - H_r)^{-1}. \quad (6.34)$$

This implies that for indices i, j in subspace B (lead r) we have

$$\hat{g}(\omega)_{ij} = [(\omega I - H_r)^{-1}]_{ij} = g_{r,ij}(\omega). \quad (6.35)$$

Using this we obtain

$$G_{r,ii}(\omega) = g_{r,ii}(\omega) + \lambda^2 g_{r,i1}(\omega) G_{\text{imp}}(\omega) g_{r,1i}(\omega). \quad (6.36)$$

which reproduces equation 6.11.

Inchworm Benchmark

Fig. 6.9 shows a comparison between results obtained using the one crossing approximation (OCA) and inchworm QMC truncated at order 3 and 4. Note that the OCA corresponds to inchworm truncated at order 2 and the exact solution is recovered as the truncation order is taken to infinity [31, 55]. The comparison is done at the smallest considered interaction strength $U = 7\Gamma$ where OCA is expected to be least accurate. The inchworm QMC results are converged at orders 3 and 4. The parameters $t_{\text{max}} = 5\Gamma^{-1}$ and $\beta = 20\Gamma^{-1}$ which are smaller than those used in main text and are chosen in order to make the inchworm calculations computationally feasible. The unit of time is given by $\hbar/\Gamma \approx 6.5$ ps. The temperature $T = 1/\beta = 0.05\Gamma$ is below the Kondo temperature estimated from the OCA

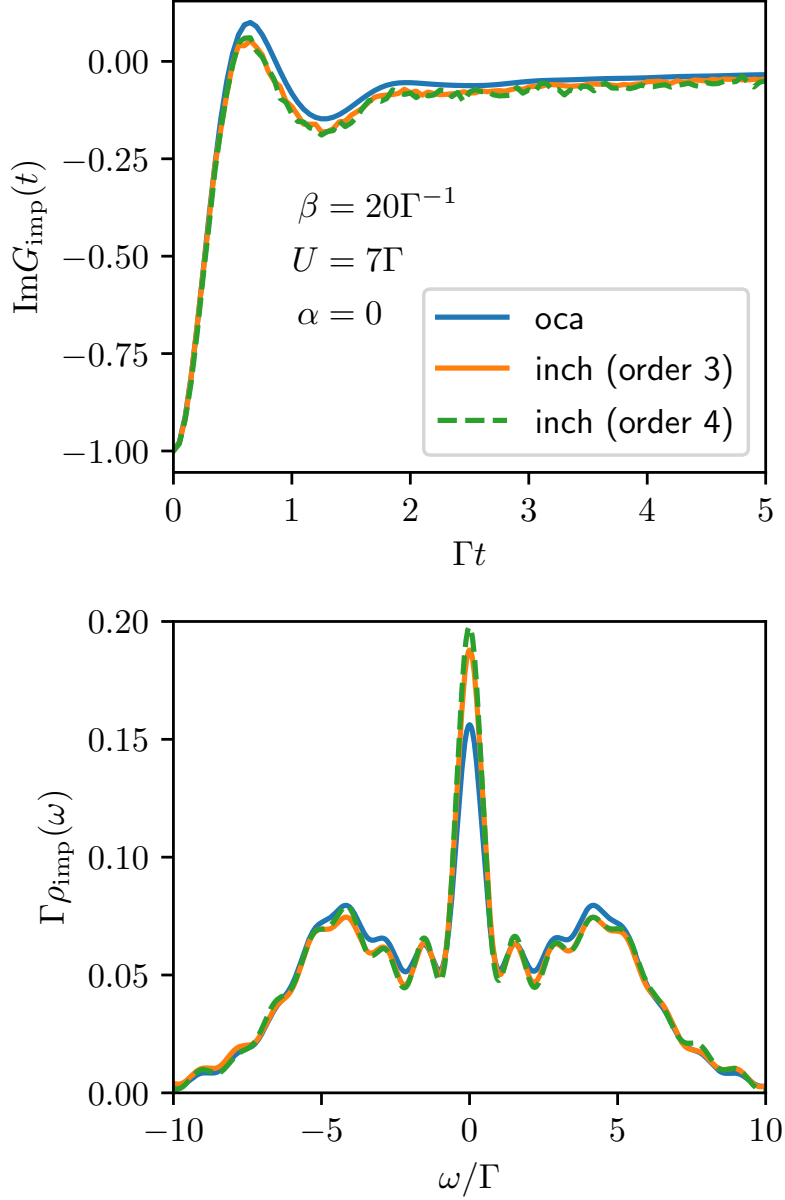


Figure 6.9: Comparison of the time-dependent retarded QD Green's function (top) and QD DOS (bottom) obtained from OCA (blue) and inchworm QMC (orange/green) at $\beta = 20\Gamma^{-1}$, $U = 7\Gamma$, $\alpha = 0$. The inchworm QMC results are parameterized by the maximum allowed expansion order (see legend).

peak width, $T_K \approx 0.075\Gamma$. The top panel shows the imaginary part of the time-dependent, retarded QD Green's function $G_{\text{imp}}(t)$ which is the direct output of the solvers. The bottom panel shows the DOS obtained via a Fourier transform of $G_{\text{imp}}(t)$. Note that the DOS is broadened significantly relative to the results in the main text due to the short maximum simulation time t_{max} .

CHAPTER VII

Inchworm DMFT

7.1 Introduction

The direct solution of quantum systems with many interacting degrees of freedom is believed to be intractable in general, and in order to understand the salient aspects of these systems, suitable approximations have to be employed. The dynamical mean field theory[176] is one such approximation. It is based on the realization that if the momentum dependence of the self-energy can be neglected, as occurs in certain infinite coordination number limits, the solution of a lattice model can be mapped onto that of an auxiliary quantum impurity model with self-consistently determined parameters [24, 25]. Note this self-energy is the usual self-energy with respect to the non-interacting system *not* the self-energy for the impurity propagators discussed in the context of M -crossing methods in chapter 3.

Quantum impurity models are amenable to numerical study, and the last decade has seen rapid advancement in the development of algorithms for their solution. In particular, remarkable progress was achieved by the continuous-time quantum Monte Carlo methods,[68, 177–181] which by now are the standard methods for studying multi-orbital and cluster impurity problems;[69] as well as in numerical renormalization group;[8] density matrix renormalization group;[182] and configuration interaction methods.[183, 184]

Modern quantum Monte Carlo methods are numerically exact, in the sense that they can provide results that converge to the exact answer with an uncertainty proportional to the square root of the number of stochastic samples taken. However, because these methods are formulated within an imaginary-time statistical mechanics formalism, real-frequency data such as spectral functions needs to be extracted from an ill-conditioned analytic continuation procedure,[185–193] in which these uncertainties are exponentially amplified. Furthermore, studying systems in general nonequilibrium states or under time-dependent

driving beyond linear response is not possible.

The desire to understand nonequilibrium transport in correlated impurity models motivated the development of real-time generalizations of continuous-time quantum Monte Carlo methods.[49, 140, 141, 145] These early methods require exponentially increasing computer time as a function of the simulated time due to the dynamical sign problem, i.e. the sign problem occurring when real-time dynamics is evaluated. The development of bold-line impurity solver algorithms[47, 73, 75, 77] substantially alleviated this sign problem and increased the accessible parameter space. A recent development, the inchworm quantum Monte Carlo method,[55] showed a reduction of the computational scaling from exponential to quadratic, effectively eliminating the dynamical sign problem altogether.

For dynamical mean field applications[194–197] of the inchworm method, two more components are necessary: the ability to obtain two-time response functions, and the extension of the method to an initial thermal ensemble. Both components have recently been implemented,[31] allowing us to test the method. As a first application, we address a lattice model for which the dynamical mean field approximation becomes exact: the Hubbard model on the infinite coordination number Bethe lattice. While we see the main application of our method in non-equilibrium,[30] we demonstrate its power here for the equilibrium case, where a large variety of well-developed and competitive methods are available and the physics is well understood.

The chapter is organized as follows. In Section 7.2, we write down the lattice model, recapitulate the dynamical mean field theory, introduce our impurity solver, discuss how self-energies are extracted, and explain how linear prediction can be used to obtain spectral functions. In Section 7.3 we present our results, including real-time Green’s functions, real-time self-energies and real-frequency spectral functions with and without linear prediction. Finally, in Section 7.4, we discuss our conclusions and outlook. The appendix contains further technical and numerical information.

7.2 Methods

Lattice model and dynamical mean field theory

We study the repulsive Hubbard model in equilibrium on the infinite coordination number Bethe lattice. The Hamiltonian is given by

$$\hat{H} = -\tilde{v} \sum_{\langle ij \rangle} c_{i\sigma}^\dagger c_{j\sigma} + U \sum_i n_{i\uparrow} n_{i\downarrow}, \quad (7.1)$$

where \tilde{v} denotes the hopping matrix element, and σ denotes the spin index. The operators $c_{i\sigma}^\dagger/c_{i\sigma}$ create/annihilate electrons with the spin σ on the corresponding site i . U is the on-site Coulomb repulsion between electrons with opposite spins. We restrict our discussion to the paramagnetic solution of a half-filled infinite coordination number Bethe lattice. The hopping matrix element must be properly scaled with the coordination number Z to remain finite in the limiting case, $\lim_{Z \rightarrow \infty}(\tilde{v}\sqrt{Z}) = v$.[\[24\]](#) Throughout this chapter we employ dimensionless units by dividing/multiplying all energy/time scales by the hopping strength v . The Bethe lattice is characterized by a semi-elliptical noninteracting density of states $D(\epsilon) = \sqrt{4 - \epsilon^2}/(2\pi)$. The model's interacting self-energy $\Sigma_{i\sigma,j\sigma'}(t, t')$, corresponding to Eq. [7.1](#), is purely local (*i.e.* zero for $i \neq j$), and its local part $\Sigma_{i\sigma,i\sigma'}(t, t')$ is equal to the self-energy of an auxiliary impurity model. The lattice Green's function can easily be obtained from this self-energy.[\[176\]](#)

We simulate the real-time dynamics of the model in equilibrium by means of the real-time dynamical mean field formulated on the L -shaped Keldysh contour.[\[92, 198\]](#) We define the impurity Green's function as the contour-ordered expectation value [\[30\]](#)

$$G_\sigma(t, t') \equiv -i \langle \mathcal{T}_C c_\sigma(t) c_\sigma^\dagger(t') \rangle, \quad (7.2)$$

where c_σ and c_σ^\dagger denote impurity operators, such that the retarded Green's function is given by

$$G_\sigma^{\text{ret}}(t, t') = -i\theta(t - t') \left\langle [c_\sigma(t), c_\sigma^\dagger(t')]_+ \right\rangle. \quad (7.3)$$

Time-translation invariance of the system in equilibrium implies that the two-time Green's function only depends on time differences: $G_\sigma(t, t') = G_\sigma(t - t')$. The DMFT self-consistency condition for the Bethe lattice thus reads

$$\Delta_\sigma(t - t') = G_\sigma(t - t') \quad (7.4)$$

for any two times t, t' on the L -shaped contour.

We solve the dynamical mean field equations iteratively, starting from a metallic, insulating, or high-temperature guess for the Green's function. Each DMFT iteration requires the solution of an impurity problem. We employ the inchworm quantum Monte Carlo solver (see chapters [3](#) and [4](#)) to obtain a numerically exact solution of the Green's function of this single impurity Anderson model, up to some finite maximal time.

Real-time self-energies

The local self energy function is of special interest in the DMFT context as it contains all relevant information about single-particle correlations in the system. Its retarded component $\Sigma^{\text{ret}}(t-t')$ is defined as the solution of the Dyson equation (spin indices are omitted for clarity)

$$G^{\text{ret}}(t-t') = G_0^{\text{ret}}(t-t') + \iint_0^{t_{\text{max}}} dt_1 dt_2 G_0^{\text{ret}}(t-t_1) \Sigma^{\text{ret}}(t_1-t_2) G^{\text{ret}}(t_2-t'). \quad (7.5)$$

Here, $G_0^{\text{ret}}(t-t')$ is the retarded Green's function of the noninteracting lattice, $G^{\text{ret}}(t-t')$ is obtained numerically as a result of a DMFT/inchworm calculation, and t_{max} is a maximum simulation time.

Eq. (7.5) is a Volterra integral equation of the first kind with respect to Σ^{ret} . In a numerical implementation, $G_0^{\text{ret}}(t)$ and $G^{\text{ret}}(t)$ are known on some finite time mesh (for example, a uniform grid). It is therefore natural to project the integral equation onto the mesh, and use numerical linear algebra methods to solve the resulting linear system. In principle, the solution of Eq. (7.5) could be obtained in Fourier space by applying the convolution theorem. However, this approach is not practical here, as $G^{\text{ret}}(t)$ is known only up to a finite time, and does not generalize to the non-equilibrium case without additional modifications.

Given a number of time slices N_t , we introduce mesh nodes $t_i = i\Delta t$ with $i \in \{0, 1, \dots, N_t - 1\}$ and $\Delta t = t_{\text{max}}/(N_t - 1)$. A discretized version of the Dyson equation then reads

$$G^{\text{ret}}(t_i - t_j) = G_0^{\text{ret}}(t_i - t_j) + (\Delta t)^2 \sum_{k,l=0}^{N_t-1} G_0^{\text{ret}}(t_i - t_k) \Sigma^{\text{ret}}(t_k - t_l) G^{\text{ret}}(t_l - t_j) w_{kl}. \quad (7.6)$$

The quadrature weights w_{kl} define the integration method, and at this point we do not specify their precise form. Using matrix notation $F_{ij} = F(t_i - t_j)$ we find

$$\Sigma_{ij}^{\text{ret}} w_{ij} = \frac{(G_0^{\text{ret}})_{ij}^{-1} - (G^{\text{ret}})_{ij}^{-1}}{(\Delta t)^2}. \quad (7.7)$$

The numerical matrix inversion used here is stable, as all retarded Green's functions are

represented by lower triangular matrices with $G^{\text{ret}}(0^+) = -i$ on the main diagonal, such that their condition number is 1. The $(\Delta t)^2$ in the denominator of (7.7) suggests that this procedure is similar to numerical calculation of the second derivative. The number of time slices at which $G^{\text{ret}}(t_i)$ is known is limited by the computational effort required by the inchworm QMC algorithm. In order to make the numerical differentiation accurate, we choose N_t much larger than used in the inchworm simulation and employ a cubic spline interpolation of G^{ret} between the original nodes.

Only certain choices of quadrature weights give a convergent solution in the small Δt limit. In his study of the one-dimensional Volterra equations of the first kind, Linz [199] showed that trapezoidal and rectangular rules are convergent, whereas higher order quadrature methods in general are not. Using this result as a starting point, we construct w_{ij} as possible direct products $w_i w_j$, where w_i and w_j correspond to the rectangular rule with the first/last point excluded and to the trapezoidal rule. Most combinations can be ruled out, as they cause $\Sigma^{\text{ret}}(t_{\text{max}})$ to diverge in the small Δt limit. We found that the following choice:

$$w_{i \geq j} = \begin{cases} 0, & i = 0, \\ 0, & j = N_t - 1, \\ 0, & i = j, \\ 1/2, & j = i - 1, \\ 1, & \text{otherwise.} \end{cases} \quad (7.8)$$

yields stable and accurate results. The first two lines in (7.8) show that we choose a rectangle rule approximation excluding the first slice from the t_1 -integral and the last slice from the t_2 -integral. Values on the first sub-diagonal receive half the weight, because retarded functions are proportional to $\theta(t - t')$. Finally, w as well as all other matrices entering the equation must be of Toeplitz form in equilibrium. We therefore also set the main diagonal of w to zero.

Equations (7.7) and (7.8) allow for extracting all mesh values of the self energy, except $\Sigma_{ii}^{\text{ret}} = \Sigma^{\text{ret}}(0^+)$. This element is known analytically, see section 7.5.

Linear Prediction

Our simulations are performed up to a finite maximum real time t_{max} determined by the available computational resources. However, many quantities are best described in the real-frequency domain, and are therefore expressed as Fourier transforms over the entire time axis. When Fourier transforming quantities with a hard time cutoff, the transform can be expressed as a convolution with a sampling kernel proportional to $\text{sinc}(\omega) = \frac{\sin(\omega)}{\omega}$

in the frequency domain, i.e.

$$\tilde{A}(\omega) = \int_{-\infty}^{\infty} d\omega' K(\omega, \omega') A(\omega'), \quad (7.9)$$

where $\tilde{A}(\omega)$ is the result from a Fourier transform with data up to finite times, $A(\omega)$ is the true result and the convolution kernel is given by

$$K(\omega, \omega') = \frac{t_{\max}}{2\pi} \operatorname{sinc} \left(\frac{(\omega - \omega') t_{\max}}{2} \right). \quad (7.10)$$

This convolution introduces broadening and unphysical oscillations into the spectral function. Linear prediction is a technique to remove these artifacts by using a physically motivated extrapolation scheme to extend data beyond the maximum simulated time. Linear prediction has previously been used for this purpose within the framework of t -DMRG[200–203]. We start with the ansatz that the value of the signal (in this case the Green’s function) at the n -th real time point is a linear function of its previous p values, i.e.

$$\tilde{x}_n = - \sum_{i=1}^p a_i x_{n-i}. \quad (7.11)$$

It can be shown that this corresponds to fitting the function in time to a superposition of p complex exponential terms. In the case of a Green’s function dominated by a few isolated poles, this approximation is justified. For the data presented here, the validity needs to be assessed by systematically varying p .

In order to use this model for extrapolation, the coefficients a_i must be fit to the known data. This is done over the region $(t_{\max} - t_{\text{fit}}, t_{\max})$ in order to exclude spurious short time behavior from the fit results. The linear prediction ansatz leads to a matrix equation

$$Q\mathbf{a} = -\mathbf{x}, \quad (7.12)$$

where $Q_{nk} = x_{n-k}$ is an $N \times p$ complex matrix with N the number of points in $(t_{\max} - t_{\text{fit}}, t_{\max})$. Solving this in the least squares sense leads to the normal equations

$$R\mathbf{a} = -\mathbf{r}. \quad (7.13)$$

This is written in terms of the autocorrelations of the data,

$$R_{ji} = \sum_n x_{n-j}^* x_{n-i}; \quad r_j = \sum_n x_{n-j}^* x_n. \quad (7.14)$$

These matrix equations are often unstable and require some form of regularization. Here we choose the simple regularization, $R^{-1} \rightarrow (R + \epsilon I)^{-1}$ and check that the results are not strongly affected by the regularization parameter.[201] With this scheme, the coefficients a_i are readily obtained and the Green's function can be extrapolated until it decays to zero. The procedure yields spectral functions free from unphysical finite time oscillations, at the cost of some additional systematic uncertainty due to the assumptions imposed by the linear prediction ansatz. We emphasize that linear prediction is only applied to our converged data as a post-processing routine, in order to interpret the real-time results as functions of frequency. The DMFT / inchworm iteration procedure preceding it is formulated in terms of real, finite times only, and independent of the linear prediction formalism.

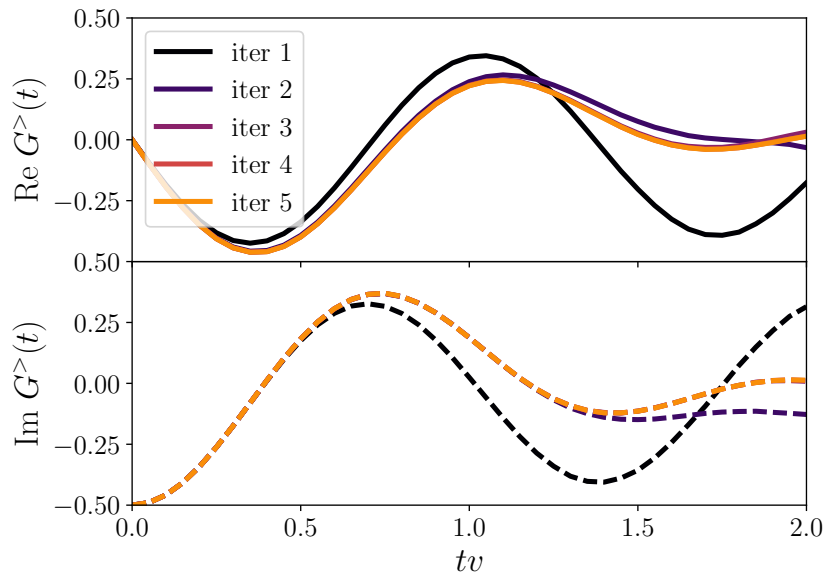


Figure 7.1: Real and imaginary parts of the greater dynamical mean field Green's function $G^>(t)$ as a function of real time t up to a maximum time of $tv = 2$. $U/v = 4$, $T/v = 0.05$, equilibrium. Shown is the convergence with DMFT iteration.

7.3 Results

Our impurity solver obtains results for $G(t, t')$ as a function of real times. A typical raw simulation output is shown in Fig. 7.1, which shows the real (solid lines) and the imaginary part (dashed lines) of the greater Green's function up to a maximum time $tv = 2$ and at a low temperature of $T/v = 0.02$. The interaction strength is taken to be $U/v = 4$, equal to the full bandwidth of the infinite coordination number Bethe lattice. The error bars of the measured Green's function could, in principle, be estimated as standard deviation from a set of completely independent DMFT/inchworm runs. With our present implementation this approach has proven too computationally expensive.

The inchworm Monte Carlo method is only exact when two numerical parameters are controlled. The first of the parameters is the discretization of the imaginary and the real time branch Δt , which we chose to be $\Delta tv = 0.05$. Second, the maximum order to which diagrams in the inchworm expansion are considered. We find, especially in the metallic low temperature regime, that results converge at an inchworm expansion order of around seven. As the inchworm order is directly related to the number of crossings considered in an M -crossing approximation (see chapter 3) this result implies that results from non-crossing or one-crossing approximations are not valid in this parameter regime. Throughout this chapter, all the results presented are converged in both Δt and maximum order.

We observe that the dynamical mean field solution converges in a causal manner, in the sense that results are converged within one iteration by time $tv = 0.3$, within two iterations by time $tv = 1.0$, and results up to $tv = 2$ are indistinguishable between iterations 4 and 5, indicating that the self-consistency loop has converged. While this causal convergence can be used to avoid the usual dynamical mean field iteration scheme and replace it with a direct solution of the self-consistency equations,^[30] this scheme has not been employed here.

As the model is tuned from metallic to insulating, the shape of the real-time Green's functions changes substantially, from slow oscillations at weak coupling to rather rapid, quickly decaying oscillations at large interaction strength. This is shown in Fig. 7.2, for interaction strengths $U = 2/v$, $U/v = 4$, $U/v = 6$, and $U/v = 8$, at a relatively high temperature of $T/v = 0.5$.

In contrast, lowering the temperature by a factor of 10, as shown in Fig. 7.3, causes relatively little change in the Green's function, with both oscillation frequency and amplitude staying more-or-less invariant for the time range simulated. Fig. 7.3 shows a regime in which a quasi-particle peak emerges upon cooling. However, the properties of

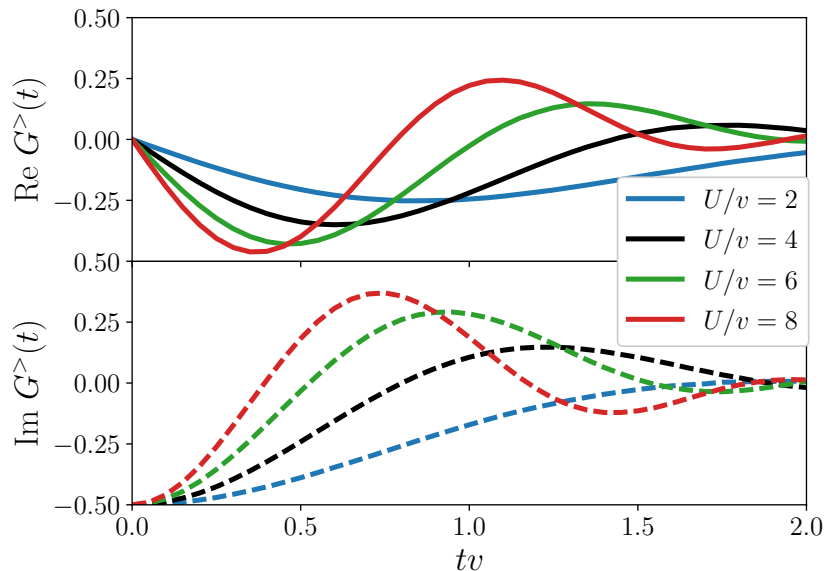


Figure 7.2: Real and imaginary parts of the greater DMFT Green’s function $G^>(t)$, for times up to $tv = 2$, with $T/v = 0.5$, half filling, equilibrium, at on-site interaction strengths $U/v \in \{2.0, 4.0, 6.0, 8.0\}$.

this peak are not obvious in the data for the greater Green’s function shown here.

Using the procedure described in Sec. 7.2, we can directly extract a real-time self-energy. Fig. 7.4 shows the imaginary parts of the noninteracting and the interacting retarded Green’s functions (left vertical axis) along with the imaginary parts of the computed self-energy (right vertical axis) as a function of time. The orange curve is the Green’s function reconstructed from replacing the bare Green’s function and the self-energy into eq. (7.6), showing that the scheme for extracting the real-time self-energy, which is numerically demanding, has converged. The numerical noise visible in the real-time self-energy may be used to qualitatively assess the size of the Monte Carlo errors intrinsic to this simulation. However, we note that in the case of inchworm simulations this approach typically underestimates the errors, and a more complicated procedure is required if one is interested in rigorous error estimates.[31, 55]

Fig. 7.5 shows the evolution of the imaginary part of the real-time self-energy with interaction strength, for the same parameters as shown in Fig. 7.2. The self-energy decays to zero within the accessible times in the weak coupling limit.

In contrast, the insulating regime shows a self-energy consistent with a constant in the long-time limit. This behavior is caused by the DMFT mechanism for opening a gap, which requires a pole at zero frequency (at half-filling) in the self-energy, such that

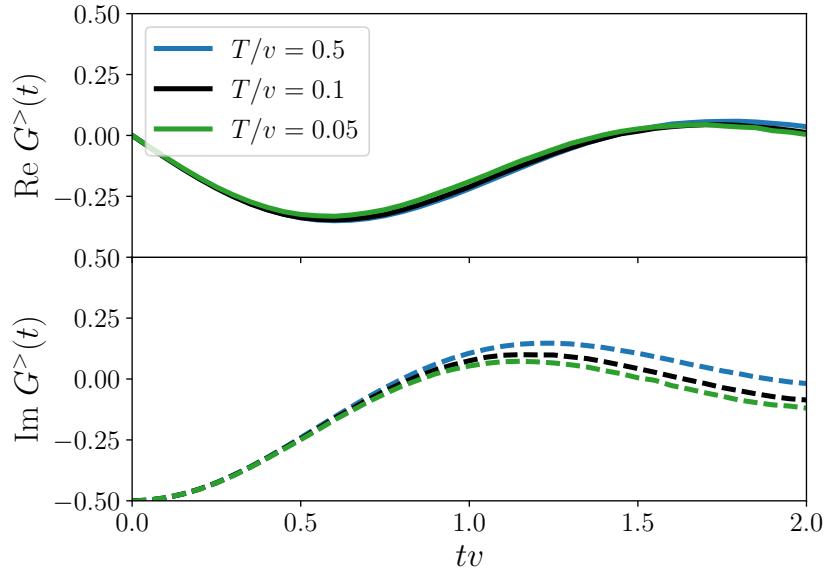


Figure 7.3: Real and imaginary parts of the greater DMFT Green's function $G^>(t)$, for times up to $tv = 2$, half filling, equilibrium, for $U/v = 4$, at temperatures $T/v \in \{0.5, 0.1, 0.05\}$.

$\text{Im}\Sigma(\omega) = \Delta^2\delta(\omega) + \text{Im}\Sigma^{\text{reg}}(\omega)$, where Δ denotes the Mott half-gap size and Σ^{reg} the non-divergent part of the self-energy. In the atomic limit, one would expect $\Delta \sim U/2$. For the lattice problem with non-zero hybridization, the gap sizes are smaller.

Interacting spectral functions in real frequency, $A(\omega) = -\frac{1}{\pi}\text{Im}G^{\text{ret}}(\omega)$, are of principal interest in dynamical mean field calculations because they allow for direct comparison with photoemission experiments. Obtaining $A(\omega)$ in imaginary-time formulations requires an ill-conditioned analytical continuation procedure, such as the maximum entropy algorithm. The real-time formulation avoids this. However, the fact that the real-time Green's function is only known up to a finite maximum time implies that spectral functions can only be resolved with a frequency resolution proportional to the inverse of that maximum time. Fig. 7.6 shows spectral functions extracted from the data in Fig. 7.2 and corresponding to the self-energies in Fig. 7.5. It demonstrates the metal-insulator crossover as the on-site interaction strength increases. Due to the finite frequency resolution, sharp features are absent and part of the spectral function turns negative, especially in the higher frequency regions.

The linear prediction method described in Sec. 7.2 is an interpolation routine designed to replace the sharp cutoff of $G(t)$ at the maximum time t_{max} with a smoothly decaying function corresponding to a set of poles in the complex plane. As is evident in Fig. 7.7,

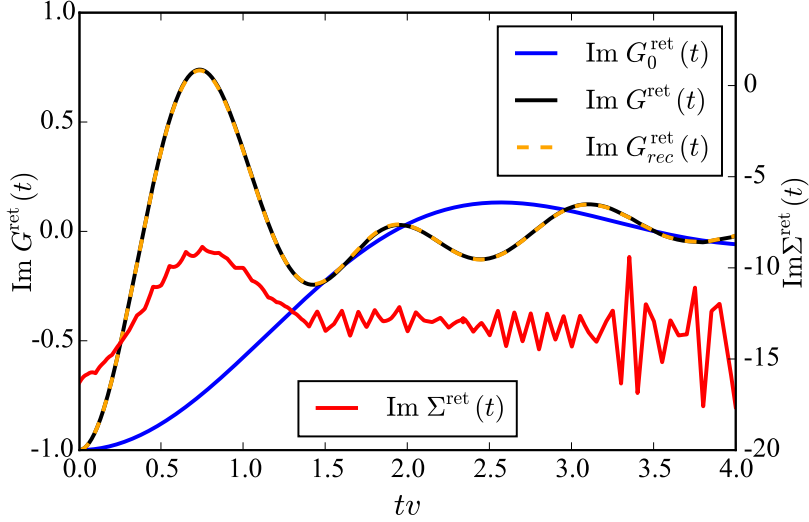


Figure 7.4: Retarded components of the DMFT Green’s function, bare Green’s function and self-energy computed for $U/v = 8.0$ at half-filling and temperature $T/v = 0.5$. $G_{rec}^{ret}(t)$ (dashed orange curve lying on top of the black one) is a Green’s function reconstructed by iterative substitution of $\Sigma^{ret}(t)$ into the Dyson equation. Data obtained using 2001 interpolation slices.

data obtained for times up to $tv = 2$ and extrapolated up to $tv = 4$ using linear prediction approximates well our data directly computed by running the dynamical mean field algorithm up to $tv = 4$.

The linear prediction results can then be used to obtain spectral functions that do not suffer from the ‘ringing’ phenomenon. Fig. 7.8 shows the results of this procedure in practice: while the straightforward continuation of the data up to time $tv = 2$ shows only a coarse frequency resolution and has substantial negative contributions between frequencies of $\omega/v = 5$ and 10, the corresponding extrapolated data shows a double-peak feature and is positive. Longer-time data (not based on linear prediction) corroborates the double-peak structure and the slightly larger gap, and similarly does not exhibit a negative contribution to the spectral function.

Linear prediction is an extrapolation procedure that needs to be carefully controlled. Results should not depend on the choice of cutoff time or the number of poles interpolated. These concerns are addressed in section 7.5.

Using linear prediction, we revisit two aspects of single-site dynamical mean field theory: the opening of the Mott gap as interaction strength is increased, and the establishment of a quasiparticle peak as temperature is lowered in the coherent metallic regime.

Fig. 7.9 shows the data of Fig. 7.6 obtained within linear prediction. It is evident that

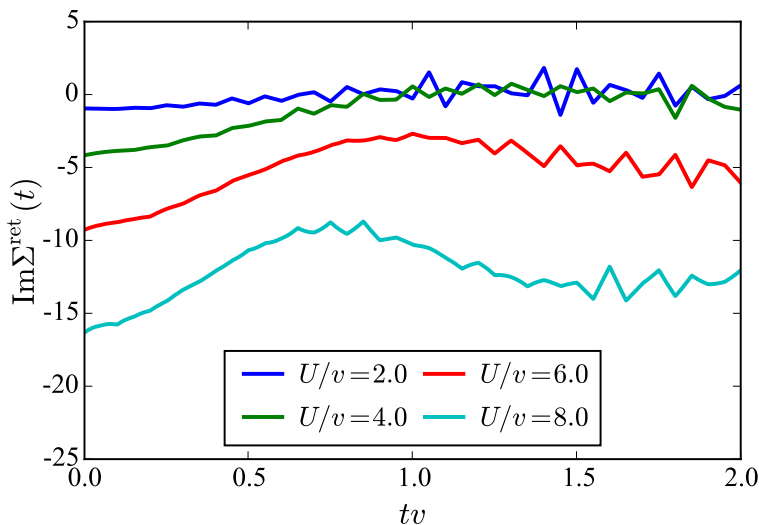


Figure 7.5: Retarded component of the imaginary part of the DMFT self-energy for interaction strengths $U/v \in \{2.0, 4.0, 6.0, 8.0\}$ at half-filling and temperature $T/v = 0.5$.

the increased frequency resolution leads to additional features in the spectral function. $U/v = 2$ is metallic with little change of the band structure due to correlations. $U/v = 4$ shows ‘bad metallic’ behavior where the spectral function near zero is suppressed due to the onset of insulating correlations. As the interaction is raised to $U/v = 6$, a gap opens and a double-peak feature develops, and by $U/v = 8$ a clear insulating structure with a wide Hubbard gap has developed.

As temperature is lowered at $U/v = 4$, the ‘bad metal’ dip in the spectral function disappears, and for a temperature of $T/v = 0.1$, a clear sign of a ‘quasiparticle peak’ has developed (Fig. 7.10). Further lowering of the temperature makes the quasiparticle peak more pronounced, while deepening the ‘dip’ between the Hubbard side bands and the peak.

7.4 Conclusions

We have presented a first application of real-time quantum Monte Carlo methods to real-time dynamical mean field theory. We showed that it is possible to obtain accurate Green’s functions and self-energies directly in real-time. We further showed that if one is interested in frequency-transformed properties, linear prediction methods for extending the range of the available data to longer times work in practice for Monte Carlo data with sufficient accuracy.

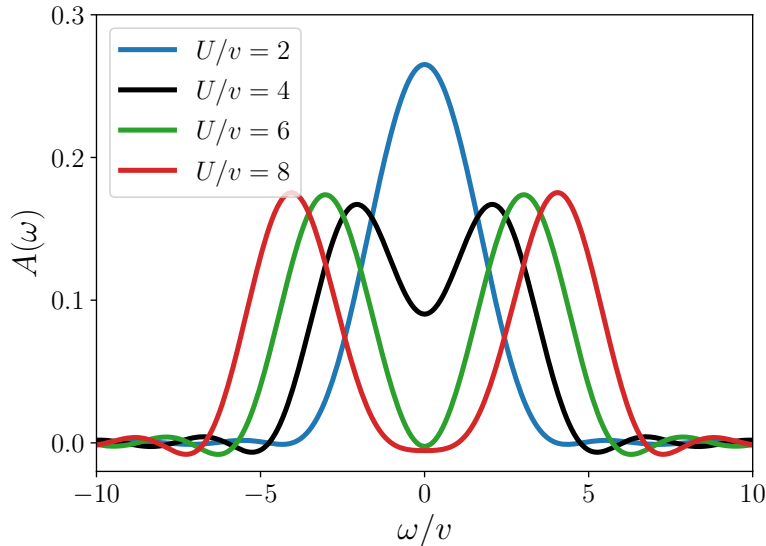


Figure 7.6: The converged DMFT spectral function $A(\omega)$ obtained by directly performing the Fourier transform on the real time Green’s function with a cutoff at $t_{\max}v = 2$ with $T/v = 0.5$ and at on-site interaction strengths $U/v \in \{2.0; 4.0; 6.0; 8.0\}$.

We expect that in the near future our algorithms will have applications mainly out of equilibrium, in the study of quenches and driven problems, which the impurity solver algorithm demonstrated here can simulate at no additional cost. In contrast, reaching substantially longer times or substantially lower temperatures than the ones demonstrated here will require additional optimizations and access to supercomputer resources.

To take a long view on the equilibrium problem, it is useful to consider the respective scaling properties of imaginary-time and real-time algorithms with regard to the desired accuracy of real frequency quantities. Whereas imaginary-time algorithms are currently far more efficient, they are limited by the exponential sensitivity to errors in the various analytical continuation methods. Real-time algorithms are substantially more expensive, but their accuracy is limited only by the maximum simulated time. In the inchworm method, extending this time requires a quadratic increase in computational effort. It is therefore entirely conceivable that in the future—as the field grows to be interested in larger, more frustrated problems and in higher frequency resolution—the real-time algorithms will eventually surpass their imaginary-time counterparts in efficiency by the sheer power of scaling.

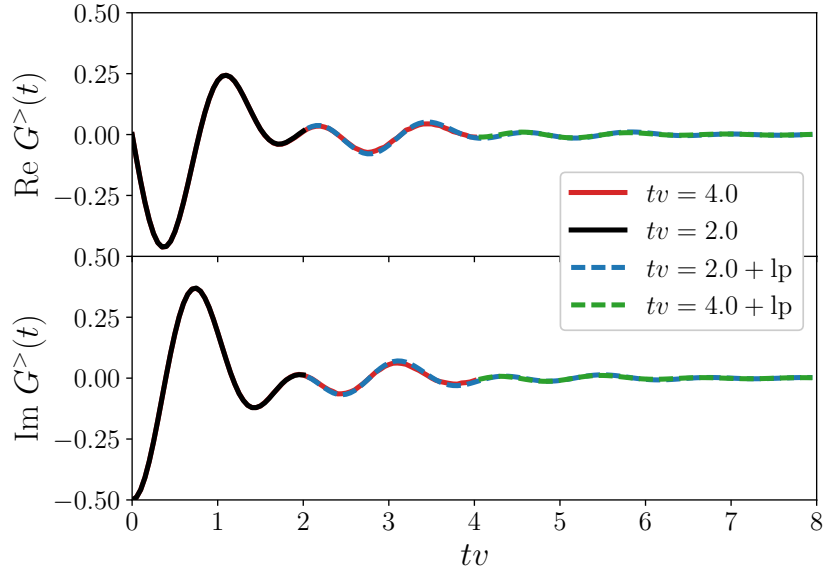


Figure 7.7: Comparison of raw Green's function data up to $tv = 2$ (black) and $tv = 4$ (red) with results from linear prediction of the $tv = 2$ data (blue) and $tv = 4$ data (green) for $U/v = 8, T/v = 0.5$. For the linear prediction we use $p = 9, t_{\text{fit}}v = 1.0$.

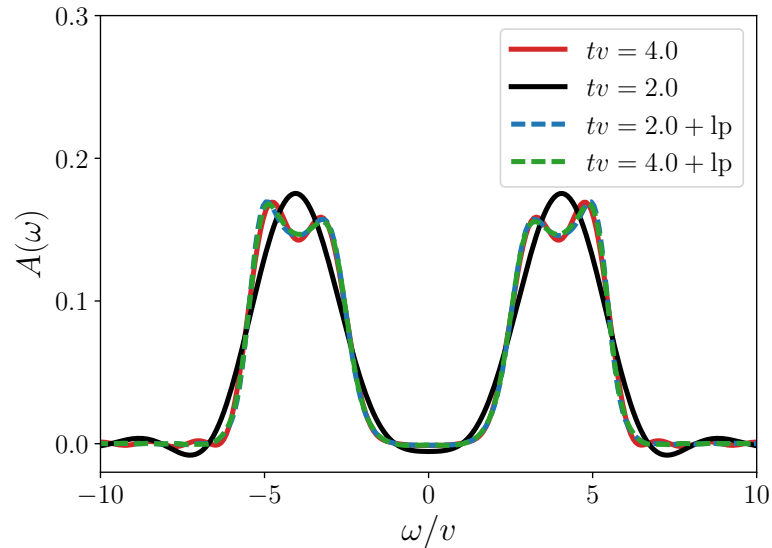


Figure 7.8: Comparison of spectral function obtained from raw Green's function data up to $tv = 2$ (black) and $tv = 4$ (red) with results from linear prediction of the $tv = 2$ data (blue) and $tv = 4$ data (green) for $U/v = 8, T/v = 0.5$. For the linear prediction we use $p = 9, t_{\text{fit}}v = 1.0$.

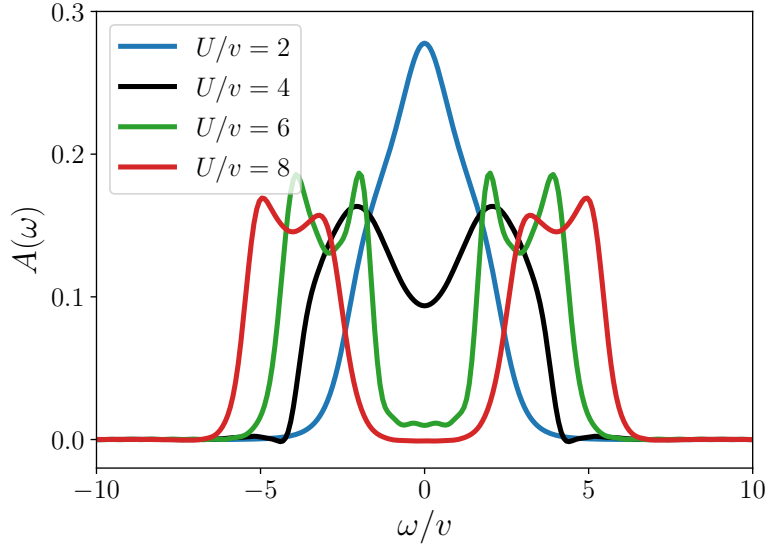


Figure 7.9: The converged DMFT spectral function $A(\omega)$ obtained by extrapolating the real-time Green's function from $tv = 2.0$ to $tv = 10.0$ using linear prediction with $p = 9$, $t_{\text{fit}}v = 1.0$ for temperature $T/v = 0.5$ at on-site interaction strengths $U/v \in \{2.0, 4.0, 6.0, 8.0\}$.

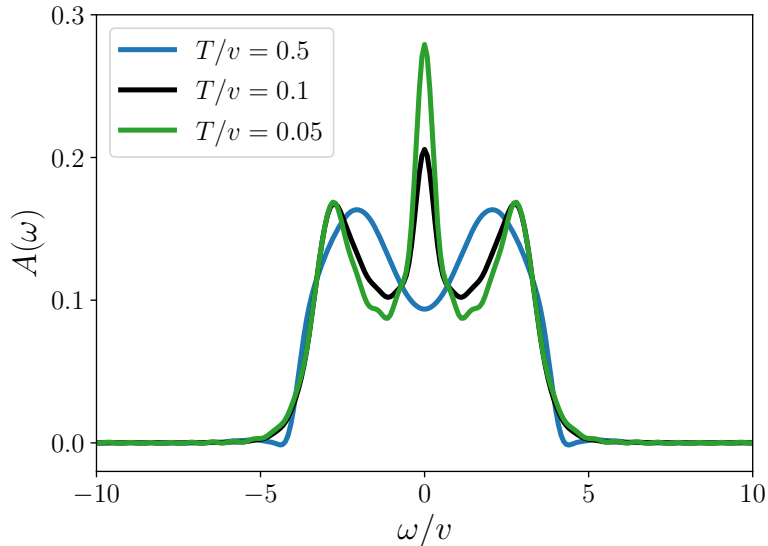


Figure 7.10: The converged DMFT spectral function $A(\omega)$ obtained by extrapolating the real-time Green's function from $tv = 2.0$ to $tv = 10.0$ using linear prediction with $p = 9$, $t_{\text{fit}}v = 1.0$ for $U/v = 4$ at temperatures $T/v \in \{0.5, 0.1, 0.05\}$.

7.5 Appendix

Convergence with respect to the inchworm truncation order

Fig. 7.11 shows the comparison of the Matsubara Green's function $G(\tau)$ computed by the inchworm nonequilibrium QMC solver and an equilibrium continuous-time hybridization expansion solver[68] (we used the solver of the open source TRIQS library[71, 204]). The data are obtained for an impurity calculation starting with a semielliptic density of states with a full bandwidth of 4 at $U/v = 4.6$ and half-filling. The upper panel of Fig. 7.11 demonstrates that at high temperature $T/v = 0.2$, a maximum order of 5 in the inchworm order truncation is sufficient. In contrast, as the temperature is lowered to $T/v = 0.04$ (near the onset of the first order coexistence in the dynamical mean field solution of this model), convergence of the inchworm calculations to the equilibrium result is only achieved at orders 5, 6 and 7. The correspondence between inchworm order truncation and the number of crossings in an N-crossing approximation (such as NCA, OCA, or the two-crossing approximation) implies that a large number of crossings is essential for obtaining correct results in the correlated metallic regime.

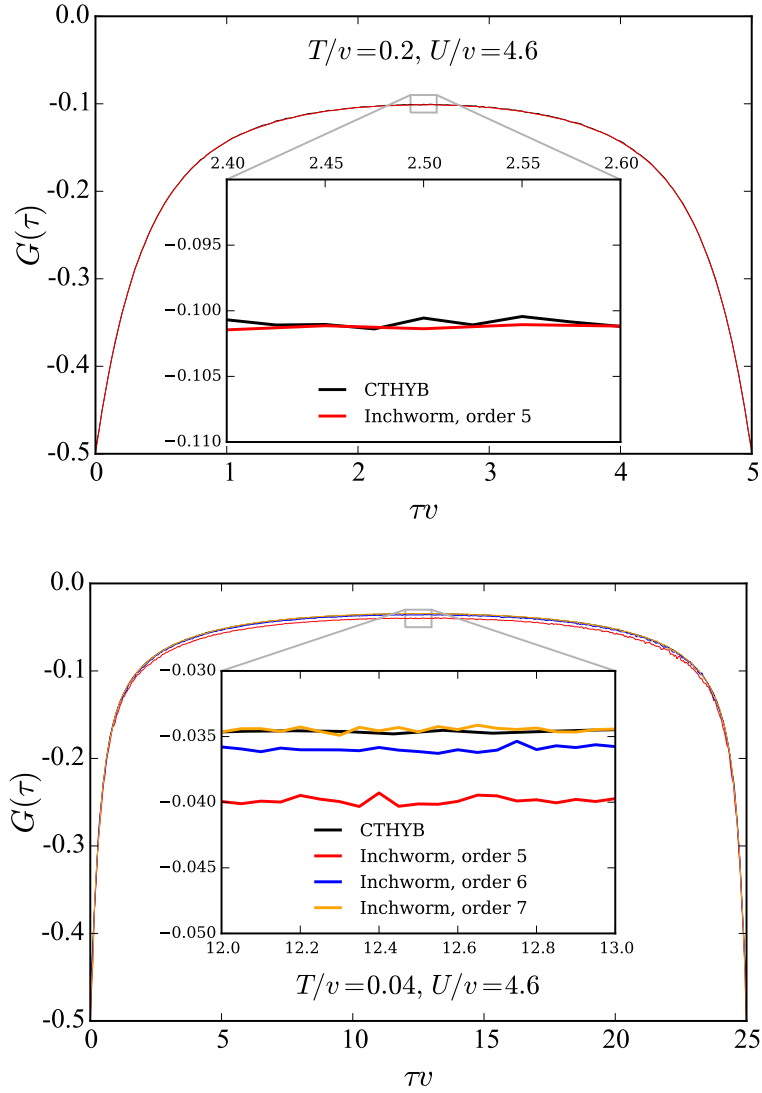


Figure 7.11: Matsubara Green's function $G(\tau)$ computed for the impurity model in equilibrium with $U/v = 4.6$ at two temperatures and with different inchworm order truncations. Results from an equilibrium hybridization expansion solver (TRIQS/CTHYB[71, 204]) are given as a reference.

Robustness of linear prediction

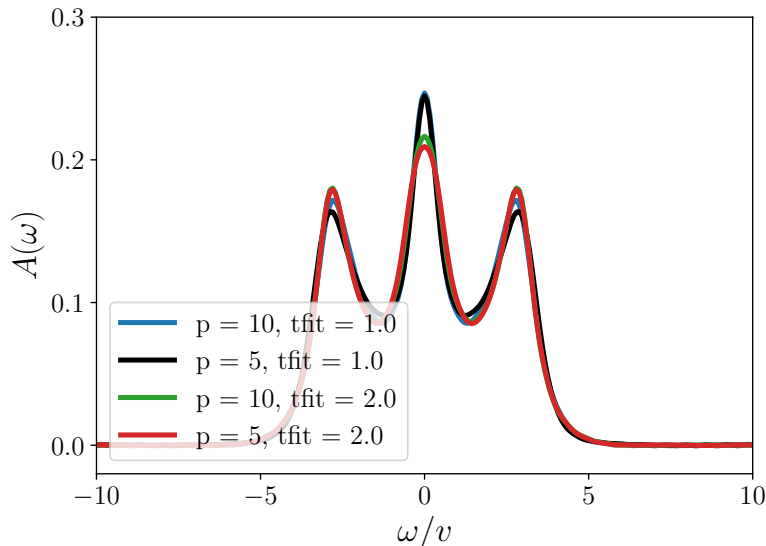


Figure 7.12: The converged DMFT spectral function $A(\omega)$ obtained by extrapolating the real-time Green's function from $t = 2.0$ to $t = 10.0$ using linear prediction with $p = \{5, 10\}$, $t_{\text{fit}} = \{1.0, 2.0\}$ for $U = 4$ at temperatures $T = 0.05$.

Linear prediction, introduced in Sec. 7.2 in the main text, is a method used to extrapolate data known up to a finite cutoff time to much longer times, such that smooth spectral functions can be extracted. The method can only succeed if the underlying data contains enough information to represent the long-time behavior accurately, and is expected to fail if this is not the case. In practice, two control parameters are available. First, the number of components (poles) p that is being fitted. Second, the time interval over which the data is extrapolated.

Fig. 7.7 and Fig. 7.8 in the main text show the behavior of the spectral function and the real-time Green's function on the final time. Fig. 7.12 and Fig. 7.13 show the dependence of the converged DMFT spectral functions on the number of poles p and the maximum fitting time. Plotted are the converged dynamical mean field spectral functions obtained by extrapolating the real-time Green's function from $tv = 2$ to $tv = 10$.

Clear differences in the data are visible in the height of the quasi-particle peak, the height of the four peaks in the insulating regime, and the size of the dip separating the quasiparticle feature from the Hubbard side bands. The ambiguities become less pronounced when the time accessed is increased. In any case, the main features, in particular the existence of a quasiparticle peak in the metal or of a double peak structure

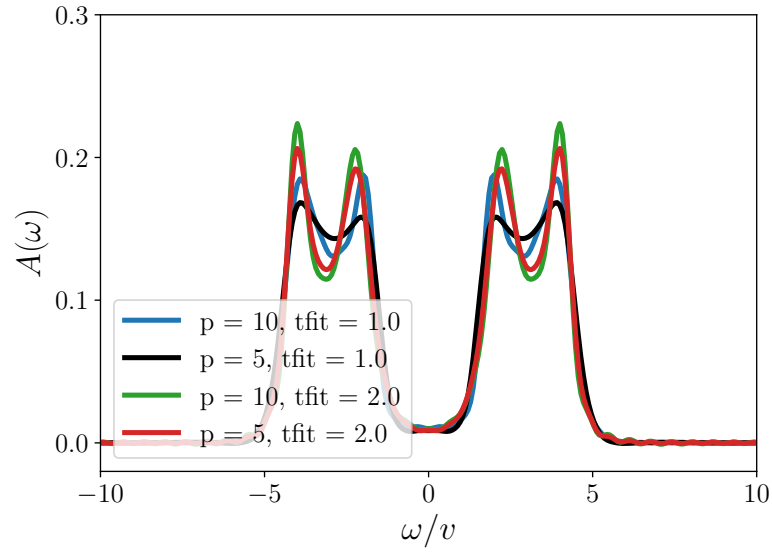


Figure 7.13: The converged DMFT spectral function $A(\omega)$ obtained by extrapolating the real-time Green's function from $tv = 2.0$ to $tv = 10.0$ using linear prediction with $p = \{5, 10\}$, $t_{\text{fit}}v = \{1.0, 2.0\}$ for $U/v = 6$ at temperature $T/v = 0.5$.

above and below the Mott gap are clearly evident in our data.

Self-energy extraction: technical issues

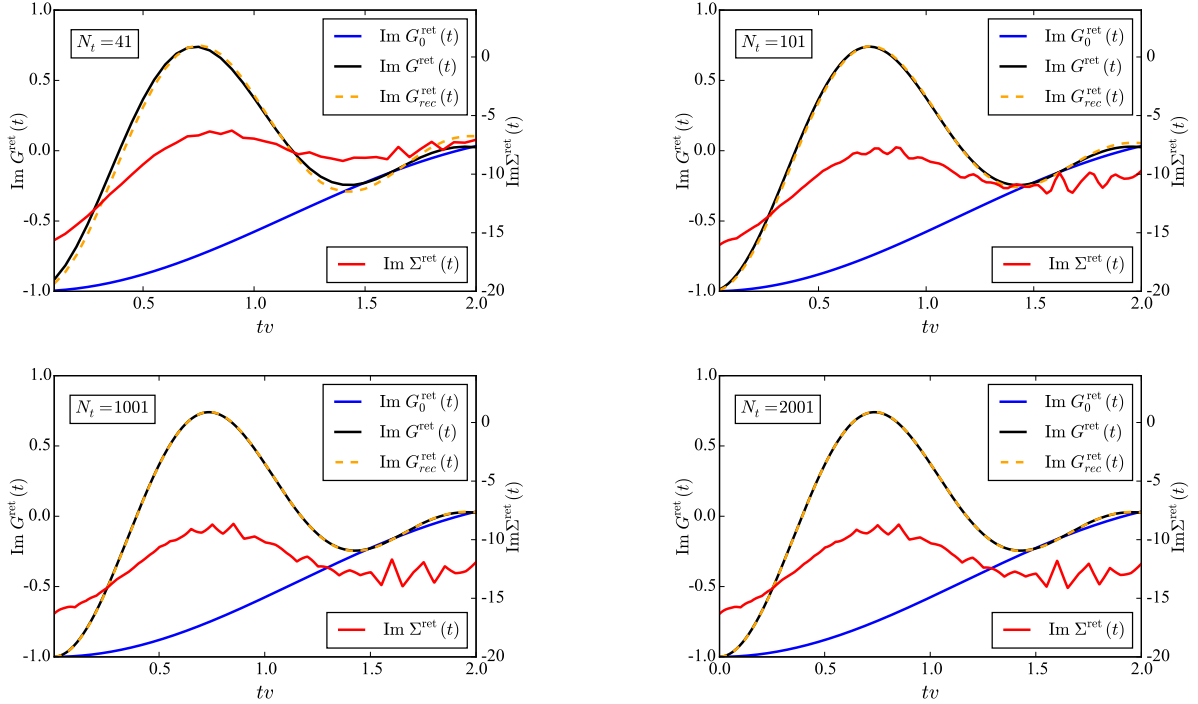


Figure 7.14: Retarded components of the DMFT Green's function, bare Green's function and self-energy computed in equilibrium with $U/v = 8.0$ at $T/v = 0.5$. The self-energy curves are obtained by a direct solution of the Dyson equation in its discretized matrix form. $G^{\text{ret}}(t)$ has been measured on 41 time slices, while a larger number of slices and cubic interpolation have been used to perform matrix inversions. The four subplots correspond to different numbers of interpolation points. $G_{\text{rec}}^{\text{ret}}(t)$ (orange curve) is a Green's function reconstructed by iterative substitution of $\Sigma^{\text{ret}}(t)$ into the Dyson equation. Top left: 41 slices. Top right: 101 slices. Bottom left: 1001 slices. Bottom right: 2001 slices.

Being limited by the complexity of the inchworm algorithm, we have to take a sparse time grid for the real-time Green's function $G_{\sigma}(t)$ and its retarded counterpart $G_{\sigma}^{\text{ret}}(t)$. The grid step Δtv used throughout this work is equal to 0.05, while $t_{\text{max}}v \in \{2.0, 4.0\}$.

The self-energy extraction procedure presented in section 7.2 involves a rectangular rule discretization of the time integrals, a first order scheme in Δt . We have found that effect of the discretization error rapidly grows as we propagate to larger times in $\Sigma_{\sigma}^{\text{ret}}(t)$. It is therefore crucial to introduce a finer time grid, and interpolate $G_{\sigma}^{\text{ret}}(t)/G_{0,\sigma}^{\text{ret}}(t)$ between the original nodes before doing matrix inversions. Fig. 7.14 shows self-energy extraction results for $T/v = 0.5$, $U/v = 8.0$, computed with $N_t = 41$ (the original number of points), 101, 1001 and 2001 interpolation slices. One can clearly see a drastic difference in the

self-energy curves for $N_t = 41$ and 2001. On the other hand, there is no visible difference between $N_t = 1001$ and 2001, which means the interpolation has converged.

The dashed orange curves are obtained by back-substitution of $\Sigma^{\text{ret}}(t)$ into a trapezoidal-rule discretization of the Dyson equation (7.5) (different choice of w_{ij}). For $N_t = 1001, 2001$ they lie on top of the input Green's function, which also signals convergence.

Short time limit of $\Sigma^{\text{ret}}(t)$

$$\Sigma^{\text{ret}}(t) = \int_{-\infty}^{+\infty} \frac{d\omega}{2\pi} e^{-i\omega t} \Sigma^{\text{ret}}(\omega). \quad (7.15)$$

Let us introduce a rescaled frequency $z = \omega t$ and consider a short time limit of the self-energy,

$$\Sigma^{\text{ret}}(0^+) = \lim_{t \rightarrow 0^+} \frac{1}{t} \int_{-\infty}^{+\infty} \frac{dz}{2\pi} e^{-iz} \Sigma^{\text{ret}}(z/t). \quad (7.16)$$

$\Sigma^{\text{ret}}(z/t)$ is an analytic function in the upper half-plane of z for any positive t . We now employ a high-frequency expansion of the self-energy in the absence of a Hartree-Fock term,

$$\Sigma^{\text{ret}}(\omega) = \lim_{\delta \rightarrow 0^+} \sum_{m=1}^{\infty} \frac{C^{(m)}}{(\omega + i\delta)^m}, \quad (7.17)$$

$$\Sigma^{\text{ret}}(0^+) = \lim_{t \rightarrow 0^+} \frac{1}{t} \lim_{\delta \rightarrow 0^+} \sum_{m=1}^{\infty} \int_{-\infty}^{+\infty} \frac{dz}{2\pi} e^{-iz} \frac{t^m C^{(m)}}{(z + i\delta t)^m} \quad (7.18)$$

It is easy to see that only the $m = 1$ term contributes in the limit of $t \rightarrow 0^+$.

$$\begin{aligned} \Sigma^{\text{ret}}(0^+) &= \lim_{t \rightarrow 0^+} \lim_{\delta \rightarrow 0^+} \int_{-\infty}^{+\infty} \frac{dz}{2\pi} e^{-iz} \frac{C^{(1)}}{z + i\delta t} \\ &= \lim_{t \rightarrow 0^+} \lim_{\delta \rightarrow 0^+} (-ie^{-\delta t} C^{(1)}) \\ &= -iC^{(1)}. \end{aligned} \quad (7.19)$$

For the symmetric single orbital Anderson model $C^{(1)} = U^2/4$ (independent of bath parameters). For a derivation see, for instance, Ref. [205]. Given this,

$$\Sigma^{\text{ret}}(0^+) = -iU^2/4. \quad (7.20)$$

CHAPTER VIII

Nonequilibrium Metal–Insulator Transitions

8.1 Introduction

Strongly correlated materials (SCMs) such as transition metal oxides exhibit remarkable intrinsic switching properties down to the nanoscale, making them an exciting future alternative to semiconductor technology [206]. Hysteretic resistive switching effects driven by electric fields, currents, Joule heating, or photoexcitation have received much experimental [207–224] and theoretical [225–231] attention in this context. Applications include both transistors [232–237] and memristors [238–243]. Additionally, memristive systems based on SCMs promise to enable neuromorphic devices that mimic the behavior of biological neurons [244–248]. It is thought that such devices could offer lower power consumption and comparable—or even faster—switching timescales than traditional semiconductor electronics [249–251]. At the core of such devices is the physics of Mott metal–insulator transitions.

Here, we describe and solve a simple model showing that a Mott metal–insulator transition can be driven by proximity to a metallic region. Furthermore, we propose a potential nanoscale device for realizing this effect and show that switching between the two states of the device can in principle be achieved on ~ 100 ps timescales. The device may be operated as either a transistor, where the system is switched fully across the phase transition; or as a memristor, taking advantage of memory effects in the coexistence region.

8.2 Model

We study the repulsive, fully frustrated, single-band Hubbard model on the infinite coordination number Bethe lattice, each site of which is coupled to a noninteracting

fermion bath [252–254]. The Hamiltonian describing the Hubbard lattice is given by

$$H_{\text{lattice}} = -v \sum_{\langle ij \rangle, \sigma} c_{i\sigma}^\dagger c_{j\sigma} + U \sum_i n_{i\uparrow} n_{i\downarrow}, \quad (8.1)$$

where $c_{i\sigma}^\dagger$ ($c_{i\sigma}$) creates (annihilates) lattice fermions with spin σ on site i ; v is the lattice hopping matrix element; and U is the on-site Coulomb repulsion. We use the hopping v as our unit of energy, \hbar/v as our unit of time and set $\hbar \equiv 1$. For example, a bare bandwidth of 4 eV would set our unit of time to be 0.66 fs. In the infinite coordination number limit considered here, this model may be solved exactly via the dynamical mean field theory (DMFT) [24, 25] and is known to exhibit a first order Mott metal–insulator transition as a function of the interaction strength U [28].

The Hamiltonian describing the baths is given by

$$H_{\text{bath}} = \sum_i H_{\text{bath}}^{(i)}, \quad (8.2a)$$

$$H_{\text{bath}}^{(i)} = \sum_{k\sigma} \epsilon_k b_{ik\sigma}^\dagger b_{ik\sigma} + \sum_{k\sigma} V_k(t) c_{i\sigma}^\dagger b_{ik\sigma} + V_k^*(t) b_{ik\sigma}^\dagger c_{i\sigma}. \quad (8.2b)$$

Here, $b_{ik\sigma}^\dagger$ ($b_{ik\sigma}$) creates (annihilates) bath fermions coupled to site i with spin σ and quasimomentum k , and $V_k(t)$ is the tunneling matrix element describing hopping between the lattice and the baths. The time dependence of the bath hopping is parameterized by a dimensionless coupling strength $\lambda(t)$ so that $V_k(t) = \lambda(t)V_k$. The baths are held in equilibrium, with their chemical potential set equal to zero. The effect of the baths is characterized by a coupling density $\Gamma_{\text{bath}}(\omega) = \pi \sum_k |V_k|^2 \delta(\omega - \epsilon_k)$ that parameterizes the bath dispersion ϵ_k and tunneling matrix elements V_k . We choose a flat coupling density with soft-edges $\Gamma_{\text{bath}}(\omega) = \Gamma / [(1 + e^{\nu(\omega-D)}) (1 + e^{-\nu(\omega+D)})]$, with parameters $\Gamma = 1v$, $\nu = 10v^{-1}$ and $D = 4v$. Time dependent manipulation of the bath coupling has previously been introduced as a method to induce cooling of the system [255, 256].

8.3 Methods

An exact solution of the model on the infinite coordination number Bethe lattice is given by the nonequilibrium DMFT mapping [30]. DMFT maps the lattice model to an Anderson impurity model with a self-consistently determined hybridization function $\Delta_\sigma(t, t')$ given

by

$$\begin{aligned} \Delta_\sigma(t, t') &= v^2 G_\sigma(t, t') \\ &+ \lambda(t) \Delta_{\text{bath}}(t, t') \lambda(t'), \end{aligned} \tag{8.3}$$

where $G_\sigma(t, t')$ is the impurity Green's function; $\Delta_{\text{bath}}(t, t')$ is the hybridization between the lattice and bath; and $\lambda(t)$ is the time-dependent coupling strength. The equations are solved by starting with an initial guess for $\Delta_\sigma(t, t')$, evaluating the impurity Green's function, and iterating until a self-consistent solution is found. In the coexistence region, the insulating and metallic solutions are found by choosing an initial guess with or without a gap respectively, otherwise the initial guess has no effect on the solution once the self-consistency has converged. These equations are formulated on the three-branch Keldysh–Matsubara contour. Because our contour includes a Matsubara branch, the initial state of the system is always a solution of the equilibrium DMFT equations.

For the solution of the impurity model we use the one crossing approximation (OCA) [53, 54, 257]. In equilibrium the OCA is known to capture the qualitative physics of the Mott transition with reasonable accuracy [67]. We further validate our OCA results against numerically exact inchworm QMC[31, 32, 55] data in the parameter regime where this is feasible (see section 8.6).

The main physical quantity of interest is the time-dependent spectral function $A(\omega, t)$ which may be defined in a number of different ways out of equilibrium. Here, we use the auxiliary lead formalism [46–48] to express the time-dependent spectral function as

$$A(\omega, t) = \lim_{\eta \rightarrow 0} -\frac{2\hbar}{e\pi\eta} [I_A^f(\omega, t) - I_A^e(\omega, t)], \tag{8.4}$$

where $I_A^f(\omega, t)$ and $I_A^e(\omega, t)$ are currents through two auxiliary leads with coupling density $\Gamma_A(\omega') = \eta\delta(\omega' - \omega)$, and with chemical potentials set such that the leads are full and empty respectively. These auxiliary currents are calculated using the Meir–Wingreen formula [153] applied to the local Green's function $G_\sigma(t, t')$ computed by the impurity solver. This definition matches the conventional equilibrium spectral function $A(\omega) = (-1/\pi) \text{Im } G^r(\omega)$ in steady state, provides frequency rich spectral information at all times, and has an operational realization.

Using this formalism we compute $A(\omega = 0, t)$ which in steady state gives the density of states at the Fermi energy and allows us to determine whether the system is in a metallic or insulating state. Outside of the steady state regime the auxiliary current spectral function inevitably mixes together the dynamics of the system with the dynamics of the

auxiliary leads themselves. This mixing is unavoidable and is an expression of the fact that one cannot give an instantaneous value to a frequency dependent quantity that strictly speaking requires integration over all times. Nevertheless, the auxiliary current spectrum is useful in understanding the non-equilibrium dynamics of the system since as it approaches a quasi-steady state it becomes conventionally interpretable.

8.4 Results

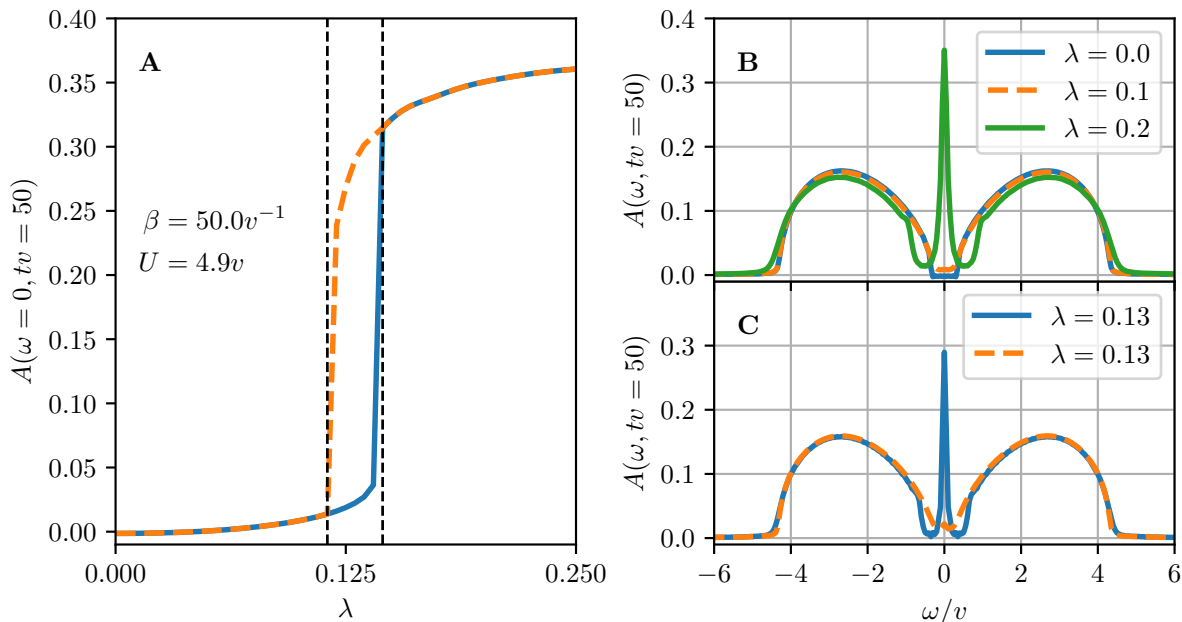


Figure 8.1: **A**: Spectral weight at $\omega = 0$ as a function of λ for metallic (dashed orange) and insulating (solid blue) initialization of the DMFT loop. The dashed black lines show the boundaries of the coexistence region ($\lambda_{c_1} = 0.115$, $\lambda_{c_2} = 0.145$). **B**: Spectral function for several different λ . **C**: Spectral functions of metallic and insulating solutions in the coexistence region.

Fig. 8.1 shows the equilibrium spectral function of the system as a function of the time-independent bath coupling λ . The interaction strength U is set to $4.9v$ and the inverse temperature β is set to $50v^{-1}$. The inverse temperature of the fermion baths is held constant at this β throughout the simulation and their chemical potential is set equal to zero. These parameters are chosen so as to generate a sizable coexistence region, and are used throughout the rest of this chapter. The maximum simulation time t_{\max} is set to $50.0v^{-1}$, which is long enough to resolve sharp features in the spectrum. Fig. 8.1A shows that $A(\omega = 0)$ increases by several orders of magnitude as λ is varied from 0.0 to 0.25,

for both metallic (dashed orange) and insulating (blue) initializations of the DMFT loop. The system goes through a first order phase transition from an insulating state at small λ to a metallic state at large λ . The area between the vertical dashed black lines denotes the coexistence region, where both metallic and insulating solutions are stable, as seen from the gap between the curves representing the two initializations. Fig. 8.1B shows the full spectral function for several different values of the bath coupling λ . When the coupling λ becomes large enough, metallicity is induced and a sharp quasiparticle peak forms at $\omega = 0$. Finally, Fig. 8.1C shows the full spectral function for the metallic and insulating solutions within the coexistence region. The two phases remain distinguishable by the presence of a sharp quasiparticle peak in the metal. This phase transition may be interpreted as arising from the bath coupling λ inducing a smaller effective U value and moving the system across the traditional interaction driven transition.

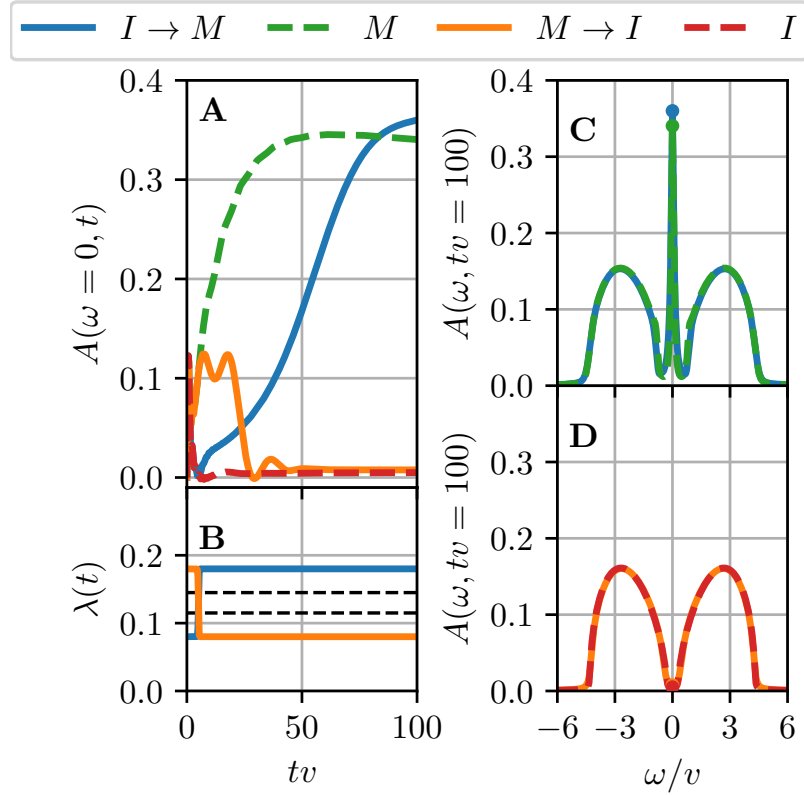


Figure 8.2: **A:** Evolution of $A(\omega = 0, t)$ for equilibrium metallic and insulating solutions (dashed green/red) and for switched solutions (solid orange/blue). **B:** Switching protocol for $\lambda(t)$. Dashed black lines show the coexistence region. **C:** $A(\omega, tv = 100)$ for equilibrium metal (dashed green) and “switched” metal (solid blue). **D:** $A(\omega, tv = 100)$ for equilibrium insulator (dashed red) and “switched” insulator (solid orange).

With the equilibrium phase diagram established, we now consider two switching protocols, implemented by time dependent bath couplings $\lambda(t)$, which flip the system between the metallic and insulating phases. In the first switching protocol, the system begins in equilibrium on one side of the phase transition. At time t_0 , the bath coupling λ is rapidly quenched to a value on the opposite side. This switching protocol is described by

$$\begin{aligned}\lambda(t) &= (1 - f(t))\lambda_0 + f(t)\lambda_1, \\ f(t) &= \frac{1}{1 + e^{-\xi(t-t_0)}},\end{aligned}\tag{8.5}$$

where ξ sets the switching rate; t_0 sets the time when the switch is applied; and λ_0 (λ_1) sets the initial (final) bath coupling. Fig. 8.2 shows the effect of this protocol on the system for four pairs of (λ_0, λ_1) : (λ_M, λ_M) (equilibrium metal), (λ_I, λ_I) (equilibrium insulator), (λ_M, λ_I) (“switched” insulator), and (λ_I, λ_M) (“switched” metal). We take $\xi = 10v$, $t_0v = 5$, $t_{\max}v = 100$, $\lambda_I = 0.08$, and $\lambda_M = 0.18$. In Fig. 8.2A we plot the time evolution of $A(\omega = 0)$. Note that even in the equilibrium cases (M, I) $A(\omega = 0)$ shows some time-dependence due to the auxiliary lead formalism which we use to compute the spectral function. In the metal to insulator ($M \rightarrow I$) transition, the switch rapidly destroys the metal ($A(\omega = 0)$ is suppressed). In the insulator to metal ($I \rightarrow M$) transition, the system gradually builds up spectral weight at $\omega = 0$ after the switch to form a metal. It is interesting to note that the formation of the metal proceeds much slower than the destruction of the insulator. A slowdown in the formation of a quasi-particle peak after a quench from the atomic limit near the Mott transition has previously been observed [258]. However, with the λ quench considered here the previously observed electronic bottleneck appears to be mostly overcome and the slowdown does not prevent the formation of a quasi-particle peak with a comparable weight to the equilibrium metal within the simulation timescale. Figs. 8.2C and 8.2D show the full spectral function at t_{\max} for all four realizations of the protocol. The full spectra of the “switched” solutions closely resemble the corresponding equilibrium solutions, demonstrating that the protocol can switch the system between metallic and insulating states. Additionally, the width of the quasi-particle peak for the equilibrium metal and “switched” metal are comparable suggesting the absence of significant heating effects.

We now consider a second switching protocol in which the system begins in equilibrium in the center of the coexistence region, in either the metallic or insulating phase. At time t_0 the bath coupling is rapidly quenched to momentarily place the system outside of the

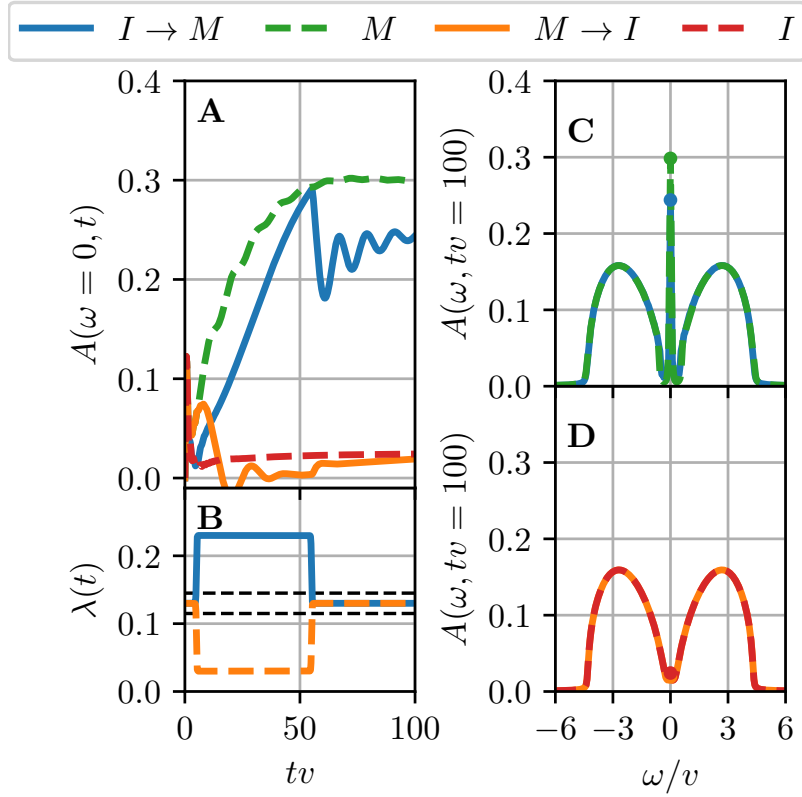


Figure 8.3: **A**: Evolution of $A(\omega = 0, t)$ for equilibrium metallic and insulating solutions (dashed green/red) and for switched solutions (solid orange/blue). **B**: Switching protocol for $\lambda(t)$. Dashed black lines show the coexistence region. **C**: $A(\omega, tv = 100)$ for equilibrium metal (dashed green) and “switched” metal (solid blue). **D**: $A(\omega, tv = 100)$ for equilibrium insulator (dashed red) and “switched” insulator (solid orange).

coexistence region on either side of the transition; then, at time t_1 , the bath coupling reverts to its initial (coexistence) value. The second switching protocol is described by

$$\lambda(t) = (1 - f(t))\lambda_0 + f(t)\lambda_1, \quad (8.6)$$

$$f(t) = \frac{1}{(1 + e^{\xi(t-t_1)})(1 + e^{-\xi(t-t_0)})},$$

where ξ sets the switching rate; t_0 and t_1 bound the switching interval; and λ_0 and λ_1 set the initial/final and intermediate values of the bath coupling, respectively. Fig. 8.3 shows the results of this switching protocol on the system for three pairs of (λ_0, λ_1) : (λ_c, λ_c) , $(\lambda_c, \lambda_c + \Delta\lambda)$ and $(\lambda_c, \lambda_c - \Delta\lambda)$, where $\lambda_c = (\lambda_{c1} + \lambda_{c2})/2$ is in the center of the coexistence region, and $\Delta\lambda = 0.1$ is large enough to move the system outside of the coexistence region in either direction. The other parameters are given by $\xi = 10v$, $t_0v = 5$, $t_1v = 55$,

and $t_{\max}v = 100$. For the equilibrium case we show both the metallic and insulating solutions. Fig. 8.3A shows the time evolution of the spectral function at the Fermi energy. In the ($M \rightarrow I$) transition, $A(\omega = 0)$ is quickly destroyed during the switch, and does not return when the bath coupling reverts to the coexistence region. In the insulator to metal ($I \rightarrow M$) transition, $A(\omega = 0)$ builds up to almost its equilibrium value during the switching period. Afterwards, the spectral weight drops somewhat, but then recovers and appears to stabilize. Panels C and D of Fig. 8.3 show the long-time spectral function $A(\omega, t_{\max})$ for each of the four time evolutions. Again, the full spectra of the “switched” solutions closely match the corresponding equilibrium solutions, demonstrating that the second protocol can switch the system between metallic and insulating states within the coexistence region.

We note that for both protocols the overall switching time, i.e. the crossover time between the two phases, assuming a band width of several eV for the SCM, is on the order of ~ 100 ps. It is important to realize that this prediction describes only the timescale needed for the electronic transitions to occur, and our minimal model does not consider any other constraints that may appear in experiments. One should also note that this timescale is dominated by the slower transitions to the metallic state, whereas the transitions to the insulating state are substantially faster.

Having demonstrated the ability to dynamically control the phase of our model system through $\lambda(t)$, we shift our attention to potential experimental realizations of this effect. Fig. 8.4 shows an illustration of a proposed device for achieving dynamic control of $\lambda(t)$. The core of our device consists of a SCM separated from a metal by a nanoscale, compressible, and weakly insulating region possibly composed of several polymer nanolayers. Electronic transport across this region should be dominated by quantum tunneling effects. This core is electrically isolated by two insulating regions and sandwiched between the plates of a capacitor (outer metallic plates). Charging the capacitor generates a force which squeezes the compressible insulator and reduces the separation L between the metal and SCM. Since the tunneling rate $\lambda \sim e^{-L/\zeta}$ depends exponentially on the separation, we expect that (at the nanoscale) large variations in λ can be achieved on fast timescales without the need for very large voltages or compression ratios. This device may be operated in two modes. In the first mode, the gate voltage across the capacitor is externally manipulated (blue signal generator in Fig. 8.4) to control the source-drain current via the SCM metal–insulator transition, making the device a transistor. In the second mode, the gate voltage across the capacitor is coupled to the source–drain voltage (red connections in Fig. 8.4), making the device a two terminal memristor.

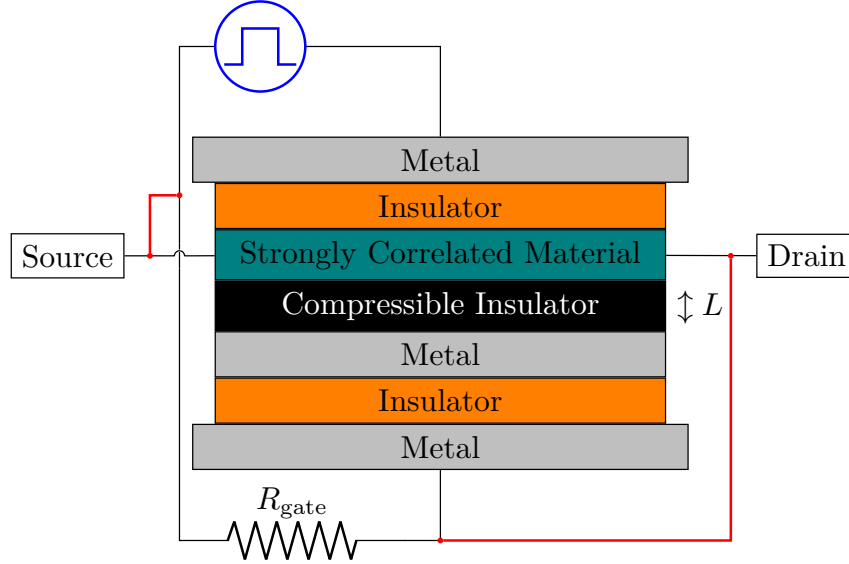


Figure 8.4: Illustration of proposed device for realizing dynamic control of $\lambda(t)$. The voltage between the outer metallic plates can be controlled in two ways depending on the mode of operation of the device. Without the red connections, the voltage between the plates is modulated by an external signal (blue circle) and the device is operated as a transistor. Adding the red connections couples the voltage between the plates to the source-drain voltage and turns the device into a two terminal memristor.

Due to computational cost, we are only able to fully simulate one switching event. In order to further investigate and characterize the dynamics of the proposed device we consider a simple phenomenological Ginzburg–Landau model of the Mott metal–insulator transition [259–262]. In this framework, we assume that the state of the system around the phase transition is governed by a potential

$$\Phi(x, \lambda) = -(\lambda - \lambda_c)x - \frac{1}{2}x^2 + \frac{1}{4}x^4, \quad (8.7)$$

where $\lambda_c = (\lambda_{c_1} + \lambda_{c_2})/2$ is at the center of the coexistence region. We take the order parameter x to be related to the resistivity of the SCM by $R_{\text{SCM}} = R_0 e^{-\alpha x}$. At $\lambda = \lambda_c$ this potential has two stable minima at $x = \pm 1$ corresponding to metallic/insulating states with a resistivity ratio of $\exp(-2\alpha)$. The minimal equation of motion for x is given by $\partial_t x(t) = -(1/\tau)\partial_x \Phi(x, \lambda(t))$ which describes exponential relaxation to equilibrium with timescale τ .

We now apply this formalism to study the expected characteristics of our proposed device when configured as a memristor. In the memristor setup, the gate voltage across the capacitor is set by the source–drain voltage $V(t)$. We assume that the compression of

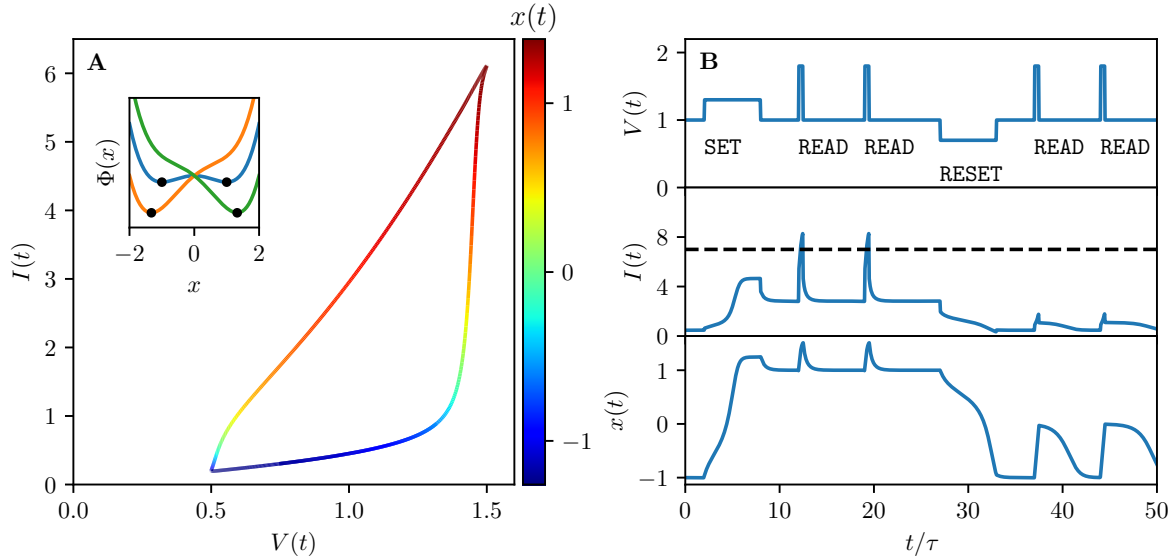


Figure 8.5: Simulation of the system configured as a two terminal memristive device. **A**: Current voltage characteristic of device under sinusoidal driving. The inset shows the shape and minima of the potential $\Phi(x, \lambda)$ at $\lambda = \lambda_c, \lambda_c \pm 1$. **B**: Use of device as a resistive memory element.

the insulator is linear in the applied force so that, to leading order, the tunneling rate is given by $\lambda(t) = \gamma V^2(t) + \delta$. Note that since λ couples to the voltage squared, the device must be operated around a finite bias in order to have bidirectional control over λ . For the device parameters we set $\lambda_c = 1$, $\gamma = 1$, and $\delta = 0$ so that at $V = 1$ the system is in the center of the coexistence region. Additionally, we set $R_{\text{gate}} = 10$, $R_0 = 1$, and $\alpha = 1$ so that the resistivity ratio between the insulating and conducting states is $\exp(2) \approx 7.4$. Finally, we use $\tau = 1$ as our time unit.

Fig. 8.5A shows the current–voltage characteristics (IV) of the device when driven by a sinusoidal voltage $V(t) = 1 + \frac{1}{2} \sin\left(\frac{t}{4}\right)$, where we assume that the current through the device is given by Ohm’s law. The IV forms a hysteresis loop due to the memory effect of the order parameter x . In the upper part of the loop, we have $x \approx 1$; the SCM is in the metallic state; and the current is high. In the lower part of the loop, we have $x \approx -1$; the SCM is in the insulating state; and the current is low. Note that the hysteresis loop is not “pinched” (i.e. does not pass through the origin) as expected for ideal memristors [263] because we are operating around a finite voltage bias.

Fig. 8.5B demonstrates usage of the device as a resistive memory element. The device is operated around a finite voltage bias $V_0 = 1$ so that the SCM is in the center of the

coexistence region and both high and low resistivity states are stable. The binary state of the device is encoded in the order parameter $x \approx \pm 1$. Here the device is driven by a sequence of different pulses. The **SET** pulse is a long low amplitude square pulse which moves the system from the $x = -1$ to the $x = 1$ state. The **READ** pulse is a short high amplitude square pulse which causes the current to spike above a threshold (black dashed line) if the SCM is in the low resistivity ($x = 1$) state. The **RESET** pulse is a long low amplitude square pulse with opposite polarity to the **SET** pulse which moves the system from the $x = 1$ to the $x = -1$ state. Combinations of these pulses allow operation of the device as a two terminal, resistive memory element.

8.5 Conclusions

We have demonstrated that the repulsive, fully frustrated, single-band Hubbard model on the infinite coordination number Bethe lattice undergoes a first order metal–insulator transition as a function of a coupling to a set of free fermion baths. By time-dependent manipulation of this coupling we are able to dynamically switch the system between its metallic and insulating states both outside and inside the coexistence region. We propose that this effect may be realized in a nanoscale device based on manipulation of the proximity between a metal and a SCM. Analysis of a simple model of such a device shows that it could be operated as a resistive memory element. These results suggest a variety of directions for future work.

From a theoretical perspective, replacing the OCA impurity solver with a numerically exact method [31, 32, 55, 83, 84, 156, 264] would allow us to obtain a better quantitative understanding of the timescales involved in the switching process. It would also be of interest to investigate this type of bath-driven switching in finite dimensional models with more realistic baths and for other metal–insulator transitions, such as the transition between an anti-ferromagnetic insulator and paramagnetic metal seen in VO_2 . Additionally, it would be interesting to investigate the effect of including spatial inhomogeneities [265] and transport in our microscopic model.

Experimentally, we expect that a variety of ways to harness this novel switching mechanism in nanoelectronic devices and nanoscale layered materials will emerge. Progress in this direction will rely on finding a compressible insulator with appropriate specifications, and on fabrication techniques. While our results suggest that the fundamental limit on switching and readout time could theoretically be on the order of femtoseconds, it remains to be seen whether other limitations and engineering considerations might dominate

in practical setups. Nevertheless, the promise of being able to fabricate an efficient single-crystal memristor is certain to make the experimental challenges worth facing.

8.6 Appendix

Inchworm Comparison

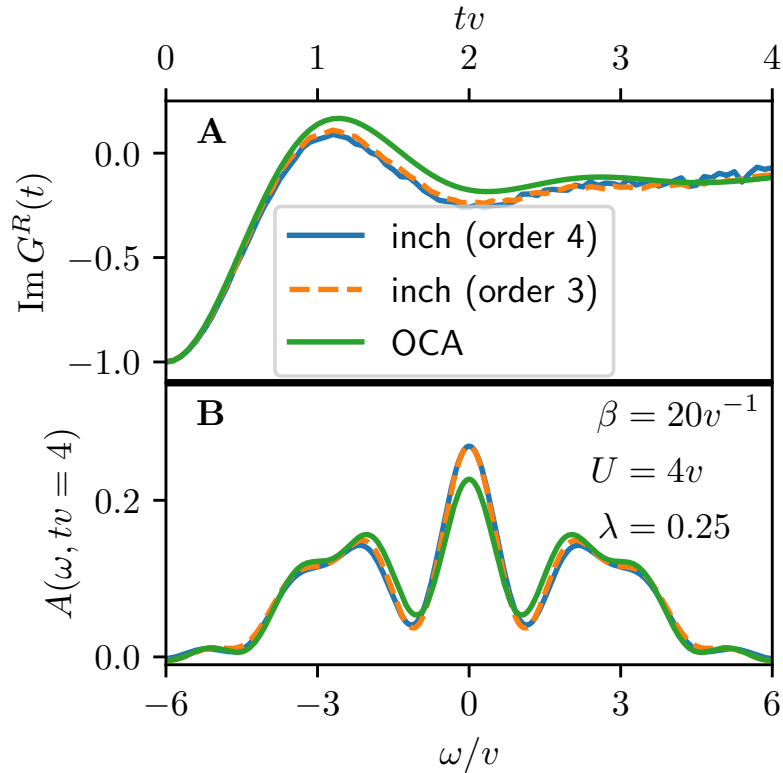


Figure 8.6: Comparison of the retarded Green's function (**A**) and spectral function (**B**) obtained from OCA (green) and inchworm (blue/orange) at $\beta = 20v^{-1}$, $U = 4.0v$, $\lambda = 0.25$.

Fig. 8.6 shows a comparison between results obtained using the one crossing approximation (OCA) and the inchworm QMC method. The parameters are chosen in order to make the inchworm calculations computationally feasible. The inchworm results are fully converged with order and numerically exact. The OCA somewhat underestimates the height of the quasi-particle peak but otherwise captures the spectrum well. These results support the reliability of OCA in capturing the real-time dynamics of the system.

CHAPTER IX

Conclusions and Outlook

In this thesis, we described several methods for the solution of the Anderson impurity model out of equilibrium, most notably the inchworm algorithm which is numerically exact and successfully overcomes the dynamical sign problem. We then applied these methods to study systems of physical interest including a voltage biased quantum dot in the Kondo regime, and a Mott metal-insulator transition in the Hubbard model via DMFT. There are a number of possible future directions building on this work.

It would be very interesting to extend the inchworm algorithm to the multi-orbital case which would open up a huge range of possible applications. This has already been done in equilibrium [80] where the inchworm algorithm was used to overcome the sign problem which appears in imaginary time for certain multi-orbital models. The extension of this to nonequilibrium is theoretically straightforward but the implementation may be technically challenging.

It would be highly desirable to develop algorithmic improvements to decrease the cost of the inchworm algorithm. Although the current inchworm algorithm overcomes the exponential scaling of the bare expansion, it is still quite expensive and reaching very long times is difficult. This is problematic because interesting physics often occurs at relatively long timescales, see e.g. the metal-insulator transition described in chapter 8 which requires access to a timescale on the order of 100 times the inverse hopping which is currently prohibitively expensive for inchworm. One approach to this problem is simply raw optimization of the existing algorithm. For example, it should be possible to cache the sub-determinants used in the fast algorithm for the hybridization weight [81] which could allow the weight ratios for moves to be computed more efficiently. Along the same lines, it should be possible to cache subsets of the impurity trace as is done in optimized versions of the bare CT-HYB algorithm [71]. These kinds of optimizations are probably necessary for implementing a performant multi-orbital version of the existing algorithm.

Another avenue for improving the performance of the algorithm lies in improvements

to the integration method. Because inchworm is a bold technique, it is often unnecessary to go to extremely high orders, and at low order other integration techniques may be much more efficient than Markov Chain Monte Carlo (MCMC). A clue pointing in this direction is the fact that an OCA solver based on direct quadrature is orders of magnitude faster than the equivalent order 2 calculation with the inchworm algorithm based on MCMC. Clearly at some expansion order there will be a crossover where the curse of dimensionality makes quadrature impracticable but currently it is unclear what this expansion order actually is. Computing the low order contributions directly and only using Monte Carlo for the high order contributions would likely be advantageous. Another possible modification along these lines would be to use Quasi-Monte Carlo integration which was recently applied in the context of the interaction expansion for nonequilibrium quantum impurity models [85].

In addition to algorithmic improvements, it is also interesting to consider possible modifications to the expansion itself which might give it better characteristics. For example, in the interaction expansion approach to nonequilibrium impurity models, the dynamical sign problem has been overcome by explicitly summing over all Keldysh indices for the vertex insertions [83, 84]. It would be interesting to apply this same idea to the bare hybridization expansion and compare it with the inchworm approach. This idea could also be applied to the bold expansion for the Green's function.

It would also be interesting to explore a numerically exact summation of the entire skeleton series for the propagator self-energy. As we have seen, the inchworm expansion truncated at order $M + 1$ sums the same diagrams as the M -crossing approximation. By summing the skeleton series for the self-energy one would trade an expansion order for a self-consistency which could be advantageous.

By some combination of the suggestions given above, and techniques still waiting to be discovered, the next generation of solvers will enable further exploration of the fascinating field of non-equilibrium strongly correlated systems.

Appendices

APPENDIX A

NCA

In this appendix, we provided a simple annotated implementations of NCA. The algorithm is implemented in the [julia](#) language [266] using the [Keldysh.jl](#) package which provides primitives for representing nonequilibrium Green's functions. The code can be executed sequentially in a script or jupyter notebook. A version of this example is also [available](#) as part of the [Keldysh.jl](#) package.

First we install the necessary dependencies.

```
using Pkg
Pkg.activate(".")
Pkg.add(url="https://github.com/kleinhenz/Keldysh.jl", rev="v0.6.1")
Pkg.add(["PyPlot", "QuadGK"])
using LinearAlgebra, Printf
using PyPlot, QuadGK, Keldysh
```

We define a structure for representing the impurity Hilbert space. We represent the state of impurity as an unsigned integer between 0 and 3 with the values of first two bits representing the occupations of each spin.

```
# type representing state of anderson impurity
# occupation of up/down stored in first two bits
struct FockState
    state: UInt8
    function FockState(s)
        @assert s < 4
        new(s)
    end
end
```


We define functions for conveniently accessing and modifying the impurity state. Because we don't have to keep track of the sign from acting on the state these are implemented with simple bit twiddles.

```

@enum SpinEnum spin_up = UInt8(1) spin_down=UInt8(2)
Base.to_index(A, sp::SpinEnum) = Int(sp)
flip(sp::SpinEnum) = sp == spin_up ? spin_down : spin_up

# check whether ith spin is occupied
function Base.getindex(st::FockState, sp::SpinEnum)
    return (st.state & 1 << (UInt8(sp)-1)) > 0
end

# flip occupation of spin sp
function flip(st::FockState, sp::SpinEnum)
    return FockState(xor(st.state, 1 << (UInt8(sp)-1)))
end

# convert internal state to index
# add 1 because julia uses one based indexing
function Base.to_index(st::FockState)
    return Int(st.state + 1)
end

```

We define a function to compute a nonequilibrium Green's function from a density of states. This function implements equation 2.46. The integrand is rearranged so that all exponentials have negative real argument in order to avoid overflow. This function is included in `Keldysh.jl`, but written out here for completeness.

```

function dos2gf(dos, D, β, t1::BranchPoint, t2::BranchPoint)
    θ = heaviside(t1, t2)
    Δt = t1.val - t2.val
    f = ω -> (ω > 0.0 ?
        exp(-im * ω * (Δt - im * (1 - θ) * β)) / (exp(-β * ω) + 1)
        : exp(-im * ω * (Δt + im * θ * β)) / (exp(β * ω) + 1))
    integral, err = quadgk(ω -> f(ω) * dos(ω), -D, D)
    return -im * (2 * θ - 1) * integral
end

```

Using this we can compute and visualize the hybridization function for a flat band coupling density. Note we include a factor of $1/\pi$ in the definition of the coupling density because `dos2gf` implements equation 2.46 rather than equation 3.78.

```
function dos2gf_example()
  # first define a contour
  tmax, β = 5.0, 10.0
  c = twist(FullContour(; tmax, β))

  # now define a grid which represents a discretization of the contour
  nt, ntau = 101, 201
  grid = FullTimeGrid(c, nt, ntau)

  # construct a flat band coupling density  $\Gamma(\omega)$ 
  # Note we include a factor of  $1/\pi$  since this is NOT included in dos2gf
  Γ, D, ν, μ = 1.0, 5.0, 10.0, 0.0
  dos = DOS(-Inf, Inf, ω -> (Γ/π)*fermi(ν*(ω-μ-D))*fermi(-ν*(ω-μ+D)))

  # compute the hybridization function from the coupling density
  # equivalent to  $\Delta = FullTimeGF(dos, grid)$ 
  Δ = FullTimeGF(grid, 1, fermionic, true) do t1, t2
    dos2gf(dos, D, β, t1.bpoint, t2.bpoint)
  end

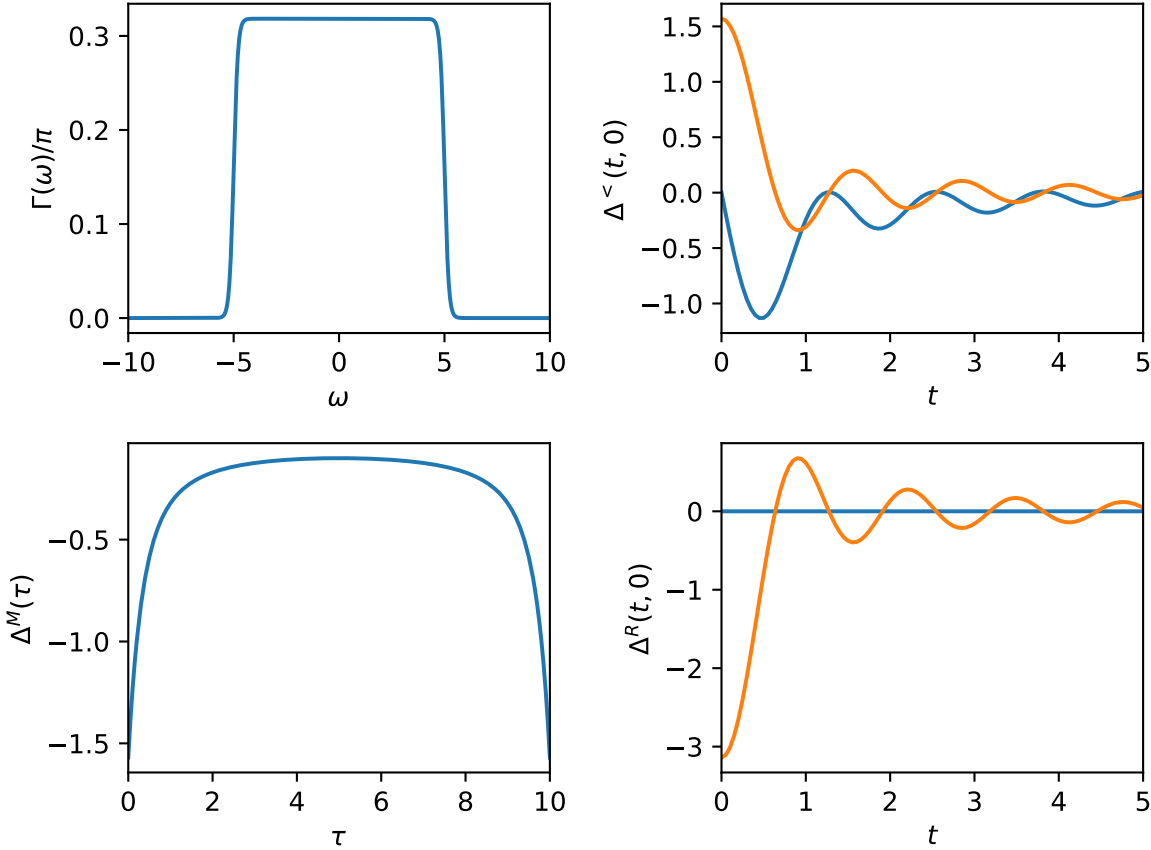
  # plot components
  fig, axes = plt.subplots(nrows=2, ncols=2)
  make_plot = (ax, xlabel, ylabel, t, f...) -> begin
    map(fi -> ax.plot(t, fi), f)
    ax.set_xlabel(xlabel); ax.set_ylabel(ylabel)
  end

  ω = range(-10.0, 10.0, length=1001)
  t = realtimes(grid)
  τ = imagtimes(grid)

  # extract components
  Δret = Δ[:retarded]
  ΔM = Δ[:matsubara]
  Δles = Δ[:lesser]

  make_plot(axes[1], L"ω", L"Γ(ω)/π", ω, dos.(ω))
  make_plot(axes[2], L"τ", L"Δ^M(τ)", τ, ΔM)
  make_plot(axes[3], L"t", L"Δ^<(t, 0)", t, real(Δles[:,1]), imag(Δles[:,1]))
  make_plot(axes[4], L"t", L"Δ^R(t, 0)", t, real(Δret[:,1]), imag(Δret[:,1]))
  fig.tight_layout()
  fig.savefig("keldysh_components.pdf")
end
dos2gf_example()
```

This code produces the following output where the real (imaginary) part is solid blue (dashed orange). Note the retarded Green's function has zero real part because the density of states is symmetric.



We define functions to compute the bare propagators. These functions implement equations 3.20 and 3.21. Note, on the two branch Keldysh contour we must provide the initial impurity density matrix. The grids are assumed to be defined on the twisted contour. The propagators $P_\alpha^{(0)}(t_1, t_2)$ are only needed for $t_1 \succ t_2$ on the twisted contour. The propagators are stored as an array of four `GenericTimeGF` objects representing the propagator for each state $|\alpha\rangle$. This puts the state index on the “outside”. In the multi-orbital case it would likely be more convenient to put the orbital indices on the inside as is done in [37].

```
function make_bare_prop(grid::KeldyshTimeGrid, ρ, ε, U)
    E = [0.0, ε, ε, 2*ε + U]
    ξ = [1.0, -1.0, -1.0, 1.0]
    P = map(1:4) do s
        GenericTimeGF(grid, 1, true) do t1, t2
            t1.cid < t2.cid && return 0.0
            φ = integrate(t -> E[s], grid, t1, t2)
            return (heaviside(t1.bpoint, t2.bpoint) ? -im*exp(-im*φ)
                : -im*ξ[s]*ρ[s]*exp(-im*φ))
        end
    end
    return P
end

function make_bare_prop(grid::FullTimeGrid, ε, U)
    E = [0.0, ε, ε, 2*ε + U]
    ξ = [1.0, -1.0, -1.0, 1.0]
    P = map(1:4) do s
        GenericTimeGF(grid, 1, true) do t1, t2
            t1.cid < t2.cid && return 0.0
            φ = integrate(t -> E[s], grid, t1, t2)
            return (heaviside(t1.bpoint, t2.bpoint) ? -im * exp(-im * φ)
                : -im * ξ[s] * exp(-im * φ))
        end
    end
    return P
end
```

We define structures for holding the parameters and data.

```

struct NCAParams
  dyson_rtol::Float64
  dyson_atol::Float64
  dyson_max_iter::Int
  max_order::Int
  function NCAParams(dyson_rtol, dyson_atol, dyson_max_iter, max_order)
    @assert 1 <= max_order <= 2
    new(dyson_rtol, dyson_atol, dyson_max_iter, max_order)
  end
end

function NCAParams(; dyson_rtol = 1e-6,
                    dyson_atol = 1e-10,
                    dyson_max_iter = 100,
                    max_order = 1)
  return NCAParams(dyson_rtol, dyson_atol, dyson_max_iter, max_order)
end

struct NCADData{T <: AbstractTimeGF, U <: AbstractTimeGrid}
  P0::Array{T,1} # bare propagator
  Δ::Array{T, 1} # hybridization function
  P::Array{T,1} # dressed propagator
  Σ::Array{T,1} # self-energy
  ΣxP::Array{T,1} # self-energy convolved with propagator
  grid::U # time grid
  states::NTuple{4, FockState}
  spins::Tuple{SpinEnum, SpinEnum}
end

function NCADData(P0, Δ)
  states = ntuple(i -> FockState(i-1), 4)
  spins = instances(SpinEnum)
  statesize = length(states)
  indexsize = length(spins)
  @assert length(P0) == statesize
  @assert length(Δ) == indexsize
  grid = first(P0).grid
  X = P0[1]
  P = [zero(X) for _ in 1:statesize]
  Σ = [zero(X) for _ in 1:statesize]
  ΣxP = [zero(X) for _ in 1:statesize]
  G = [zero(X) for _ in 1:indexsize]
  NCADData(P0, Δ, P, Σ, ΣxP, grid, states, spins)
end

```

We define a function to compute the NCA approximation to the self-energy. This implements equations 3.49-3.52 for a single state and pair of times points.

```
function  $\Sigma_{nca}$ (data::NCAData,  
                t1::TimeGridPoint,  
                t2::TimeGridPoint,  
                st_sigma::FockState)  
    sum(data.spins) do sp  
        st_prop = flip(st_sigma, sp)  
        hyb = st_sigma[sp] ? data. $\Delta$ [sp][t1, t2] : -data. $\Delta$ [sp][t2, t1, false]  
        loc = im * data.P[st_prop][t1, t2]  
        return loc * hyb  
    end  
end
```

We define a function to solve the Dyson equation. This implements equation 3.46 for a pair of times points. Because this equation is solved contour causally, the first iteration is usually quite close to the solution so nothing more sophisticated than forward iteration is necessary. It would be interesting to see if a more advanced scheme, such as Anderson mixing [267], or Broyden's method [268], could be beneficial.

```
function dyson!(data::NCADData,
               t1::TimeGridPoint,
               t2::TimeGridPoint,
               params::NCAParams)
    @assert t1.cid >= t2.cid
    rtol = params.dyson_rtol
    atol = params.dyson_atol

    p_t1t2_cur = zeros(ComplexF64, length(data.states))
    p_t1t2_next = zeros(ComplexF64, length(data.states))

    for st in data.states
        p_t1t2_cur[st] = data.P0[st][t1,t2]
        data.P[st][t1,t2] = data.P0[st][t1,t2] # initial guess
    end

    v = (A, B) -> integrate(t -> @inbounds(A[t1,t]*B[t,t2]),data.grid,t1,t2)

    done = false
    iter = 1
    diff = 0.0
    while iter <= params.dyson_max_iter && !done

        for st in data.states
            p_t1t2_next[st] = 0.0
            data.Σ[st][t1, t2] = Σnca(data, t1, t2, st)

            # p = p_0 + p_0 v Σ v p
            data.ΣxP[st][t1, t2] = data.Σ[st] v data.P[st]
            p_t1t2_next[st] += data.P0[st] v data.ΣxP[st]
            p_t1t2_next[st] += data.P0[st][t1, t2]
        end

        diff = norm(p_t1t2_cur - p_t1t2_next)
        done = diff < max(atol, rtol*norm(p_t1t2_cur))
        for st in data.states
            data.P[st][t1,t2] = p_t1t2_next[st]
        end
        p_t1t2_cur .= p_t1t2_next
        iter += 1
    end
end
```

We define a function to solve the Dyson equation over the whole time domain diagonal by diagonal. For simplicity we do not take advantage of the time symmetries of the propagators here.

```
function nca!(data::NCADData, params::NCAParams)
    N = length(data.grid)
    for d in 0:(N-1) # solve diagonal by diagonal
        for j in 1:(N-d)
            i = j + d
            t1 = data.grid[i]
            t2 = data.grid[j]
            dyson!(data, t1, t2, params)
        end
    end
    return data
end
```

We define a function to extract the populations, i.e. the diagonal elements of the impurity density matrix from the bold propagators. This implements equation 3.9.

```
function populations(P)
    nstates = length(P)
    ξ = [1.0, -1.0, -1.0, 1.0]
    P_lsr_diag = reduce(hcat,
        (1.0im * ξ[s] * diag(P[s][:lesser]) for s in 1:nstates))
    Zt = sum(P_lsr_diag, dims=2)
    pt = P_lsr_diag ./ Zt
    return pt, Zt
end
```


Using this machinery we can compute and visualize the populations. Here we compute the populations for the Anderson impurity model coupled to a flat band hybridization with $\Gamma = 1$, $D = 10$, $\epsilon_d = -4$, and $U = 8$ starting from an initially empty state.

```

function run_nca()
    # first we define a contour and a time grid
    tmax,  $\beta$  = 5.0, 10.0
    c = twist(KeldyshContour(; tmax))
    grid = KeldyshTimeGrid(c, 101)
    t = realtimes(grid)

    # define bare propagator parameters
     $\rho$  = [1.0, 0.0, 0.0, 0.0]
     $\epsilon$  = -4.0
    U = 8.0
    P0 = make_bare_prop(grid,  $\rho$ ,  $\epsilon$ , U)

    # use Keldysh.jl convenience functions to compute  $\Delta$ 
    dos = flat_dos(;D=10.0, v=10.0)
     $\Delta$  = [GenericTimeGF(dos,  $\beta$ , grid) for s in 1:2]

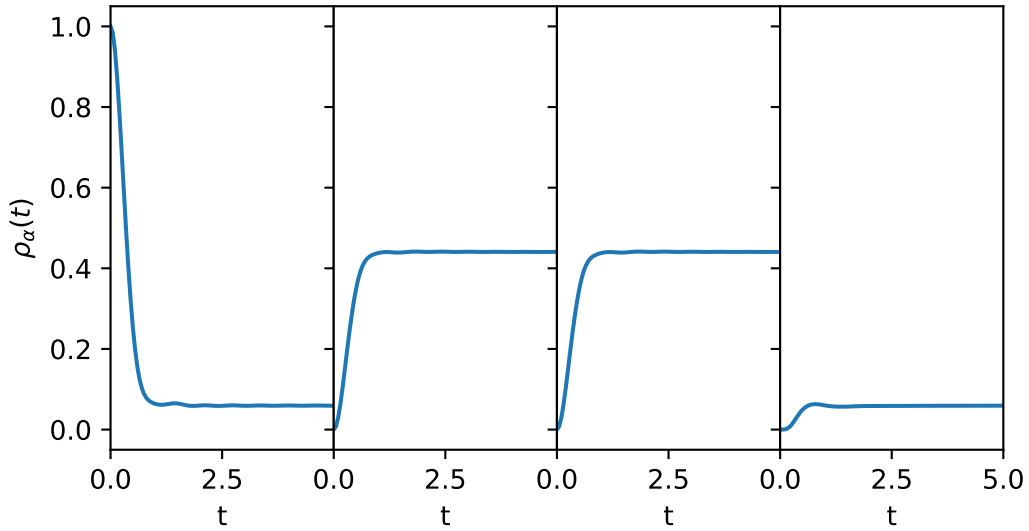
    nca_params = NCAParams(max_order = 1)
    nca_data = NCADData(P0,  $\Delta$ )
    nca!(nca_data, nca_params)

    pt, Zt = populations(nca_data.P)

    fig, axes = plt.subplots(figsize=(6,3), ncols=4, sharey=true)
    for s in 1:4
        axes[s].plot(t, real(pt[:,s]))
        axes[s].set_xlabel("t")
        axes[s].set_xticks([0, 2.5])
    end
    fig.subplots_adjust(wspace=0.0)
    axes[4].set_xticks([0, 2.5, 5.0])
    axes[1].set_ylabel(L" $\rho_\alpha(t)$ ")
    fig.savefig("nca_pop.pdf", bbox_inches="tight")
end
run_nca()

```

This code produces the following output where each panel shows the population for state $|\alpha\rangle \in \{|0\rangle, |\uparrow\rangle, |\downarrow\rangle, |\uparrow\downarrow\rangle\}$. Note, initially the population on the empty state is 1, which reflects our chosen initial condition. The system quickly relaxes to a spin-symmetric, and particle-hole symmetric state. The particle-hole symmetry arises because we chose $U = -2\epsilon_d$ so the empty and doubly occupied state have the same energy.



Bibliography

- ¹A. Einstein, “Planck’s theory of radiation and the theory of specific heat”, *Ann. Phys* **22**, 180–190 (1907).
- ²M. J. Klein, “Einstein, Specific Heats, and the Early Quantum Theory”, *Science* **148**, 173–180 (1965).
- ³P. A. M. Dirac and R. H. Fowler, “Quantum mechanics of many-electron systems”, *Proceedings of the Royal Society of London. Series A, Containing Papers of a Mathematical and Physical Character* **123**, 714–733 (1929).
- ⁴P. W. Anderson, “Localized Magnetic States in Metals”, *Physical Review* **124**, 41–53 (1961).
- ⁵W. J. de Haas, J. de Boer, and G. J. van dën Berg, “The electrical resistance of gold, copper and lead at low temperatures”, *Physica* **1**, 1115–1124 (1934).
- ⁶J. Kondo, “Resistance Minimum in Dilute Magnetic Alloys”, *Progress of Theoretical Physics* **32**, 37–49 (1964).
- ⁷K. G. Wilson, “The renormalization group: Critical phenomena and the Kondo problem”, *Reviews of Modern Physics* **47**, 773 (1975).
- ⁸R. Bulla, T. A. Costi, and T. Pruschke, “Numerical renormalization group method for quantum impurity systems”, *Reviews of Modern Physics* **80**, 395–450 (2008).
- ⁹H. Keiter and J. C. Kimball, “Perturbation Technique for the Anderson Hamiltonian”, *Physical Review Letters* **25**, 672–675 (1970).
- ¹⁰N. E. Bickers, “Review of techniques in the large-N expansion for dilute magnetic alloys”, *Reviews of Modern Physics* **59**, 845–939 (1987).
- ¹¹P. Werner, A. Comanac, L. de’Medici, M. Troyer, and A. J. Millis, “Continuous-Time Solver for Quantum Impurity Models”, *Physical Review Letters* **97**, 076405 (2006).
- ¹²T. K. Ng and P. A. Lee, “On-Site Coulomb Repulsion and Resonant Tunneling”, *Physical Review Letters* **61**, 1768–1771 (1988).
- ¹³R. Hanson, L. P. Kouwenhoven, J. R. Petta, S. Tarucha, and L. M. K. Vandersypen, “Spins in few-electron quantum dots”, *Reviews of Modern Physics* **79**, 1217–1265 (2007).
- ¹⁴D. Goldhaber-Gordon, H. Shtrikman, D. Mahalu, D. Abusch-Magder, U. Meirav, and M. A. Kastner, “Kondo effect in a single-electron transistor”, *Nature* **391**, 156 (1998).

- ¹⁵D. Goldhaber-Gordon, J. Göres, M. A. Kastner, H. Shtrikman, D. Mahalu, and U. Meirav, “From the Kondo Regime to the Mixed-Valence Regime in a Single-Electron Transistor”, [Physical Review Letters](#) **81**, 5225–5228 (1998).
- ¹⁶R. Brako and D. M. Newns, “Theory of electronic processes in atom scattering from surfaces”, [Reports on Progress in Physics](#) **52**, 655–697 (1989).
- ¹⁷D. C. Langreth and P. Nordlander, “Derivation of a master equation for charge-transfer processes in atom-surface collisions”, [Physical Review B](#) **43**, 2541–2557 (1991).
- ¹⁸V. Madhavan, W. Chen, T. Jamneala, M. F. Crommie, and N. S. Wingreen, “Tunneling into a Single Magnetic Atom: Spectroscopic Evidence of the Kondo Resonance”, [Science](#) **280**, 567–569 (1998).
- ¹⁹J. Li, W.-D. Schneider, R. Berndt, and B. Delley, “Kondo Scattering Observed at a Single Magnetic Impurity”, [Physical Review Letters](#) **80**, 2893–2896 (1998).
- ²⁰G. D. Scott and D. Natelson, “Kondo Resonances in Molecular Devices”, [ACS Nano](#) **4**, 3560–3579 (2010).
- ²¹M. A. Ochoa, Y. Selzer, U. Peskin, and M. Galperin, “Pump–Probe Noise Spectroscopy of Molecular Junctions”, [The Journal of Physical Chemistry Letters](#) **6**, 470–476 (2015).
- ²²J. C. Cuevas and E. Scheer, *Molecular electronics: an introduction to theory and experiment*, 2nd Edition, World Scientific Series in Nanoscience and Nanotechnology volume 15 (World Scientific, New Jersey, 2017), 825 pp.
- ²³J. Hubbard and B. H. Flowers, “Electron correlations in narrow energy bands”, [Proceedings of the Royal Society of London. Series A. Mathematical and Physical Sciences](#) **276**, 238–257 (1963).
- ²⁴W. Metzner and D. Vollhardt, “Correlated Lattice Fermions in $d = \infty$ Dimensions”, [Physical Review Letters](#) **62**, 324–327 (1989).
- ²⁵A. Georges and G. Kotliar, “Hubbard model in infinite dimensions”, [Physical Review B](#) **45**, 6479–6483 (1992).
- ²⁶N. F. Mott, “The transition to the metallic state”, [The Philosophical Magazine: A Journal of Theoretical Experimental and Applied Physics](#) **6**, 287–309 (1961).
- ²⁷M. J. Rozenberg, X. Y. Zhang, and G. Kotliar, “Mott-Hubbard transition in infinite dimensions”, [Physical Review Letters](#) **69**, 1236–1239 (1992).
- ²⁸M. J. Rozenberg, G. Kotliar, and X. Y. Zhang, “Mott-Hubbard transition in infinite dimensions. II”, [Physical Review B](#) **49**, 10181–10193 (1994).
- ²⁹W. Kohn and L. J. Sham, “Self-Consistent Equations Including Exchange and Correlation Effects”, [Physical Review](#) **140**, A1133–A1138 (1965).
- ³⁰H. Aoki, N. Tsuji, M. Eckstein, M. Kollar, T. Oka, and P. Werner, “Nonequilibrium dynamical mean-field theory and its applications”, [Reviews of Modern Physics](#) **86**, 779–837 (2014).

- ³¹A. E. Antipov, Q. Dong, J. Kleinhenz, G. Cohen, and E. Gull, “Currents and Green’s functions of impurities out of equilibrium: Results from inchworm quantum Monte Carlo”, [Physical Review B **95**, 085144 \(2017\)](#).
- ³²Q. Dong, I. Krivenko, J. Kleinhenz, A. E. Antipov, G. Cohen, and E. Gull, “Quantum Monte Carlo solution of the dynamical mean field equations in real time”, [Physical Review B **96**, 155126 \(2017\)](#).
- ³³I. Krivenko, J. Kleinhenz, G. Cohen, and E. Gull, “Dynamics of Kondo voltage splitting after a quantum quench”, [Physical Review B **100**, 201104 \(2019\)](#).
- ³⁴J. Kleinhenz, I. Krivenko, G. Cohen, and E. Gull, “Dynamic control of nonequilibrium metal-insulator transitions”, [Physical Review B **102**, 205138 \(2020\)](#).
- ³⁵J. Kleinhenz, I. Krivenko, G. Cohen, and E. Gull, “The Kondo Cloud in a 1D Nanowire”, (In Preparation).
- ³⁶G. Stefanucci and R. Van Leeuwen, *Nonequilibrium Many-Body Theory of Quantum Systems: a Modern Introduction*. (Cambridge University Press, Cambridge, 2013).
- ³⁷M. Schüler, D. Golež, Y. Murakami, N. Bittner, A. Herrmann, H. U. R. Strand, P. Werner, and M. Eckstein, “NESSi: The Non-Equilibrium Systems Simulation package”, [Computer Physics Communications **257**, 107484 \(2020\)](#).
- ³⁸J. Schwinger, “Brownian Motion of a Quantum Oscillator”, [Journal of Mathematical Physics **2**, 407–432 \(1961\)](#).
- ³⁹L. Keldysh, “Diagram technique for nonequilibrium processes”, *Sov. Phys. JETP* **20**, 1018–1026 (1965).
- ⁴⁰M. Ridley, V. N. Singh, E. Gull, and G. Cohen, “Numerically exact full counting statistics of the nonequilibrium Anderson impurity model”, [Physical Review B **97**, 115109 \(2018\)](#).
- ⁴¹L. P. Kadanoff and G. Baym, *Quantum Statistical Mechanics: Green’s Function Methods in Equilibrium and Nonequilibrium Problems* (Benjamin-Cummings Publishing Company, 1962).
- ⁴²O. Konstantinov and V. Perel, “A diagram technique for evaluating transport quantities”, *SOVIET PHYSICS JETP-USSR* **12**, 142–149 (1961).
- ⁴³G. D. Mahan, *Many particle physics*, Third edition, Physics of Solids and Liquids (Springer Science + Business Media, LLC, New York, 2000), 785 pp.
- ⁴⁴A. Damascelli, Z. Hussain, and Z.-X. Shen, “Angle-resolved photoemission studies of the cuprate superconductors”, [Reviews of Modern Physics **75**, 473–541 \(2003\)](#).
- ⁴⁵A. Dirks, M. Eckstein, T. Pruschke, and P. Werner, “Extracting spectral properties from Keldysh Green functions”, [Physical Review E **87**, 023305 \(2013\)](#).
- ⁴⁶Q.-f. Sun and H. Guo, “Kondo resonance in a multiprobe quantum dot”, [Physical Review B **64**, 153306 \(2001\)](#).
- ⁴⁷G. Cohen, D. R. Reichman, A. J. Millis, and E. Gull, “Green’s functions from real-time bold-line Monte Carlo”, [Physical Review B **89**, 115139 \(2014\)](#).

- ⁴⁸E. Lebanon and A. Schiller, “Measuring the out-of-equilibrium splitting of the Kondo resonance”, *Physical Review B* **65**, 035308 (2001).
- ⁴⁹M. Schiró and M. Fabrizio, “Real-time diagrammatic Monte Carlo for nonequilibrium quantum transport”, *Physical Review B* **79**, 153302 (2009).
- ⁵⁰T. L. Schmidt, P. Werner, L. Mühlbacher, and A. Komnik, “Transient dynamics of the Anderson impurity model out of equilibrium”, *Physical Review B* **78**, 235110 (2008).
- ⁵¹P. Werner, T. Oka, and A. J. Millis, “Diagrammatic Monte Carlo simulation of nonequilibrium systems”, *Physical Review B* **79**, 035320 (2009).
- ⁵²M. Schiró, “Real-time dynamics in quantum impurity models with diagrammatic Monte Carlo”, *Physical Review B* **81**, 085126 (2010).
- ⁵³M. Eckstein and P. Werner, “Nonequilibrium dynamical mean-field calculations based on the noncrossing approximation and its generalizations”, *Physical Review B* **82**, 115115 (2010).
- ⁵⁴T. Pruschke and N. Grewe, “The Anderson model with finite Coulomb repulsion”, *Zeitschrift für Physik B Condensed Matter* **74**, 439–449 (1989).
- ⁵⁵G. Cohen, E. Gull, D. R. Reichman, and A. J. Millis, “Taming the Dynamical Sign Problem in Real-Time Evolution of Quantum Many-Body Problems”, *Physical Review Letters* **115**, 266802 (2015).
- ⁵⁶D. J. Scalapino, “Curie Law for Anderson’s Model of a Dilute Alloy”, *Physical Review Letters* **16**, 937–939 (1966).
- ⁵⁷H. Keiter and J. C. Kimball, “Diagrammatic Approach to the Anderson Model for Dilute Alloys”, *Journal of Applied Physics* **42**, 1460–1461 (1971).
- ⁵⁸N. Grewe and H. Keiter, “Diagrammatic approach to the intermediate-valence compounds”, *Physical Review B* **24**, 4420–4444 (1981).
- ⁵⁹Y. Kuramoto, “Self-consistent perturbation theory for dynamics of valence fluctuations”, *Zeitschrift für Physik B Condensed Matter* **53**, 37–52 (1983).
- ⁶⁰S. E. Barnes, “New method for the Anderson model”, *Journal of Physics F: Metal Physics* **6**, 1375–1383 (1976).
- ⁶¹P. Coleman, “New approach to the mixed-valence problem”, *Physical Review B* **29**, 3035–3044 (1984).
- ⁶²N. E. Bickers, D. L. Cox, and J. W. Wilkins, “Self-consistent large-N expansion for normal-state properties of dilute magnetic alloys”, *Physical Review B* **36**, 2036–2079 (1987).
- ⁶³E. Müller-Hartmann, “Self-consistent perturbation theory of the anderson model: Ground state properties”, *Zeitschrift für Physik B Condensed Matter* **57**, 281–287 (1984).
- ⁶⁴C. N. Sposetti, L. O. Manuel, and P. Roura-Bas, “Qualitative breakdown of the non-crossing approximation for the symmetric one-channel Anderson impurity model at all temperatures”, *Physical Review B* **94**, 085139 (2016).

- ⁶⁵K. Haule, S. Kirchner, J. Kroha, and P. Wölfle, “Anderson impurity model at finite Coulomb interaction U : Generalized noncrossing approximation”, [Physical Review B **64**, 155111 \(2001\)](#).
- ⁶⁶L. Tosi, P. Roura-Bas, A. M. Llois, and L. O. Manuel, “Effects of vertex corrections on diagrammatic approximations applied to the study of transport through a quantum dot”, [Physical Review B **83**, 073301 \(2011\)](#).
- ⁶⁷V. Vildosola, L. V. Pourovskii, L. O. Manuel, and P. Roura-Bas, “Reliability of the one-crossing approximation in describing the Mott transition”, [Journal of Physics: Condensed Matter **27**, 485602 \(2015\)](#).
- ⁶⁸P. Werner and A. J. Millis, “Hybridization expansion impurity solver: General formulation and application to Kondo lattice and two-orbital models”, [Physical Review B **74**, 155107 \(2006\)](#).
- ⁶⁹E. Gull, A. J. Millis, A. I. Lichtenstein, A. N. Rubtsov, M. Troyer, and P. Werner, “Continuous-time Monte Carlo methods for quantum impurity models”, [Reviews of Modern Physics **83**, 349–404 \(2011\)](#).
- ⁷⁰H. Shinaoka, E. Gull, and P. Werner, “Continuous-time hybridization expansion quantum impurity solver for multi-orbital systems with complex hybridizations”, [Computer Physics Communications **215**, 128–136 \(2017\)](#).
- ⁷¹P. Seth, I. Krivenko, M. Ferrero, and O. Parcollet, “TRIQS/CTHYB: A continuous-time quantum Monte Carlo hybridisation expansion solver for quantum impurity problems”, [Computer Physics Communications **200**, 274–284 \(2016\)](#).
- ⁷²M. Wallerberger, A. Hausoel, P. Gunacker, A. Kowalski, N. Parragh, F. Goth, K. Held, and G. Sangiovanni, “W2dynamics: Local one- and two-particle quantities from dynamical mean field theory”, [Computer Physics Communications **235**, 388–399 \(2019\)](#).
- ⁷³E. Gull, D. R. Reichman, and A. J. Millis, “Bold-line diagrammatic Monte Carlo method: General formulation and application to expansion around the noncrossing approximation”, [Physical Review B **82**, 075109 \(2010\)](#).
- ⁷⁴P. Nordlander, M. Pustilnik, Y. Meir, N. S. Wingreen, and D. C. Langreth, “How Long Does It Take for the Kondo Effect to Develop?”, [Physical Review Letters **83**, 808–811 \(1999\)](#).
- ⁷⁵E. Gull, D. R. Reichman, and A. J. Millis, “Numerically exact long-time behavior of nonequilibrium quantum impurity models”, [Physical Review B **84**, 085134 \(2011\)](#).
- ⁷⁶G. Cohen, E. Gull, D. R. Reichman, A. J. Millis, and E. Rabani, “Numerically exact long-time magnetization dynamics at the nonequilibrium Kondo crossover of the Anderson impurity model”, [Physical Review B **87**, 195108 \(2013\)](#).
- ⁷⁷G. Cohen, E. Gull, D. R. Reichman, and A. J. Millis, “Green’s Functions from Real-Time Bold-Line Monte Carlo Calculations: Spectral Properties of the Nonequilibrium Anderson Impurity Model”, [Physical Review Letters **112**, 146802 \(2014\)](#).

- ⁷⁸H.-T. Chen, G. Cohen, and D. R. Reichman, “Inchworm Monte Carlo for exact non-adiabatic dynamics I. Theory and algorithms”, [The Journal of Chemical Physics](#) **146**, 054105 (2017).
- ⁷⁹H.-T. Chen, G. Cohen, and D. R. Reichman, “Inchworm Monte Carlo for exact non-adiabatic dynamics II. Benchmarks and comparison with established methods”, [The Journal of Chemical Physics](#) **146**, 054106 (2017).
- ⁸⁰E. Eidelstein, E. Gull, and G. Cohen, “Multiorbital Quantum Impurity Solver for General Interactions and Hybridizations”, [Physical Review Letters](#) **124**, 206405 (2020).
- ⁸¹A. Boag, E. Gull, and G. Cohen, “Inclusion-exclusion principle for many-body diagrammatics”, [Physical Review B](#) **98**, 115152 (2018).
- ⁸²Z. Cai, J. Lu, and S. Yang, “Inchworm Monte Carlo Method for Open Quantum Systems”, [Communications on Pure and Applied Mathematics](#) **73**, 2430–2472 (2020).
- ⁸³R. E. V. Profumo, C. Groth, L. Messio, O. Parcollet, and X. Waintal, “Quantum Monte Carlo for correlated out-of-equilibrium nanoelectronic devices”, [Physical Review B](#) **91**, 245154 (2015).
- ⁸⁴C. Bertrand, O. Parcollet, A. Maillard, and X. Waintal, “Quantum Monte Carlo algorithm for out-of-equilibrium Green’s functions at long times”, [Physical Review B](#) **100**, 125129 (2019).
- ⁸⁵M. Mačėk, P. T. Dumitrescu, C. Bertrand, B. Triggs, O. Parcollet, and X. Waintal, “Quantum Quasi-Monte Carlo Technique for Many-Body Perturbative Expansions”, [Physical Review Letters](#) **125**, 047702 (2020).
- ⁸⁶N. Metropolis, A. W. Rosenbluth, M. N. Rosenbluth, A. H. Teller, and E. Teller, “Equation of State Calculations by Fast Computing Machines”, [The Journal of Chemical Physics](#) **21**, 1087–1092 (1953).
- ⁸⁷N. V. Prokof’ev and B. V. Svistunov, “Polaron Problem by Diagrammatic Quantum Monte Carlo”, [Physical Review Letters](#) **81**, 2514–2517 (1998).
- ⁸⁸F. Wang and D. P. Landau, “Determining the density of states for classical statistical models: A random walk algorithm to produce a flat histogram”, [Physical Review E](#) **64**, 056101 (2001).
- ⁸⁹F. Wang and D. P. Landau, “Efficient, Multiple-Range Random Walk Algorithm to Calculate the Density of States”, [Physical Review Letters](#) **86**, 2050–2053 (2001).
- ⁹⁰M. Troyer, S. Wessel, and F. Alet, “Flat Histogram Methods for Quantum Systems: Algorithms to Overcome Tunneling Problems and Calculate the Free Energy”, [Physical Review Letters](#) **90**, 120201 (2003).
- ⁹¹H. Kaiser, P. Diehl, A. S. Lemoine, B. A. Lelbach, P. Amini, A. Berge, J. Biddiscombe, S. R. Brandt, N. Gupta, T. Heller, K. Huck, Z. Khatami, A. Kheirkhahan, A. Reverdell, S. Shirzad, M. Simberg, B. Wagle, W. Wei, and T. Zhang, “HPX - The C++ Standard Library for Parallelism and Concurrency”, [Journal of Open Source Software](#) **5**, 2352 (2020).

- ⁹²J. K. Freericks, V. M. Turkowski, and V. Zlatić, “Nonequilibrium Dynamical Mean-Field Theory”, *Physical Review Letters* **97**, 266408 (2006).
- ⁹³F. B. Anders, “Steady-State Currents through Nanodevices: A Scattering-States Numerical Renormalization-Group Approach to Open Quantum Systems”, *Physical Review Letters* **101**, 066804 (2008).
- ⁹⁴S. M. Cronenwett, T. H. Oosterkamp, and L. P. Kouwenhoven, “A Tunable Kondo Effect in Quantum Dots”, *Science* **281**, 540–544 (1998).
- ⁹⁵A. C. Hewson, *Kondo Problem to Heavy Fermions*. (Cambridge University Press, Cambridge, GBR, 2009).
- ⁹⁶M. Pustilnik and L. Glazman, “Kondo effect in quantum dots”, *Journal of Physics: Condensed Matter* **16**, R513–R537 (2004).
- ⁹⁷H. T. M. Nghiem and T. A. Costi, “Time Evolution of the Kondo Resonance in Response to a Quench”, *Physical Review Letters* **119**, 156601 (2017).
- ⁹⁸S. De Franceschi, R. Hanson, W. G. van der Wiel, J. M. Elzerman, J. J. Wijkema, T. Fujisawa, S. Tarucha, and L. P. Kouwenhoven, “Out-of-Equilibrium Kondo Effect in a Mesoscopic Device”, *Physical Review Letters* **89**, 156801 (2002).
- ⁹⁹R. Leturcq, L. Schmid, K. Ensslin, Y. Meir, D. C. Driscoll, and A. C. Gossard, “Probing the Kondo Density of States in a Three-Terminal Quantum Ring”, *Physical Review Letters* **95**, 126603 (2005).
- ¹⁰⁰R. Leturcq, L. Schmid, K. Ensslin, Y. Meir, D. C. Driscoll, and A. C. Gossard, “Probing the Kondo density of states in a three-terminal quantum ring”, *Physica E: Low-dimensional Systems and Nanostructures* **34**, 441–444 (2006).
- ¹⁰¹A. Rosch, J. Kroha, and P. Wölfle, “Kondo Effect in Quantum Dots at High Voltage: Universality and Scaling”, *Physical Review Letters* **87**, 156802 (2001).
- ¹⁰²T. Fujii and K. Ueda, “Perturbative approach to the nonequilibrium Kondo effect in a quantum dot”, *Physical Review B* **68**, 155310 (2003).
- ¹⁰³P. Fritsch and S. Kehrein, “Nonequilibrium Kondo model with voltage bias in a magnetic field”, *Physical Review B* **81**, 035113 (2010).
- ¹⁰⁴Y. Meir, N. S. Wingreen, and P. A. Lee, “Low-temperature transport through a quantum dot: The Anderson model out of equilibrium”, *Physical Review Letters* **70**, 2601–2604 (1993).
- ¹⁰⁵N. Shah and A. Rosch, “Nonequilibrium conductance of a three-terminal quantum dot in the Kondo regime: Perturbative renormalization group study”, *Physical Review B* **73**, 081309 (2006).
- ¹⁰⁶D. M. Fugger, A. Dorda, F. Schwarz, J. von Delft, and E. Arrigoni, “Nonequilibrium Kondo effect in a magnetic field: auxiliary master equation approach”, *New Journal of Physics* **20**, 013030 (2018).

- ¹⁰⁷H. Schoeller, “A perturbative nonequilibrium renormalization group method for dissipative quantum mechanics”, [The European Physical Journal Special Topics](#) **168**, 179–266 (2009).
- ¹⁰⁸S. Andergassen, M. Pletyukhov, D. Schuricht, H. Schoeller, and L. Borda, “Renormalization group analysis of the interacting resonant-level model at finite bias: Generic analytic study of static properties and quench dynamics”, [Physical Review B](#) **83**, 205103 (2011).
- ¹⁰⁹D. M. Kennes and V. Meden, “Quench dynamics of correlated quantum dots”, [Physical Review B](#) **85**, 245101 (2012).
- ¹¹⁰P. Wang and S. Kehrein, “Flow equation calculation of transient and steady-state currents in the Anderson impurity model”, [Physical Review B](#) **82**, 125124 (2010).
- ¹¹¹N. Lanatà and H. U. R. Strand, “Time-dependent and steady-state Gutzwiller approach for nonequilibrium transport in nanostructures”, [Physical Review B](#) **86**, 115310 (2012).
- ¹¹²M. Pletyukhov and H. Schoeller, “Nonequilibrium Kondo model: Crossover from weak to strong coupling”, [Physical Review Letters](#) **108**, 260601 (2012).
- ¹¹³N. S. Maslova, P. I. Arseyev, and V. N. Mantsevich, “Kondo correlations formation and the local magnetic moment dynamics in the Anderson model”, [Solid State Communications](#) **252**, 78–81 (2017).
- ¹¹⁴K. Balzer, Z. Li, O. Vendrell, and M. Eckstein, “Multiconfiguration time-dependent Hartree impurity solver for nonequilibrium dynamical mean-field theory”, [Physical Review B](#) **91**, 045136 (2015).
- ¹¹⁵M. Balzer, N. Gdaniec, and M. Potthoff, “Krylov-space approach to the equilibrium and nonequilibrium single-particle Green’s function”, [Journal of Physics: Condensed Matter](#) **24**, 035603 (2011).
- ¹¹⁶C. Gramsch, K. Balzer, M. Eckstein, and M. Kollar, “Hamiltonian-based impurity solver for nonequilibrium dynamical mean-field theory”, [Physical Review B](#) **88**, 235106 (2013).
- ¹¹⁷C. Lin and A. A. Demkov, “Quench dynamics of Anderson impurity model using configuration interaction method”, [Physical Review B](#) **92**, 155135 (2015).
- ¹¹⁸S. R. White and A. E. Feiguin, “Real-Time Evolution Using the Density Matrix Renormalization Group”, [Physical Review Letters](#) **93**, 076401 (2004).
- ¹¹⁹A. J. Daley, C. Kollath, U. Schollwöck, and G. Vidal, “Time-dependent density-matrix renormalization-group using adaptive effective Hilbert spaces”, [Journal of Statistical Mechanics: Theory and Experiment](#) **2004**, P04005 (2004).
- ¹²⁰S. Weiss, J. Eckel, M. Thorwart, and R. Egger, “Iterative real-time path integral approach to nonequilibrium quantum transport”, [Physical Review B](#) **77**, 195316 (2008).
- ¹²¹D. Segal, A. J. Millis, and D. R. Reichman, “Numerically exact path-integral simulation of nonequilibrium quantum transport and dissipation”, [Physical Review B](#) **82**, 205323 (2010).

- ¹²²J. Eckel, F. Heidrich-Meisner, S. G. Jakobs, M. Thorwart, M. Pletyukhov, and R. Egger, “Comparative study of theoretical methods for non-equilibrium quantum transport”, [New Journal of Physics](#) **12**, 043042 (2010).
- ¹²³S. Weiss, R. Hütten, D. Becker, J. Eckel, R. Egger, and M. Thorwart, “Iterative path integral summation for nonequilibrium quantum transport”, [physica status solidi \(b\)](#) **250**, 2298–2314 (2013).
- ¹²⁴F. B. Anders and A. Schiller, “Real-Time Dynamics in Quantum-Impurity Systems: A Time-Dependent Numerical Renormalization-Group Approach”, [Physical Review Letters](#) **95**, 196801 (2005).
- ¹²⁵F. B. Anders and A. Schiller, “Spin precession and real-time dynamics in the Kondo model: Time-dependent numerical renormalization-group study”, [Physical Review B](#) **74**, 245113 (2006).
- ¹²⁶H. T. M. Nghiem and T. A. Costi, “Time-dependent numerical renormalization group method for multiple quenches: Application to general pulses and periodic driving”, [Physical Review B](#) **90**, 035129 (2014).
- ¹²⁷H. T. M. Nghiem and T. A. Costi, “Time-dependent numerical renormalization group method for multiple quenches: Towards exact results for the long-time limit of thermodynamic observables and spectral functions”, [Physical Review B](#) **98**, 155107 (2018).
- ¹²⁸F. Schwarz, I. Weymann, J. von Delft, and A. Weichselbaum, “Nonequilibrium Steady-State Transport in Quantum Impurity Models: A Thermofield and Quantum Quench Approach Using Matrix Product States”, [Physical Review Letters](#) **121**, 137702 (2018).
- ¹²⁹J. Jin, X. Zheng, and Y. Yan, “Exact dynamics of dissipative electronic systems and quantum transport: Hierarchical equations of motion approach”, [The Journal of Chemical Physics](#) **128**, 234703 (2008).
- ¹³⁰X. Zheng, J. Jin, S. Welack, M. Luo, and Y. Yan, “Numerical approach to time-dependent quantum transport and dynamical Kondo transition”, [The Journal of Chemical Physics](#) **130**, 164708 (2009).
- ¹³¹S. Wang, X. Zheng, J. Jin, and Y. Yan, “Hierarchical Liouville-space approach to nonequilibrium dynamical properties of quantum impurity systems”, [Physical Review B](#) **88**, 035129 (2013).
- ¹³²P. Wang, G. Cohen, and S. Xu, “Numerical operator method for the real-time dynamics of strongly correlated quantum impurity systems far from equilibrium”, [Physical Review B](#) **91**, 155148 (2015).
- ¹³³F. Schwarz, M. Goldstein, A. Dorda, E. Arrigoni, A. Weichselbaum, and J. von Delft, “Lindblad-driven discretized leads for nonequilibrium steady-state transport in quantum impurity models: Recovering the continuum limit”, [Physical Review B](#) **94**, 155142 (2016).
- ¹³⁴A. Dorda, M. Nuss, W. von der Linden, and E. Arrigoni, “Auxiliary master equation approach to nonequilibrium correlated impurities”, [Physical Review B](#) **89**, 165105 (2014).

- ¹³⁵A. Dorda, M. Ganahl, H. G. Evertz, W. von der Linden, and E. Arrigoni, “Auxiliary master equation approach within matrix product states: Spectral properties of the nonequilibrium Anderson impurity model”, [Physical Review B **92**, 125145 \(2015\)](#).
- ¹³⁶A. Dorda, M. Sorantin, W. von der Linden, and E. Arrigoni, “Optimized auxiliary representation of non-Markovian impurity problems by a Lindblad equation”, [New Journal of Physics **19**, 063005 \(2017\)](#).
- ¹³⁷F. Chen, G. Cohen, and M. Galperin, “Auxiliary Master Equation for Nonequilibrium Dual-Fermion Approach”, [Physical Review Letters **122**, 186803 \(2019\)](#).
- ¹³⁸J. E. Han and R. J. Heary, “Imaginary-Time Formulation of Steady-State Nonequilibrium: Application to Strongly Correlated Transport”, [Physical Review Letters **99**, 236808 \(2007\)](#).
- ¹³⁹A. Dirks, P. Werner, M. Jarrell, and T. Pruschke, “Continuous-time quantum Monte Carlo and maximum entropy approach to an imaginary-time formulation of strongly correlated steady-state transport”, [Physical Review E **82**, 026701 \(2010\)](#).
- ¹⁴⁰L. Mühlbacher and E. Rabani, “Real-Time Path Integral Approach to Nonequilibrium Many-Body Quantum Systems”, [Physical Review Letters **100**, 176403 \(2008\)](#).
- ¹⁴¹P. Werner, T. Oka, M. Eckstein, and A. J. Millis, “Weak-coupling quantum Monte Carlo calculations on the Keldysh contour: Theory and application to the current-voltage characteristics of the Anderson model”, [Physical Review B **81**, 035108 \(2010\)](#).
- ¹⁴²A. Koga, “Quantum Monte Carlo study of nonequilibrium transport through a quantum dot coupled to normal and superconducting leads”, [Physical Review B **87**, 115409 \(2013\)](#).
- ¹⁴³L. Mühlbacher, D. F. Urban, and A. Komnik, “Anderson impurity model in nonequilibrium: Analytical results versus quantum Monte Carlo data”, [Physical Review B **83**, 075107 \(2011\)](#).
- ¹⁴⁴A. Dirks, S. Schmitt, J. E. Han, F. Anders, P. Werner, and T. Pruschke, “Double occupancy and magnetic susceptibility of the Anderson impurity model out of equilibrium”, [EPL \(Europhysics Letters\) **102**, 37011 \(2013\)](#).
- ¹⁴⁵A. E. Antipov, Q. Dong, and E. Gull, “Voltage Quench Dynamics of a Kondo System”, [Physical Review Letters **116**, 036801 \(2016\)](#).
- ¹⁴⁶P. Kubiczek, A. Rubtsov, and A. Lichtenstein, “Exact real-time dynamics of single-impurity Anderson model from a single-spin hybridization-expansion”, [SciPost Physics **7**, 016 \(2019\)](#).
- ¹⁴⁷T. L. Cocker, V. Jelic, M. Gupta, S. J. Molesky, J. A. J. Burgess, G. D. L. Reyes, L. V. Titova, Y. Y. Tsui, M. R. Freeman, and F. A. Hegmann, “An ultrafast terahertz scanning tunnelling microscope”, [Nature Photonics **7**, 620–625 \(2013\)](#).
- ¹⁴⁸S. Loth, M. Etzkorn, C. P. Lutz, D. M. Eigler, and A. J. Heinrich, “Measurement of Fast Electron Spin Relaxation Times with Atomic Resolution”, [Science **329**, 1628–1630 \(2010\)](#).

- ¹⁴⁹M. Eisele, T. L. Cocker, M. A. Huber, M. Plankl, L. Viti, D. Ercolani, L. Sorba, M. S. Vitiello, and R. Huber, “Ultrafast multi-terahertz nano-spectroscopy with sub-cycle temporal resolution”, *Nature Photonics* **8**, 841–845 (2014).
- ¹⁵⁰P. B. Wiegmann and A. M. Tselick, “Exact solution of the Anderson model: I”, *Journal of Physics C: Solid State Physics* **16**, 2281–2319 (1983).
- ¹⁵¹A. Gaenko, A. E. Antipov, G. Carcassi, T. Chen, X. Chen, Q. Dong, L. Gamper, J. Gukelberger, R. Igarashi, S. Iskakov, M. Könz, J. P. F. LeBlanc, R. Levy, P. N. Ma, J. E. Paki, H. Shinaoka, S. Todo, M. Troyer, and E. Gull, “Updated core libraries of the ALPS project”, *Computer Physics Communications* **213**, 235–251 (2017).
- ¹⁵²M. Wallerberger, S. Iskakov, A. Gaenko, J. Kleinhenz, I. Krivenko, R. Levy, J. Li, H. Shinaoka, S. Todo, T. Chen, X. Chen, J. P. F. LeBlanc, J. E. Paki, H. Terletska, M. Troyer, and E. Gull, *Updated Core Libraries of the ALPS Project*, (Nov. 19, 2018) <http://arxiv.org/abs/1811.08331>.
- ¹⁵³Y. Meir and N. S. Wingreen, “Landauer formula for the current through an interacting electron region”, *Physical Review Letters* **68**, 2512–2515 (1992).
- ¹⁵⁴D. Qiaoyuan, “Non-Equilibrium Dynamics with Quantum Monte Carlo” (University of Michigan, 2017).
- ¹⁵⁵N. S. Wingreen and Y. Meir, “Anderson model out of equilibrium: Noncrossing-approximation approach to transport through a quantum dot”, *Physical Review B* **49**, 11040–11052 (1994).
- ¹⁵⁶C. Bertrand, S. Florens, O. Parcollet, and X. Waintal, “Reconstructing Nonequilibrium Regimes of Quantum Many-Body Systems from the Analytical Structure of Perturbative Expansions”, *Physical Review X* **9**, 041008 (2019).
- ¹⁵⁷I. Affleck, “The Kondo screening cloud: what it is and how to observe it”, in *Perspectives of Mesoscopic Physics: Dedicated to Yoseph Imry’s 70th Birthday* (WORLD SCIENTIFIC, Aug. 2010).
- ¹⁵⁸L. Borda, M. Garst, and J. Kroha, “Kondo cloud and spin-spin correlations around a partially screened magnetic impurity”, *Physical Review B* **79**, 100408 (2009).
- ¹⁵⁹L. Borda, “Kondo screening cloud in a one-dimensional wire: Numerical renormalization group study”, *Physical Review B* **75**, 041307 (2007).
- ¹⁶⁰A. Holzner, I. P. McCulloch, U. Schollwöck, J. von Delft, and F. Heidrich-Meisner, “Kondo screening cloud in the single-impurity Anderson model: A density matrix renormalization group study”, *Physical Review B* **80**, 205114 (2009).
- ¹⁶¹J. B. Boyce and C. P. Slichter, “Conduction-Electron Spin Density around Fe Impurities in Cu above and below T_{K} ”, *Physical Review Letters* **32**, 61–64 (1974).
- ¹⁶²C. A. Büsser, G. B. Martins, L. Costa Ribeiro, E. Vernek, E. V. Anda, and E. Dagotto, “Numerical analysis of the spatial range of the Kondo effect”, *Physical Review B* **81**, 045111 (2010).

- ¹⁶³L. C. Ribeiro, G. B. Martins, G. Gómez-Silva, and E. V. Anda, “Numerical study of the Kondo cloud using finite-U slave bosons”, *Physical Review B* **99**, 085139 (2019).
- ¹⁶⁴I. Affleck, L. Borda, and H. Saleur, “Friedel oscillations and the Kondo screening cloud”, *Physical Review B* **77**, 180404 (2008).
- ¹⁶⁵O. Újsághy, J. Kroha, L. Szunyogh, and A. Zawadowski, “Theory of the Fano Resonance in the STM Tunneling Density of States due to a Single Kondo Impurity”, *Physical Review Letters* **85**, 2557–2560 (2000).
- ¹⁶⁶A. E. Antipov, P. Ribeiro, J. Kroha, and S. Kirchner, “Identifying Kondo orbitals through spatially resolved STS”, *physica status solidi (b)* **250**, 562–567 (2013).
- ¹⁶⁷H. Prüser, M. Wenderoth, P. E. Dargel, A. Weismann, R. Peters, T. Pruschke, and R. G. Ulbrich, “Long-range Kondo signature of a single magnetic impurity”, *Nature Physics* **7**, 203–206 (2011).
- ¹⁶⁸J. Park, S.-S. B. Lee, Y. Oreg, and H.-S. Sim, “How to Directly Measure a Kondo Cloud’s Length”, *Physical Review Letters* **110**, 246603 (2013).
- ¹⁶⁹I. V. Borzenets, J. Shim, J. C. H. Chen, A. Ludwig, A. D. Wieck, S. Tarucha, H.-S. Sim, and M. Yamamoto, “Observation of the Kondo screening cloud”, *Nature* **579**, 210–213 (2020).
- ¹⁷⁰K. Nagaoka, T. Jamneala, M. Grobis, and M. F. Crommie, “Temperature Dependence of a Single Kondo Impurity”, *Physical Review Letters* **88**, 077205 (2002).
- ¹⁷¹D. P. Daroca, P. Roura-Bas, and A. A. Aligia, “Relation between width of zero-bias anomaly and Kondo temperature in transport measurements through correlated quantum dots: Effect of asymmetric coupling to the leads”, *Physical Review B* **98**, 245406 (2018).
- ¹⁷²P. W. Anderson, “A poor man’s derivation of scaling laws for the Kondo problem”, *Journal of Physics C: Solid State Physics* **3**, 2436–2441 (1970).
- ¹⁷³A. Weichselbaum, F. Verstraete, U. Schollwöck, J. I. Cirac, and J. von Delft, “Variational matrix-product-state approach to quantum impurity models”, *Physical Review B* **80**, 165117 (2009).
- ¹⁷⁴A. Kaminski, Y. V. Nazarov, and L. I. Glazman, “Suppression of the Kondo Effect in a Quantum Dot by External Irradiation”, *Physical Review Letters* **83**, 384–387 (1999).
- ¹⁷⁵J. Schwenk, S. Kim, J. Berwanger, F. Ghahari, D. Walkup, M. R. Slot, S. T. Le, W. G. Cullen, S. R. Blankenship, S. Vranjkovic, H. J. Hug, Y. Kuk, F. J. Giessibl, and J. A. Stroscio, “Achieving eV tunneling resolution in an in-operando scanning tunneling microscopy, atomic force microscopy, and magnetotransport system for quantum materials research”, *Review of Scientific Instruments* **91**, 071101 (2020).
- ¹⁷⁶A. Georges, G. Kotliar, W. Krauth, and M. J. Rozenberg, “Dynamical mean-field theory of strongly correlated fermion systems and the limit of infinite dimensions”, *Reviews of Modern Physics* **68**, 13–125 (1996).
- ¹⁷⁷A. N. Rubtsov, V. V. Savkin, and A. I. Lichtenstein, “Continuous-time quantum Monte Carlo method for fermions”, *Physical Review B* **72**, 035122 (2005).

- ¹⁷⁸E. Gull, P. Werner, O. Parcollet, and M. Troyer, “Continuous-time auxiliary-field Monte Carlo for quantum impurity models”, *EPL (Europhysics Letters)* **82**, 57003 (2008).
- ¹⁷⁹J. Otsuki, H. Kusunose, P. Werner, and Y. Kuramoto, “Continuous-Time Quantum Monte Carlo Method for the Coqblin–Schrieffer Model”, *Journal of the Physical Society of Japan* **76**, 114707 (2007).
- ¹⁸⁰N. Prokof’ev and B. Svistunov, “Bold Diagrammatic Monte Carlo Technique: When the Sign Problem Is Welcome”, *Physical Review Letters* **99**, 250201 (2007).
- ¹⁸¹N. V. Prokof’ev and B. V. Svistunov, “Bold diagrammatic Monte Carlo: A generic sign-problem tolerant technique for polaron models and possibly interacting many-body problems”, *Physical Review B* **77**, 125101 (2008).
- ¹⁸²F. A. Wolf, I. P. McCulloch, O. Parcollet, and U. Schollwöck, “Chebyshev matrix product state impurity solver for dynamical mean-field theory”, *Physical Review B* **90**, 115124 (2014).
- ¹⁸³P. J. Knowles and N. C. Handy, “A new determinant-based full configuration interaction method”, *Chemical Physics Letters* **111**, 315–321 (1984).
- ¹⁸⁴D. Zgid, E. Gull, and G. K.-L. Chan, “Truncated configuration interaction expansions as solvers for correlated quantum impurity models and dynamical mean-field theory”, *Physical Review B* **86**, 165128 (2012).
- ¹⁸⁵M. Jarrell and J. E. Gubernatis, “Bayesian inference and the analytic continuation of imaginary-time quantum Monte Carlo data”, *Physics Reports* **269**, 133–195 (1996).
- ¹⁸⁶R. K. Bryan, “Maximum entropy analysis of oversampled data problems”, *European Biophysics Journal* **18**, 165–174 (1990).
- ¹⁸⁷H. J. Vidberg and J. W. Serene, “Solving the Eliashberg equations by means of N-point Padé approximants”, *Journal of Low Temperature Physics* **29**, 179–192 (1977).
- ¹⁸⁸A. W. Sandvik, “Stochastic method for analytic continuation of quantum Monte Carlo data”, *Physical Review B* **57**, 10287–10290 (1998).
- ¹⁸⁹K. S. D. Beach, *Identifying the maximum entropy method as a special limit of stochastic analytic continuation*, (Mar. 1, 2004) <http://arxiv.org/abs/cond-mat/0403055>.
- ¹⁹⁰A. S. Mishchenko, N. V. Prokof’ev, A. Sakamoto, and B. V. Svistunov, “Diagrammatic quantum Monte Carlo study of the Fröhlich polaron”, *Physical Review B* **62**, 6317–6336 (2000).
- ¹⁹¹S. Fuchs, T. Pruschke, and M. Jarrell, “Analytic continuation of quantum Monte Carlo data by stochastic analytical inference”, *Physical Review E* **81**, 056701 (2010).
- ¹⁹²N. V. Prokof’ev and B. V. Svistunov, “Spectral analysis by the method of consistent constraints”, *JETP Letters* **97**, 649–653 (2013).
- ¹⁹³J. Otsuki, M. Ohzeki, H. Shinaoka, and K. Yoshimi, “Sparse modeling approach to analytical continuation of imaginary-time quantum Monte Carlo data”, *Physical Review E* **95**, 061302 (2017).

- ¹⁹⁴M. Eckstein, M. Kollar, and P. Werner, “Thermalization after an Interaction Quench in the Hubbard Model”, *Physical Review Letters* **103**, 056403 (2009).
- ¹⁹⁵M. Eckstein, M. Kollar, and P. Werner, “Interaction quench in the Hubbard model: Relaxation of the spectral function and the optical conductivity”, *Physical Review B* **81**, 115131 (2010).
- ¹⁹⁶M. Eckstein and P. Werner, “Damping of Bloch Oscillations in the Hubbard Model”, *Physical Review Letters* **107**, 186406 (2011).
- ¹⁹⁷N. Tsuji, T. Oka, P. Werner, and H. Aoki, “Dynamical Band Flipping in Fermionic Lattice Systems: An ac-Field-Driven Change of the Interaction from Repulsive to Attractive”, *Physical Review Letters* **106**, 236401 (2011).
- ¹⁹⁸P. Schmidt and H. Monien, *Nonequilibrium dynamical mean-field theory of a strongly correlated system*, (Feb. 4, 2002) <http://arxiv.org/abs/cond-mat/0202046>.
- ¹⁹⁹P. Linz, “Numerical methods for Volterra integral equations of the first kind”, *The Computer Journal* **12**, 393–397 (1969).
- ²⁰⁰S. R. White and I. Affleck, “Spectral function for the $S=1$ Heisenberg antiferromagnetic chain”, *Physical Review B* **77**, 134437 (2008).
- ²⁰¹T. Barthel, U. Schollwöck, and S. R. White, “Spectral functions in one-dimensional quantum systems at finite temperature using the density matrix renormalization group”, *Physical Review B* **79**, 245101 (2009).
- ²⁰²R. G. Pereira, K. Penc, S. R. White, P. D. Sacramento, and J. M. P. Carmelo, “Charge dynamics in half-filled Hubbard chains with finite on-site interaction”, *Physical Review B* **85**, 165132 (2012).
- ²⁰³J. Ren and J. Sirker, “Spinons and helimagnons in the frustrated Heisenberg chain”, *Physical Review B* **85**, 140410 (2012).
- ²⁰⁴O. Parcollet, M. Ferrero, T. Ayrar, H. Hafermann, I. Krivenko, L. Messio, and P. Seth, “TRIQS: A toolbox for research on interacting quantum systems”, *Computer Physics Communications* **196**, 398–415 (2015).
- ²⁰⁵M. Potthoff, T. Wegner, and W. Nolting, “Interpolating self-energy of the infinite-dimensional Hubbard model: Modifying the iterative perturbation theory”, *Physical Review B* **55**, 16132–16142 (1997).
- ²⁰⁶H. Takagi and H. Y. Hwang, “An Emergent Change of Phase for Electronics”, *Science* **327**, 1601–1602 (2010).
- ²⁰⁷D. Ruzmetov, G. Gopalakrishnan, J. Deng, V. Narayanamurti, and S. Ramanathan, “Electrical triggering of metal-insulator transition in nanoscale vanadium oxide junctions”, *Journal of Applied Physics* **106**, 083702 (2009).
- ²⁰⁸Y. Zhou, X. Chen, C. Ko, Z. Yang, C. Mouli, and S. Ramanathan, “Voltage-Triggered Ultrafast Phase Transition in Vanadium Dioxide Switches”, *IEEE Electron Device Letters* **34**, 220–222 (2013).

- ²⁰⁹M. D. Pickett and R. Stanley Williams, “Sub-100 fJ and sub-nanosecond thermally driven threshold switching in niobium oxide crosspoint nanodevices”, *Nanotechnology* **23**, 215202 (2012).
- ²¹⁰F. A. Chudnovskii, L. L. Odynets, A. L. Pergament, and G. B. Stefanovich, “Electroforming and Switching in Oxides of Transition Metals: The Role of Metal–Insulator Transition in the Switching Mechanism”, *Journal of Solid State Chemistry* **122**, 95–99 (1996).
- ²¹¹J. Leroy, A. Crunteanu, A. Bessaudou, F. Cosset, C. Champeaux, and J.-C. Orlianges, “High-speed metal-insulator transition in vanadium dioxide films induced by an electrical pulsed voltage over nano-gap electrodes”, *Applied Physics Letters* **100**, 213507 (2012).
- ²¹²S. D. Ha, Y. Zhou, C. J. Fisher, S. Ramanathan, and J. P. Treadway, “Electrical switching dynamics and broadband microwave characteristics of VO₂ radio frequency devices”, *Journal of Applied Physics* **113**, 184501 (2013).
- ²¹³J. Sakai and M. Kurisu, “Effect of pressure on the electric-field-induced resistance switching of VO₂ planar-type junctions”, *Physical Review B* **78**, 033106 (2008).
- ²¹⁴I. Valmianski, P. Y. Wang, S. Wang, J. G. Ramirez, S. Guénon, and I. K. Schuller, “Origin of the current-driven breakdown in vanadium oxides: Thermal versus electronic”, *Physical Review B* **98**, 195144 (2018).
- ²¹⁵P. Stoliar, L. Cario, E. Janod, B. Corraze, C. Guillot-Deudon, S. Salmon-Bourmand, V. Guiot, J. Tranchant, and M. Rozenberg, “Universal Electric-Field-Driven Resistive Transition in Narrow-Gap Mott Insulators”, *Advanced Materials* **25**, 3222–3226 (2013).
- ²¹⁶E. Janod, J. Tranchant, B. Corraze, M. Querré, P. Stoliar, M. Rozenberg, T. Cren, D. Roditchev, V. T. Phuoc, M.-P. Besland, and L. Cario, “Resistive Switching in Mott Insulators and Correlated Systems”, *Advanced Functional Materials* **25**, 6287–6305 (2015).
- ²¹⁷F. Giorgianni, J. Sakai, and S. Lupi, “Overcoming the thermal regime for the electric-field driven Mott transition in vanadium sesquioxide”, *Nature Communications* **10**, 1159 (2019).
- ²¹⁸P. Diener, E. Janod, B. Corraze, M. Querré, C. Adda, M. Guilloux-Viry, S. Cordier, A. Camjayi, M. Rozenberg, M. P. Besland, and L. Cario, “How a dc electric field drives mott insulators out of equilibrium”, *Physical Review Letters* **121**, 016601 (2018).
- ²¹⁹A. Cavalleri, C. Tóth, C. W. Siders, J. A. Squier, F. Ráksi, P. Forget, and J. C. Kieffer, “Femtosecond Structural Dynamics in VO₂ during an Ultrafast Solid-Solid Phase Transition”, *Physical Review Letters* **87**, 237401 (2001).
- ²²⁰A. Cavalleri, T. Dekorsy, H. H. W. Chong, J. C. Kieffer, and R. W. Schoenlein, “Evidence for a structurally-driven insulator-to-metal transition in VO₂ : A view from the ultrafast timescale”, *Physical Review B* **70**, 161102 (2004).

- ²²¹M. M. Qazilbash, M. Brehm, B.-G. Chae, P.-C. Ho, G. O. Andreev, B.-J. Kim, S. J. Yun, A. V. Balatsky, M. B. Maple, F. Keilmann, H.-T. Kim, and D. N. Basov, “Mott Transition in VO₂ Revealed by Infrared Spectroscopy and Nano-Imaging”, *Science* **318**, 1750–1753 (2007).
- ²²²D. Wegkamp, M. Herzog, L. Xian, M. Gatti, P. Cudazzo, C. L. McGahan, R. E. Marvel, R. F. Haglund, A. Rubio, M. Wolf, and J. Stähler, “Instantaneous Band Gap Collapse in Photoexcited Monoclinic VO₂ due to Photocarrier Doping”, *Physical Review Letters* **113**, 216401 (2014).
- ²²³M. Liu, H. Y. Hwang, H. Tao, A. C. Strikwerda, K. Fan, G. R. Keiser, A. J. Sternbach, K. G. West, S. Kittiwatanakul, J. Lu, S. A. Wolf, F. G. Omenetto, X. Zhang, K. A. Nelson, and R. D. Averitt, “Terahertz-field-induced insulator-to-metal transition in vanadium dioxide metamaterial”, *Nature* **487**, 345–348 (2012).
- ²²⁴T. Bar, S. K. Choudhary, M. A. Ashraf, K. S. Sujith, S. Puri, S. Raj, and B. Bansal, “Kinetic Spinodal Instabilities in the Mott Transition in V₂O₃: Evidence from Hysteresis Scaling and Dissipative Phase Ordering”, *Physical Review Letters* **121**, 045701 (2018).
- ²²⁵J. Li, C. Aron, G. Kotliar, and J. E. Han, “Electric-Field-Driven Resistive Switching in the Dissipative Hubbard Model”, *Physical Review Letters* **114**, 226403 (2015).
- ²²⁶J. Li, C. Aron, G. Kotliar, and J. E. Han, “Microscopic Theory of Resistive Switching in Ordered Insulators: Electronic versus Thermal Mechanisms”, *Nano Letters* **17**, 2994–2998 (2017).
- ²²⁷J. E. Han, J. Li, C. Aron, and G. Kotliar, “Nonequilibrium mean-field theory of resistive phase transitions”, *Physical Review B* **98**, 035145 (2018).
- ²²⁸G. Mazza, A. Amaricci, M. Capone, and M. Fabrizio, “Field-Driven Mott Gap Collapse and Resistive Switch in Correlated Insulators”, *Physical Review Letters* **117**, 176401 (2016).
- ²²⁹P. Werner, H. U. R. Strand, S. Hoshino, and M. Eckstein, “Ultrafast switching of composite order in A₃C₆₀”, *Physical Review B* **95**, 195405 (2017).
- ²³⁰J. Li, H. U. R. Strand, P. Werner, and M. Eckstein, “Theory of photoinduced ultrafast switching to a spin-orbital ordered hidden phase”, *Nature Communications* **9**, 4581 (2018).
- ²³¹G.-W. Chern, *Kinetics of thermal Mott transitions in the Hubbard model*, (July 12, 2019) <http://arxiv.org/abs/1907.05880>.
- ²³²D. M. Newns, J. A. Misewich, C. C. Tsuei, A. Gupta, B. A. Scott, and A. Schrott, “Mott transition field effect transistor”, *Applied Physics Letters* **73**, 780–782 (1998).
- ²³³G. Stefanovich, A. Pergament, and D. Stefanovich, “Electrical switching and Mott transition in VO₂”, *Journal of Physics: Condensed Matter* **12**, 8837–8845 (2000).
- ²³⁴H.-T. Kim, B.-G. Chae, D.-H. Youn, S.-L. Maeng, G. Kim, K.-Y. Kang, and Y.-S. Lim, “Mechanism and observation of Mott transition in VO₂ -based two- and three-terminal devices”, *New Journal of Physics* **6**, 52–52 (2004).

- ²³⁵D. Ruzmetov, G. Gopalakrishnan, C. Ko, V. Narayanamurti, and S. Ramanathan, “Three-terminal field effect devices utilizing thin film vanadium oxide as the channel layer”, *Journal of Applied Physics* **107**, 114516 (2010).
- ²³⁶M. Nakano, K. Shibuya, D. Okuyama, T. Hatano, S. Ono, M. Kawasaki, Y. Iwasa, and Y. Tokura, “Collective bulk carrier delocalization driven by electrostatic surface charge accumulation”, *Nature* **487**, 459–462 (2012).
- ²³⁷H. Yamada, M. Marinova, P. Altuntas, A. Crassous, L. Bégon-Lours, S. Fusil, E. Jacquet, V. Garcia, K. Bouzehouane, A. Gloter, J. E. Villegas, A. Barthélémy, and M. Bibes, “Ferroelectric control of a Mott insulator”, *Scientific Reports* **3**, 2834 (2013).
- ²³⁸T. Driscoll, H.-T. Kim, B.-G. Chae, M. Di Ventra, and D. N. Basov, “Phase-transition driven memristive system”, *Applied Physics Letters* **95**, 043503 (2009).
- ²³⁹L. Pellegrino, N. Manca, T. Kanki, H. Tanaka, M. Biasotti, E. Bellingeri, A. S. Siri, and D. Marré, “Multistate Memory Devices Based on Free-standing VO₂/TiO₂ Microstructures Driven by Joule Self-Heating”, *Advanced Materials* **24**, 2929–2934 (2012).
- ²⁴⁰M. Son, X. Liu, S. M. Sadaf, D. Lee, S. Park, W. Lee, S. Kim, J. Park, J. Shin, S. Jung, M.-H. Ham, and H. Hwang, “Self-Selective Characteristics of Nanoscale VO_x Devices for High-Density ReRAM Applications”, *IEEE Electron Device Letters* **33**, 718–720 (2012).
- ²⁴¹F. J. Wong, T. S. Sriram, B. R. Smith, and S. Ramanathan, “Bipolar resistive switching in room temperature grown disordered vanadium oxide thin-film devices”, *Solid-State Electronics* **87**, 21–26 (2013).
- ²⁴²Y. Ye, J. Zhao, L. Xiao, B. Cheng, Y. Xiao, and S. Lei, “Reversible Negative Resistive Switching in an Individual Fe@Al₂O₃ Hybrid Nanotube for Nonvolatile Memory”, *ACS Applied Materials & Interfaces* **10**, 19002–19009 (2018).
- ²⁴³S.-H. Bae, S. Lee, H. Koo, L. Lin, B. H. Jo, C. Park, and Z. L. Wang, “The Memristive Properties of a Single VO₂ Nanowire with Switching Controlled by Self-Heating”, *Advanced Materials* **25**, 5098–5103 (2013).
- ²⁴⁴M. D. Pickett, G. Medeiros-Ribeiro, and R. S. Williams, “A scalable neuristor built with Mott memristors”, *Nature Materials* **12**, 114–117 (2013).
- ²⁴⁵D. B. Strukov, G. S. Snider, D. R. Stewart, and R. S. Williams, “The missing memristor found”, *Nature* **453**, 80–83 (2008).
- ²⁴⁶Y. Kalcheim, A. Camjayi, J. del Valle, P. Salev, M. Rozenberg, and I. K. Schuller, *Non-Thermal Resistive Switching in Mott Insulators*, (Aug. 22, 2019) <http://arxiv.org/abs/1908.08555>.
- ²⁴⁷J. del Valle, Y. Kalcheim, J. Trastoy, A. Charnukha, D. N. Basov, and I. K. Schuller, “Electrically Induced Multiple Metal-Insulator Transitions in Oxide Nanodevices”, *Physical Review Applied* **8**, 054041 (2017).
- ²⁴⁸J. del Valle, P. Salev, Y. Kalcheim, and I. K. Schuller, *A caloritronics-based Mott neuristor*, (Mar. 3, 2019) <http://arxiv.org/abs/1903.01062>.

- ²⁴⁹Y. Zhou and S. Ramanathan, “Mott Memory and Neuromorphic Devices”, [Proceedings of the IEEE](#) **103**, 1289–1310 (2015).
- ²⁵⁰Z. Yang, C. Ko, and S. Ramanathan, “Oxide Electronics Utilizing Ultrafast Metal-Insulator Transitions”, [Annual Review of Materials Research](#) **41**, 337–367 (2011).
- ²⁵¹J. S. Brockman, L. Gao, B. Hughes, C. T. Rettner, M. G. Samant, K. P. Roche, and S. S. P. Parkin, “Subnanosecond incubation times for electric-field-induced metallization of a correlated electron oxide”, [Nature Nanotechnology](#) **9**, 453–458 (2014).
- ²⁵²J. E. Han and J. Li, “Energy dissipation in a dc-field-driven electron lattice coupled to fermion baths”, [Physical Review B](#) **88**, 075113 (2013).
- ²⁵³J. E. Han, “Solution of electric-field-driven tight-binding lattice coupled to fermion reservoirs”, [Physical Review B](#) **87**, 085119 (2013).
- ²⁵⁴A. Mitra and A. J. Millis, “Current-driven quantum criticality in itinerant electron ferromagnets”, [Physical Review B](#) **77**, 220404 (2008).
- ²⁵⁵P. Werner, M. Eckstein, M. Müller, and G. Refael, “Light-induced evaporative cooling of holes in the Hubbard model”, [Nature Communications](#) **10**, 5556 (2019).
- ²⁵⁶P. Werner, J. Li, D. Golež, and M. Eckstein, “Entropy-cooled nonequilibrium states of the Hubbard model”, [Physical Review B](#) **100**, 155130 (2019).
- ²⁵⁷T. Pruschke, D. L. Cox, and M. Jarrell, “Hubbard model at infinite dimensions: Thermodynamic and transport properties”, [Physical Review B](#) **47**, 3553–3565 (1993).
- ²⁵⁸S. Sayyad and M. Eckstein, “Slowdown of the Electronic Relaxation Close to the Mott Transition”, [Physical Review Letters](#) **117**, 096403 (2016).
- ²⁵⁹P. C. Hohenberg and B. I. Halperin, “Theory of dynamic critical phenomena”, [Reviews of Modern Physics](#) **49**, 435–479 (1977).
- ²⁶⁰G. Kotliar, “Landau theory of the Mott transition in the fully frustrated Hubbard model in infinite dimensions”, [The European Physical Journal B - Condensed Matter and Complex Systems](#) **11**, 27–39 (1999).
- ²⁶¹G. Kotliar, E. Lange, and M. J. Rozenberg, “Landau Theory of the Finite Temperature Mott Transition”, [Physical Review Letters](#) **84**, 5180–5183 (2000).
- ²⁶²H. U. R. Strand, A. Sabashvili, M. Granath, B. Hellsing, and S. Östlund, “Dynamical mean field theory phase-space extension and critical properties of the finite temperature Mott transition”, [Physical Review B](#) **83**, 205136 (2011).
- ²⁶³L. Chua, “If it’s pinched it’s a memristor”, [Semiconductor Science and Technology](#) **29**, 104001 (2014).
- ²⁶⁴A. Moutenet, P. Seth, M. Ferrero, and O. Parcollet, “Cancellation of vacuum diagrams and the long-time limit in out-of-equilibrium diagrammatic quantum Monte Carlo”, [Physical Review B](#) **100**, 085125 (2019).
- ²⁶⁵R. W. Helmes, T. A. Costi, and A. Rosch, “Kondo Proximity Effect: How Does a Metal Penetrate into a Mott Insulator?”, [Physical Review Letters](#) **101**, 066802 (2008).

- ²⁶⁶J. Bezanson, A. Edelman, S. Karpinski, and V. B. Shah, “Julia: A Fresh Approach to Numerical Computing”, [SIAM Review](#) **59**, 65–98 (2017).
- ²⁶⁷D. G. Anderson, “Iterative Procedures for Nonlinear Integral Equations”, [Journal of the ACM](#) **12**, 547–560 (1965).
- ²⁶⁸C. G. Broyden, “A class of methods for solving nonlinear simultaneous equations”, [Mathematics of Computation](#) **19**, 577–593 (1965).